University of South Florida
Scholar Commons

Graduate Theses and Dissertations

Graduate School

2011

Theoretical and Experimental Analysis of Power and Cooling Cogeneration Utilizing Low Temperature Heat Sources

Gökmen Demirkaya
University of South Florida, gdemirka@mail.usf.edu

Follow this and additional works at: http://scholarcommons.usf.edu/etd

Part of the American Studies Commons, and the Mechanical Engineering Commons

Scholar Commons Citation
Demirkaya, Gökmen, "Theoretical and Experimental Analysis of Power and Cooling Cogeneration Utilizing Low Temperature Heat Sources" (2011). *Graduate Theses and Dissertations.*
http://scholarcommons.usf.edu/etd/3069

This Dissertation is brought to you for free and open access by the Graduate School at Scholar Commons. It has been accepted for inclusion in Graduate Theses and Dissertations by an authorized administrator of Scholar Commons. For more information, please contact scholarcommons@usf.edu.

المنارة للاستشارات

www.manaraa.com

Theoretical and Experimental Analysis of Power and Cooling Cogeneration Utilizing Low Temperature Heat Sources

by

Gökmen Demirkaya

A dissertation submitted in partial fulfillment
of the requirements for the degree of
Doctor of Philosophy
Department of Mechanical Engineering
College of Engineering
University of South Florida

Major Professor: D. Yogi Goswami, Ph.D.
Elias Stefanakos, Ph.D.
Muhammad M. Rahman, Ph.D.
Ashok Kumar, Ph.D.
George S. Nolas, Ph.D.

Date of Approval:
June 21, 2011

Keywords: Combined cycle, Thermodynamic analysis, Multi-turbine stage, Ammonia-water mixture, Scroll expander

Copyright © 2011, Gökmen Demirkaya

www.manaraa.com

Dedication

To my beloved wife, Burcu, who is infinitely supportive, inspiring, patient, and full of love...

المنارة للاستشارات

www.manaraa.com

Acknowledgements

I would like to thank my advisor, Dr. D. Yogi Goswami, for his teaching, patience, guidance, and encouragement during this study. I am also grateful to Dr. Muhammad Rahman for discussions. I also appreciate the guidance and valuable contributions of my Ph.D committee members Dr. Elias Stefanakos, Dr. Nolas, and Dr. Kumar. From time to time, I needed help from Mr. Charles Garretson, Clean Energy Research Lab (CERC). His marvelous skills solved many problems during experiments, and I have learned a lot from him. Special thanks to Ms. Ginny Cosmides and Ms. Barbara Graham helped me in many ways in the course of my stay here.

My fellow students at the CERC lab have been helpful, I would like to acknowledge their valuable contributions, Ali Emre Erçelebi, Saeb Besarati, Huijuan Chen, Antonio Ramos Archibold, Kofi Dalrymple, Chennan Li, Derviş Emre Demirocak and Jamie Trahan. I would like to thank to Ricardo Vasquez Padilla specially, who has been at the lab almost as long as I have, and has been always supportive. I would also like to thank Dr. Goswami's former students, Dr. Nitin Goel, Dr. Chris Martin and Dr. Gunnar Tamm, whose work on the experimental setup helped me to design and build the present set-up. Even though I have not met with them in person, they helped me whenever I have asked help by email.

المنارة للاستشارات

www.manaraa.com

I would like to particularly thank my family for putting up with my being so far away from home, and for their love and support. I would like to thank to my elder brother Gökhan, my sister Nazlı, and my lovely mother Hatice for their support and motivation. I am also grateful to my father, Adem, who passed away during my study. Without them, I could not go so far to come to U.S. and, this dissertation would not have been written. I would like to thank also my family-in-law, Zeki, Nezahat and Burçin for their continuous support. Finally, I want to thank my wife Burcu for her unquestioning support during this work. Without her support and love, I doubt that I would have reached this personal milestone.

www.manaraa.com

Table of Contents

المنارة للاستشارات
www.manaraa.com

المنارة للاستشارات

www.manaraa.com

www.manaraa.com

List of Tables

www.manaraa.com

المنارة للاستشارات

www.manaraa.com

List of Figures

المنارة للاستشارات

www.manaraa.com

المنارة للاستشارات

www.manaraa.com

المنارة للاستشارات

www.manaraa.com

المنارة للاستشارات

www.manaraa.com

المنارة للاستشارات

www.manaraa.com

المنارة للاستشارات

www.manaraa.com

المنارة للاستشارات

www.manaraa.com

List of Symbols

BTU	British thermal unit
x	ammonia concentration $(\frac{kg\ NH_3}{kg\, solution})$
COP	coefficient of performance
D	diameter (mm)
X	exergy destruction $(\frac{kJ}{kg\, solution})$
E	exergy $(\frac{kJ}{kg\, solution})$
h	enthalpy $(\frac{kJ}{kg})$
$\dot{m}$	mass flow ratio $(\frac{kg}{kg\, solution})$
MF	mass flow $(\frac{g}{s})$
MJ	mega joule
Mtoe	million tonnes of oil equivalent
P	Pressure (bar)
PR	pressure ratio
Q	heat transfer $(\frac{kJ}{kg\, solution})$, volumetric flow rate $(\frac{m^3}{s})$
S	Speed (rpm)
U	rotor tip speed $(\frac{m}{s})$
s	entropy $(\frac{kJ}{kg\, K})$
N	specific speed
T	temperature $(C\, or\, K)$

المنارة للاستشارات
www.manaraa.com

C	velocity based on the ideal enthalpy drop of turbine $(\frac{m}{s})$
W	work $(\frac{kJ}{kg\,solution})$

Greek Symbols

α	constant to calculate exergy of a binary mixture
β	constant to calculate exergy of a binary mixture
η	efficiency
ε	heat exchanger effectiveness, exergy per unit mass $(\frac{kJ}{kgsolution})$
ω	Rotational speed $(\frac{rad}{s})$

Subscripts

absorber	absorber
boiler	boiler
boiler heat exchanger	boiler heat exchanger
cf	chilled fluid
cv	control volume
c	cooling
eff	effective value
exergy	exergy
e	exit
h	heat
hs	heat source
ideal	ideal
I	first law
II	exergy
i	inlet

المنارة للاستشارات

www.manaraa.com

in	inlet
liquid	liquid
net	net
out	outlet
pump	pump
recovery heat exchanger	recovery heat exchanger
rectifier	rectifier
o	reference
ref	reference
sat	saturated
separator	separator
s	specific
strong solution	strong solution
superheater	superheater
throttling valve	throttling valve
turbine	turbine
t	turbine
vapor	vapor
weak	weak solution

المنارة للاستشارات

www.manaraa.com

Abstract

Development of innovative thermodynamic cycles is important for the efficient utilization of low-temperature heat sources such as solar, geothermal, and waste heat sources. Binary mixtures exhibit variable boiling temperatures during the boiling process, which leads to a good thermal match between the heating fluid and working fluid for efficient heat source utilization. This study presents a theoretical and an experimental analysis of a combined power/cooling cycle, which combines the Rankine and absorption refrigeration cycles, uses ammonia-water mixture as the working fluid and produces power and refrigeration, while power is the primary goal. This cycle, also known as the Goswami Cycle, can be used as a bottoming cycle using waste heat from a conventional power cycle or as an independent cycle using low to mid-temperature sources such as geothermal and solar energy. A thermodynamic analysis of power and cooling cogeneration was presented.

The performance of the cycle for a range of boiler pressures, ammonia concentrations, and isentropic turbine efficiencies were studied to find out the sensitivities of net work, amount of cooling and effective efficiencies. The thermodynamic analysis covered a broad range of boiler temperatures, from 85 °C to 350 °C. The first law efficiencies of 25-31% are achievable with the boiler temperatures of 250-350 °C. The cycle can operate at an effective exergy efficiency of 60-68% with the boiler temperature range of 200-350 °C. An experimental study was conducted to verify the predicted trends and to test the performance

المنارة للاستشارات

www.manaraa.com

of a scroll type expander. The experimental results of vapor production were verified by the expected trends to some degree, due to heat transfer losses in the separator vessel. The scroll expander isentropic efficiency was between 30-50%, the expander performed better when the vapor was superheated. The small scale of the experimental cycle affected the testing conditions and cycle outputs. This cycle can be designed and scaled from a kilowatt to megawatt systems. Utilization of low temperature sources and heat recovery is definitely an active step in improving the overall energy conversion efficiency and decreasing the capital cost of energy per unit.

المنارة للاستشارات
www.manaraa.com

Chapter 1

Introduction

Fossil fuels like coal, oil, and natural gas are the main energy resources in modern day and they are considered non-renewable energy sources because they take millions of years to form and cannot be renewed after use. Renewable energy technologies are those that harness energy from an inexhaustible source such as the sun, wind, falling water, waves, tides, biomass, or heat generated beneath the surface of the Earth. All of the renewable energy resources are derived from the sun except the geothermal energy. Solar energy comes directly from the thermal energy released by the sun; however, sources like wind, hydropower, waves and tides are the indirect result of solar energy. The other alternative source is nuclear power that does not emit CO_2 but is nonrenewable.

Current world primary energy consumption and the forecasted demand for limited fossil fuels, nuclear and renewable resources are presented in Fig. 1.1 [1]. Of the world's energy demand in 2008, the fossil fuels accounted for about 81.2% with oil, coal and natural gas making up 33.1%, 27.0%, and 21.1% of that total, respectively. Renewable energy sources make up only 13.0% of the total world energy use. Statistics from the Internation Energy Agency (IEA) show that the world energy consumption is projected to increase by 37% from 2008 to 2035 as shown in Fig. 1.1 [1]. According to their forecast, renewables,

المنارة للاستشارات
www.manaraa.com

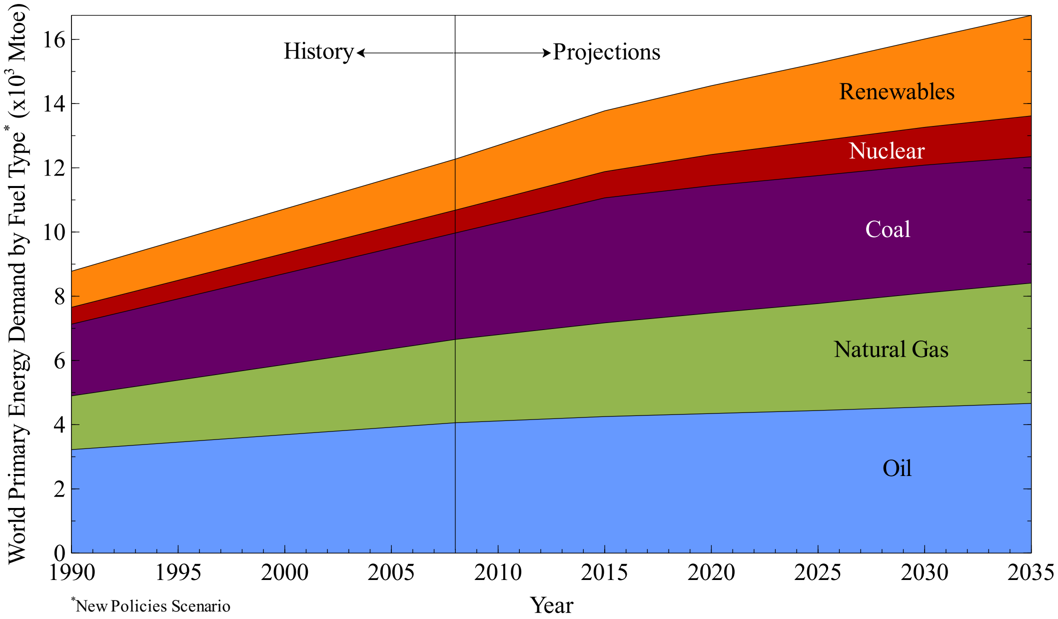

Figure 1.1 Current and projections of the world primary energy demand by fuel type. Data is adapted from [1]

natural gas and coal account for the largest increments in fuel consumption for energy use over the projected period.

Sustained high prices for oil and natural gas make coal-fired generation more attractive economically, especially for coal-rich nations like China, India, and the United States, however coal is also the most carbon intensive energy source. Carbon dioxide is the largest human-caused greenhouse gas in the atmosphere [2]. Atmospheric concentrations of carbon dioxide have been rising at a rate of about 0.6% annually in recent years, and that growth rate is likely to increase. As a result, by the middle of the 21st century, carbon dioxide concentrations in the atmosphere could be doubled since the industrialization started in 1900s. Despite these facts, global energy demand continues to be supplied from nonrenewable sources over the long term as seen by projections in Fig. 1.1.

المنارة للاستشارات
www.manaraa.com

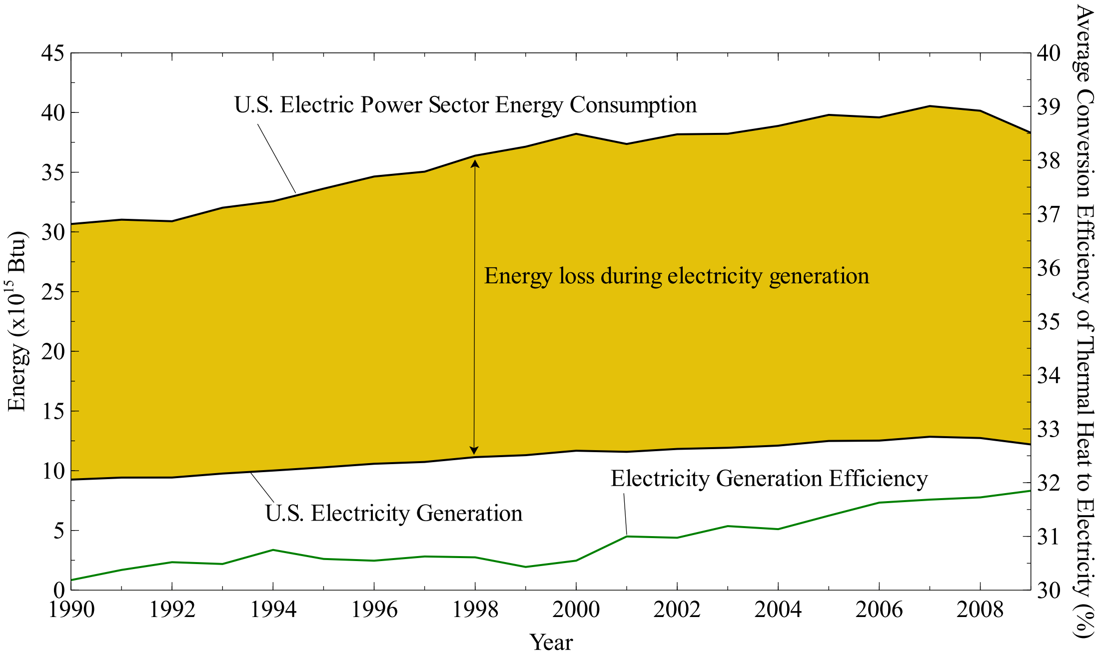

Figure 1.2 U.S. electric power sector energy consumption, electricity generation, and conversion efficiency. Data is adapted from [3]

U.S. electric power sector energy consumption, electricity generation, and conversion efficiency are shown in Fig. 1.2. Electrical system energy losses are calculated as the difference between the total primary consumption by the electric power sector and the total energy content of electricity retail sales. Most of these losses occur at steam-electric power plants (conventional and nuclear) in the conversion of heat energy into mechanical energy to turn electric generators. In addition to conversion losses, other losses include power plant use of electricity (~5%), transmission and distribution (~7%) of electricity from power plants to end-use consumers, which is also called line losses [2]. Overall, about two thirds of total energy input is lost in conversion. As it is shown in the figure, the average conversion efficiency of thermal heat to electricity is increased approximately 2% since 1990. The average electricity conversion was close to 32% in 2009.

للاستشارات المنارة
www.manaraa.com

To reduce the transmission and distribution losses, the generation should be done by more locally, rather than in a centralized power plant where the electricity is transmitted thousands of miles to the consumers. The motivation for this work comes from the possible recovery of energy losses shown in Fig. 1.2, this would increase the overall energy conversion efficiency, and decrease the dependency on the limited fossil fuels.

1.1 Motivation

Utilization of low temperature sources and heat recovery is an active step in improving the overall energy conversion efficiency and decreasing the capital cost of energy per unit. The ammonia-water combined power/cooling cycle proposed by Goswami [4, 5] utilizes a binary ammonia-water working fluid to produce both power and refrigeration. The cycle, also known as the Goswami Cycle, is a combination of an ammonia-based Rankine cycle and an ammonia-water absorption refrigeration cycle. This cycle can be designed and scaled from a kilowatt to megawatt systems, and can be used as a bottoming cycle using waste heat from a conventional power cycle or as an independent cycle using solar or geothermal energy. The heat source temperature can be varied from a low temperature source such as 60 °C to mid temperature sources such as 350 °C. The cycle can be optimized for power, cooling, or efficiency, whichever is the priority for the designer. The use of Goswami cycle is one candidate of the distributed technologies that could connect to the power grid.

The distinguishing feature of this cycle is the method in which cooling is produced. In conventional Rankine power cycle the working fluid is regenerated by pure condensation, however in this cycle absorption condensation is used to regenerate the working fluid. This

المنارة للاستشارات
www.manaraa.com

allows the expander exhaust temperature to be significantly below the ambient temperature. In the power/cooling cycle, it is possible to expand the vapor to sub-ambient temperatures, which can be used for cooling since the vapor is condensed by absorption in a liquid. A detailed literature survey on the combined power/cooling cycle, and a detailed analysis of the Goswami cycle will be presented in Chapter 2.

Martin and Goswami [6,7] performed experiments on the cycle at the Solar Energy and Energy Conversion Laboratory of the University of Florida, and found that the expander is one of the critical components. The aim of the experiments was to demonstrate that power and cooling could be obtained simultaneously. The potential of cooling output from the cycle was verified by the temperature difference between the absorber and expander exit, however the minimum cooling temperatures obtained in the experiments were higher than expected. They explained the reason as the low conversion efficiency of the expander, which they estimated to be between 20% and 35%. After the experiments [7–9] were done at the Solar Energy and Energy Conversion Laboratory of University of Florida, some of the cycle components were moved to Clean Energy Research Center of the University of South Florida.

Scroll compressors have been widely adopted by the HVAC industry because of the advantages they offer, including: simple design, low friction, low torque pulsation, and compliance. Literature suggests the potential use of a scroll compressor as a high efficiency expander [10,11]. Therefore, in this work, scroll expander was chosen as a suitable expander candidate. Based on the experiments and recommendations of the previous re-

المنارة للاستشارات
www.manaraa.com

searchers, experimental cycle was re-assembled with major modifications. The modifications regarding the experimental setup will be discussed in Chapter 4.

1.2 Research Objectives

The overall objective of this research is to assemble the Goswami cycle with the modified components as well as detailed analysis of the cycle with simulations and study the performance based on experiments and simulations. Theoretical studies are aimed to investigate the cooling and power output sensitivity of the combined cycle to a range of boiler pressures, strong solution concentrations and different boiler exit configurations. Analytical and experimental study will determine the strong and weak points of the cycle. The experimental study is very important since very limited experimental study of the cycle was accomplished before this research. The following are the detailed objectives of this research work:

1. Conduct a literature review of the state-of-art power and cooling cycles.
2. Develop a thermodynamic model to analyze the Goswami cycle for a set of heat source temperatures.
3. Conduct a literature review of the expanders used in low-temperature cycles.
4. Assemble the cycle on a moveable strut-channel frame, and upgrade or renew the components such as pumps, absorber heat exchanger and piping.
5. Assemble boiler and condenser units for the cycle, to simulate the experiments in the lab environment.

المنارة للاستشارات
www.manaraa.com

6. Modify and test the expander in experiments and compare with the theoretical cycle analysis.

www.manaraa.com

Chapter 2

Background and Summary of Previous Work

Development of innovative thermodynamic cycles is important for efficient utilization of renewable energy sources such as solar, geothermal, and waste heat sources. Thermal power cycles can be classified on the basis of the working fluid used, as vapor power cycles and gas power cycles. In a vapor power cycle, the gas that spins the turbine is obtained from vaporizing a liquid. An example of such a cycle is the classic Rankine cycle. In a gas power cycle, such as the Brayton cycle, the working fluid is in a gaseous state throughout the cycle.

Selection of the appropriate thermodynamic cycles and the working fluids depends strongly on the temperature of the heat source. In this research, we are focusing on the low and mid temperature sources such as solar energy, geothermal or waste heat in the temperature range of 60-350 °C. The Goswami cycle is applicable within this range. In this chapter, we will review important thermodynamical cycles in this temperature range. Finally, this chapter will review the literature and the previous work on the Goswami cycle.

2.1 Solar Thermal Power

Solar thermal electric power plants generate electricity by converting concentrated solar energy to heat, which is then converted to electricity as in a conventional thermal power plant. The three major concepts used today are line-focus systems (parabolic trough and

www.manaraa.com

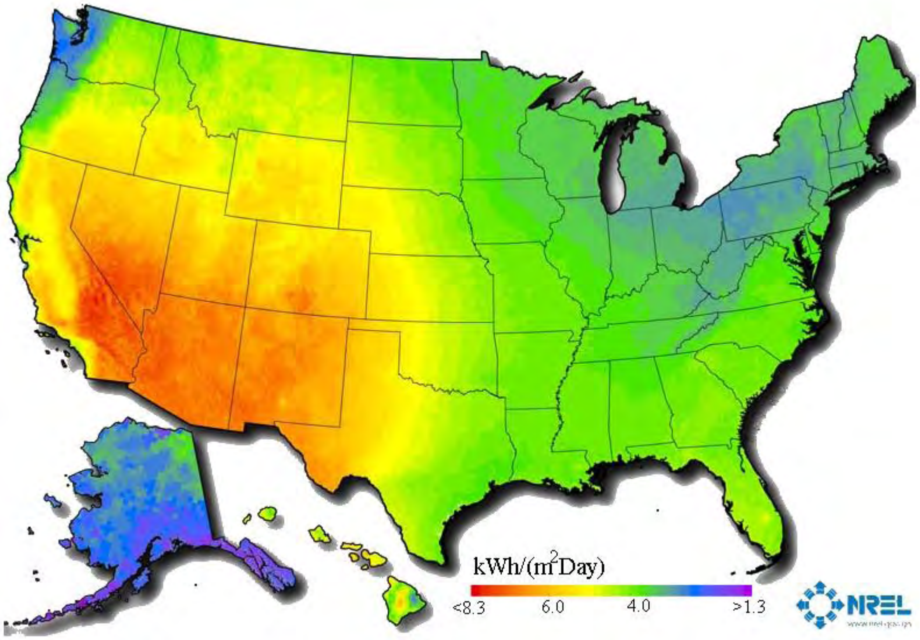

Figure 2.1 Concentrating solar resource of the U.S. Map is taken from [12]

continuous linear Fresnel reflector (CLFR)), point-focus central receiver (power towers), and point-focus distributed receiver (dish-engine systems). Each of these technologies can be hybridized with fossil fuels. This hybrid operation has the potential to increase the value of concentrated solar power (CSP) technology by increasing its power availability and decreasing its cost by making more effective use of the power block.

2.1.1 Parabolic Trough Systems

Parabolic trough systems are usually oriented in a north-south direction and the collectors track the sun from east to west focusing solar energy on a long tubular receiver, as shown in Fig. 2.2. They are able to concentrate the solar radiation flux 30 to 80 times, heating the thermal fluid up to about 400 °C-450 °C. A synthetic heat transfer oil or molten salt is usually used as a the heat transfer fluid. This heat transfer fluid is pumped from the solar field to a power block, where the fluid's heat is converted to high-pressure steam in

المنارة للاستشارات
www.manaraa.com

Figure 2.2 LS2 trough fields at Kramer Junction power plant in the Mojave desert. Photo is taken from [16]

a series of heat exchangers. This steam is directed to a conventional steam turbine, which converts the thermal heat into electricity. A schematic drawing of solar thermal power cycle is shown in Fig. 2.3. Steam Rankine cycle is usually used in parabolic trough based solar thermal power [13–15].

2.1.2 Continuous Linear Fresnel Reflector (CLFR) Systems

Fresnel mirror systems use long flat mirrors at different angles to concentrate sunlight on to a tube containing heat-collecting fluid as shown in Fig. 2.4. They differ from troughs in that the mirrors are located near the ground and rotate individually while focusing on a fixed receiver tube. CLFR companies suggest that their systems are less costly than

المنارة للاستشارات
www.manaraa.com

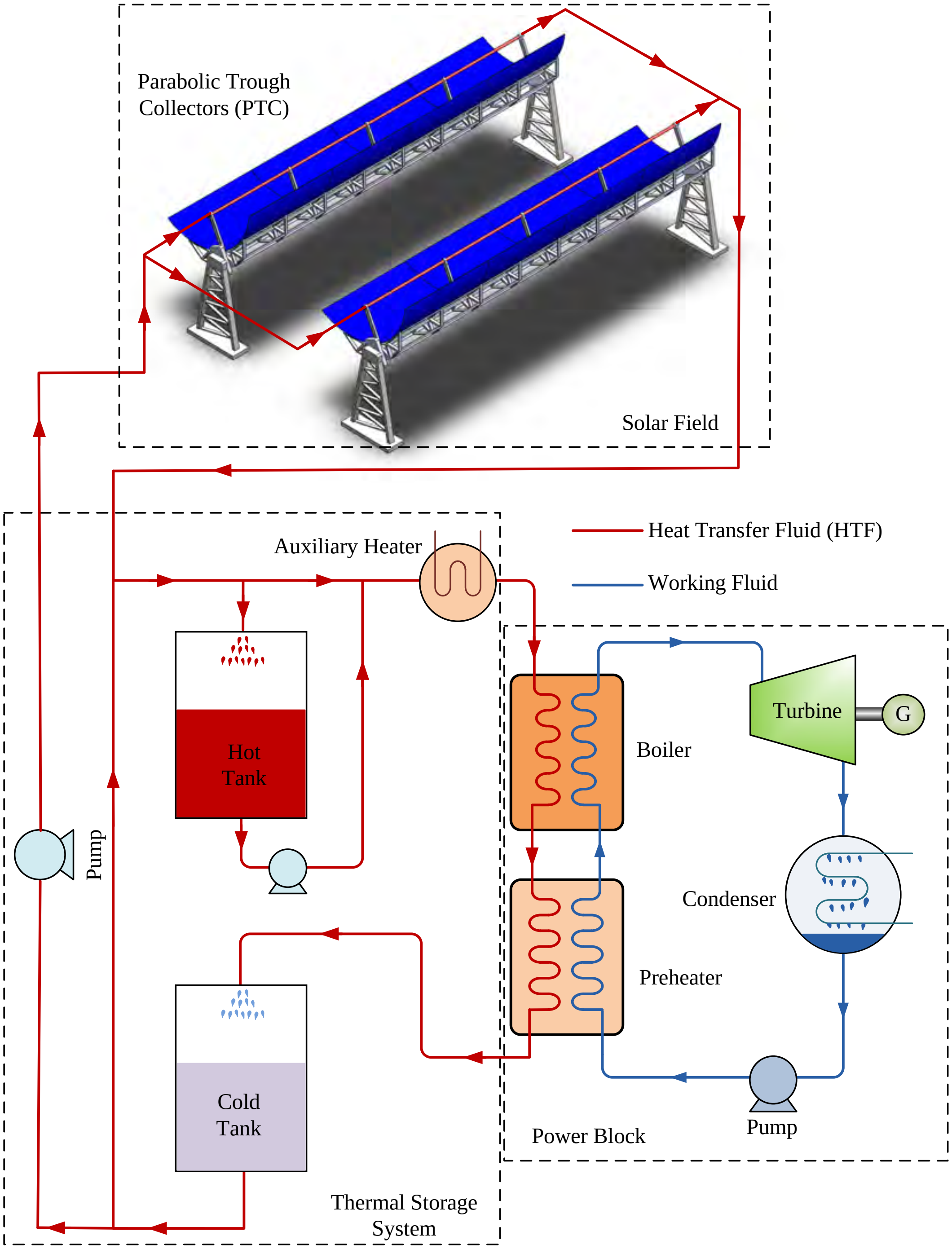

Figure 2.3 Schematic description of the solar thermal power cycle

parabolic troughs and will result in lower energy costs. However, there are no operating CLFR based power plants to allow a comparison of costs.

www.manaraa.com

Figure 2.4 Solar power group's fresnel mirror test rig at the plataforma solar de Almeria in Spain. Photo is taken from [17]

2.1.3 Dish/Engine Systems

Solar Dish/Engine systems are small modular units with autonomous generation of electricity by engines, such as Stirling engines located at the focal point. The parabolic dish reflector concentrates the solar radiation on a small area. The dish structure must track the sun continuously to reflect the beam into the thermal receiver. The thermal receiver is the interface between the dish and the engine/generator. It absorbs the concentrated beam of solar energy, converts it to heat, and transfers the heat to the engine/generator. A thermal receiver can be a bank of tubes with a heat transfer fluid, usually air, hydrogen or helium, which is also the working fluid for the engine. Alternate thermal receivers are heat pipes wherein the boiling and condensation of an intermediate fluid is used to transfer the heat to the engine. Due to aerodynamical constraints like wind forces which deform the surface of

المنارة للاستشارات
www.manaraa.com

the concentrator, the maximum size is limited to a few 100 m^2 and its electric power output to about 10-50 kW. Two different dish concentrators are shown in Fig. 2.5.

(a) Science App. Int. Corp., Golden, CO, U.S.

(b) Boeing Co., Daggett, CA, U.S.

Figure 2.5 Dish/engine systems. Photos are taken from [16].

2.1.4 Power Tower Systems

Power tower systems consist of a field of large, nearly-flat mirror assemblies (heliostats) that track the sun and focus the sunlight onto a receiver at the top of a tower. The system uses hundreds to thousands of sun-tracking heliostats to reflect the incident sunlight onto the receiver (Fig. 2.6). In a typical configuration, a heat-transfer fluid such as water/steam, atmospheric or pressurized air or molten nitrate salt mixture is pumped through the receiver, and used to generate steam to power a conventional steam-turbine power cycle generating electricity. Large receiver systems with thousands of heliostats, each with 100 m^2 mirror area, would require towers up to 100-200 m high. They could collect several hundred MW

www.manaraa.com

of solar radiation power. An advantage of power tower systems over linear concentrator systems is that higher temperatures can be achieved in the working fluid, leading to higher efficiencies and lower-cost electricity. Power towers can achieve very high operating temperatures of over 1000 °C, enabling them to produce hot air for gas turbine operation. Gas turbines can be used in combined cycles, yielding very high conversion efficiencies of the thermal cycle of more than 50%.

(a) Solar Two, California, U.S.

(b) PS 10, Sanlúcar la Mayor, Spain

Figure 2.6 Power tower systems in operation. Photos are taken from [16]

المنارة للاستشارات
www.manaraa.com

2.2 Geothermal Energy

Geothermal energy is used in several ways, heating applications for residential or commercial buildings and generating electricity. The advantage of geothermal energy compared to solar thermal and wind energy is that it is available around the clock, which makes it especially attractive for base-load power plants. Today, most of the large geothermal power plants in the world use hot water from volcanically active regions to generate electric power. However, the occurrence of geothermal heat sources is not limited to regions with noticeable volcanism. In principle, there is geothermal heat everywhere, but it must be drilled down to depths of four to five kilometers (~ 3000-5000 m) in order to tap a level of temperatures, which is high enough to effectively generate electric power using steam turbines. The challenge lies in the establishment of technologies that improve the yield of geothermal repositories and reduce the risks associated with their exploration and exploitation.

Geothermal power plants fall into one of three categories: direct steam, flash, and binary plants. Dry steam power plants systems were the first type of geothermal power generation plants built. In the dry steam power plants, the steam is piped directly from underground wells to the power plant, where it is directed into a turbine. Flash steam plants are used at sites that produce high-temperature waters (between 175 °C and 300 °C). In these designs, water is pumped under high pressure to the generation equipment at the surface. When the fluid reaches the surface, where pressures are lower, the fluid "flashes" to steam, which is sent to turbine. Binary cycle plants differ from dry steam and flash steam systems in that the water or steam from the geothermal reservoir never comes in contact with the turbine;

المنارة للاستشارات
www.manaraa.com

these systems convert lower temperature geothermal water (90°–175°C) to electricity by first routing the fluid through a closed-loop heat exchanger, where it heats a hydrocarbon working fluid. A typical example of this type of energy source is the 60 MW power plant at the Krafla volcano in Iceland. Iceland provides 60% of electricity demand from geothermal systems. The plant gets hot hydrothermal brine at initially 400 °C from 2200 m depth. The water expands and cools on rising up the well shaft and finally is input to the power plant as steam at 170 °C.

The geothermal resource potential map for the U.S. shows locations of identified hydrothermal sites and favorability of deep enhanced geothermal systems (EGS) in Fig. 2.7. In the United States, most geothermal reservoirs are located in the western states, Alaska, and Hawaii.

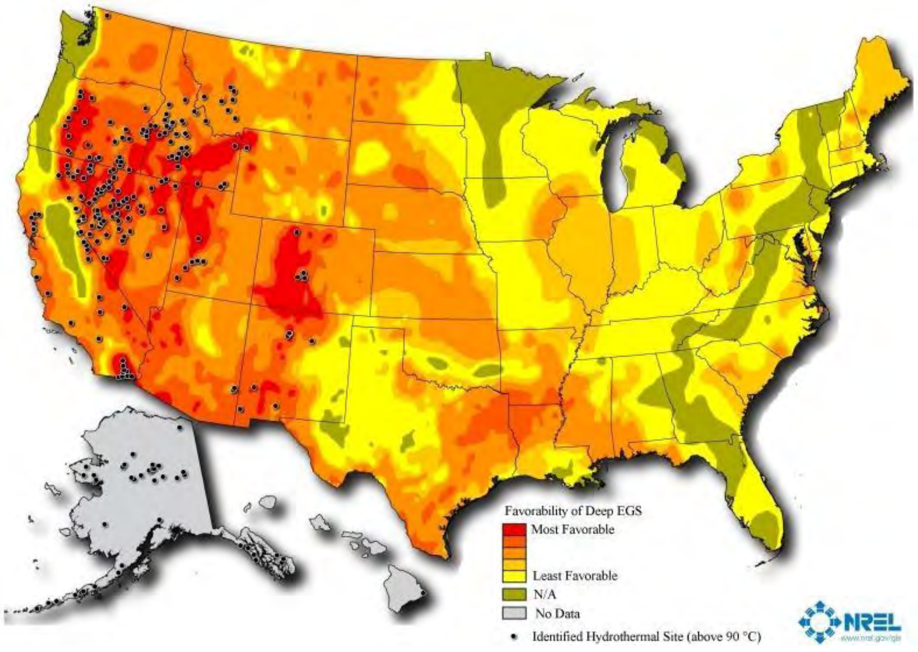

Figure 2.7 Geothermal resource of the U.S. Map is taken from [12]

Note: The map does not include shallow EGS resources located near hydrothermal sites or U.S. Geological Survey (USGS) assessment of undiscovered hydrothermal resources

www.manaraa.com

The most recent data by N.R.E.L. shows that 3086.6 MW of geothermal electric generating capacity is on-line in 9 states as shown in the Fig. 2.8. With the current projects both under development and in confirmation phases, it is expected to increase by 5256.2 MW to 7877.2 MW, which will make the total in the range of 8342.8 MW to 10963.8 MW. Geothermal resources are not only used for power generation but also used for agricultural heating, industrial, and bathing applications.

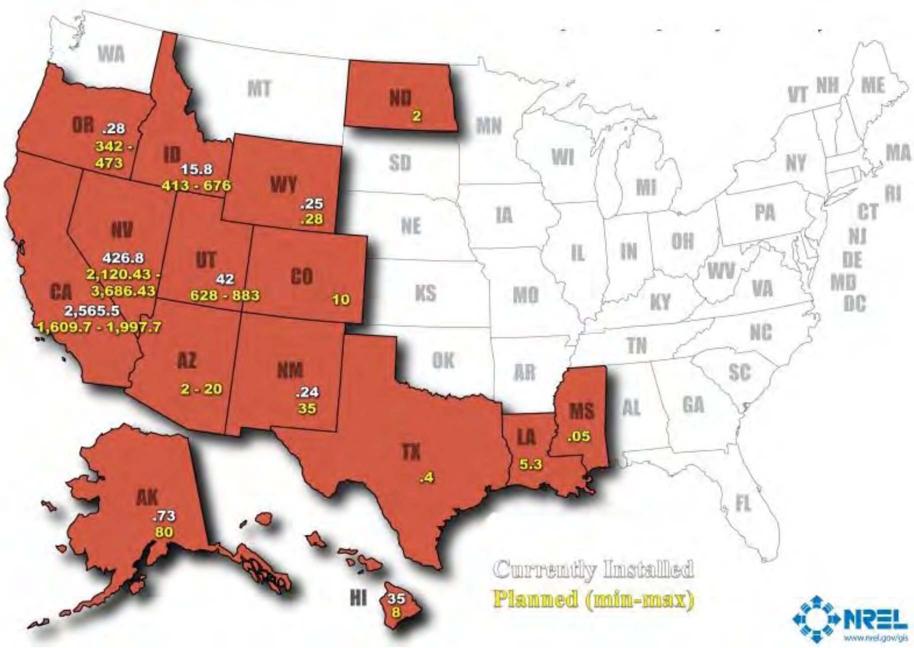

Figure 2.8 Geothermal power generation in the U.S. Map is taken from [12]

Franco and Villani [18] explored the possible use of binary cycles with dry cooling systems for the geothermal applications. Their study revealed that first law and exergy efficiencies of 6-12% and 22-45% are achievable for the binary cycles. For this study, the geothermal fluid, rejection, and condensation temperatures were 110–160°C, 70-80 °C and 30-40 °C, respectively. Their parametric study for a geothermal heat source of 160 °C compared the performance of supercritical and dual pressure Rankine cycles. The dual

www.manaraa.com

pressure Rankine cycle using isobutene have a higher first law and exergy efficiency than supercritical Rankine cycle using R152a.

In Germany, there are several examples of hydrothermal sources where the temperature of the water is between 60 °C to 120 °C, it is not suitable for effective power generation by ORC or Kalina cycle, therefore it is used for space heating. Recent studies by Demirkaya et al. [19] and Vasquez et al. [20] showed that Goswami cycle can produce power and cooling using such low temperatures. They showed that an effective first law efficiency of 3.5–5.5% and an effective exergy efficiency of 22–33% with 50–75% turbine efficiency could be achieved for a boiler temperature of 83.4 °C [19]. When the heat source temperature is 130 °C with a 50% efficient turbine, the effective first law and exergy efficiencies were 10% and 42%, respectively [20]. There are many hotel resorts that provide hot spring water for the customers, so with low temperature source, Goswami cycle can be used for power generation and cooling for HVAC applications in the hotels. Some examples of geothermal power plants with the type of cycle, geothermal fluid temperature, and working fluid are given in Table 2.2.

Table 2.1 Geothermal power plants examples

Location	Cycle	T_{fluid} °C	Working Fluid
Chena Hot Spring, AK, U.S. [21]	Rankine	80	R134a
Husavik, Iceland [22]	Kalina	124	Ammonia-Water
Simav, Turkey [23]	Rankine	145	R124
Otake, Japan [18]	Rankine	130	Isobutane
Amedee, U.S. [24]	Rankine	104	R-114
Wabuska, U.S. [24]	Rankine	104	Iso-pentane and R-114
Covefort, U.S. [24]	Rankine	138	Steam

www.manaraa.com

2.3 Waste Heat

Waste heat sources can be low-grade (<100°C), medium grade (100°C–400°C) or high grade (>400°C) [25]. Low-grade waste heat can be found in all areas of industry and buildings however, it is the hardest to recover cost-effectively. Typical examples of recovering low-grade waste heat would be ventilation, hot water systems, low temperature solar flat panels, solar ponds etc. Mid-grade waste heat is most widely found in the chemicals, food and drink, oil refineries, and other process industries, as well as building utilities. It has been estimated that a typical petroleum refinery in the U.S. rejects about 256 MW of thermal energy to the environment through warm gases at temperatures of 150 °C to 300 °C [26]. Inoue et al. [27] found that utilizing 5% efficient cycles, 1200 MW of power can be generated with waste heat through exhaust gas at temperatures below 200 °C and hot water above 80 °C from the industrial plants in Japan. In general, high-grade waste heat is mainly limited to the iron and steel, glass, nonferrous metals, bricks, ceramics and cement industries [28]. In cement production, recoverable heat is available in clinker coolers hot air and preheater gases.

2.4 Power Cycles

2.4.1 Rankine Cycle

The most commonly used vapor power cycle is the Rankine cycle, that provides approximately 85% of worldwide electricity production [29]. A simple Rankine cycle, shown in Fig. 2.9 consists of four steps [30]. The working fluid is pumped to a high pressure and circulated through the boiler. The fluid is boiled at a constant pressure in the boiler af-

المنارة للاستشارات
www.manaraa.com

ter which the high-pressure vapor produced is expanded through a turbine, thus extracting work from it. The vapor exiting the turbine is condensed in a condenser by rejecting heat to a cooling fluid. Water is used as the working fluid for most of the vapor power cycles as it works over a broad range of temperatures and pressures, has a large heat capacity, and is stable, safe, and very environmentally friendly.

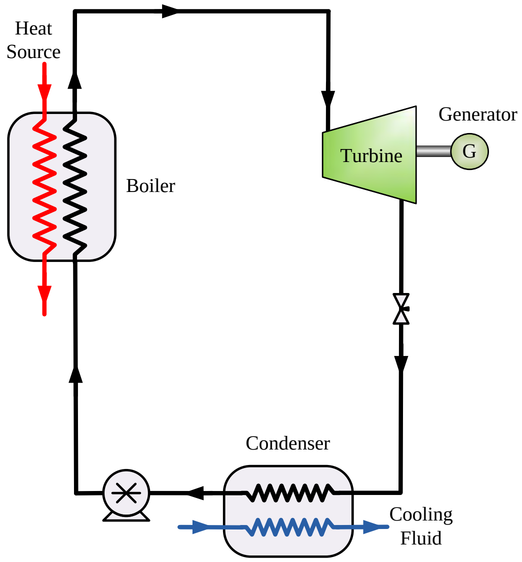

Figure 2.9 Schematic description of the Rankine cycle

There are several modifications to the Rankine cycle that are used to achieve better efficiencies: lowering the condenser temperature which decreases the low temperature average limit, superheating the steam to higher temperatures, or boiler pressure which increases the average high temperature [30]. In a real Rankine cycle, the compression and expansion processes are irreversible. In particular, the efficiency of the steam turbine will be limited by water droplet formation. As the water condenses, water droplets hit the turbine blades at high speed causing pitting and erosion, gradually decreasing the life of turbine blades and

www.manaraa.com

efficiency of the turbine. The easiest way to overcome this problem is by superheating the steam.

2.4.2 Organic Rankine Cycle

Since the first Rankine cycle-based thermal power plant was built, there have been several improvements in the configuration, components, and materials used, but the working fluid of choice has usually been water. While water has several properties that make it a very good choice as a working fluid, better choices are available in low temperature applications. Organic working fluids are a popular choice for such applications. The Organic Rankine cycle (ORC) is named for its use of an organic, high molecular mass fluid with a liquid-vapor phase change, occurring at a lower temperature than the water-steam phase change. The fluid allows Rankine cycle heat recovery from lower temperature sources such as biomass combustion, industrial waste heat, geothermal heat, solar ponds etc.

The low-temperature heat is converted into useful work that can itself be converted into electricity. They are most often used when exploiting low temperature thermal resources for power generation, or small-scale applications (typically <5 MW). Typical working fluids that are used in ORC plants are, Toluene, Xylene, n-pentane, n-butane, R-11, R-22, and R-248fa. Despite the fact that these fluids have lower heats of vaporization than water, which requires larger flow rates, smaller turbine sizes are obtained due to the higher density at the turbine exit conditions. The size and complexity advantage of organic fluid turbines is driven by higher fluid density at typical turbine operating conditions as well as much smaller expansion pressure ratios (inlet/outlet). Simplified turbine design is then another

المنارة للاستشارات
www.manaraa.com

advantage associated with high condensing pressures. Several existing ORC applications are producing 3 to 6.5 MW of electricity [31].

2.4.3 Supercritical Rankine Cycle

The use of mixtures is one way to obtain good thermal matching with sensible heat sources. Other methods that have been proposed include multi-pressure boiling and supercritical operation. Multi pressure boiling has not been very popular in the industry because of the costs involved. The other option is to use supercritical cycles [30]. A schematic drawing of a supercritical Rankine cycle is illustrated in Fig 2.10. The main advantage of the supercritical process is the fact that the average high temperature in which the heat input is taking place is higher than in the case of the subcritical fluid process. Therefore, the Carnot efficiency is higher. The boiling process does not pass through a distinct two-phase region, and a better thermal match is obtained in the boiler. There are several works that studied the performance of the supercritical cycles using solar energy, the power generation efficiency estimated was 25%, and the heat recovery efficiency was 65% [32]. Supercritical cycles have to operate at a higher pressure, since the boiler pressure has to exceed the critical pressure of the working fluid. High operating pressure increases the equipment costs, although it improves the performance of the cycle.

Most of the previous studies on supercritical Rankine cycle used pure fluids. Recently, Chen et al. [33] performed a comparative study between an ORC and the supercritical Rankine cycle by using zeotropic mixtures as the working fluids. Their study showed that supercritical cycle could achieve thermal efficiencies of 10.8 to 13.4% with the cycle high temperature of 120 to 200 °C as compared to 9.7 to 10.1% for the organic Rankine cycle

المنارة للاستشارات
www.manaraa.com

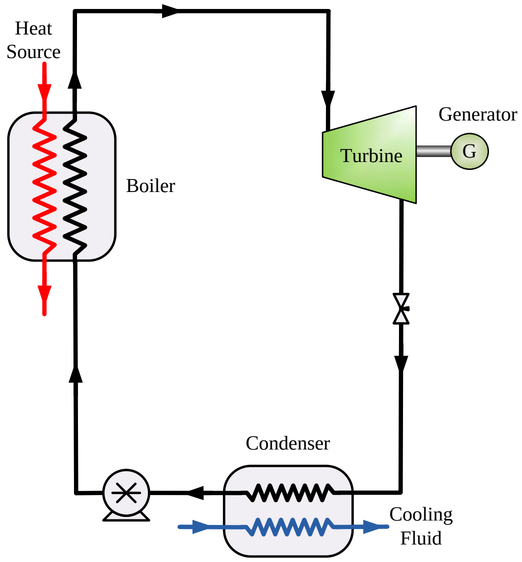

Figure 2.10 Schematic description of the Supercritical cycle

[33]. They claim a significant improvement of 10 to 30% over the organic Rankine cycle. Their study also showed that the heating and condensation processes efficiency was 38.6% for the supercritical Rankine cycle as compared to 24.1% for the organic Rankine cycle [33], as this would help in the cost reduction of condensing and boiling heat exchangers.

2.4.4 Ammonia-Water Cycles

Thermodynamic cycles using binary mixtures as a working fluid offer interesting characteristics and a high potential for generating electricity from a low-temperature heat source [4, 34, 35]. It is been shown that optimum power produced by the Lorentz cycle can be higher than the optimum power produced by the Carnot cycle at the same working conditions [36, 37].

Binary mixtures such as ammonia-water mixture can be used to provide an approximation to the ideal Lorentz cycle by varying both pressure and mass fraction to match

www.manaraa.com

the ideal triangular shape in a temperature-entropy diagram. The temperature difference between the heat source and the working fluid remains small to allow for a good thermal match between the source and working fluid, such that less irreversibility results during the heat addition process. The first study of power cycle using a binary mixture as the working fluid was performed by Maloney and Robertson [38] who concluded no significant advantage to the configuration over steam cycle operation at the conditions considered. However, Kalina [34] reintroduced the idea of an ammonia-water power cycle as a superior bottoming cycle option over steam Rankine cycle, which showed an increase in the overall efficiency of 14.5% to 23% above the efficiency of the combined systems using the Rankine bottoming system at the same border conditions.

2.4.5 Kalina Cycle

The Kalina cycle utilizes an ammonia-water mixture as a working fluid to improve system efficiency and provide more flexibility in various operating conditions [22, 34, 39–43]. A simplified arrangement for the Kalina cycle is shown in Fig. 2.11. Besides using a binary fluid, the cycle includes the ability to use different compositions of the working fluid in different parts of the cycle. The distinguishing feature of the Kalina cycle is its distillation condensation subsystem (DCSS). Much of the Kalina cycle's improvement is the direct result of the DCSS. The DCSS consists of nine heat exchangers; seven are recuperative and two are condensers that reject the waste heat to cooling water [41]. The DCSS changes the composition of the working fluid and condenses it in two steps at two different pressures. The high pressure condenser pressure corresponds to the pressure of condensation of the 70% ammonia-water mixture while the low pressure condenser pressure corresponds to

المنارة للاستشارات
www.manaraa.com

that of the 40% working fluid. The turbine back pressure is determined by the low pressure condenser, so the ability to reduce the low pressure condenser below that of the high pressure condenser leads directly to an over-expansion in the turbine and the Kalina cycle's improvement over the Rankine cycle.

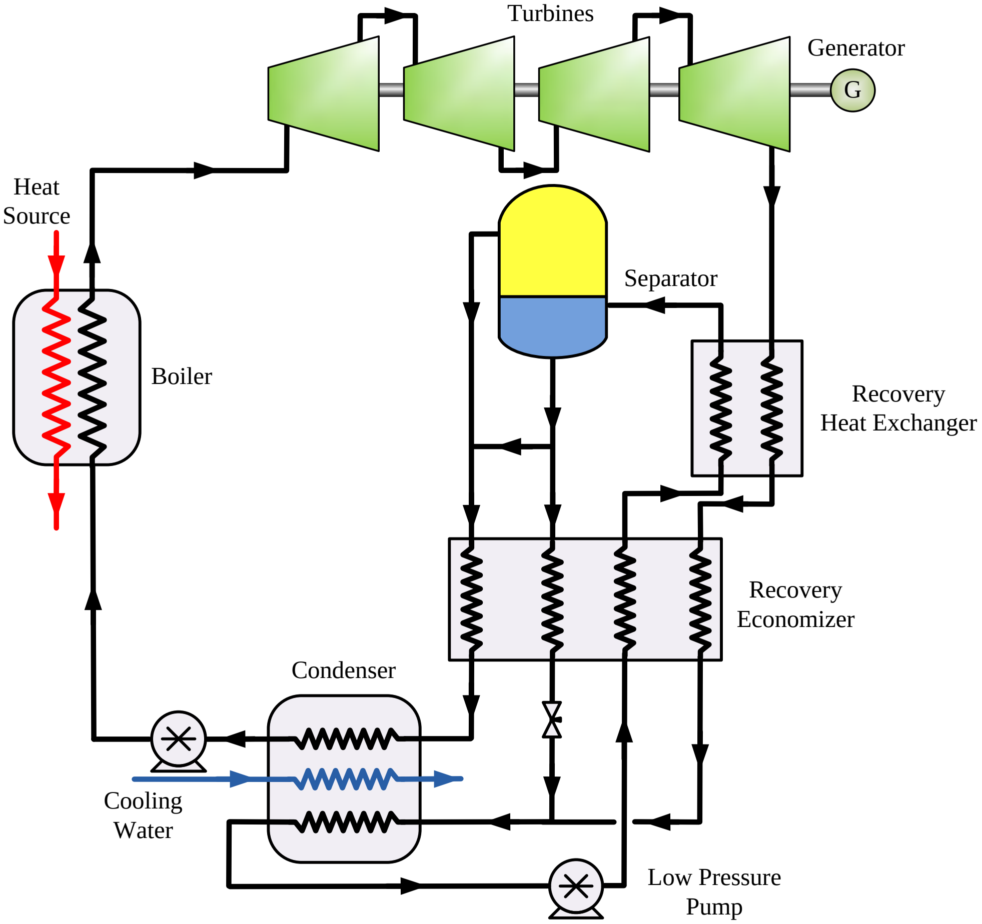

Figure 2.11 Schematic description of the Kalina cycle

The first Kalina cycles were designed for using the hot exhaust gas from diesel engines and gas turbines as heat sources, the so-called bottoming cycle application, [34]. Kalina [34] investigated the Kalina cycle performance for a boiler temperature of 532 °C, and found that the bottoming cycle produces 2.7 $\mathrm{MW_e}$ with a first law and exergy efficien-

المنارة للاستشارات
www.manaraa.com

cies of 32.9% and 70.0%, respectively. Kalina and Leibowitz [22] presented a different configuration of the Kalina cycle for geothermal applications. In that study, it was shown that the Kalina cycle has a higher power output for a specified geothermal heat source compared with organic Rankine cycles using isobutene and steam flash cycles. Kalina and Leibowitz [39] showed improved performance of the Kalina cycle (KCS6D2) over the Rankine steam cycle during off-design and partial load operations. They showed that the plant's mass flow might be kept at or near design levels, which keeps turbine efficiency high, during partial load operation. In an another study by Kalina et al. [40] they compared the performance of the Kalina cycle, which was designed to produce 86 MW, with the two-pressure steam bottoming cycle; Kalina cycle provided an additional 12.1 MW, 16.4% of the total capacity at a boiler temperature and pressure of 497.6 °C and 160.1 bar, respectively. The first and second law efficiencies of the Kalina cycle were 35.6% and 78%, respectively. They also compared the economics of the Kalina cycle with the steam Rankine cycle, $1,058/kW and $1,033/kW, respectively. Kalina cycle power plants can use steam turbines with a smaller size and therefore less expensive than in Rankine cycle plants of the same output. Condensers are usually works under gauge pressure. As ammonia vapor has a smaller specific volume compared to steam, a smaller exhausting area is needed for the turbine last stage, which creates the difference in cost. In addition, the use of the ammonia-water mixtures does not require any special design materials; carbon steel is quite acceptable for low temperature application.

In 1992 [44], a Kalina demonstration plant started operation at the U.S. Department of Energy's Energy Technology Engineering Center in California. During the initial 540

المنارة للاستشارات
www.manaraa.com

hours of trial period, the Distillation condensation subsystem performed as designed [41]. The average low and high pressure of the condenser during the initial experiments were 20 and 110 psig, respectively. In 1996, a gas turbine replaced the waste heat stream as the Kalina cycle heat source. As a combined cycle, the plant generated 4.6-5.7 MW_e, 1.6 to 2.6 MW_e was from the bottoming Kalina cycle, and operated for a total of 1,500 hours. The maximum pressure and temperature of the Kalina cycle were 114 bars and 516 °C [42].

During this period, there were several problems encountered such as low performances of the vapor turbine and condenser components. The most serious problem encountered was the failure of the turbine's high pressure interstage seals. Pure nickel was originally selected because of its nitriding resistance and tolerance to rubbing; however, nickel in pure form does not have sheer strength at high temperature. The seals were replaced with a nickel/chrome alloy. The rotor, which was nickel-based alloy, was observed to be in excellent condition, and showed no evidence of nitriding, oxidation corrosion, erosion or foreign object damage. Another problem during the experiments was the dissolving of solids, which were in the form of iron. The ammonia working fluid was able to dissolve some scale on the walls of the heat exchangers and piping. Overall plant performance confirmed the theoretical basis of the technology; the plant's output was 10% short of the design condition. This was due to the turbine's mechanical problems.

After this demo-plant, the first commercial Kalina cycle was built in Husavik, Iceland. The plant design and economics, compared with an organic Rankine cycles, were described by Leibowitz and Micak [43]. The system was designated as Kalina cycle system 34 (KCS 34). The plant was designed to produce 2 MW net of power using brine at a mass flowrate

المنارة للاستشارات
www.manaraa.com

of 90 kg/s and temperature of 124 °C. The ammonia-water cycle decreases the temperature of the geothermal brine stream from 124 °C to 80 °C and the remaining energy in the stream is used for district heating purposes. For the same heat source temperature, they stated that KCS 34 provides 25% greater work outputs than the ORC [43]. KCS 34 contains two additional heat exchangers (the two recuperators) and a separator (flash tank) that are not found in the ORC. They predicted that the cost of this additional equipment, including piping, valves, and installation, was approximately $75/kW for the Husavik plant. However, they stated that the costs of a steam turbine for KCS 34 and the primary heat exchangers (evaporator and condenser) were expected to be less than the costs of those in ORC by more than the $75/kW.

The cost of the turbine for the KCS 34 would be cheaper than the ORC as steam turbines have been manufactured for over a century and are available from numerous suppliers. In addition, hydrocarbons have lower enthalpy than ammonia-water, thus the ORC turbine requires more volume and mass flow to provide the same output [45]. This results in larger casing and blading sizes for the ORC. The ORC brine evaporator and condenser are also more expensive because they have much lower heat transfer coefficients, and require larger shell sizes to accommodate the higher mass and volume flow rates, compared to ammonia-water systems [45]. Leibowitz and Micak [43] stated that the economic cost predictions of KCS 34 had advantage over a hydrocarbon based ORC.

The Husavik plant began generation operations in July 2000, which produces more than 1.6 MW. Maack and Valdimarsson [46] summarized the two years of experience in the Husavik plant. The main problems in the startup and operation were pump seal fail-

المنارة للاستشارات
www.manaraa.com

ure, undersized condenser, turbine axial seal failure, and carry-over from the separator, which caused erosion in the turbine. Start-up problems, component failure and equipment malfunction had been overcome and the plant was running according to specifications.

Global Geothermal Ltd. [28] company owns and controls the Kalina cycle rights associated with the proprietary technology since 2007. Recently, another project is going on in Germany, Unterhaching power plant, which is designed to produce 3.4 MW of electricity [28]. The application of Kalina cycle is explored in cement plants to utilize waste heat sources to generate electricity [47, 48]. Based on this research, it is announced that Kalina cycle power plant will generate 8.6 MW of power from the waste heat stream of the Khairpur cement plant [28]. The project will be the largest Kalina cycle power plant in the world, and it is expected to reduce the CO_2 emissions of the cement plant by up to 31,000 tons per year [49].

Independent studies have been performed that concede some advantage of the Kalina cycle under certain conditions. Park and Sonntag [50] compared the Kalina cycle and the Rankine cycle at the same thermal boundary conditions, and they showed that the Kalina cycle bottoming systems have higher efficiencies of 5% of first law and 15% of second law than the Rankine cycle. The temperature difference between the heat source and the working fluid remains small to allow for a good thermal match between the source and working fluid, such that less irreversibility results during the heat addition process. In a study by Olsson et al. [51], the Kalina cycle with a gas turbine topping cycle was investigated for a district heating system. Olsson et al. [51] found the first law and exergy efficiencies of the cycle as 23% and 69.7%, respectively. The turbine inlet pressure and temperatures were

المنارة للاستشارات
www.manaraa.com

110 bar and 494 °C. Their results showed that the Kalina cycle power output was between 4 and 7% higher than that the ammonia-water mixture Rankine cycle for the same amount of heat supplied to the district heating system. They concluded that the advantages of the Kalina cycle were greater when the district heating temperatures were lower. Bisio [52] investigated Kalina cycles for power generation from waste heat in iron- and steel-works, and showed an exergy efficiency of 9.1% higher than the Rankine cycle. Olsson et al. [53] explored the waste heat (300-400 °C) recovery from the iron and steel industries by the Kalina cycle. They compared the Kalina cycle with a steam cycle, and showed that the Kalina cycle performs better especially when the minimum outlet temperature of the heat source is low; Kalina cycle produced 9% to 32% more work than the Rankine cycle.

Ibrahim [35] provided a detailed evaluation of the Kalina and Maloney and Robertson absorption power cycles and compared their performances with the maximum power cycle. Their results showed that at a very high (~20) thermal-capacitance-rate ratio (ratio of the heating fluid to cooling fluid mass flow rate and specific heat product), the Kalina cycle produces about 80% of the maximum power and the Maloney and Robertson cycle about 70% of the maximum power.

Bjorge et al. [54] presented the performance characteristics of the Kalina combined cycle system with a MS900lFA type gas turbine. They compared the three-pressure reheat Steam Rankine cycle with Kalina cycle (KC109FA), and found that Kalina cycle can increase combined cycle system output by 4 to 5% and efficiency by 2 to 2.5%. Nag and Gupta [55] examined the exergy analysis of the Kalina cycle, they varied the temperature of ammonia-water mixture at the condenser, and they found that the cycle efficiency varies

المنارة للاستشارات
www.manaraa.com

between 30-36% for a boiler temperature of 500 °C. The second law efficiency for the same operating conditions is in the range of 51-60%.

Hettiarachchi et al. [56] examined the performance of the Kalina cycle system 11 (KCS11) for low-temperature geothermal heat sources. They compared the results of the Kalina cycle with ORC. Kalina cycle performed 1-3% higher first law efficiency when the evaporator pressure was higher than 20 bar. Lolos and Rogdakis [57] recently analyzed the use of Kalina cycle at low temperature such as 130 °C. The main heat source of the cycle is provided from flat solar collectors. The cycle operates at low pressure levels (0.2-4.5 bar) and low maximum temperature (130 °C). They found that the cycle has a maximum first law efficiency of 8.3% at a system high pressure of 4.6 bar, boiler temperature of 130 °C, and condenser temperature of 20°C. The first law efficiency drops from 7.4% to 5.6% when the condensation temperature increases from 25 °C to 35 °C. Recently, another numerical study was conducted by Ogriseck [58], the study showed that the net efficiency of an integrated Kalina plant was between 12.3% and 15% for a heat source of 120 °C, and condensing fluid temperature of 20 °C.

2.4.6 Other Ammonia-Water Mixture Cycles

The non-regenerative single-pressure Rankine cycle is the simplest steam cycle, which can be used as bottoming cycle with a topping gas turbine. Desideri et al. [59] investigated the performance of a non-regenerative single-pressure Rankine cycle using an ammonia-water mixture. The ammonia mass fraction in the working fluid varied from 0 to 1. Their results showed the ammonia concentration in the mixture is in the range of 0.10-0.16 for the maximum work output from the bottoming cycle. They stated that the effect of ammonia

المنارة للاستشارات
www.manaraa.com

concentration on power output is largely influenced by the exergy losses in the condenser; condenser losses were minimal when the concentration was between 0.10 and 0.16.

Rogdakis and Antonopoulos [60] offered a new cycle, which uses an absorption condensation instead of the complex DCSS of Kalina cycle. Their proposed cycle uses an absorption process similar to that employed in absorption refrigeration systems. The cycle had three turbine stages with two reheaters. The boiler temperature was 400 °C. The cycle was compared with Rankine cycle and it was shown that the thermal efficiency of the proposed ammonia-water and Rankine cycles were 30-36% and 10-30%, respectively.

Roy et al. [61] analyzed the two ammonia-water Rankine cycles for fixed source and sink inlet temperatures; one with and one without a regenerator, both using a mixture as the working fluid. The regenerator recovers heat from the turbine exhaust and increases the temperature of the working fluid that goes to the boiler. The first law efficiency with regenerator and without regenerator was 11.39% and 11.01%, respectively.

2.4.7 Combined Power and Cooling Cycles

Combined power and refrigeration cycles have been explored for improving the overall energy conversion efficiency and decreasing the cost of energy per unit capital expense. There is now a small class of combined power and cooling cycles since it was proposed by Goswami [4].

In several studies, waste heat is recovered from the top gas turbine or engine based cycles and it is utilized to generate refrigeration. These are not shown in Table 2.2 as the focus of this study is on the heat recovery of thermodynamic cycles where the working fluid exhibits phase change during the cycle loop.

www.manaraa.com

Erickson et al. [26] proposed an ammonia-water absorption cycle, which produces power and refrigeration interchangeably and utilizes heat in the range of 120 °C to 300 °C. The dual-function cycle consists of a heat-recovery unit, desorber, recuperator, absorber, turbine plus electric generator, condenser and evaporator. The power and the refrigeration cycle use the same absorption cycle equipment that improves the economics of recovering low-level waste heat. Their simulation results showed that the thermal efficiencies of the system are 11.9%, 18.9%, and 26.6%, when the heat source temperatures are 175 °C, 230 °C, and 290 °C, respectively. Erickson et al. [26] emphasized the advantage of a power cycle, which uses absorption cycle for the condensation process; the liquid is not totally evaporated, only partly desorbed, and a residual amount of absorbent liquid is recirculated to the lower pressure for absorption. Thus, the absorption cycle does not require a problematic total-evaporation step as the Kalina cycle.

Agnew et al. [62] explored the theoretical performance of a combined turbocharged Diesel engine and absorption refrigeration systems. The exhaust gas temperature was around 500-800 °C, which is too high for the scope of this study, however they showed the combined system efficiency improves the thermal efficiency from 33-40% to 47-52%. Talbi and Agnew [63] examined the interfacing of a diesel engine with an absorption refrigeration unit. They studied four different configurations when operating in a high ambient day temperature of 35 °C. Their study showed that the combined efficiency of the combustion engine and the cooling system could be as high as 58-61%. Thermal power in the exhaust gas ranged from 45 to 53 kW and the cooling output from the absorption refrigeration system was in the range of 30-35 kW. Liu et al. [64] highlighted the practical utilization

المنارة للاستشارات
www.manaraa.com

of an adsorption chiller, which makes possible the recovery of low-grade thermal energy. Their experimental study showed that the COP and cooling capacity of silica/gel–water adsorption chiller reaches over 0.5 and 9 kW, respectively, with a heat source of 80 °C. There is another study where Maidment and Tozer [65] developed an economical and mathematical model to predict the energy performance of the combined power and cooling system based on an internal combustion engine and absorption chiller. Their model showed that the optimum cycle should include a Li-Br absorption chiller because of the low cost of the Li-Br absorption chiller, and this system offers a payback period under 7 years.

Colonna and Gabrielli [66] worked on a combined system where a gas turbine or gas internal combustion engine drives an ammonia-water absorption refrigeration cycle through a heat recovery exchanger. In contrast to the cycle configuration proposed by Erickson et al. [26], Colonna and Gabrielli [66] system drives the power and refrigeration cycles independently. They showed that with a waste heat source temperature of 120 °C, a COP value of 0.57-0.59 could be reached. The system was a trigeneration system, which was driven by a 10 MW capacity of gas turbine, and utilizing the waste heat from the gas turbine can produce approximately 6.4 MW of refrigeration and 11.2 MW of thermal heat. Alexis [67] proposed a combined system which is similar to Colonna and Gabrielli's [66] system, except that a steam ejector refrigeration cycle replaces the ammonia absorption system to produce refrigeration. This cycle utilizes extraction steam from the steam turbine, for the conventional Rankine cycle, to heat up the working fluid in an independent steam ejector refrigeration cycle.

المنارة للاستشارات
www.manaraa.com

Oliveira et al. [68] presented a hybrid solar/gas system that is based on the combination of an ejector heat pump cycle with a Rankine cycle. This cycle provides cooling/heating and electricity generation for buildings. To test the system reliability two prototype units of cooling capacities up to 5 kW and electrical output up to 1.5 kW, were built. For a boiler temperature of 95 °C and a turbine efficiency of 28%, average coefficient of performance (COP) of the cooling cycle was around 30% and electricity production efficiency was between 3% and 4%.

The ejector refrigeration systems integration with the Rankine cycle was first proposed by Nord et al. [69]. Their proposed system was the combination of vapor compression and Rankine cycles with the compression device being a jet-pump instead of a conventional compressor. Jet-pump, is also called as ejector, is one of the simplest flow induction device. The jet-pump acts as the joining device between the thermal and power parts of the system, by mixing the high pressure flow from the power cycle with the low pressure flow from the refrigeration part of the system providing a pressure increase in the refrigeration cycle. Nord et al. [69] used R134-a as the working fluid in their analysis. Zheng and Weng [70] showed another configuration of a Rankine and ejector refrigeration cycle in which an organic fluid, R245fa, is used as the working fluid. The ejector is driven by the exhausts from the turbine to produce power and refrigeration simultaneously. The principle of this combined ORC and ejector system is as follows; saturated liquid is pumped to the operating pressure of the ORC vapor generator, then the working fluid is vaporized at the boiler. The saturated or superheated vapor leaves the vapor generator and expands in the turbine, and the vapor from the turbine exit enters the ejector nozzle as the primary fluid. The very

المنارة للاستشارات
www.manaraa.com

high velocity vapor at the exit of the nozzle produces a high vacuum at the inlet of the mixing chamber and entrains secondary vapor into the chamber from the evaporator. The primary and secondary fluids are mixed in the mixing chamber of the ejector at a constant pressure. As refrigeration cycle is driven by the nozzle, no compressor is needed for this refrigeration system. Then the mixed fluid recovers the pressure in the diffuser of the ejector and the vapor leaves the ejector and enters the condenser. The working fluid is condensed by rejecting heat to the cooling water and the saturated liquid condensate is separated into two streams; one stream returns to the pump and the pressure increased to the vapor generator, and the other goes to the refrigeration cycle, which is throttled to the evaporating pressure by an expansion valve. Then the working fluid from the expansion valve enters the evaporator to produce refrigeration. They used R245fa as the working fluid, and ideal turbine and pumps are assumed for their simulations of the ORC ejector refrigeration cycle.

Zheng and Weng [70] compared their results with the theoretical study of Hasan et al. [71]. They showed that the work output of the cycle is less than the Goswami cycle; however, their proposed cycle refrigeration output is significantly higher than the Goswami cycle. The refrigeration output is higher due to the phase change of the working fluid during the refrigeration process. The turbine exit pressure is higher so that the vapor can be used to drive a refrigeration ejector cycle. On the other hand, the potential of producing work is sacrificed to produce more refrigeration. Their exergy analysis showed that the main exergy loss occurs at the ejector due to the friction and mixing between the primary and secondary fluids and the normal shock in the constant-area section; almost 30% of the

المنارة للاستشارات
www.manaraa.com

total exergy input in the vapor generator is lost. Wang et al. [72] proposed a trigeneration system of organic Rankine and ejector refrigeration cycle, which produces cooling , heating output and power simultaneously. The difference between the Zheng and Weng [70] and the Wang et al. [72] study is that the turbine exhaust is divided into two streams in the latter, the first stream enters the supersonic nozzle of the ejector system, and the other stream enters the heater system, which provides the heat output of the combined cycle. As the system is driven by a solar system, they investigated the effect of solar parameters such as hour angle and the slope angle of the aperture plane for the solar collectors on the system performance. In another study, the same research group investigated the performance of the cycle without the heating system; they showed the performance of the cycle for combined power and cooling output [73]. As the results are shown in Table 2.4.7, the thermal efficiency difference between the trigeneration system and combined system is approximately 0.7%. Recent studies [74–76] also presented analysis of an ejector-absorption refrigeration cycle for cogeneration of power and cooling. Dai et al. [75] performed an optimization of the cycle by using the exergy efficiency. Their results showed that the combined cycle was operating at a maximum exergy efficiency of 27.1% when the turbine inlet pressure and temperature and the turbine back pressure were 7.9 bar, 118.9 °C and 1.5 bar, respectively. Their exergy analysis results showed that the amounts of exergy loss in the boiler and ejector accounted large percentage.

Zheng et al. [77] proposed a combined power and cooling cycle based on the Kalina cycle. The flash tank in Kalina cycle was replaced by a rectifier, which could obtain a higher concentration ammonia–water vapor for refrigeration. To produce almost pure ammonia,

المنارة للاستشارات
www.manaraa.com

a rectifier was used to replace the flash tank in the Kalina cycle. The outflow from the top of the rectifier is throttled by a valve and then the working fluid produces refrigeration before mixing with the main stream. In terms of equipment, this cycle requires additional condenser and evaporator between the rectifier and the second absorber.

Liu and Zhang [78] proposed another combined system that integrates a splitting /absorption unit with a Rankine cycle and absorption refrigeration cycle. In this configuration, the ammonia-water basic solution is separated into a high concentration ammonia vapor and a relatively weak solution liquid in a device similar in operation to a distillation column. The vapor is condensed and throttled to produce cooling while the weak solution liquid is vaporized and superheated, then expanded in a turbine for power production. The streams are then cooled and rejoined in an absorber.

Zhang and Lior [79] studied an ammonia-water system, which operated in a parallel combined cycle mode with an ammonia-water Rankine cycle and an ammonia refrigeration cycle. The ammonia-water outflow from the absorber is pumped to the rectification pressure, and it is preheated by the external heat source to its saturation temperature before being fed to the rectifier. The basic concentration solution is separated into a high concentration vapor and low concentration solution in the rectifier. The vapor is sent to the condenser and the low concentration solution is sent to the boiler. The weak solution from the boiler is brought into the power cycle by being pumped to the system high pressure and then evaporated and superheated by the heat source gas to the highest power cycle temperature. It then expands in the turbine to generate power, then the vapor enters the condenser and the exit liquid solution is pumped to the absorption pressure and sent back to the ab-

المنارة للاستشارات
www.manaraa.com

sorber. The high concentration vapor from the rectifier is condensed first, and then the high concentration saturated liquid is subcooled by preheating the evaporator return vapor. The subcooled liquid is then throttled to the refrigeration pressure, it provides refrigeration during its evaporation process in the evaporator, and finally it combines in the absorber with stream from the power cycle. The two streams mix there to form the basic concentration solution, which is cooled to its saturated state, and this completes the whole cycle. Zhang and Lior [79] investigated the effects of the key thermodynamic parameters on both energy and exergy efficiencies. The superheater temperature of the power cycle of this combined cycle is 450 °C; therefore, this cycle requires a gas turbine at the top with a exhaust temperature higher than 450 °C. Zhang and Lior [80] also summarized some guidelines for integration of refrigeration and power systems to produce higher energy and exergy efficiencies.

Zamfirescu and Dincer [81] proposed a trilateral Rankine flash cycle, which uses ammonia–water mixture as a working fluid. They assessed the performance of an ammonia–water Rankine cycle with no boiler; the saturated liquid is flashed by a volumetric expander (e.g., reciprocating, centrifugal, screw or scroll type expander) for power generation. The saturated liquid is flashed into two phase, the resulted vapor-liquid mixture is then fully condensed and the liquid is pumped to high pressures and heated up to the saturation temperature. Wagar et al. [82] expanded the analysis for the concentration range of 0-0.5, and maximum turbine inlet temperature of 350 °C. The cycle thermal efficiency was found between 5% and 35%.

Badami and Portoraro [83] proposed a trigeneration system that is composed of gas fired internal combustion engine and liquid LiCl–water desiccant cooling system. The

المنارة للاستشارات
www.manaraa.com

cooling system recovers heat from the flue gases and from the internal combustion engine cooling water. The system produces power and heating during the winter season, and power and cooling during the summer. The unit produces 126 kW of electricity in the winter and 220 kW of thermal heat with 29.5% electricity and 51.5% thermal efficiencies. During the summer, the combined system produces 110.2 kW_e and 210 kW_c of electricity and cooling, respectively. Their economic analysis showed that the payback period of the trigeneration system was 6.8 to 7.6 years.

Zhai et al. [84] presented a hybrid solar heating, cooling and power generation system based on helical screw expander and silica gel–water adsorption chiller. The hybrid solar system is able to produce 23.5 kW electric power and 79.8 kW cooling with solar radiation of 600 W/m^2 and collector area of 600 m^2. They proposed helical screw expander in their analysis as it could work with low vapor quality and steady internal efficiency. The shortcoming of this expander is that it has a higher outlet temperature and pressure, which results in serious outlet thermal loss and lower thermal efficiency. However, this provides high temperature latent thermal energy of exhaust steam that can be recovered and supply the refrigeration system as heat input. The high-pressure working medium pushes against the vanes of a screw-type expander, converting some of its heat energy into mechanical power, turning the shaft of a generator and producing a net power output. The waste heat recovery system mainly consists of two heat exchangers, a hot water tank, and silica gel–water adsorption chillers (in summer) and radiation heating system (in winter). The relatively high temperature exhaust steam from the helical screw expander is separated in steam separator, and dry steam flows into the first heat exchanger. Zhai et al. [84] showed

المنارة للاستشارات
www.manaraa.com

the exergy analysis of the overall system, and found that the second law efficiency is 9.9% during the summer. They found that both the main energy and exergy losses take place at the parabolic trough collector, and amount to 36.2% and 70.4%, respectively.

In another study, a vapor-compression refrigeration cycle is driven by an organic Rankine cycle (ORC), and they are coupled by a device called an expander–compressor unit [85]. This device is a free-piston, and the compressor and expander are integrated in the same unit. The work produced in the expander is transferred to the refrigeration cycle by the piston; the output from the combined system is only refrigeration. The organic Rankine and the vapor-compression refrigeration cycles also share the same condenser and working fluid. R22 and R134a were used as the working fluids. The generator, condenser and evaporator temperatures were between 60-95 °C, 30-50 °C, and -10 to 10 °C, respectively. The COP was found to be 0.1-0.6. The system with R22 provided better COP than the system with R134a for all ranges of operating temperatures.

Takezawa et al. [86] proposed a cogeneration system by a series connection of solid oxide fuel cell (SOFC), gas turbine, and Li-Br absorption chiller to convert the exhaust heat to cooling. The exhaust gas temperature of the combined cycle is high, about 280 °C, and they investigated using this exhaust gas to generate cold by an absorption chiller. Their results showed that the combined system with 500-kW-class SOFC, the bottoming absorption chiller can produce a refrigerating capacity of about 120-30 kW depending on the absorption chiller type. In another recent study, Al-Sulaiman et al. [87] investigated a trigeneration system, which consists of a solid oxide fuel cell, an ORC, a heating process, and a single-effect absorption chiller. The waste heat from the SOFC was used as input heat

المنارة للاستشارات
www.manaraa.com

to the ORC and the waste heat from the ORC was used for heating and cooling system. The waste heat from the SOFC was used as input heat the ORC, and consecutively, the waste heat from the ORC was used for producing steam in the heating process using a heat exchanger and cooling using a single-effect absorption chiller. Their study showed that there was 3-25% gain in exergy efficiency when a trigeneration system was used compared with only the power system. Their exergy analysis also showed that the most significant sources of exergy destruction rates were the ORC evaporator and air heat exchanger at the SOFC inlet.

Recently, there are studies that used waste heat-powered refrigeration systems. Venegas et al. [88] presented a theoretical study that compared different working pairs for the absorption refrigeration systems, which was driven by 50-90 °C heat source. Their study showed that for evaporation temperatures ranging between -40 and 0 °C, the double- and triple-stage refrigeration cycles reached a higher COP using a Li-NO_3-NH_3 solution than using an H_2O-NH_3 pair. The results obtained for the double-stage cycle show that in the refrigeration cycle the Li-NO_3-NH_3 solution operates with a COP of 0.32, the H_2O-NH_3 pair with a COP of 0.29 and the Na-SCN-NH_3 solution with a COP of 0.27, when it evaporates at -15 °C, condenses and absorbs refrigerant at 40 °C and generates vapor at 90 °C.

Suzuki et al. [89] proposed an ammonia-water mixture turbine system (W-MTS) which is the combination of two different Kalina cycle types, KCS-1 and KCS-34. KCS-1 has a distillation/condensation subsystem and it is effective for heat source temperatures of 200-400 °C. KCS-34 is a Kalina system specifically designed for geothermal systems, which is suitable for heat source temperatures of 100-200 °C. Suzuki et al. [89] compared the

www.manaraa.com

power output of this cycle with the KCS-1 and KCS-34 cycles, and they showed that the W-MTS generates more power rather than two Kalina cycles. The exergy efficiency of the W-MTS is 38% when the ammonia mass fraction is 0.6 kg NH_3/kg solution and the heat source temperature is 160 °C. The exergy efficiencies of the KCS-1 and the KCS-34 for the same operating conditions are 33% and 30%, respectively. Amano et al. [90] conducted experiments with the W-MTS by using a 40% efficiency axial impulse type turbine, the heat source temperature was between 165-180 °C. Their experimental study showed that the power output decreased from 45.0 kW to 10.0 kW when the evaporating pressure was increased. They also concluded that the flow rate of the AWM basic composition must be controlled when the heat source was changed, especially during partial load operation. Another conclusion they reached was that the evaporating pressure should be as low as possible to create high enthalpy in the turbine inlet vapor. Amano et al. [91] combined the W-MTS with an absorption refrigeration system and proposed a hybrid power generating and refrigerating cycle. The refrigeration cycle is a single-stage ammonia absorption refrigeration cycle. They coupled the power and refrigeration cycle by connecting the separator of the power cycle to the absorber of the refrigeration cycle, and they feed the power cycle by the strong solution stream of the refrigeration cycle. However, the same heat source both feed the power and refrigeration cycles separately. They compared the hybrid configuration with the stand alone power and refrigeration systems used, and their results showed that the hybrid configuration produce higher power output and COP than those of the stand-alone power and refrigeration systems.

www.manaraa.com

Takeshita et al. [92–94] extended the W-MTS experimental cycle by including a gas turbine at the top and a Rankine cycle at the middle cycles. The topping cycle, is a typical Brayton Cycle with a gas turbine, which spins at 30,000 rpm at 700 kW, and a synchronous generator. The second stage, the middle cycle, is a Rankine Cycle with a backpressure steam turbine, which spins at 3000 rpm at 55 kW, and an induction generator. The bottom stage was the combined W-MTS and absorption refrigeration cycle described in Amano et al. [91]; power generating system consist of an AWM turbine, which spins 3000 rpm at 60 kW, and an induction generator, and the refrigeration system consist of an ammonia-absorption refrigerator and ice storage tanks, which had a capacity of 3000 MJ. They initially investigated the effect of ammonia mass fraction on the turbine performance [92]. Their experiments showed that pressure ratio between inlet and outlet of the turbine and turbine shaft power decreases with the basic composition. Their results indicate that the bottoming power and refrigeration cycle contribution to the overall cycle efficiency was significant, which was about 7% in electric power [94]. However, the system is not simple; it includes evaporator, two pre-heaters, two separators, high and low pressure condensers, and a recuperator. They found that the Rankine cycle required 60 kg/h of steam per unit kW power output, however the AWM cycle required only 28 kg/h, which was 46% that of a Rankine Cycle system. The temperature of the heat source steam was varied between 139 and 162 °C, and they found that the AWM turbine system was not able to produce power when the heat source temperature was 139 °C [93]. Thermal efficiency of the system also reduced by decreasing the heat source temperature. The maximum efficiency of the cycle was 1.7% and 2.5%, respectively for heat source temperatures of 148 °C and 162 °C [93].

www.manaraa.com

They stated that with the improved turbine efficiency, the AWM system should theoretically produce power at a thermal and exergy efficiency of 6% and 16%, respectively with a heat source steam temperature of 139 °C. However, this cycle is not suitable for heat source temperatures below 100 °C.

Wang et al. [95] developed a combined cycle that was consist of an ORC and vapor compression cycles. Essentially, an organic Rankine cycle is coupled to a vapor compression cycle to produce the cooling. The cooling side is a standard vapor compression cycle. Instead of using an electrical motor to drive the compressor, the compressor was directly coupled to the expander. A nominal 5 kW cooling capacity prototype system was developed based on this concept and tested under laboratory conditions. Although the system was tested off of its design point, it performed well achieving 4.4 kW of cooling at a measured heat activated COP of 0.48.

Most of these cycles showed some prospect in terms of thermal and exergy efficiency, however these systems are relatively complicated compared to the Goswami cycle [4], resulting in a higher capital investment. The cogeneration of power and refrigeration systems are summarized in Table 2.2 with thermal and exergy efficiencies. Other parameters such as heat source, turbine conditions etc. are also given in Table 2.3.

www.manaraa.com

Table 2.2 Combined power/cooling and ammonia-water cycles from the literature

Reference	Cycle	Type	Working Fluid	Efficiency %	
				Thermal	Exergy
Erickson et al. [26]	GAX cycle+Absorption Ref	Theoretical	Ammonia-water	11.9	N.A.
Oliveira et al. [68]	Rankine+Ejector Ref.	Experimental	n-pentane	4.0%	NA
Alexis [67]	Rankine+Ejector Ref.	Theoretical	Water	32.0	N.A.
Wang et al. [74]	Rankine+Ejector Ref.	Theoretical	Ammonia-water	20.9	35.8
Dai et al. [75]	Rankine+Ejector Ref.	Theoretical	R123	13.7	22.2
Wang et al. [76]	Rankine+Ejector Ref.	Theoretical	Ammonia–water	20.5	35.5
Zheng and Weng [70]	ORC+Ejector Ref.	Theoretical	R245fa	34.1	56.8
Wang et al. [72]	ORC+Ejector Ref.	Theoretical	R123	15.6	39.8
Wang et al. [73]	ORC+Ejector Ref.	Theoretical	R123	14.9	27.5
Zheng et al. [77]	Kalina+Absorption Ref.	Theoretical	Ammonia-water	24.2	37.3
Amano et al. [90]	Kalina+Absorption Ref.	Experimental	Ammonia-water	N.A.	N.A.
Amano et al. [91]	Kalina+Absorption Ref.	Theoretical	Ammonia-water	N.A.	N.A.
Takeshita et al. [94]	Kalina+Absorption Ref.	Experimental	Ammonia-water	26	NA
Liu and Zhang [78]	Rankine+Absorption Ref.	Theoretical	Ammonia-water	27.8	57.6
Zhang and Lior [79]	Rankine+Absorption Ref.	Theoretical	Ammonia-water	27.7	55.7%
Zhai et al. [84]	Rankine+Absorption Ref.	Theoretical	Steam/Silica gel–water	27.3	9.9
Zamfirescu and Dincer [81]	Trilateral flash Rankine	Theoretical	Ammonia-water	8	30
Wagar et al. [82]	Trilateral flash Rankine	Theoretical	Ammonia-water	16	N.A.
Aphornratana and Sriveerakul [85]	ORC+Vapor Compression Ref.	Theoretical	R134a and R22	N.A.	N.A.
Wang et al. [95]	ORC+Vapor Compression Ref.	Theoretical	R-245fa	12	22

www.manaraa.com

Table 2.3 Operating conditions of the combined power/cooling cycles found in the literature

Reference	Temperature °C		Turbine Parameters		
	Heat Source	Boiler/Condenser	Efficiency %	P (bar)	T (°C)
Erickson et al. [26]	175	155/28	75	25.1/5.2	155/61.7
Oliveira et al. [68]	N.A.	95/N.A.	28	N.A.	N.A.
Alexis [67]	N.A.	360.0/60.1	85	20/0.2	360.0/241.6
Wang et. al [74]	300	212/25	85	25/1.19	285/96.9
Dai et al. [75]	150	140/20	85	8.0/2.0	140/101.7
Wang et al. [76]	300	285/25	85	25/1.19	285/96.9
Zheng and Weng [70]	N.A.	122.0/21.9	100.0	19.93/4.0	122.0/67.9
Wang et al. [72]	140	130.0/25	85	10.0/3.0	130.0/94.2
Wang et al. [73]	140	130.0/25	82	7.0/2.2	130.0/99.0
Zheng et al. [77]	N.A.	350/35	N.A.	49/0.98	350/84.5
Amano et al. [90]	165-180	N.A./N.A.	40	12.0-17.0/N.A.	164/N.A.
Amano et al. [91]	165	155.0/42.0	100.0	28.0/2.9	155.0/N.A.
Takeshita et al. [94]	163.9 °C	158.9/27	40	15/N.A.	158.9/N.A.
Liu and Zhang [78]	465	450/35	87	111/0.39	450/68
Zhang and Lior [79]	465	450/45.1	87	52.4/0.2	450/61.3
Zhai et al. [84]	N.A.	180/82.1	70	10.0/0.7	180/90
Zamfirescu and Dincer [81]	150 °C	130/25	80	6/N.A.	130/50
Wagar et al. [82]	210	200/N.A.	85	N.A.	N.A.
Aphornratana and Sriveerakul [85]	N.A.	80.0/40.0	N.A.	26.3/10.2	80.0/40.0
Wang et. al [95]	N.A.	190/	75	34/N.A.	190/N.A.

المنارة للاستشارات

www.manaraa.com

2.5 Goswami Cycle

The ammonia-water combined power/cooling cycle proposed by Goswami [4, 5] utilizes a binary mixture, such as ammonia-water, working fluid to produce both power and refrigeration simultaneously in the same loop and require less equipment; simply an absorber, separator, boiler, heat recovery and refrigeration heat exchangers and a turbine. The cycle is a combination of Rankine cycle and an absorption refrigeration system. This cycle can be used as a bottoming cycle using waste heat from a conventional power cycle or as an independent cycle using low temperature sources such as geothermal and solar energy. Power is produced by expansion of a high pressure vapor through an expander and cooling comes from the sensible heating of the expander exhaust. Absorption condensation is used to regenerate the working fluid, this allows the expander exhaust temperature to be significantly below the temperature at which absorption is taking place. It differs from pure working fluid Rankine cycle operation, where the limiting expander exhaust temperature is the vapor condensation temperature. Therefore, in the power/cooling cycle, it is possible to expand the vapor to sub-ambient temperatures, to produce a low temperature stream that can be used for cooling. Although, the Goswami cycle is applicable to all binary fluid systems consisting of two fluids of different boiling temperatures such that one may condense by absorption in the other, the description below is based on the amonia-water binary fluid system.

As shown in Fig. 2.12; the cycle's binary fluid mixture leaves the absorber (state 1) as a saturated solution at low pressure with a relatively high ammonia concentration. It is pumped to high pressure (state 2) where it recovers heat from the returning weak ammonia

المنارة للاستشارات

www.manaraa.com

liquid solution in the recovery heat-exchanger, before entering the boiler. As the boiler operates between the bubble and dew-point temperatures of the mixture at the system pressure, the basic solution is partially boiled to produce a two-phase mixture: a liquid (state 10), which is relatively weak in ammonia; and a vapor (state 4) with a high concentration of ammonia. This two-phase mixture is separated, and the weak liquid transfers heat to the high concentration stream before it is throttled to the system low pressure and sprayed into the absorber. The rectifier cools the saturated ammonia vapor (state 6) to condense out most of the remaining water. Heat can be added in the superheater as the vapor (state 7) proceeds to the turbine. The turbine extracts energy from the high-pressure vapor as it is expanded to the system's low-pressure (state 8) and cooling comes from the sensible heating of the turbine exhaust. The vapor (state 9) rejoins the weak liquid in the absorber where absorption condensation is used to regenerate the working fluid; this allows the turbine exhaust temperature to be significantly below the temperature at which absorption is taking place. This differs from pure working fluid Rankine cycle operation, where the limiting turbine exhaust temperature is the same as the vapor condensation temperature. Therefore, in the power/cooling cycle, it is possible to expand the vapor to sub-ambient temperatures, to produce a low temperature stream that can be used for cooling.

Goswami et al. [4–6, 71, 96–100] proposed the system in the mid-1990s and a number of studies have been completed since that time. Xu et al. [96] presented a parametric study of the Goswami cycle under idealized conditions, neglecting the irreversibilities associated with the heat transfer and expansion processes, and concluded that the cycle can achieve thermal efficiencies as high as 24% for heat source temperatures around 123 °C.

www.manaraa.com

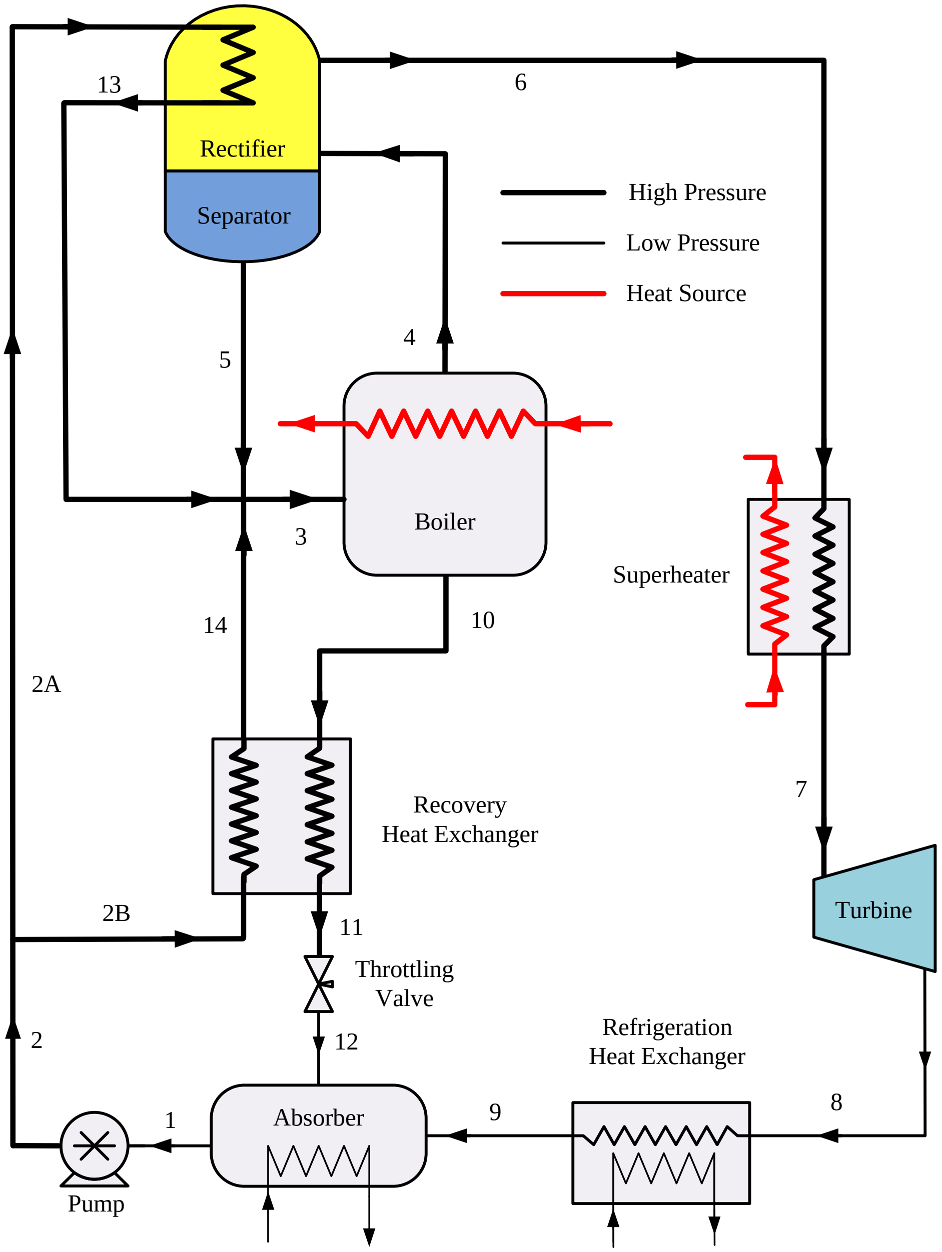

Figure 2.12 Schematic description of the Goswami cycle with internal cooling

Hasan and Goswami [97] used the exergy analysis to improve the performance of the combined cycle system. They found out that the highest irreversibility occurs at the absorber since it involves two highly irreversible processes of condensation and mixing of ammonia and water components. They also found out that total exergy destruction in the cycle

المنارة للاستشارات
www.manaraa.com

increases with an increase in the heat source temperature. Although the assumptions of idealized conditions limit the usefulness of the analysis, those results showed the potential of the proposed cycle for using low temperature sensible heat sources. Vijayaraghavan and Goswami [101] presented the efficiency definitions of first law, second law, and exergy for the power/cooling cycle and performed optimization using these efficiencies. Lu and Goswami [102] concluded that the cycle could be optimized for work or cooling outputs and efficiency. Goswami et al. [103] calculated the second law efficiency of the cycle for heat source temperatures between 57 °C and 197 °C. They found that the second law efficiency of the cycle could reach 60% when the boiler temperature is higher than 127 °C. In addition, an initial experimental study was conducted, which generally verified the expected boiling and absorption processes [98].

Martin and Goswami [100] detailed the experimental facility, factors affecting cooling production, and experimental measurements of the expander temperature drop. Martin and Goswami performed experiments to provide a demonstration of the cooling output of the cycle [6]. They showed the potential of cooling output from the cycle by verifying the temperature difference between the absorber and expander exit. However, the minimum cooling temperatures obtained in the experiments were higher than expected, and they explained that the reason was the poor performance of the expander. Turbine performance is a crucial factor to utilize the potential of cooling output. The expander used in the experiments was a modified single-stage, partial admission turbine originally for use in an air-cycle cooling system. The mechanical power generated by the expander was not di-

المنارة للاستشارات
www.manaraa.com

rectly measured, also heat transfer across the expander could account for the low efficiency observed during the experiments.

2.5.1 Cycle Operation

The amount of vapor leaving the separator column also dictates the system high pressure, to give an example, when more vapor is allowed to leave the separator, pressure in the boiler and separator decreases. The inverse relation between vapor mass flow rate and system high pressure is illustrated in Fig. 2.13. As shown in the figure, the mass flow rate fraction of vapor decreases with the increase of boiler pressure. However, a binary mixture working fluid, at constant temperature and concentration, boils at a pressure between the saturated liquid and vapor pressures. If the pressure is higher than the saturated liquid pressure, no vapor can be produced, and if the pressure is lower than saturated vapor pressure, all of the fluid will be vaporized. These limiting pressures are evidenced when net work output is zero as shown in Fig. 2.13. Work output from the cycle is zero when the pressure ratio is a unity or no vapor flows to the expander.

Another parameter that is related with the vapor flow rate is the vapor concentration. As pressure decreases more vapor is formed and its concentration continues to drop until the saturation pressure is reached and all of the basic solution has vaporized. Vapor concentration and mass flow rate fraction relation is presented in Fig. 2.14. The cooling output from the cycle is very sensitive to vapor concentration; this will be discussed later in this chapter.

www.manaraa.com

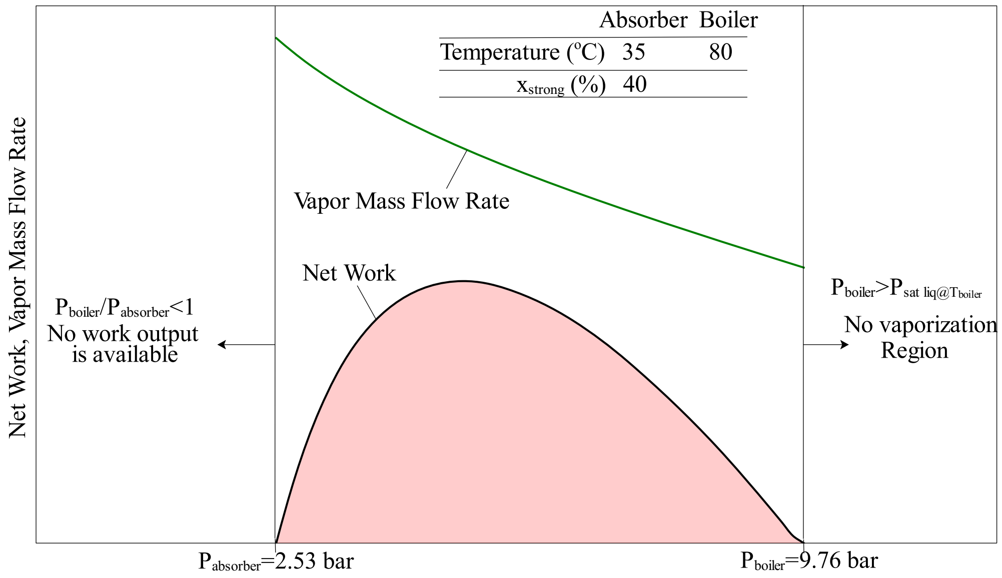

Figure 2.13 Vapor mass flow rate and work output relation with respect to boiler pressure

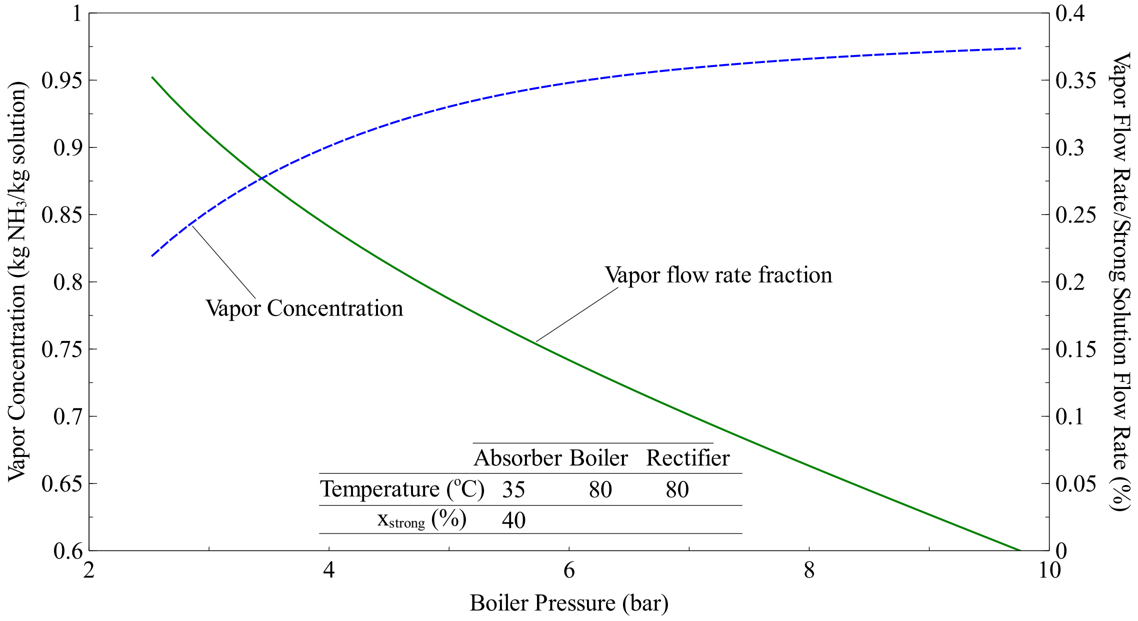

Figure 2.14 Vapor concentration and mass flow rate fraction with respect to boiler pressure

www.manaraa.com

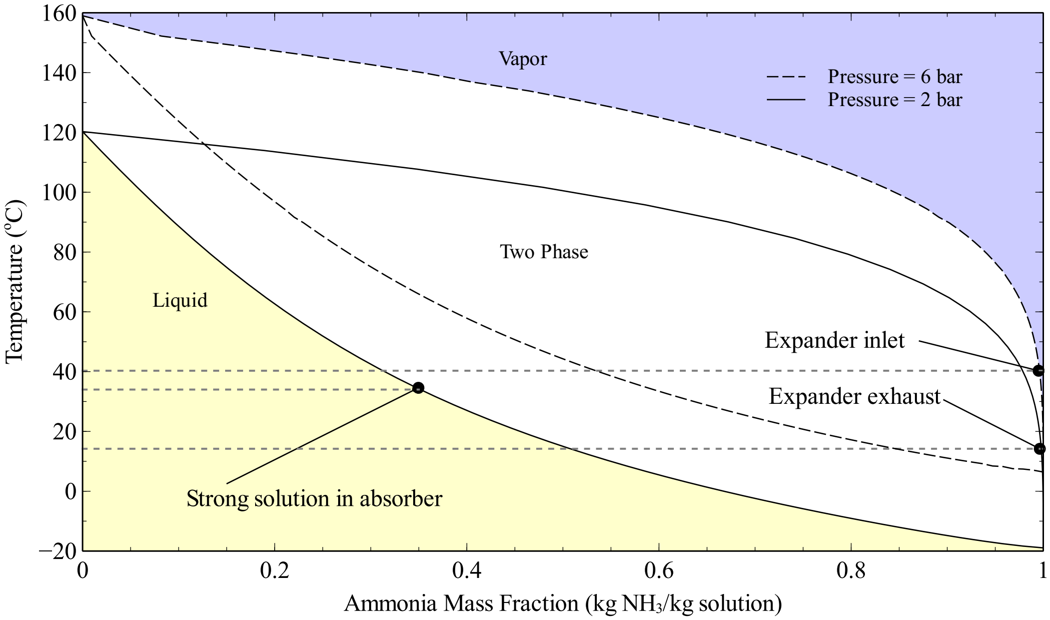

Figure 2.15 Ammonia-water phase equilibrium diagrams at two different pressures highlighting the source of cooling temperatures

2.5.2 Cooling Aspect of the Cycle

The cooling aspect of the Goswami cycle is due to the fact that the working fluid is a binary mixture and at constant pressure, the condensing temperature of an ammonia rich vapor can be below the saturation temperature for a lower concentration liquid. The vapor (state 8), which is shown in Fig. 2.12, rejoins the weak liquid in the absorber where absorption condensation is used to regenerate the working fluid; this allows the turbine exhaust temperature to be significantly below the temperature at which absorption is taking place. This differs from pure working fluid Rankine cycle operation, where the limiting turbine exhaust temperature is the same as the vapor condensation temperature. Cooling can be obtained by sensibly heating the expander exhaust. This is illustrated with a binary mixture, phase equilibrium diagram, as shown in Fig. 2.15. The effect of ammonia concentration

www.manaraa.com

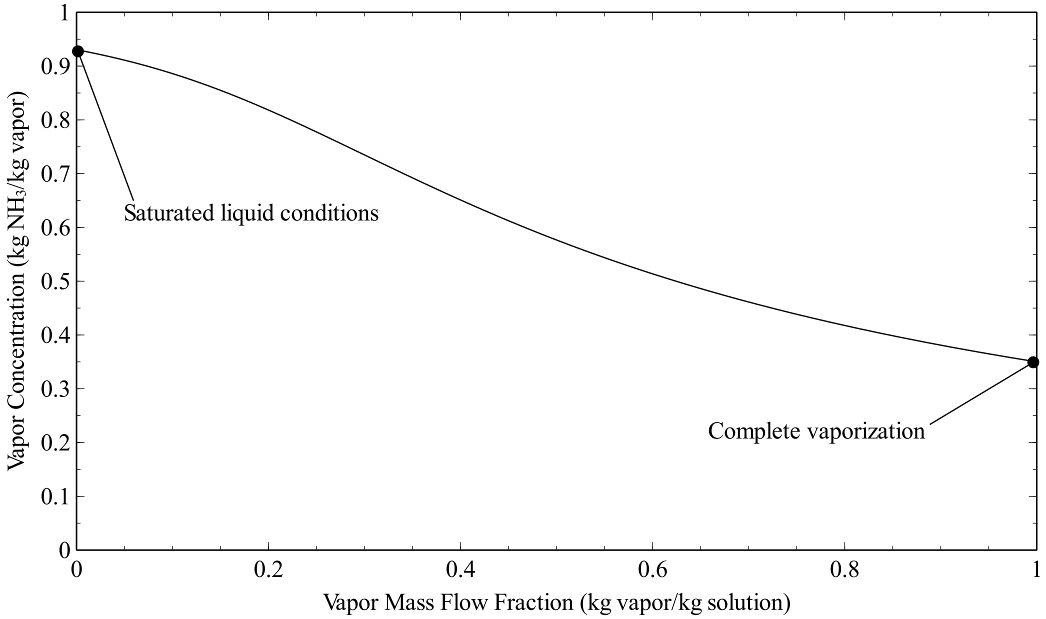

Figure 2.16 Relationship between vapor concentration and amount of partial vaporization (state 4) at 6 bar

on expander inlet and outlet temperature is also shown in Fig. 2.15. The low concentration saturated liquid state represents the basic solution exiting from the absorber, while the high concentration vapor is typical of the expander exhaust conditions. This shows how it is possible for the vapor to be expanded to a temperature below the ambient.

As illustrated in Fig. 2.15, the basic solution should be kept as low as possible in ammonia concentration and the vapor should be as high as possible to increase the temperature gap between the absorber and turbine exhaust temperature. In addition, if the turbine works very efficiently, it is a high chance that partial condensation of the expander exhaust can happen, such as 95% expander exhaust quality, and this would cause to reach lower vapor temperature at the turbine exit. Therefore, in the power/cooling cycle, it is possible to expand the vapor to sub-ambient temperatures, to produce a low temperature stream that can

المنارة للاستشارات
www.manaraa.com

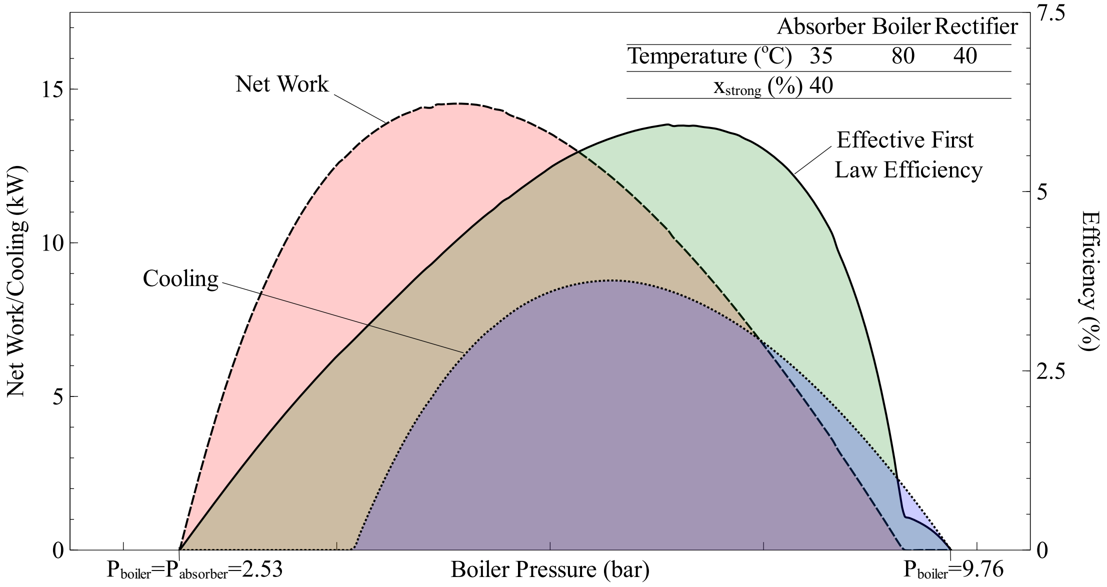

Figure 2.17 Net work and cooling outputs and effective first law efficiency of the Goswami cycle with respect to boiler pressure

be used for cooling. Figure 2.15 shows that high ammonia mass concentration is needed at the expander exhaust to reach low temperatures; however, this is coupled with the mechanisms of vapor production. Vapor concentration as a function of the ratio of the vapor mass-flow (state 4) to the basic solution mass-flow (state 3) (Vapor mass flow fraction) is shown in Fig. 2.16. The working fluid was partially vaporized in the boiler (state 4) and separated by phase in the separator. As shown in Fig. 2.16, the concentration is highest with a minimal vaporization. High concentrations are preferred for cooling, since they lead to low expander exhaust temperatures although this implies low vaporization rates.

As a further example, Fig. 2.17 presents computed results of cycle outputs for the variation of boiling pressure. The relative position of the maxima for work production, first law efficiency, and cooling production are shown. Similar to work output, cooling also has

المنارة للاستشارات
www.manaraa.com

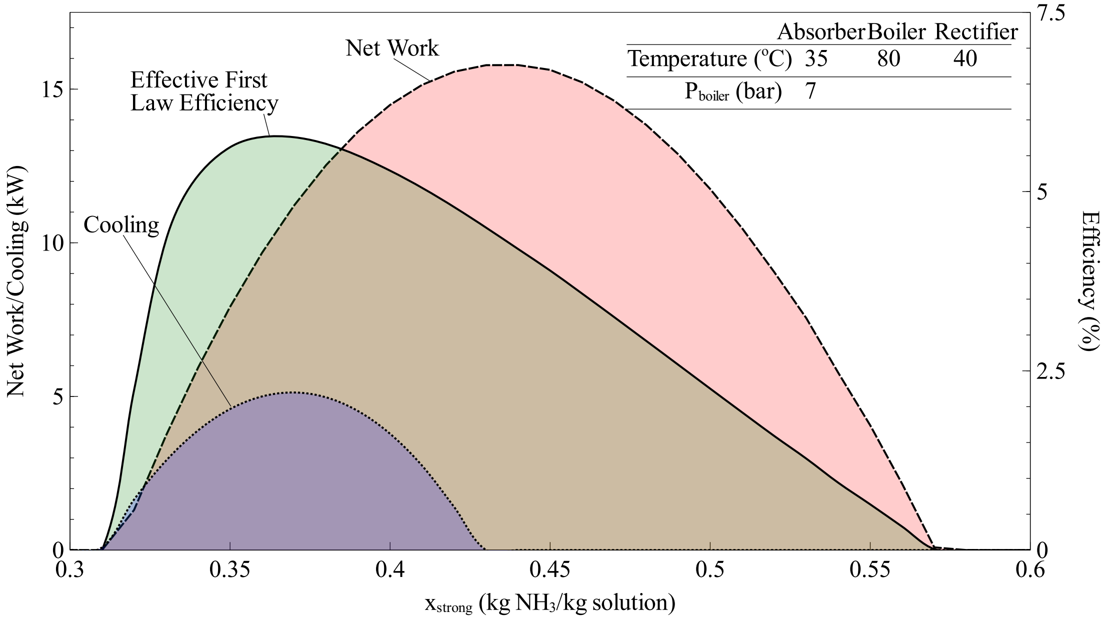

Figure 2.18 Net work and cooling outputs and effective first law efficiency of the Goswami cycle with respect to strong solution concentration

a maximum, which is limited at low pressures by higher turbine exhaust temperatures and bounded at higher pressures by the low production of vapor.

Fig. 2.18 shows that each cycle parameter also has a maximum value for a range of basic solution ammonia concentration. The ammonia concentration takes an important role in the maximum values; so any parametric study that is searching for the optimum conditions and outputs should consider concentration value. Based on the cycle design and requirements, this figure shows that the cycle can be optimized for each parameter that is shown.

The main parameters that can be varied to influence the cycle are the heat source temperature, system high pressure, basic solution mass fraction, and absorber pressure and temperature. Saturation in the absorber reduces the number of independent parameters that

www.manaraa.com

govern the cycle to four. Rectifier and superheater temperatures can also be modified, as well as the conditions of heat transfer from the source to the ammonia-water mixture.

المنارة للاستشارات
www.manaraa.com

Chapter 3

Theoretical Modeling of Goswami Cycle

In this chapter, important operating mechanisms affecting the Goswami cycle operation and the performance of the cycle utilizing low-grade and mid-grade temperature are presented. Simulations are conducted to study the performance of the cycle for different parameters such as boiler temperature and pressure, strong solution concentration, absorber temperature and rectifier exit conditions and to determine the operational limits.

The cycle is shown in Fig. 3.1. The binary fluid mixture leaves the absorber (state 1) as a saturated solution at the cycle low pressure with a relatively high ammonia concentration. It is pumped to the system high pressure (state 2) and it recovers heat from the returning weak ammonia liquid solution in the recovery heat-exchanger before entering the boiler. As the boiler operates between the bubble and dew-point temperatures of the mixture at the system pressure, the basic solution is partially boiled to produce a two-phase mixture-a liquid (state 10), which is relatively weak in ammonia, and a vapor (state 4) with a high concentration of ammonia. This two-phase mixture is separated in the separator, and the weak liquid transfers heat to the high concentration stream before it is throttled to the system low pressure and sprayed into the absorber. The rectifier cools the saturated ammonia vapor (state 6) to condense out any remaining water. Heat can be added in the superheater as the vapor (state 7) proceeds to the expander. The expander extracts energy from the

المنارة للاستشارات

www.manaraa.com

high-pressure vapor as it is throttled to the system's low-pressure (state 8). It provides cooling in the refrigeration heat exchanger. The vapor (state 9) rejoins the weak liquid in the absorber where the basic solution is regenerated and heat is rejected.

3.1 Efficiency Terms Used in the Study

In most applications, refrigeration is more expensive product than power since it requires refrigeration equipment as well as power to produce conventional refrigeration. Therefore, the additional output of refrigeration by the combined cycle provides greater benefit than the conventional power systems. In order to measure the performance of the combined cycle in a proper way, the refrigeration produced by the cycle should be taken as the electric power equivalent to generate the same cooling effect by a conventional refrigeration system. The cascade cycle analogy [101] provides the suitable efficiency terms to measure the performance of the combined cycle. The effective first law efficiency is given by:

$$\eta_{I,eff} = (W_{net} + E_c/\eta_{II,ref})/Q_h \tag{3.1}$$

In the above equation, E_c term is the exergy associated with the refrigeration. In order to account for the irreversibilities of heat transfer in the refrigeration heat exchanger, the exergy change of the chilled fluid was considered.

$$E_c = \dot{m}_{cf}\left[h_{cf,in} - h_{cf,out} - T_o(s_{cf,in} - s_{cf,out})\right] \tag{3.2}$$

Effective exergy efficiency is given as:

المنارة للاستشارات
www.manaraa.com

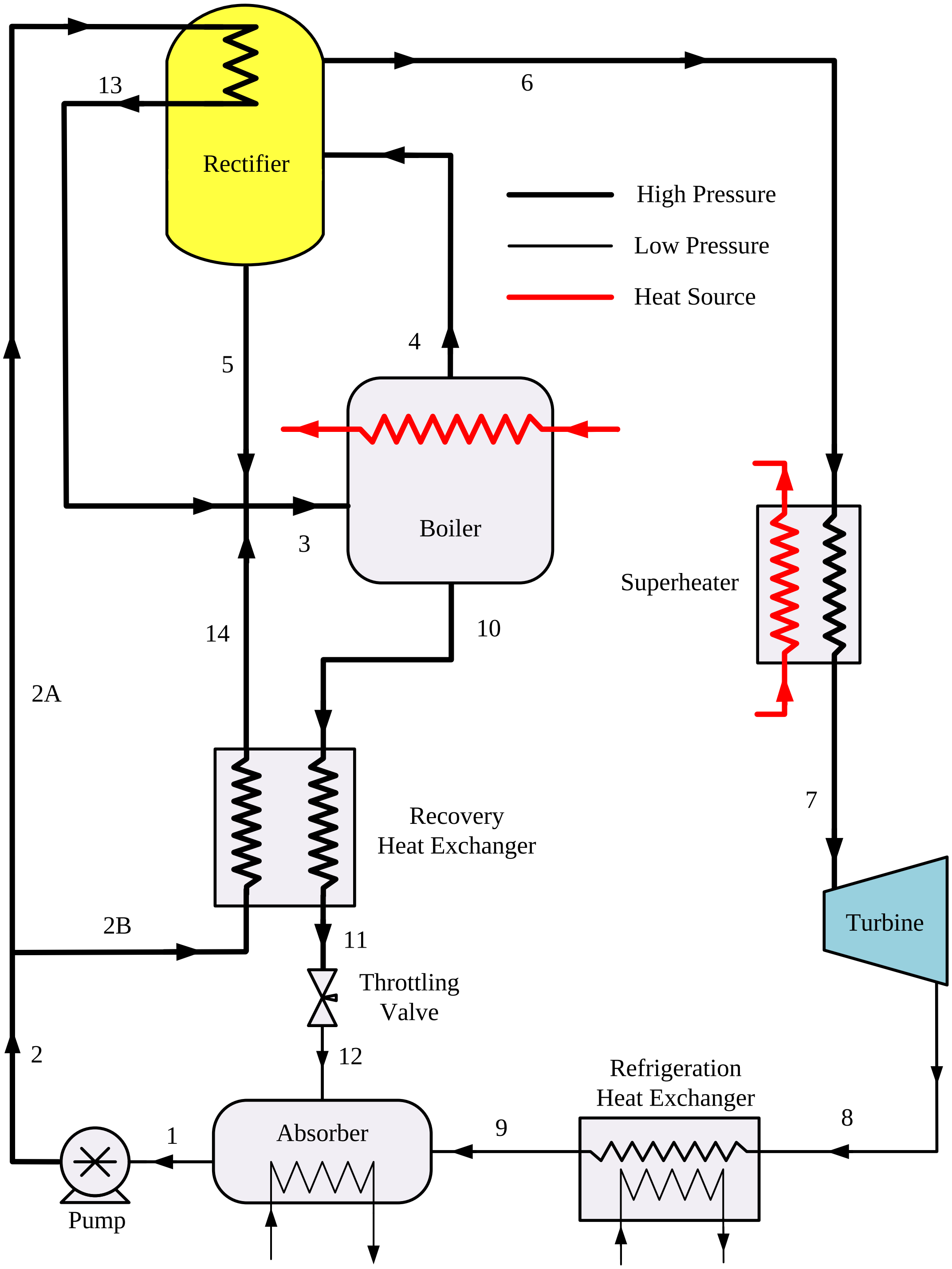

Figure 3.1 Schematic description of the Goswami cycle with internal cooling

www.manaraa.com

$$\eta_{exergy,eff} = \left(W_{net} + E_c/\eta_{II,ref}\right) / \left(E_{hs,in} - E_{hs,out}\right) \tag{3.3}$$

In this equation, the denominator is the change in exergy of the heat source, which is equivalent to the exergy input.

3.2 Simulation Details

Cycle parameters assumed for the parametric study are given in Table 3.1. Commercial software, Chemcad [104], was used to simulate the combined power and cooling thermodynamic cycle, details of the thermodynamic properties used for the simulation are given in Appendix A. The following assumptions were used in the analysis:

- Water was used as the chilled fluid in the refrigeration heat exchanger;
- An exhaust turbine temperature of 20°C or lower was required to generate refrigeration;
- Minimum temperature difference for each heat exchanger was 5°C;
- Pressure drops were neglected.

The main parameters that can be varied to influence the cycle are the heat source temperature, system high pressure, basic solution mass fraction, and absorber pressure and temperature. Saturation in the absorber reduces the number of independent main parameters that govern the cycle to four. Rectifier and superheater temperatures can also be modified, as well as the conditions of heat transfer from the source to the ammonia-water mixture.

www.manaraa.com

Table 3.1 Cycle parameters assumed for parametric study

Parameter	Value	Units
Reference Temperature	25	°C
Reference Pressure	1	bar
Absorber Temperature	31.4	°C
Absorber Pressure	2.08	bar
Boiler Temperature	83.4	°C
Rectifier Temperature	41.7	°C
Ammonia mass fraction, (x)	0.376	kg NH_3/kg solution
Second law efficiency of refrigeration $\eta_{II,ref}$ [101]	30%	
Isentropic turbine efficiency η_t	25%, 50%, 75%, 100%	
Isentropic pump efficiency η_{pump}	80%	

3.3 Rectification Cooling Source

In the experimental setup, external cooling for the rectifier needs is chosen due to simplicity in the installation and flexibility in controlling the rectifier exit temperature. With the intention of examining the effect of rectification cooling sources on cycle efficiencies, a parametric study is conducted in this section. The experimental conditions considered by Martin and Goswami [100] are used for the parametric analysis. In the experimental setup that Martin and Goswami [100] used, the condensed liquid at the rectifier was directly returned to the absorber without the flow measurement. This caused an uncertainty for the energy and mass balance across the absorber. In order to tackle this problem, the experimental setup is built as shown in Fig. 3.2. As the experimental operating conditions of Martin and Goswami [100] are used to show the effect of the parameters being considered, their configuration is used only in this section.

In addition, Xu et al. [96] provided the maximum potential of the cycle although those results are not practically achievable. To address this shortcoming, the cooling and power

www.manaraa.com

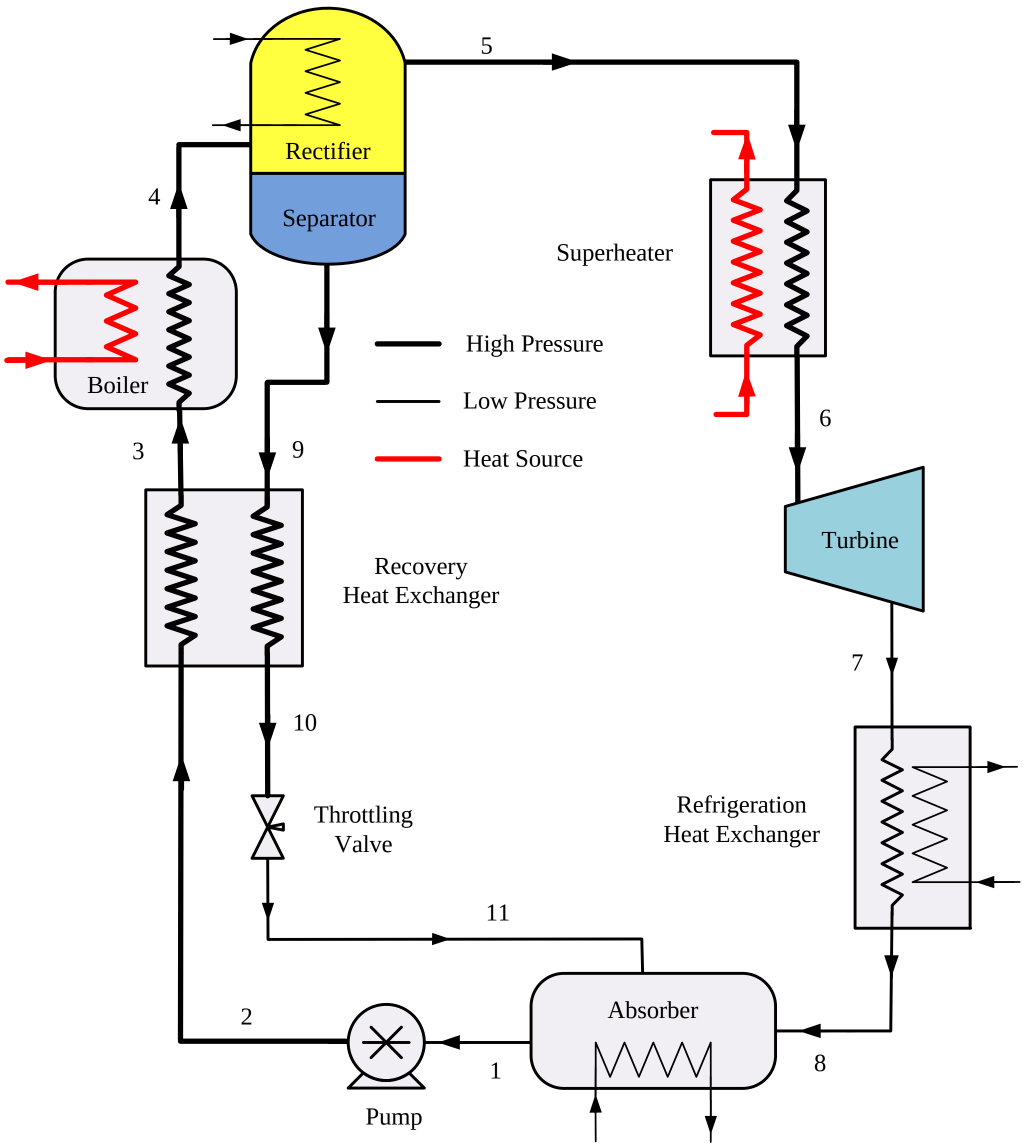

Figure 3.2 Schematic description of the Goswami cycle with external cooling

output of the combined cycle are investigated for a turbine efficiency of 50-75% with the reversible expansion process to show the effects of irreversibilities in the expansion process on the cycle output parameters. A 25% turbine efficiency is also included in this parametric study since that was the case in the Martin and Goswami [6] experimental study, which showed no cooling output. This parametric study that shows the effect of turbine perfor-

المنارة للاستشارات
www.manaraa.com

mance is aimed to show the expected improvement of the net work and cooling outputs using a scroll turbine.

In Case I, rectification cooling is provided by the diverted portion of the basic solution stream from the absorber as shown in Fig. 3.1, and in Case II, rectification cooling is provided by an external cooling source as shown in Fig. 3.2. The net work, cooling output, and effective first law and exergy efficiencies of the cycle are also presented in order to find out the sensitivity to the boiling pressure, ammonia concentration, and isentropic turbine efficiency.

The variations of effective first law efficiency and effective exergy efficiency with the pressure ratio ($P_{boiler}/P_{absorber}$) and basic solution concentration for the two rectification cooling sources are shown in Figures 3.3-3.4. There is a significant difference in the effective first law and exergy efficiencies in favor of an internal cooling source (Case I) when the turbine efficiency is high (see Figures 3.3(a-b)). As discussed before, the efficiency of the turbine is crucial to the cycle performance. Although the first law efficiencies around 7% seem low, they compare well with the ideal Lorenz cycle efficiency of 7.6% with finite heat sources for the same boiler and absorber temperatures for maximum power [37].

The ammonia concentration takes an important role in the maximum values; the sensitivity of ammonia concentration is demonstrated in Figures 3.4(a-b). For this analysis, boiling pressure was constant at 5.16 bar and the stream exiting from the absorber was kept under saturated liquid condition at a constant temperature of 31.4 °C. The lowest ammonia mass fraction ($\sim$0.25) is the saturation concentration point for the given boiler temperature and pressure. As the ammonia mass fraction in the basic solution increases, absorber sat-

للاستشارات المنارة
www.manaraa.com

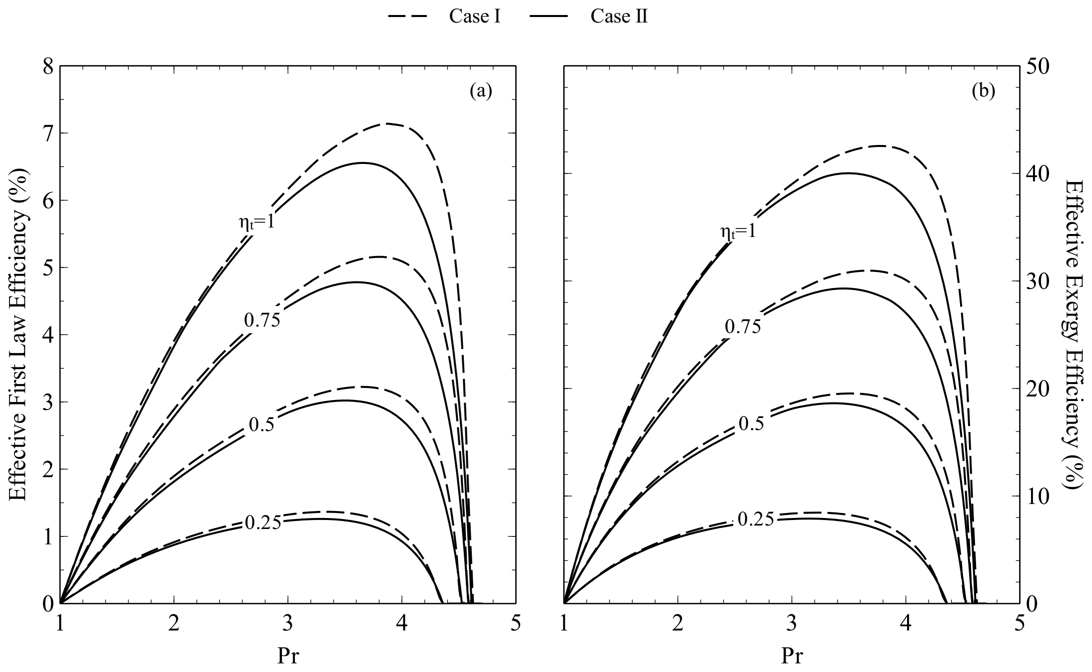

Figure 3.3 Effects of pressure ratio on the effective first law and exergy efficiencies for different rectification cooling sources for no superheater condition. Case I -Rectification by internal cooling source, and Case II -Rectification by external cooling source

uration pressure also increases. When the absorber saturation pressure increases up to the high pressure of the cycle, the maximum limit for the ammonia mass fraction is reached. These limiting pressures are evidenced when net work output and either first law or exergy efficiency are zero as shown in Figures 3.4(a-b). The difference between the cases of internal and external rectification becomes very small when the ammonia concentration is increased as shown in Figure 3.4.

The effects of pressure ratio and superheater on the cycle net work and cooling outputs are shown in Figure 3.5. The effect of superheater on the net work output is significant at high turbine efficiency, as the maxima point of the net work output increases approximately 10% for turbine efficiency higher than 75%. However, as shown in Fig. 3.5(b), the cooling

المنارة للاستشارات
www.manaraa.com

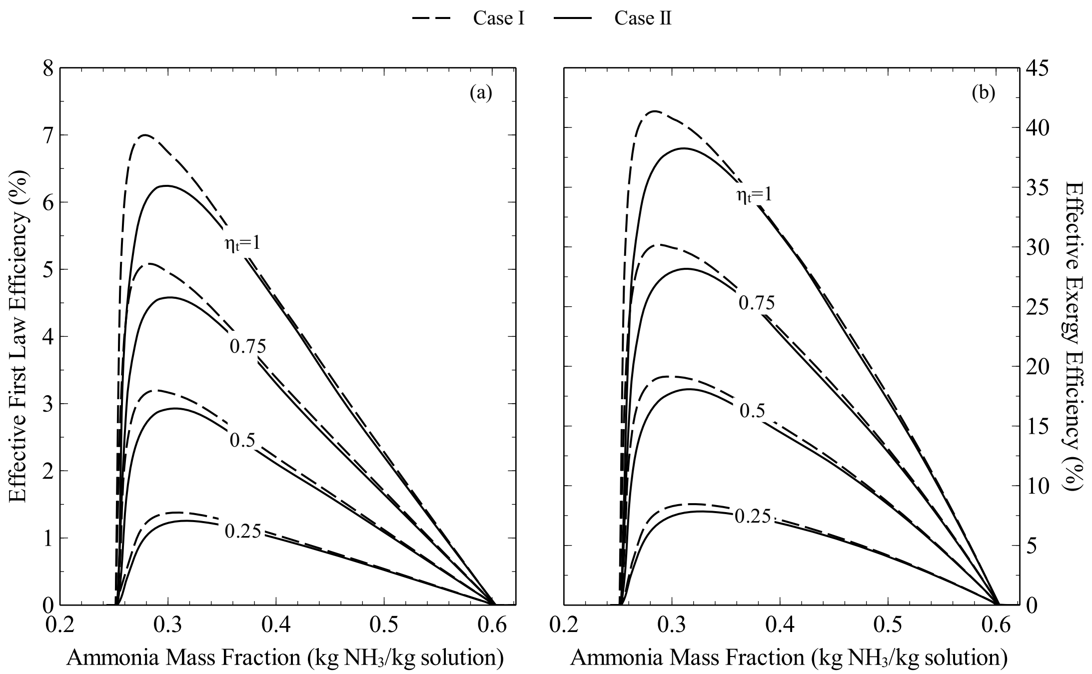

Figure 3.4 Effects of ammonia mass fraction on the effective first law and exergy efficiencies for different rectification cooling sources for no superheater condition. Case I-Rectification by internal cooling source, and Case II-Rectification by external cooling source

output notably decreases for the superheater case. The cycle produces no cooling output for turbine efficiency less than 50%. Cooling output is limited at low pressures by higher turbine exhaust temperatures and bounded at higher pressures by the low production of vapor as shown in Fig. 3.5(b). When the turbine inlet temperature is increased with a superheater, the work output is increased; however, the cooling output is decreased as the turbine exit temperature is increased.

For different rectification cooling sources, the effects of pressure ratio and superheater on the effective first law and exergy efficiencies are shown in Figures 3.6(a-b). When external cooling is used in the rectifier (Case II), the effect of superheater on the effective first law efficiency shows no significant difference; however, the maxima point of the effective

المنارة للاستشارات
www.manaraa.com

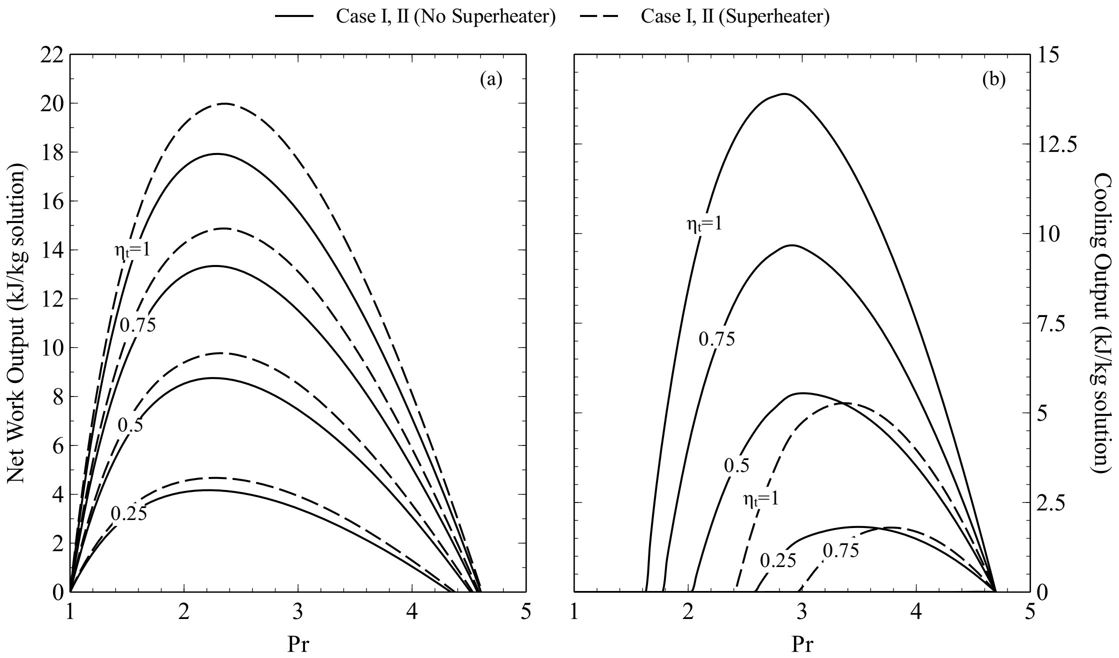

Figure 3.5 Effects of pressure ratio and superheater on the net work and cooling outputs for different rectification cooling sources. Case I-Rectification by internal cooling source, and Case II-Rectification by external cooling source

first law efficiency for internal cooling is increased approximately 0.1-0.5% for different turbine efficiencies as shown in Fig. 3.6(a). The effective exergy efficiency maxima point increases approximately by 1-5% for internal cooling (Case I) as shown in Fig. 3.6(b), though the superheater effect on the effective first law efficiency for the external cooling case (Case II) is not considerable. The effects of ammonia mass fraction and superheater on the effective first law and exergy efficiencies for different rectification cooling sources are shown in Figures 3.7(a-b). When the ammonia mass fraction is higher than 0.35, there is a slight difference in the effective first law and exergy efficiencies between the superheat and no superheat cases as shown in Figures 3.7(a-b).

المنارة للاستشارات
www.manaraa.com

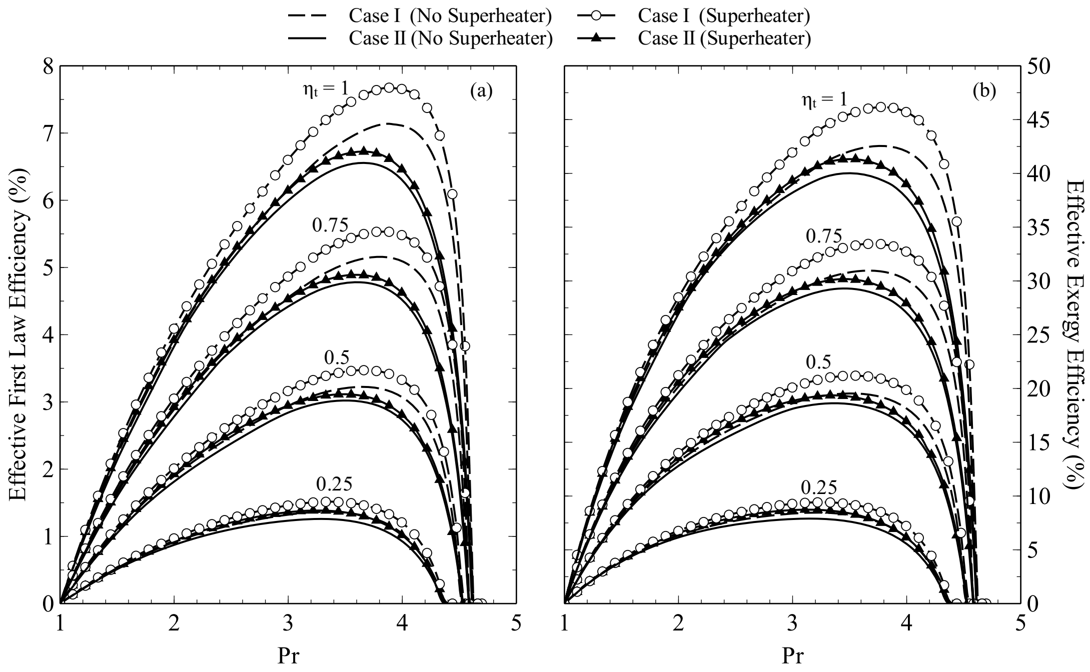

Figure 3.6 Effects of pressure ratio and superheater on the effective first law and exergy efficiencies for different rectification cooling sources. Case I-Rectification by internal cooling source, and Case II-Rectification by external cooling source

It can be concluded that, for external rectification cooling source (Case II), an effective first law efficiency of 3–5% and an effective exergy efficiency of 18–28% with 50–75% turbine efficiency could be achieved for a boiler temperature of 83.4 °C and a rectifier temperature of 41.7 °C. The maximum effective first law and effective exergy efficiencies, for 50% and 75% turbine efficiency, can be increased to 3.5–5.5% and 22–33%, respectively by using the internal rectification cooling source (Case I) and superheating the ammonia vapor. No significant difference was observed between the external and internal cooling source for rectification cases at ammonia mass fractions higher than 0.35. The boiler pressure is kept constant when the ammonia concentration in the absorber is increased. For the operating conditions that are experimentally studied, the optimum concentration for the

www.manaraa.com

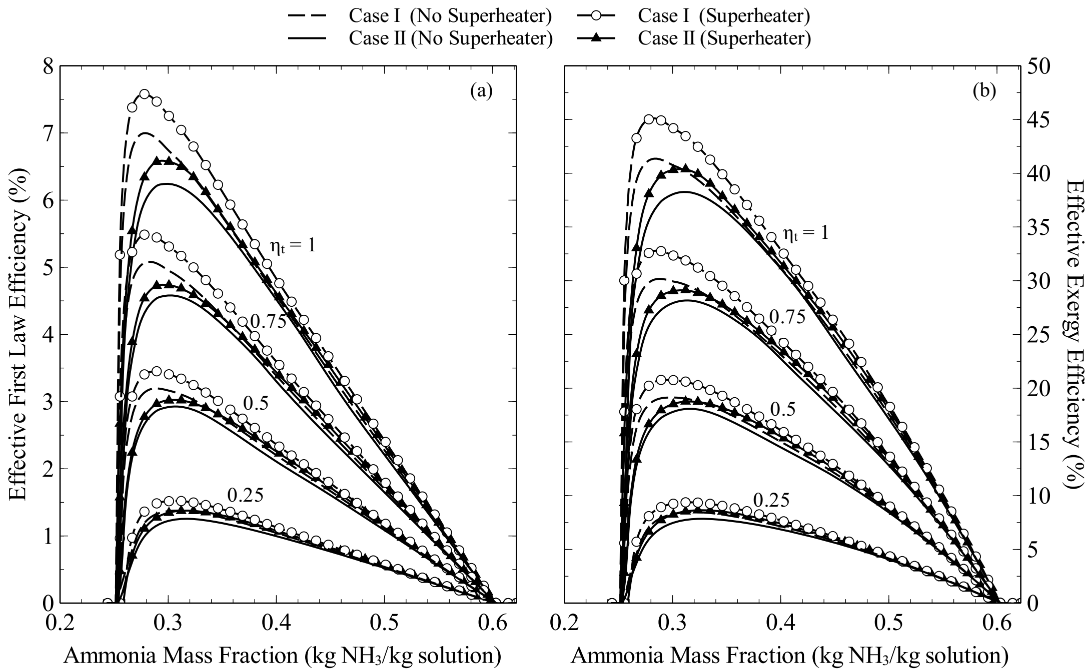

Figure 3.7 Effects of ammonia mass fraction and superheater on the effective first law and exergy efficiencies for different rectification cooling sources. Case I-Rectification by internal cooling source, and Case II-Rectification by external cooling source

effective first law and exergy efficiencies is in the range of 0.3 to 0.35. In order to see the effect of ammonia mass concentration on the other cycle parameters, such as, vapor concentration, mass flow rate fraction, quality after turbine, and cooling and net work outputs, the results are given in Table 3.2 for three different ammonia mass concentrations. The boiler and absorber temperatures were kept at 83.4 °C and 31.4 °C, respectively, and the turbine efficiency was 90% for all cases. In addition, another boiler pressure case is shown to see the difference between the previous boiler pressure case and the higher pressure case.

The pressure at the separator and the temperature at the rectifier column exit determine the vapor concentration. As seen in the table, the vapor concentration has a significant effect on the turbine exit temperature. The higher the vapor concentration at the turbine

المنارة للاستشارات
www.manaraa.com

Table 3.2 The effect of strong solution concentration and boiler pressure on cycle outputs

Parameter	x=0.35		x=0.40		x=0.50	
P_{boiler}	5.16	7.00	5.16	7.00	5.16	7.00
$P_{absorber}$ (bar)	1.6		2.2		3.9	
x_{vapor} (kg NH_3/kg vapor)	0.993	0.995	0.993	0.995	0.993	0.995
x_{weak} (kg NH_3/kg solution)	0.272	0.322	0.275	0.324	0.284	0.330
$\dot{m}_{vapor}/\dot{m}_{strong\ solution}(\%)$	10.9	4.2	17.4	11.3	30.5	25.6
Turbine exit temperature (°C)	-12.0	-20.5	2.0	-10.9	28.8	12.9
Turbine exit vapor quality (%)	97.97	96.29	98.49	97.50	99.41	98.88
Cooling output (kW)	9.38	5.62	7.26	10.33	0.00	1.88
Net work output (kW)	13.86	5.31	16.94	13.63	10.29	17.12

inlet, the lower the turbine exit temperature, which increases the cooling output from the cycle. The mass fraction of the vapor with respect to the strong solution mass flow rate increases when the ammonia concentration is increased in the strong solution. However, when the boiler pressure is increased from 5.16 to 7.0 bar, the vapor mass flow rate fraction decreases, and the effect of boiler pressure on the vapor mass fraction is significant for the ammonia concentration of 0.35. The speed of the scroll expander is increased, if the vapor flowrate increases, which in turn gives higher efficiency. In order to maximize the turbine efficiency, the higher flow rates were targeted in the experiments. The choice of 0.40 ammonia concentration would give higher flowrates than 0.35 concentration, although the effective efficiencies are higher for the 0.35 case. If we increase the concentration further to 0.5, the cooling output almost vanishes as seen in the Table 3.2. Therefore, the experimental study was targeted to use the strong solution concentration of 0.40.

3.4 Vapor Concentration

In this section, the parametric study of the previous section is extended to understand the effect of different boiler exit configurations and absorber temperature on vapor produc-

www.manaraa.com

tion, net work, and cooling output. The theoretical simulations are based on the ideal cycle, which is shown in Fig. 3.1. Rectifier exit temperature, which was constant in the previous section, is controlled by the vapor concentration that leaves the rectifier. The effects of rectifier and superheater on the cycle performance are investigated for three cases as described in Table 3.3. In the first case (R), the ammonia vapor leaves the boiler and goes to the rectifier and the ammonia mass concentration is increased by providing cooling. Then the vapor expands through the turbine. A superheater is included for the second case (R+S), in which the ammonia vapor that leaves the rectifier is superheated to 125 °C as the same heat source is used for the boiler and the superheater . The final case is the base case (B), in which no superheater or rectifier is used, so that the ammonia vapor goes directly from the boiler to the expander without being rectified or superheated.

The simulations are also extended to determine the performance of the cycle at different heat source temperatures, over a range of 90 °C to 170 °C. A range of technically sound isentropic turbine efficiencies are assumed regardless of the type of the expander, and their impact on the cycle efficiency is illustrated with the results. In addition, the turbine exit quality is shown with respect to the pressure ratio and for different boiler exit cases.

Several assumptions used in the previous section are changed: The absorber temperature is decreased to 10 °C to find out the theoretical limits of the cycle outputs. In addition, the absorber pressure, which is 2.0 bar, is kept close to the experimental condition given in the previous section. The absorber concentration, 0.54 kg NH_3/kg solution, is calculated as the saturated liquid concentration at the given absorber pressure and temperature, so that saturated liquid flows through the strong solution pump to eliminate cavitation prob-

www.manaraa.com

lem. Isentropic pump efficiency is increased to 85%, which more common in the industrial applications.

Table 3.3 Rectifier exit scenarios that control the vapor concentration

Case	Rectifier	Superheater	Controlled Parameter	η_t
R	Yes	No	$x_{rectifier} = 0.98, 0.995$	0.5, 0.75, 1.0
R+S	Yes	Yes	$x_{rectifier} = 0.98, 0.995$, $T_{superheater}$=125 °C	0.5, 0.75, 1.0
B	No	No	Saturated vapor condition at the boiler exit	0.5, 0.75, 1.0

The variation of net work, cooling output, effective first law and exergy efficiencies with pressure ratio ($P_{boiler}/P_{absorber}$), isentropic turbine efficiency (η_t) for a heat source temperature of 130 °C are shown in Figures. 3.8-3.9. The maximum theoretical net work and cooling output from the cycle (when η_t=1.0) are approximately 160 kJ/kg solution and 75 kJ/kg solution, respectively. The maximum points of net work output for different boiler exit cases are seen between the pressure ratios of 4 to 8, however the highest cooling output occurs between the pressure ratios of 8 to 19. The third case (B), where the saturated vapor exiting from the boiler goes to the turbine directly, has the highest net work and effective efficiencies.

As shown in Fig. 3.8(b), cooling is not possible for case B except at high pressure ratios of 13-20. The effect of ammonia concentration on the rectifier exit is also illustrated in Figures 3.8-3.9 for two different concentrations. When the saturated vapor is rectified to a concentration of 0.995, the cooling output is substantially higher than for the concentration of 0.98, but the difference is not significant in the net work output. The importance of turbine efficiency is also illustrated in Fig. 3.10. The net work and cooling outputs of the

المنارة للاستشارات
www.manaraa.com

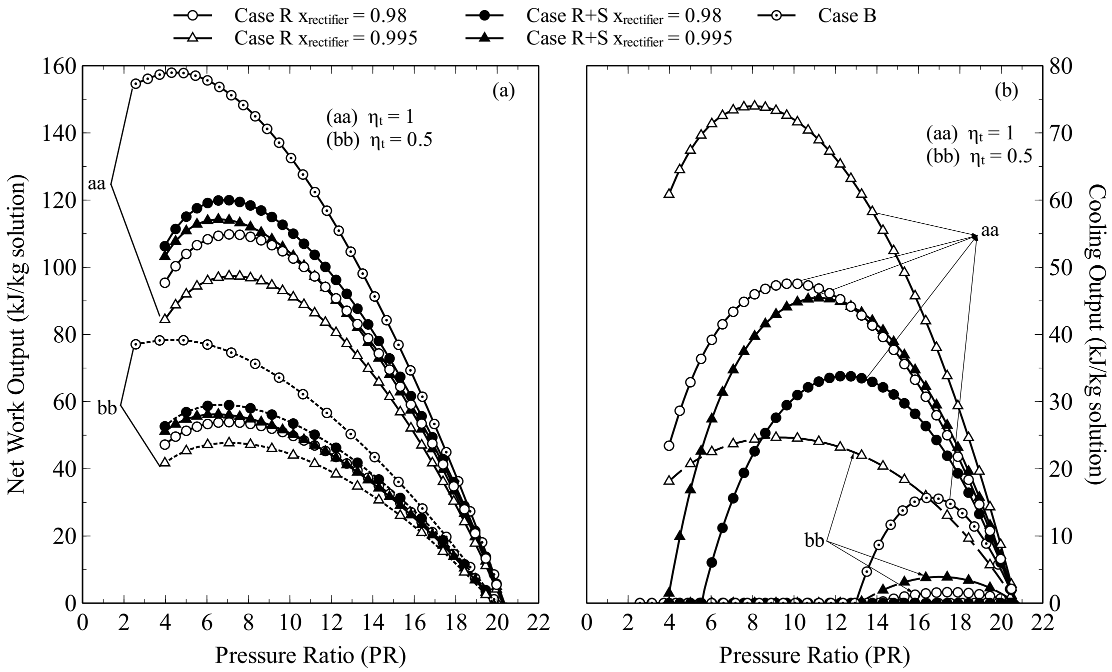

Figure 3.8 Effects of pressure ratio, cycle configurations, and expander isentropic efficiency on the net work and cooling outputs. a) Net work output b) Cooling output

cycle are very sensitive to the turbine performance. For the case (R), a reduction in turbine efficiency from 100% to 50% leads to a reduction in the cooling output by 66%.

3.5 Vapor Production

A comparison of the vapor mass flow rate between the base case and the two cases shows that the mass flow rate is adversely affected by the rectifier process as shown in Fig. 3.10. The practical temperature of the absorber is typically 30-40 °C, so a 30 °C case is also included and compared with the 10 °C case in this section. It is shown in Fig. 3.10 that the vapor mass flow produced by the cycle higher at a lower absorber temperature. At a given absorber temperature, all three cases produce equal vapor flow rate after a certain pressure ratio. The lower effective efficiency results for R and R+S cases show that purifying the

www.manaraa.com

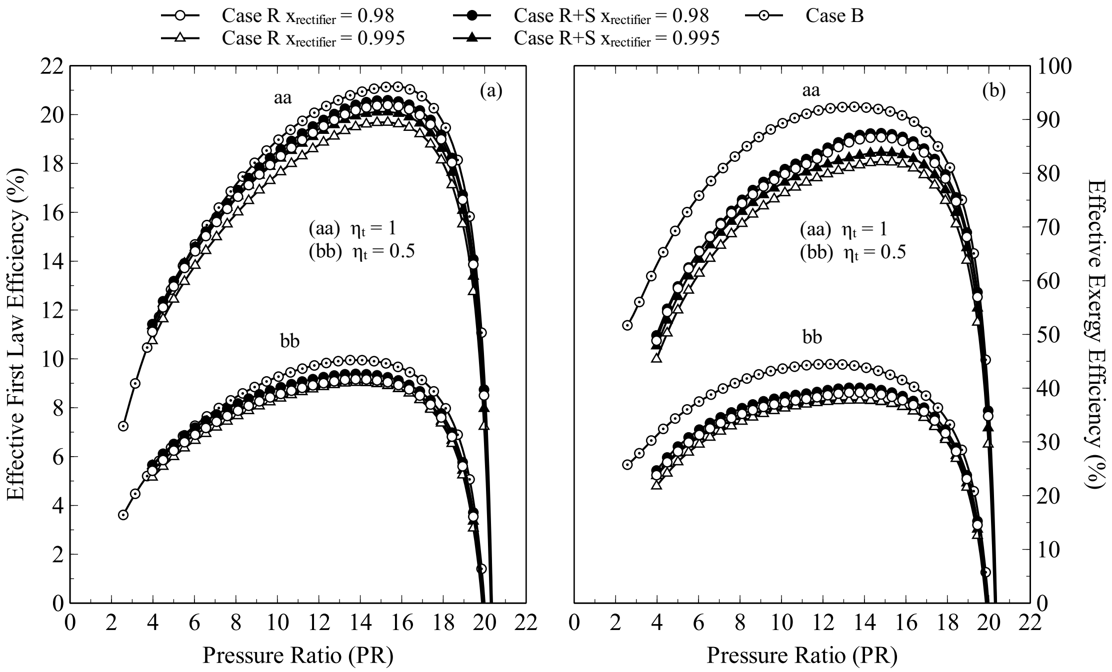

Figure 3.9 Effects of pressure ratio, cycle configurations, and expander isentropic efficiency on the effective first law and exergy efficiency. a) Effective first law efficiency b) Effective exergy efficiency

ammonia vapor increases the cooling output of the cycle significantly, however it does not compensate for the power loss due to rectification.

In practical applications, the pressure ratios will be in the range of 6 to 12, where substantial amount of power and cooling outputs can be obtained as shown in Fig. 3.8. The effective efficiencies at high pressure ratios such as 16-18 are high, as shown in Fig. 3.9, although the cooling and power outputs per unit solution flow rate are low due to the low vapor production. As shown in Fig. 3.10, only 10-15% of the strong solution is vaporized while the rest of the fluid is used for heat recovery.

www.manaraa.com

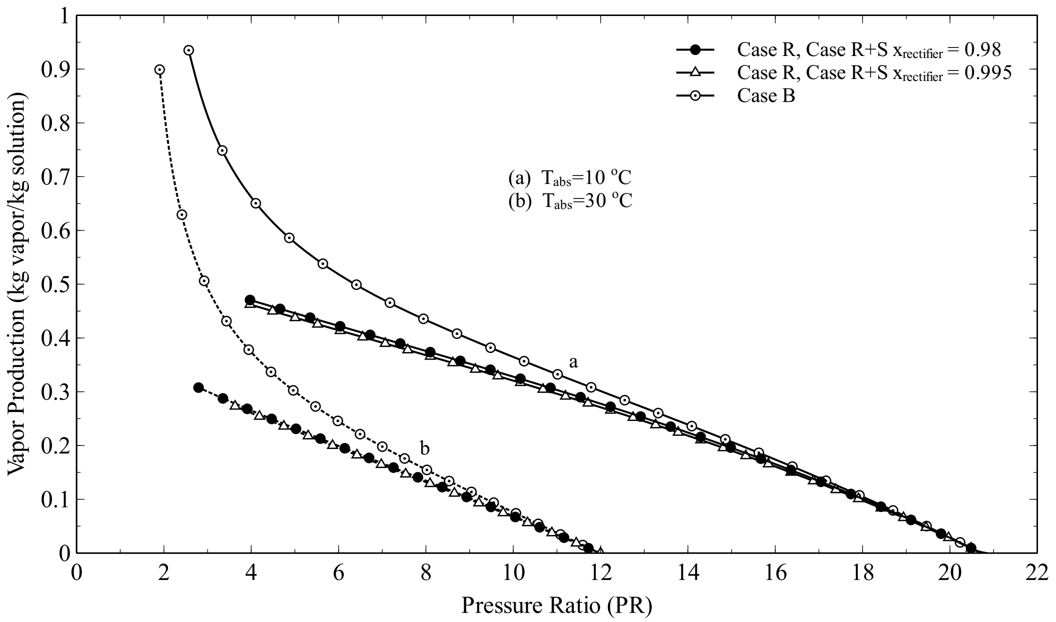

Figure 3.10 Effects of pressure ratio, cycle configurations, and absorber temperature on vapor production

3.6 Absorber Temperature

As discussed in the sections 3.4 and 3.5, purifying the vapor by the rectifier does not provide higher net work output as the vapor mass flow rate decreases. To expand the analysis, an analysis for the absorber temperatures of 10 °C and 30 °C is performed to see the effect of absorber temperature on vapor production. The ammonia mass fractions for the absorber temperatures of 10 °C and 30 °C are 0.54 and 0.37, respectively. When the absorber temperature is increased for the comparative study, the ammonia mass fraction in the basic solution is decreased to keep the absorber exit as saturated liquid. As ammonia mass fraction in the basic solution increases, the absorber saturation pressure also increases. The higher boiling pressure is limited by the corresponding saturation pressure, above which no vapor is produced as shown in Fig. 3.10. The lower pressure extreme is bound by the

المنارة للاستشارات
www.manaraa.com

absorption-condensation pressure. The mass flow rate of the base case (B) is higher than the other cases up to a pressure ratio of 14 for the absorber temperature of 10 °C. Even after this point, the first two cases (R, R+S) have lower efficiencies than the base case (B) as shown in Figures 3.9(a) and 3.9(b) due to the available exergy destruction by the rectifying process.

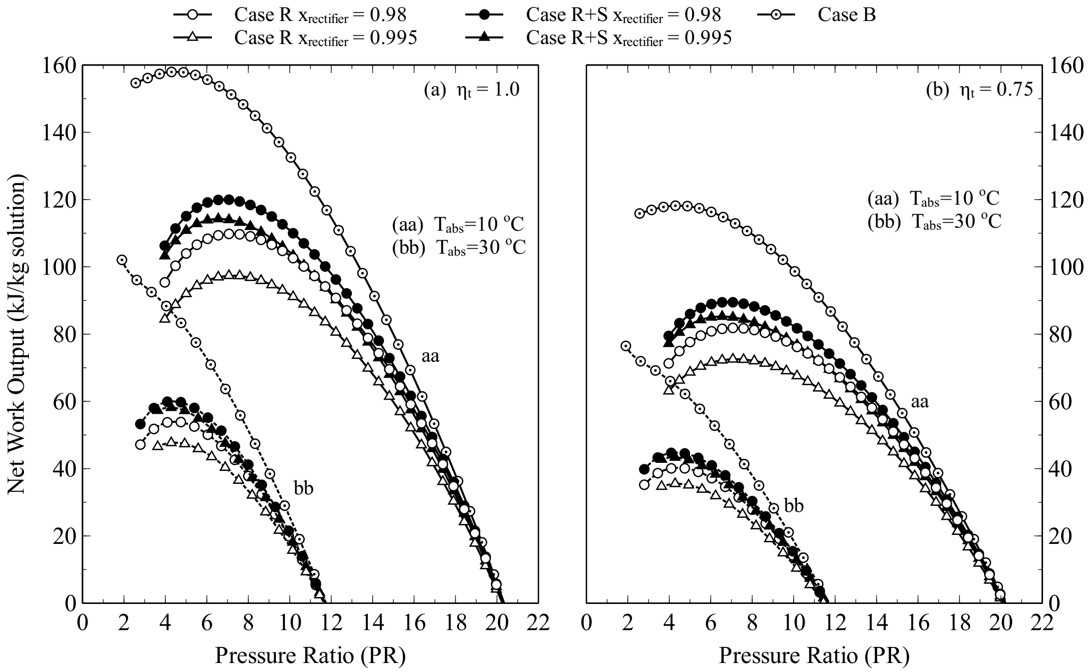

Figure 3.11 Effects of pressure ratio, cycle configurations, absorber temperature and expander isentropic efficiency on net work output. a) Turbine efficiency of 100% b) Turbine efficiency of 75%

The effect of absorber temperature on the cycle output is shown in Figures 3.11 and 3.14. As shown previously in Fig. 3.10, the vapor mass flow rate decreases as the absorber temperature increases. Therefore, the net work and cooling outputs are unfavorably affected as shown in Figures 3.11-3.12. As demonstrated in Figure 3.11(a), increasing the absorber temperature from 10 °C to 30 °C decreases the maximum net work by approx-

المنارة للاستشارات
www.manaraa.com

imately 35%. The same temperature increase has more significant effect on the cooling output, decreasing it approximately 53% as shown in Figure 3.12(a). As expected, a decrease in the turbine efficiency adversely affects the cycle output as illustrated in Figures 3.11(b) and 3.12(b).

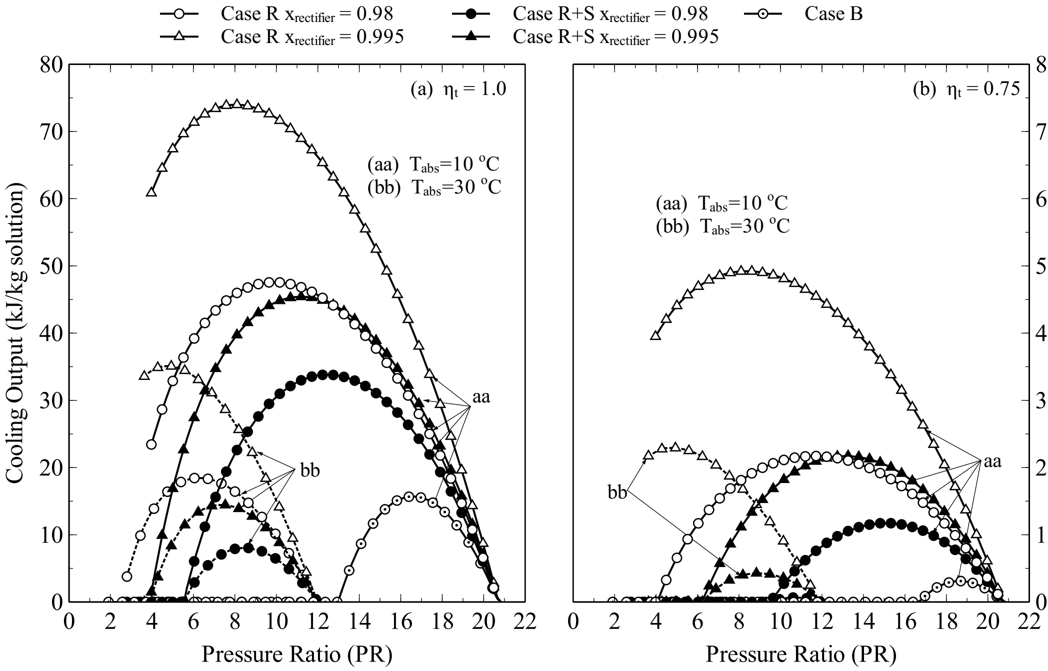

Figure 3.12 Effects of pressure ratio, cycle configurations, absorber temperature and expander isentropic efficiency on the cooling output. a) Turbine efficiency of 100% b) Turbine efficiency of 75%

The efficiency of the turbine is crucial to the cycle performance especially for the cooling output. When the turbine efficiency is 75%, the cycle cannot produce cooling for the cases (R and $x_{rectifier} = 0.98$), (R+S and $x_{rectifier} = 0.98$) and (B) cases at 30 °C absorber temperature as shown in Figure 3.12(b). As the cycle net work and cooling outputs decrease by increasing the absorber temperature, the effective efficiencies also decrease as shown in Figures 3.13-3.14. As the absorber temperature is increased from 10 °C to 30 °C

المنارة للاستشارات
www.manaraa.com

the maximum obtainable effective first law efficiency decreases from 21% to 16%. It must be pointed out that the pressure ratios for these maxima are not the same (the pressure ratios are 15.5 and 9 for 10 °C and 30 °C, respectively). A similar result is seen for the maximum effective exergy efficiency, which goes down from 92% to 65% as the absorber temperature goes up from 10 °C to 30 °C. The corresponding maximum effective first law and exergy efficiencies for a turbine efficiency of 75% are approximately 15% and 67% respectively for a 10 °C absorber temperature, which go down to 12% and 45% respectively for a 30 °C absorber temperature as shown in Figures 3.13(b) and 3.14(b).

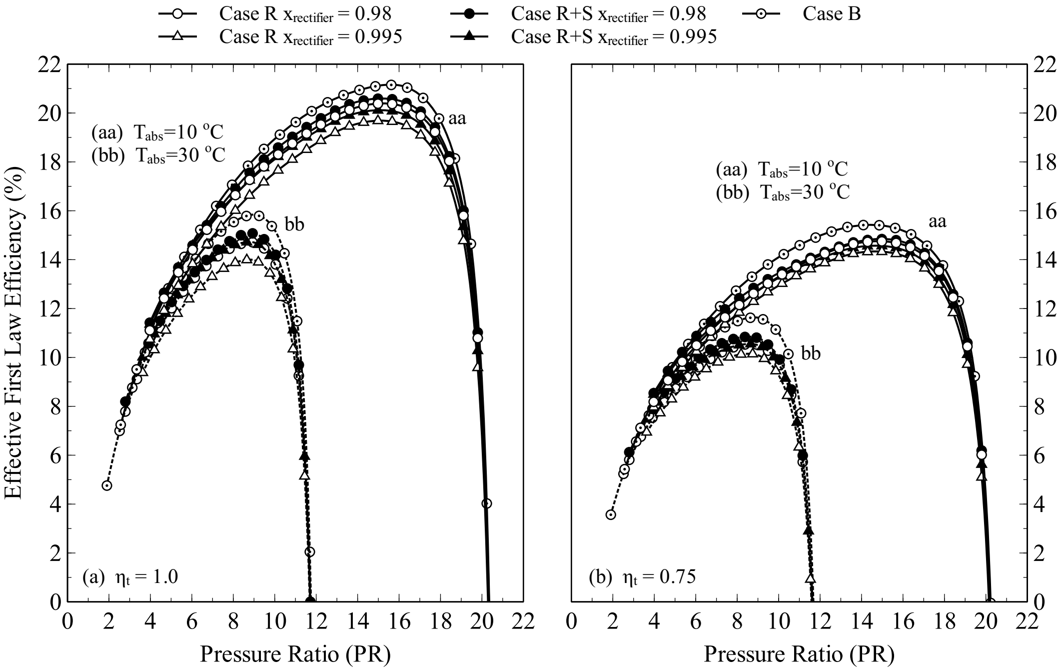

Figure 3.13 Effects of pressure ratio, cycle configurations, absorber temperature and expander isentropic efficiency on effective first law efficiency. a) Turbine efficiency of 100% b) Turbine efficiency of 75%

The absorber temperatures in the experimental study of Kalina cycle [34] and the theoretical work by Xu et al. [96] were 15 °C and 10 °C, respectively. Therefore, an absorber

www.manaraa.com

temperature of 10 °C is used in this study in order to be able to compare the maximum theoretical performance with these studies. However, a 10 °C absorber temperature may not be practical except at special locations and times of the year [105].

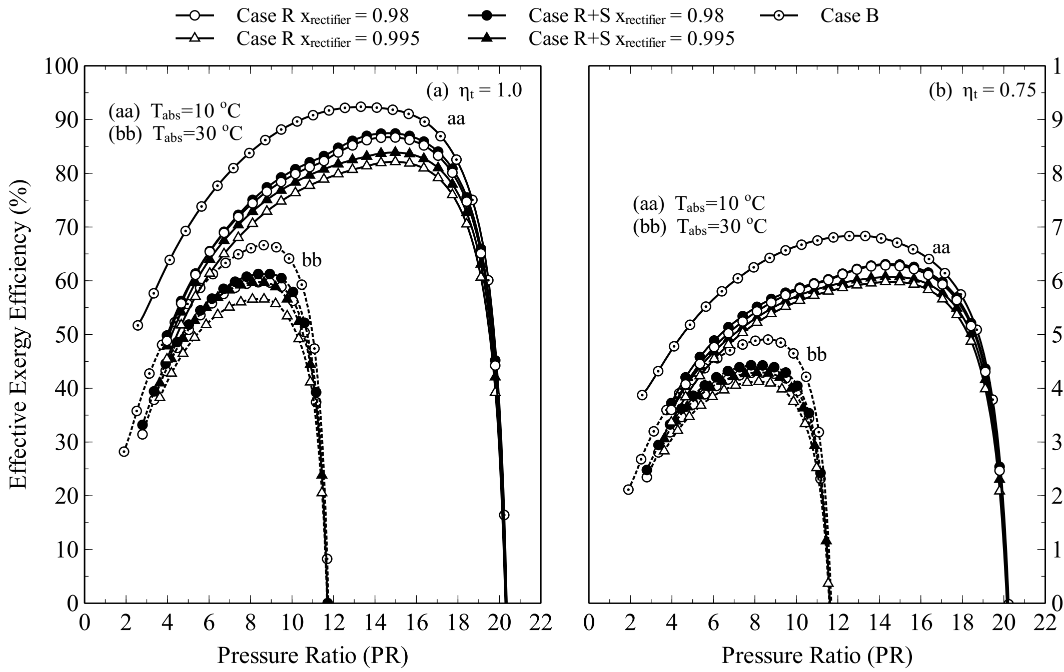

Figure 3.14 Effects of pressure ratio, cycle configurations, absorber temperature and expander isentropic efficiency on effective exergy efficiency. a) Turbine efficiency of 100% b) Turbine efficiency of 75%

3.7 Turbine Exit Quality

The turbine exit quality is another important parameter that should be taken into account as the presence of liquid droplets in the turbine can cause blade damage and decrease the thermal efficiency of the cycle. The quality of the exit stream from the turbine is shown in Figure 3.15 for 30 °C absorber temperature case. An ideal turbine efficiency of 100% is used in the analysis since maximum wetness is obtained with an ideal expansion process. At 30 °C absorber temperature, the first case (R) with a higher ammonia concentration of

www.manaraa.com

0.995 could cause wetness problems as the quality decreases to less than 90% for a pressure ratio greater than 10.

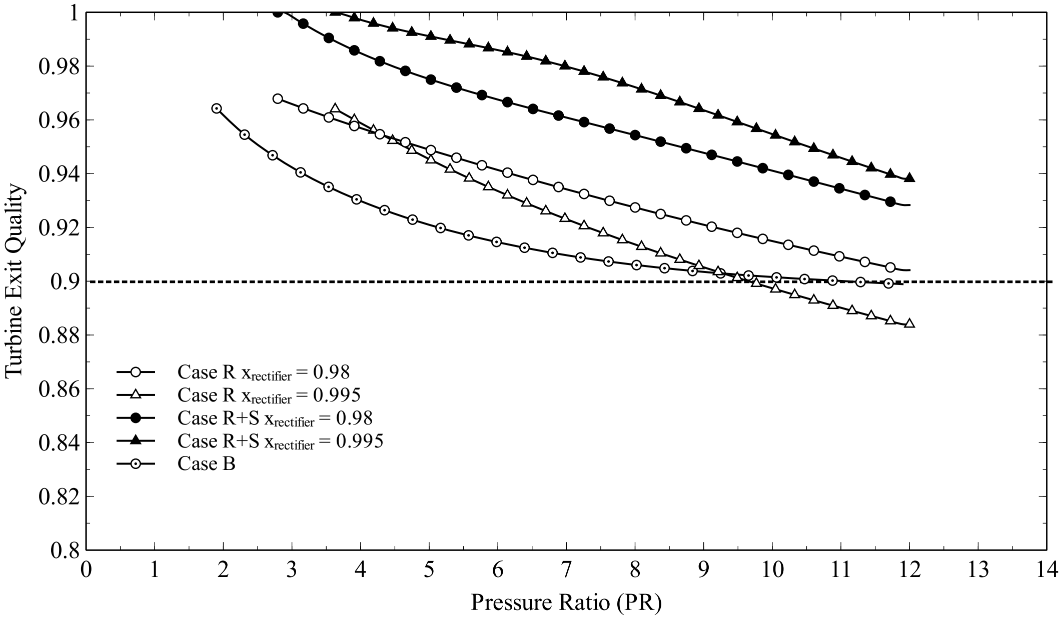

Figure 3.15 Effects of pressure ratio and cycle configurations on turbine exit quality

3.8 Heat Source Temperature

The heat source temperature is varied for a range of 90-170 °C to find out the effect on the cycle performance as shown in Fig. 3.16. As discussed in the previous section, in order to assume a practical absorber temperature, a 30 °C absorber temperature is selected for this study. Since the base case (Case B) produces the highest efficiencies as discussed before, the effect of heat source temperature is studied for the base case only. The maximum effective first law efficiency is 20% when the heat source temperature is 170 °C. The effective first law efficiency is in the range of 4-7.5%, 7-15%, and 10-20%, for turbine efficiencies of 50%, 75%, and 100%, respectively. The effective exergy efficiency is in the

www.manaraa.com

range of 28-35%, 42-53%, and 58-72%, for turbine efficiencies of 50%, 75%, and 100%, respectively. The effective first law and exergy efficiencies increase linearly with the heat source temperature.

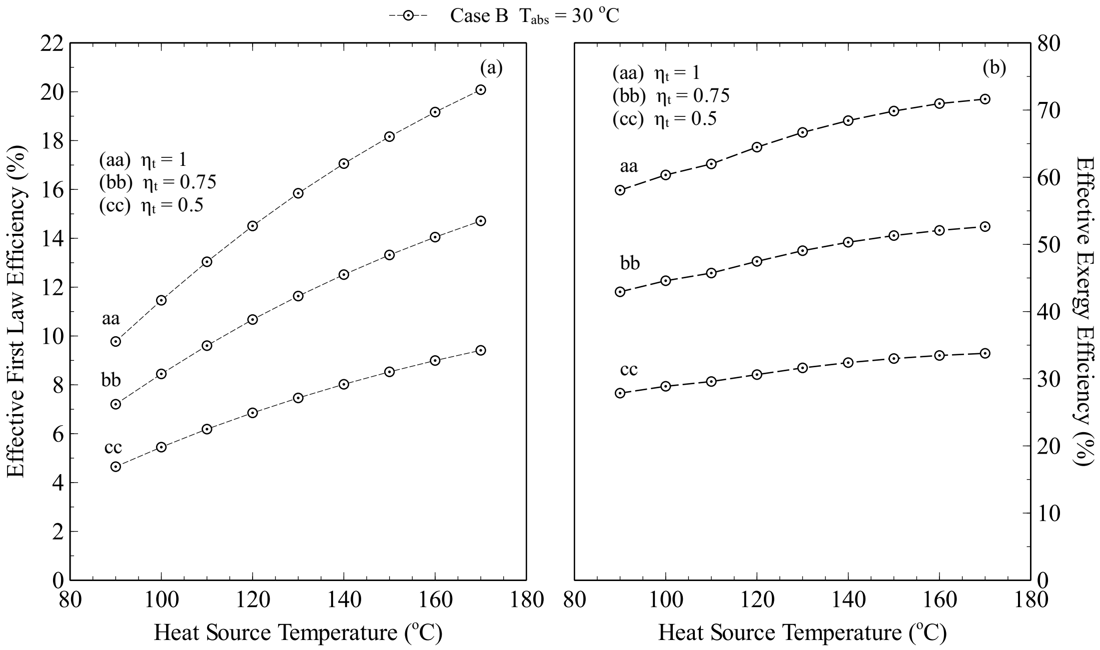

Figure 3.16 Effects of heat source temperature and expander isentropic efficiency on cycle efficiencies. a) Effective first law efficiency b) Effective exergy efficiency

3.9 Optimization Study

In this section, the cycle configuration shown in Fig. 3.2 is used to search the maximum outputs of the Goswami cycle for low-grade to mid-grade heat sources and to find out the operational limits of the Goswami cycle for a broader range of parameters. In the previous section, Chemcad was used to perform the theoretical study to show the effect of operating parameters, however due to the thermodynamic property limitation in the software, boiler temperature was limited by 170 °C. Therefore, a new computational tool is developed which uses previously developed thermodynamic property method by Xu and

المنارة للاستشارات
www.manaraa.com

Goswami [106]. The details of thermodynamic properties and computational tool are given in Appendices A and B, respectively. This tool is also required to analyze the experimental data and calculate the performance of the experimental cycle. Cycle parameters that are updated for the optimization study are given in Table 3.4, other parameters that are not mentioned in the table are given in Table 3.1. As different turbine efficiency values are studied in the previous sections, a fixed 85% turbine efficiency is assumed in this section, this value can be realized practically when the system size output is scaled up to several MW.

Initially, 85 °C boiler temperature case is aimed to provide the basis for the experimental work, which targeted the same boiler temperature. The maximum values of cycle output and operational limits of the experimental study are found by varying the strong solution concentration and boiler pressure. Then, boiler temperature was varied between 100 °C to 350 °C to find out the cycle performance for low-grade to mid-grade heat sources.

Table 3.4 Cycle parameters assumed for the optimization study

Parameter	Value	Units
Pinch Point	10	°C
Minimum turbine exit vapor quality	90%	
Recovery heat exchanger effectiveness ε	85%	
Isentropic turbine efficiency η_t	85%	

The following assumptions are used in the analysis:

- The system low pressure was dictated by the basic solution concentration (x_{strong}) and the absorption temperature of 35 °C.

www.manaraa.com

- The boiling conditions were completely specified, i.e. boiling temperature, pressure, and basic solution concentration are provided as inputs.
- Effectiveness value was used for the heat recovery heat exchanger, while pinch point limitation was 10 °C for the boiler, superheater, and refrigeration heat exchangers.
- Entropy generation for the boiler heat exchanger is checked during the simulations, whenever the entropy generation is less than zero, the heat source mass flow rate is increased to ensure that entropy generation in the boiler heat exchanger is greater than zero.
- The degree of rectification was limited by either the specified rectifier exit temperature or an ammonia mass fraction of 0.999, whichever was encountered first.
- The quantity of cooling produced (if any) was calculated as the energy needed to heat the expander exhaust from the exhaust temperature to 15 °C.
- Water was used as the chilled fluid in the refrigeration heat exchanger.
- Superheating is not considered in this simulation.
- Pressure drops were neglected.

3.10 Low-Grade Heat Source Analysis

The maximum points for net work, effective first law and effective exergy efficiencies with respect to the strong solution concentration (x_{strong}) for a boiler temperature of 85 °C are shown in Fig. 3.17. The temperature of the saturated vapor leaving the separator

www.manaraa.com

is not changed; rectifier and superheater are not active in this analysis. The ammonia concentration in the strong solution takes an important role as it defines the mass fraction of the volatile component, which is ammonia for this study, however as seen in Fig. 3.17, the maximum values of effective efficiencies do not change significantly with the strong solution concentration. The effective first law efficiency is approximately 7.5% for the whole range and the effective exergy efficiency changes from 38% to 45%. The maximum work output is obtained at the highest concentration value of 0.8; the reason is explained later in this section. If the strong solution concentration is chosen as 0.4, with a 1 kg/s strong solution mass flow rate, this cycle can produce approximately 13 kW, the effective first law and exergy efficiencies are 7% and 38%, respectively.

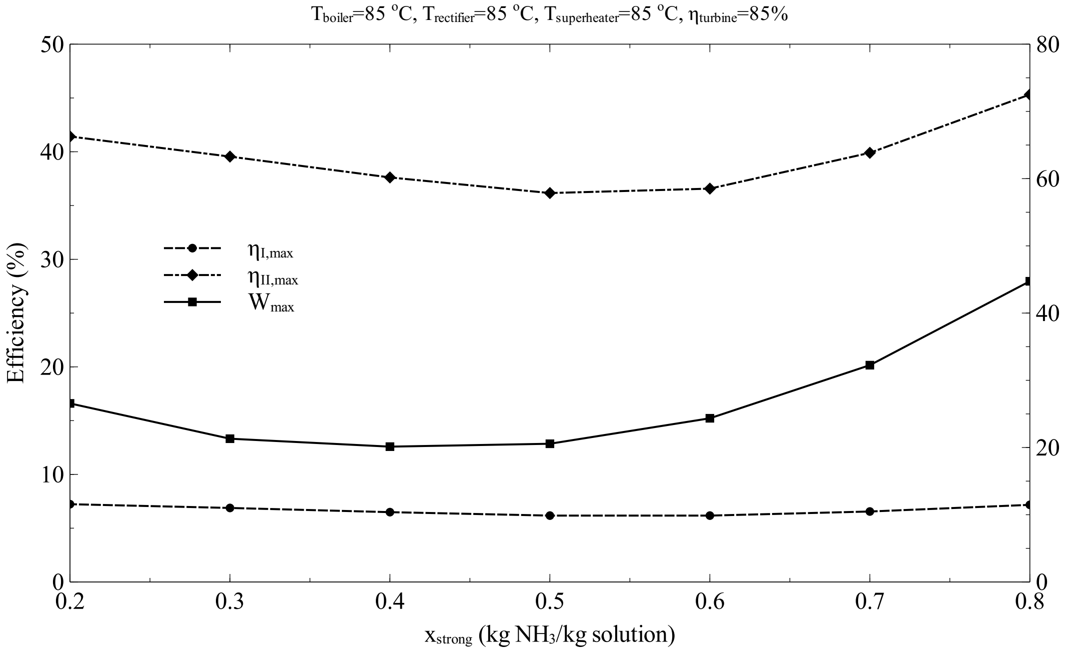

Figure 3.17 Effective first law and exergy and work output of the Goswami cycle at a boiler temperature of 85 °C

المنارة للاستشارات
www.manaraa.com

For the maximum values of the cycle efficiencies and net work output, the vapor concentrations for each case are plotted in Fig. 3.18. The vapor concentration values for maximum net work output are lower than the values for maximum cycle efficiencies. In order to produce more work, more vapor should be produced, and this requires boiling of water component as well. The vapor concentration values for maximum effective first law and exergy efficiencies are very close to each other. It is shown in Fig. 3.18 that after a strong solution concentration of 0.5, the vapor concentration is almost constant between 0.95 and 0.98. As the concentration in the strong solution increases, the vapor concentration at the turbine inlet also increases. The dew and bubble pressures increases when the strong solution concentration increases, therefore the boiler pressure also increases. The higher the pressure in the boiler, the lower the vaporization of water component, which yields high vapor concentration.

The results for the ratio of vapor mass flow rate to strong solution flow rate for the maximum values of cycle efficiencies and net work output are shown in Fig. 3.19. The pressure ratio across the turbine is almost constant at 2.0 for maximum work output, which is shown in Fig 3.20; therefore, the vapor flow rate should be maximized in order to maximize work output. As shown in Fig. 3.19, the vapor flowrate for maximum net work output varies between 20% and 50%. The mass flowrate ratios for the maximum effective first law and exergy efficiencies are close to each other. The vapor flowrate ratios for the efficiencies vary between 7.5% and 40%. The vapor flowrate ratios for cycle efficiencies increase gradually with increasing strong solution concentration. In order to maximize the cycle efficiencies, the heat transfer irreversibilities across the cycle heat exchanger should

المنارة للاستشارات
www.manaraa.com

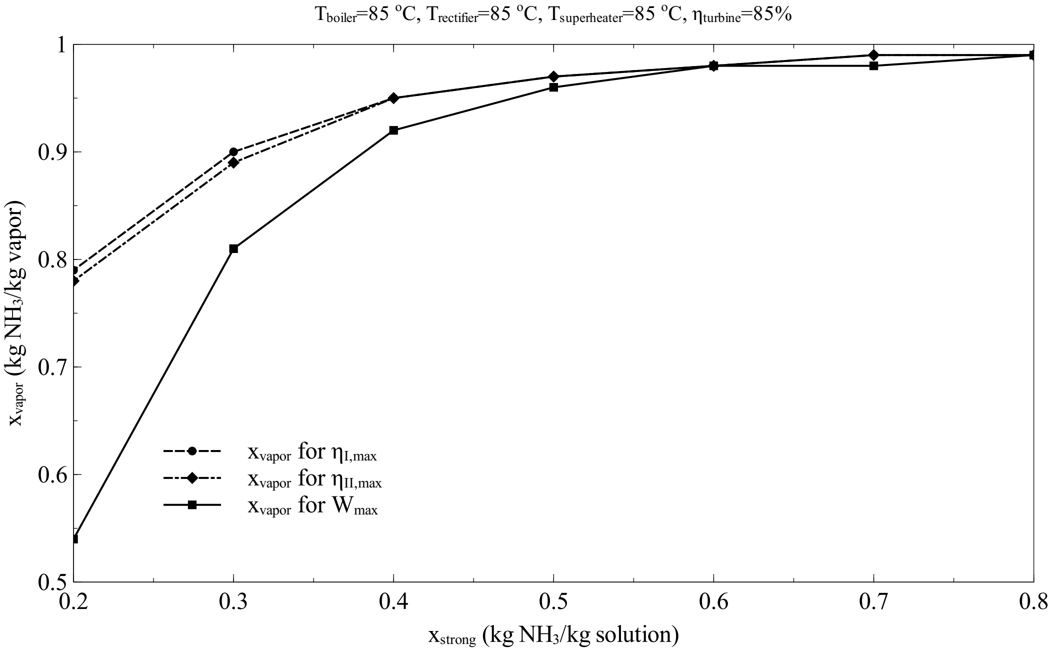

Figure 3.18 Vapor concentration values for the maximum values of effective first law, exergy and work output at a boiler temperature of 85 °C

be minimized, the weak solution flow rate to strong solution mass flow rate for the recovery heat exchanger should be maximized, however it should be mentioned that it is always less than unity.

The pressure ratio of boiler to absorber, which defines the expansion ratio through the turbine, is another important parameter. The pressure ratio of boiler to absorber for each cycle output maximum is shown in Fig. 3.20. If the pressure ratio is increased, the potential of producing more work increases; however, the increase in boiler pressure decreases the vapor flow rate for the Goswami cycle, which hinders the potential of producing more work. The pressure ratio across the turbine is almost constant at around 2.0 for maximum work output as shown in Fig 3.20. The maximum points for the pressure ratio will help the decision of turbine selection and design for the cycle.

المنارة للاستشارات
www.manaraa.com

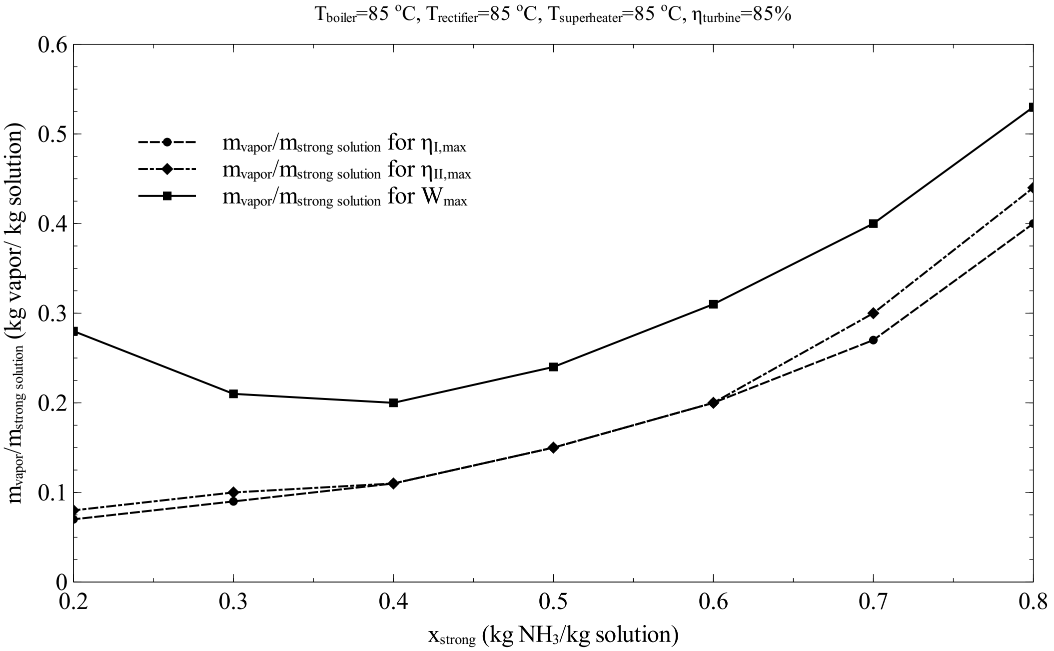

Figure 3.19 Mass fraction values for the maximum values of effective first law, exergy and work output at a boiler temperature of 85 °C

Effective first law efficiency of the Goswami cycle with respect to pressure ratio at the boiler temperature of 85 °C is shown in Fig. 3.22. As seen in the figure, when the strong solution concentration is at the lowest, which is 0.2, the pressure ratio is limited in the range of 1 to 5.5. The maximum effective first law efficiency decreases with increasing the concentration until the strong solution concentration reaches 0.6, and then it starts to increase from this point. The maximum effective first law efficiency is approximately 7%, which can be reached at a strong solution concentration of 0.2 at a pressure ratio of 4.5 or at a strong solution concentration of 0.8 at a pressure ratio of 2.75. However, as shown in Fig. 3.21, the boiler pressures are approximately 2.5 and 27.5 bars for strong solution concentrations of 0.2 and 0.8, respectively. Although the first law efficiencies around 7% seem low, they compare well with the ideal Lorenz cycle efficiency of 7.2% with finite heat

www.manaraa.com

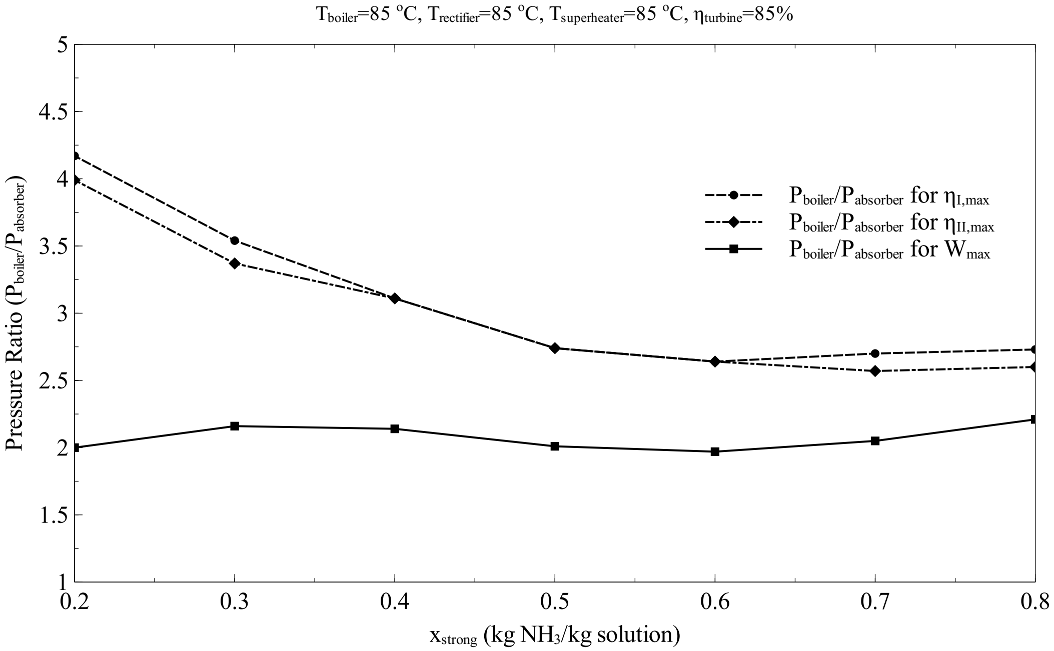

Figure 3.20 Pressure ratios ($P_{boiler}/P_{absorber}$) for the maximum values of effective first law, exergy and work output at a boiler temperature of 85 °C

sources for the same boiler and absorber temperatures for maximum power [37]. It can be concluded that low pressure conditions will decrease the cost of the equipment used in the cycle, so the low strong solution concentration case is more favorable. Effective exergy efficiency of the Goswami cycle with respect to pressure ratio at a boiler temperature of 85 °C is shown in Fig. 3.23. The maximum exergy efficiency varies between 35% and 45%. Similar to the effective first law efficiency, the maximum exergy efficiencies are seen at the strong solution concentration of 0.2 and 0.8.

The variation of net work with the pressure ratio ($P_{boiler}/P_{absorber}$) is shown in Fig. 3.24. The limiting pressures of the cycle are evidenced when net work outputs are zero as shown in the figure. The net work from the cycle is maximum at an ammonia mass fraction of 0.8.

المنارة للاستشارات
www.manaraa.com

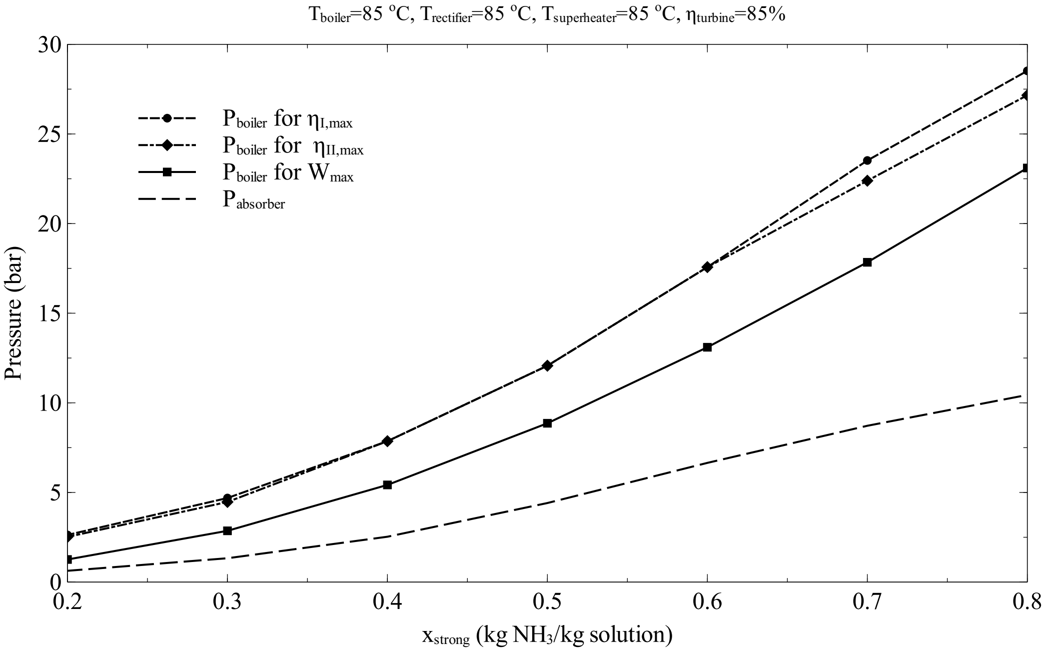

Figure 3.21 Boiler pressures for the maximum values of effective first law, exergy and work output at a boiler temperature of 85 °C

In order to evaluate the cooling output performance of the cycle, the rectifier exit temperature is decreased from 75 °C to 35 °C. As shown in Fig. 3.26, cooling output increases when the rectifier exit temperature decreases. Maximum cooling output occurs at ammonia mass concentration of 0.5 and 0.6; as compared to the net work output (0.8), the cooling output from the cycle is not possible above the strong solution concentration of 0.7. As stated above the pressure ratio decreases when the ammonia concentration increases, which leads to higher turbine exhaust temperatures due to the lower pressure ratios across the turbine. This explains why cooling output decreases and not possible at higher ammonia concentrations. As seen in Fig. 3.25, the effective first law and exergy efficiencies decrease as the rectification temperature is reduced. This shows that the cycle performance sacrifices in order to produce cooling. The decreases in efficiency terms are more signifi-

المنارة للاستشارات
www.manaraa.com

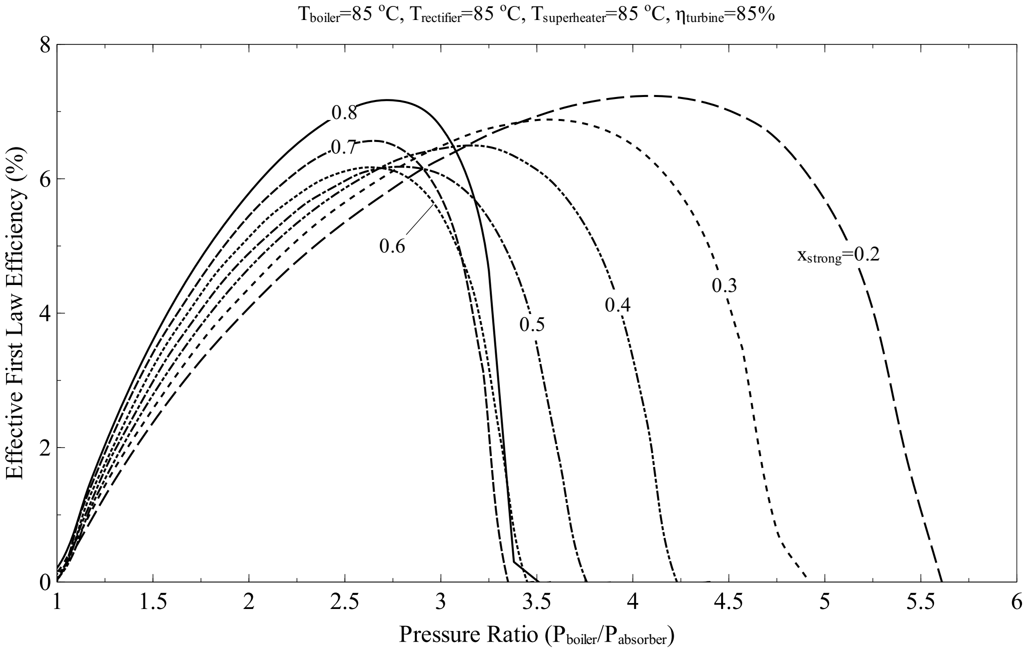

Figure 3.22 Effective first law efficiency of the Goswami cycle at a boiler temperature of 85 °C.

cant after a strong solution concentration of 0.5. As discussed above, purifying the vapor by the rectifier does not provide higher net work output as the vapor mass flow rate decreases.

3.11 Mid-Grade Heat Source Analysis

This section is focused on finding out the maximum performance of the cycle when it utilizes solar thermal energy or geothermal sources, for this reason the boiling temperature is changed between 100 °C to 350 °C. The cycle parameters for simulation are given in Table 3.4. Since the pinch point temperature is set at 10 °C, this section covers the heat sources between 110 °C to 360 °C. The design variables for the simulations are again boiler pressure, temperature and basic solution concentration while net work output, effective first law and exergy efficiencies are the main three parameters to evaluate the performance of the cycle.

المنارة للاستشارات
www.manaraa.com

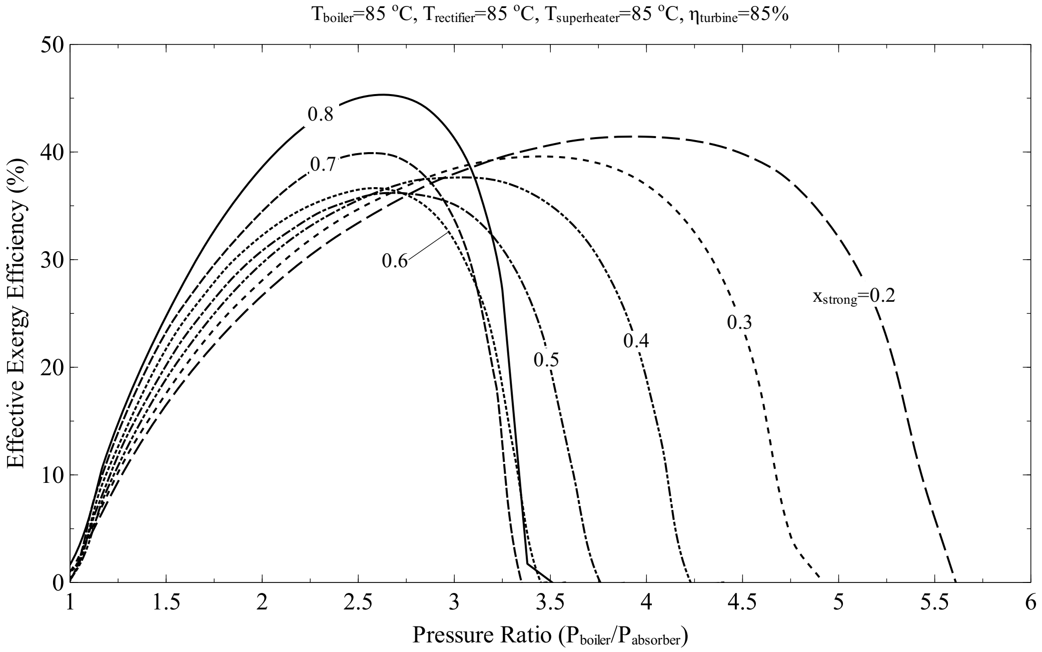

Figure 3.23 Effective exergy efficiency of the Goswami cycle at a boiler temperature of 85 °C

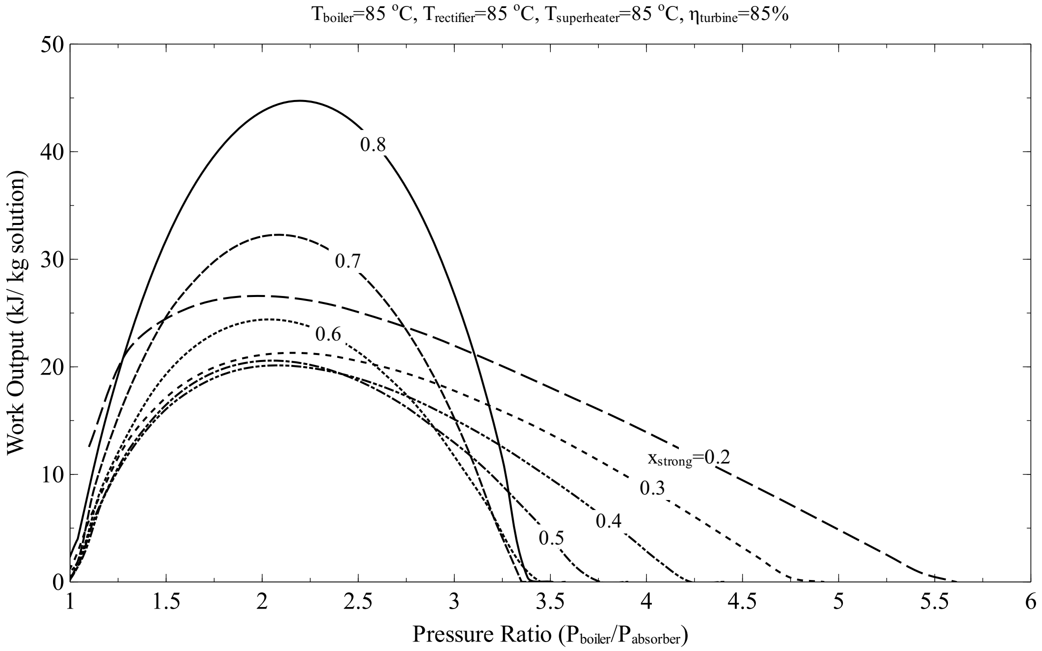

Figure 3.24 Net work output of the Goswami cycle at a boiler temperature of 85 °C

المنارة للاستشارات
www.manaraa.com

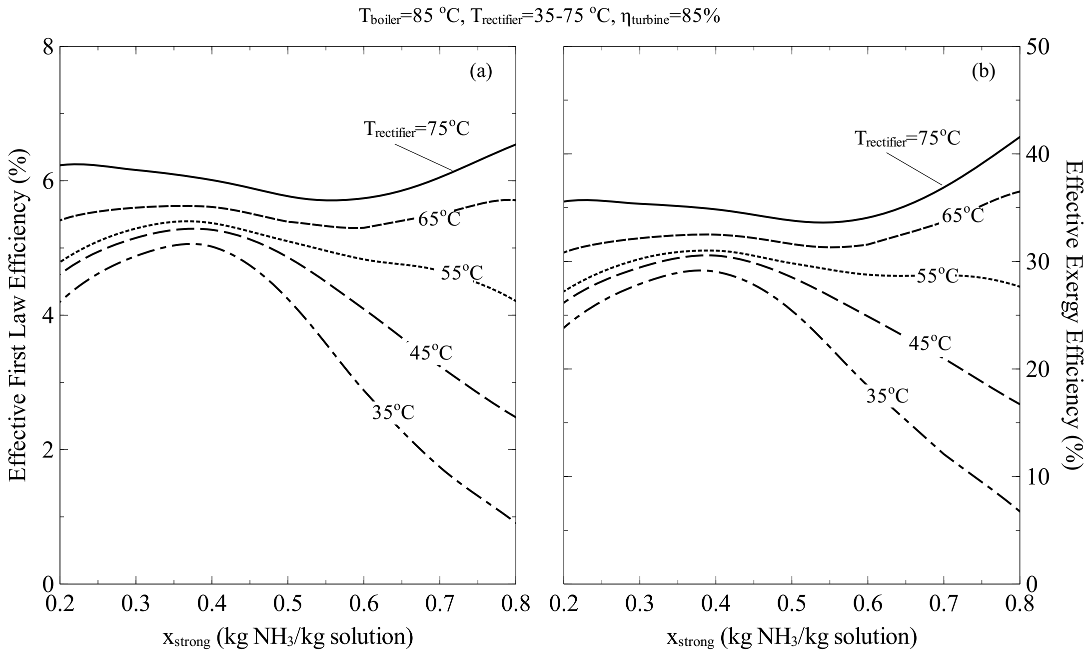

Figure 3.25 Effective first law and exergy efficiency of the Goswami cycle for rectification analysis at a boiler temperature of 85 °C

The simulation process is as follows. Initially, boiler temperature is specified, and then strong solution concentration is varied for this boiler temperature. This step requires special attention above 150 °C of boiler temperature, as strong solution concentration has a certain range in which an ammonia-water mixture can exist. The critical temperature and pressure of the ammonia-water mixture are shown in Fig. 3.27. To give an example, ammonia-water mixture can exist at 250 °C as a saturation mixture if the concentration is less than 0.6736. Therefore, the concentration range for 250 °C was chosen as 0.10 to 0.60 kg NH_3/kg solution. The same principle applies to other boiler temperatures.

Then dew and bubble pressures for the corresponding temperature and concentration are calculated. In order to have a liquid-vapor saturation mixture at the separator, the system high pressure should be adjusted between the dew and bubble pressures. Fig. 3.28

المنارة للاستشارات
www.manaraa.com

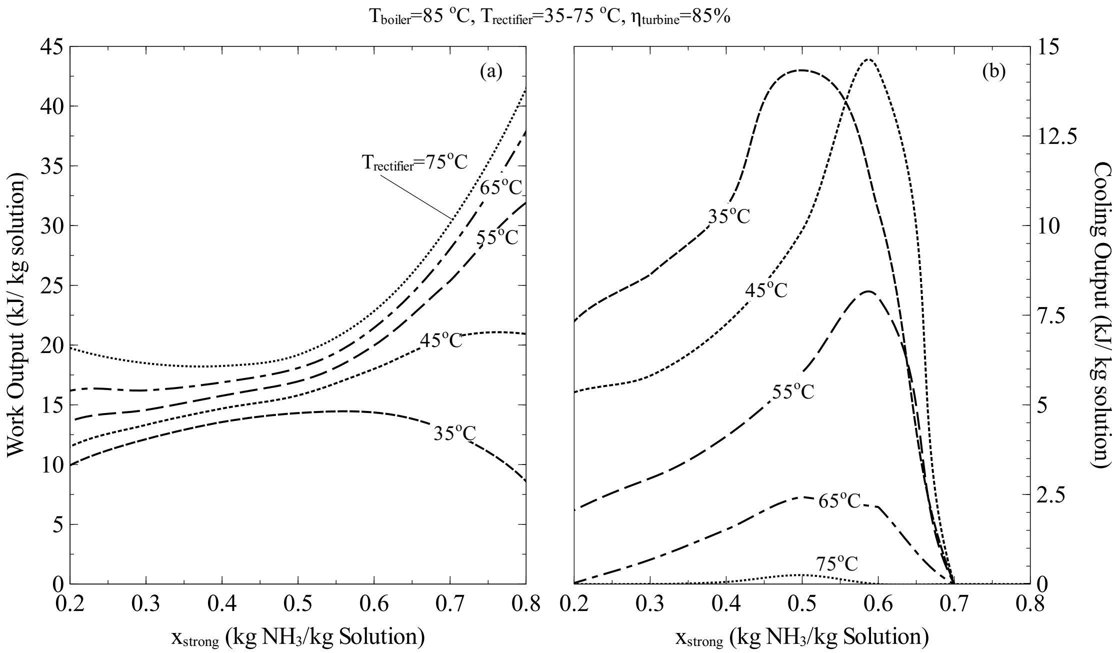

Figure 3.26 Net work and cooling outputs of the Goswami cycle for rectification analysis at a boiler temperature of 85 °C

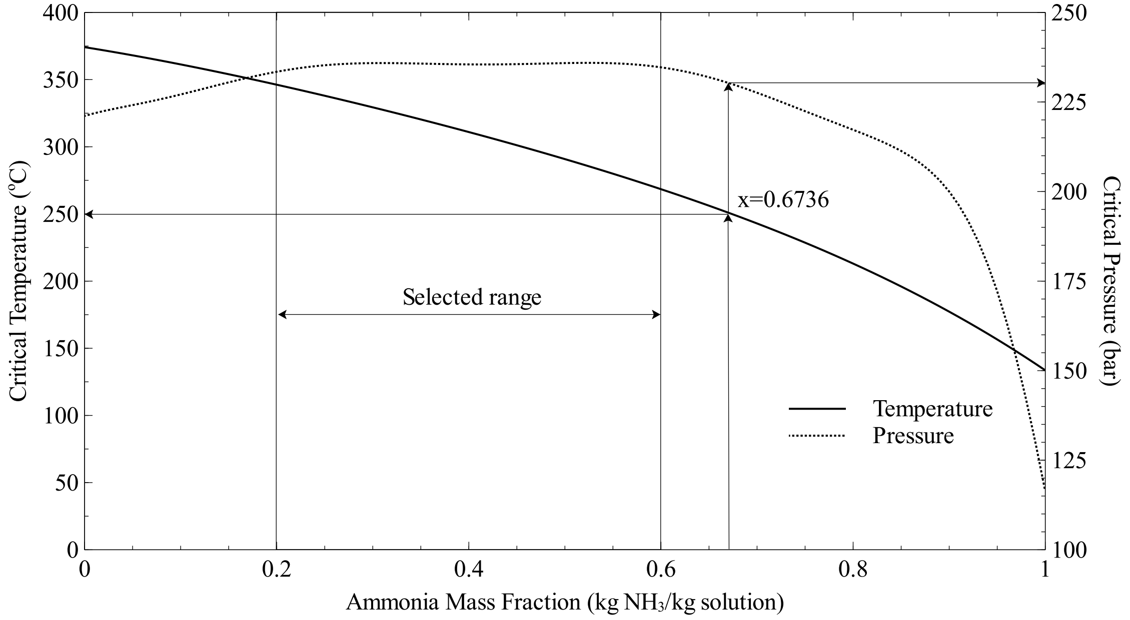

Figure 3.27 Critical temperature and pressure of the ammonia-water mixture

www.manaraa.com

shows the pressure range at the temperature of 250 °C for different ammonia concentrations. Therefore, the pressure range cannot be fixed and should be updated for every boiler temperature and ammonia concentration. If the pressure is higher than the bubble pressure (142.8 bar at 250 °C and 0.4 kg NH_3/kg solution), the solution is in compressed state. If the pressure is lower than the dew pressure (65.4 bar at 250 °C and 0.4 kg NH_3/kg solution) all of the solution is vaporized, which will result in no flow through the weak solution line. In the simulations, a minimum ratio of the weak solution return mass flowrate to strong solution mass flowrate is assumed as 10%. Therefore, the cycle performance is evaluated by increasing the boiler pressure starting from $P_{sat,vapor}$ (dew pressure) to $P_{sat,liquid}$ (bubble pressure). After defining boiler temperature, pressure, and strong solution concentration, the rectifier exit and superheater temperatures are chosen for the simulation. By using the following inputs, P_{boiler}, T_{boiler}, x_{strong}, $T_{rectifier}$, $T_{superheater}$ and the other cycle assumptions given previously in Tables 3.1 and 3.4, the cycle simulation can be performed.

Before the results, it is noteworthy to mention that the turbine exit quality is an important parameter, and it should be taken seriously into account as the presence of liquid droplets in the turbine can cause blade damage and decrease the thermal efficiency of the cycle. Therefore, it is assumed during the simulations that the turbine exit quality cannot be lower than 90%. Simulations showed that for the boiler temperature below 150 °C, the turbine exit quality is always higher than 90%, however, in the case of above 150 °C there are some conditions at which the quality drops to lower values. To eliminate low quality exit conditions, expansion stage is increased and reheaters are included in the simulations. If the turbine exit quality is lower than 90%, a two stage turbine is used. The vapor is

www.manaraa.com

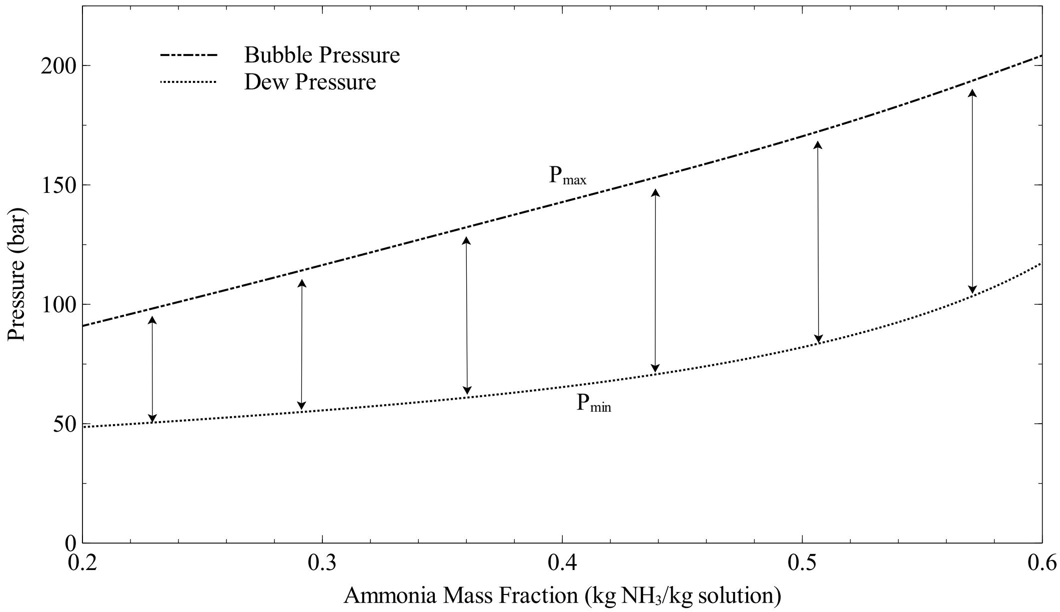

Figure 3.28 Bubble and dew pressure of the ammonia-water mixture at 250 °C

expanded to a 90% quality through the first turbine, and then reheated and sent to second stage. The turbine exit condition is checked again, and the simulation is continued until the turbine exit quality higher than 90% is satisfied. Fig. 3.29 shows the effect of reheating and multi-stage expansion. As seen in the figure, both efficiencies are significantly increased with the use of multi-stage turbines.

In the plots, both single and multi-stage results are shown to compare the values. For the single stage simulations, if the turbine exit quality is less than 90%, the vapor is expanded through the turbine until the turbine exhaust quality reaches 90%, then the exhaust is throttled to the absorber pressure and sent to the absorber.

Net work output comparison of the Goswami cycle with multiple and single turbine stages at boiler temperature of 100-350 °C are shown in Figures 3.30-3.31. The work out-

www.manaraa.com

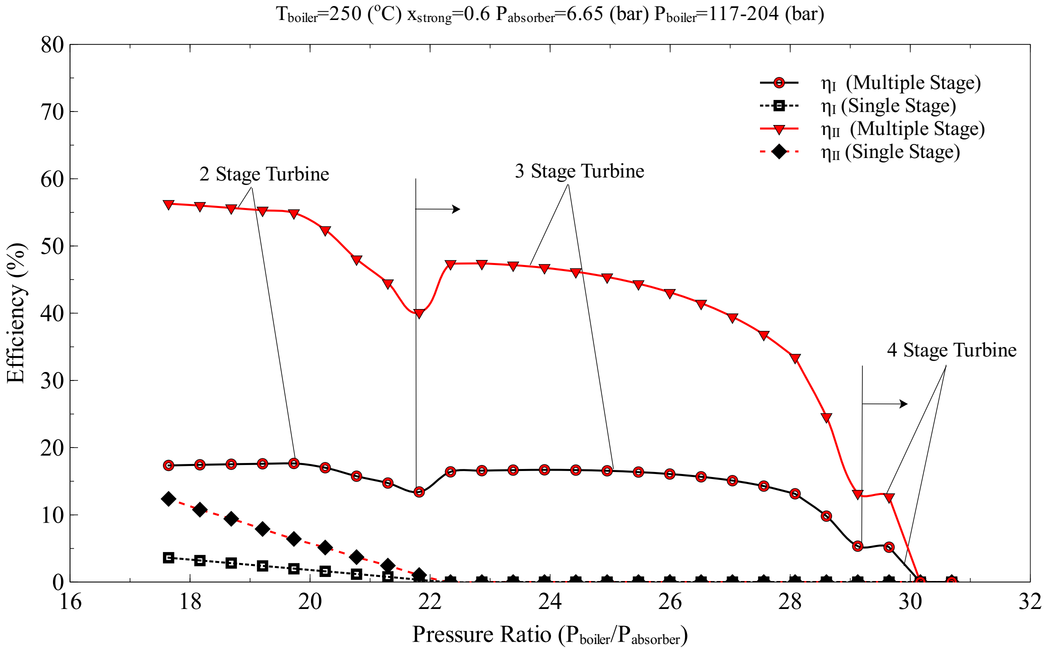

Figure 3.29 Effective first law and exergy efficiencies for single and multi-stage turbines at a boiler temperature of 250 °C

put of the Goswami cycle increases with the heat source temperature for the multi-stage expansion case, however it follows a reverse path for the single stage turbine for the heat source temperatures between 200-350 °C as shown in Fig. 3.31. The effect of using multi stage turbine is critical above heat sources temperature of 175 °C. As the system high pressure is varied between the bubble and dew pressures for the corresponding boiler temperature and strong solution concentration, and maximum work output is chosen. Therefore, each point shown in the figures has a different system high pressure, and the only common operating condition is the absorber temperature, which is 35 °C for all cases.

The maximum net work occurs at the lowest strong solution for the multi-stage expansion. The enthalpy values of the ammonia-water mixtures increases by decreasing the ammonia concentration, in addition the system low pressure is at a minimum (~0.25 bar)

www.manaraa.com

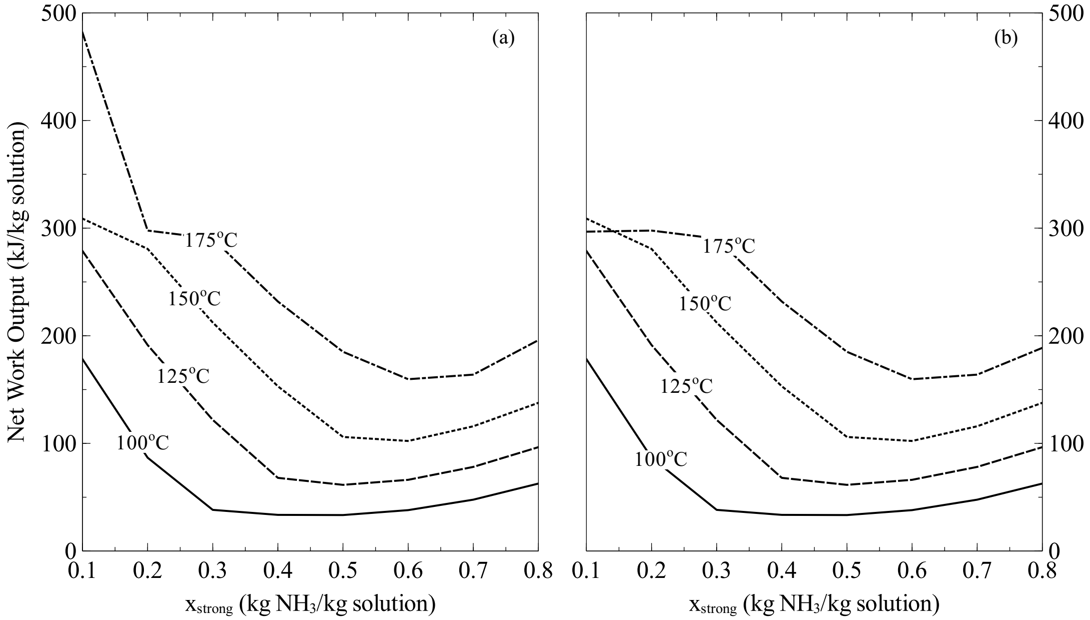

Figure 3.30 Net work output comparison of the Goswami cycle at boiler temperatures of 100-175 °C. a) Multiple Turbine Stages and b) Single Stage Turbine

for the strong solution concentration of 0.1 kg NH_3/kg solution. Boiler pressure values for the maximum work output for the boiler temperatures of 100-350 °C are shown in Fig. 3.32. The minimum pressure required at the boiler is 50 bar for 250 °C and higher, however the maximum boiler pressure value for the heat source temperature of 150 °C and lower is approximately 50 bar.

The number of stage used for the multi-stage turbine simulations are given in Table 3.5. The first additional stage is required at the boiler temperature of 150 °C and the strong solution of 0.1 kg NH_3/kg solution. For the low ammonia concentration cases, the turbine exhaust is more prone to wetness because of high water content; this requires additional reheater and turbine stage when the turbine exhaust is still at higher pressure than the system low pressure. It is seen from Fig. 3.30 that for the boiler temperature of 175

www.manaraa.com

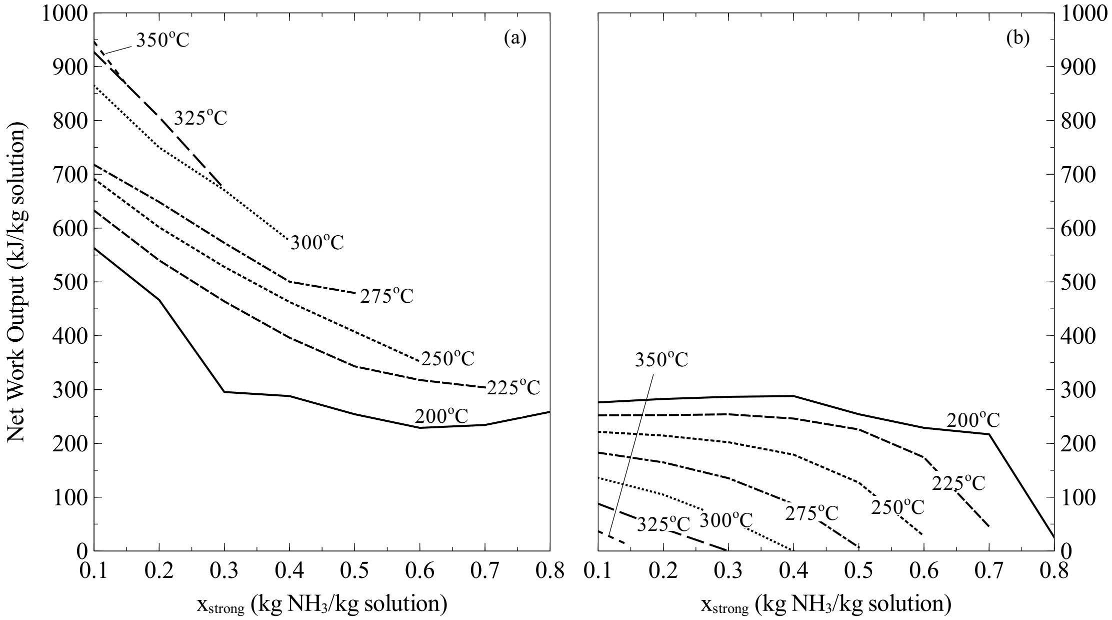

Figure 3.31 Net work output comparison of the Goswami cycle at boiler temperatures of 200-300 °C. a) Multiple Turbine Stages and b) Single Stage Turbine

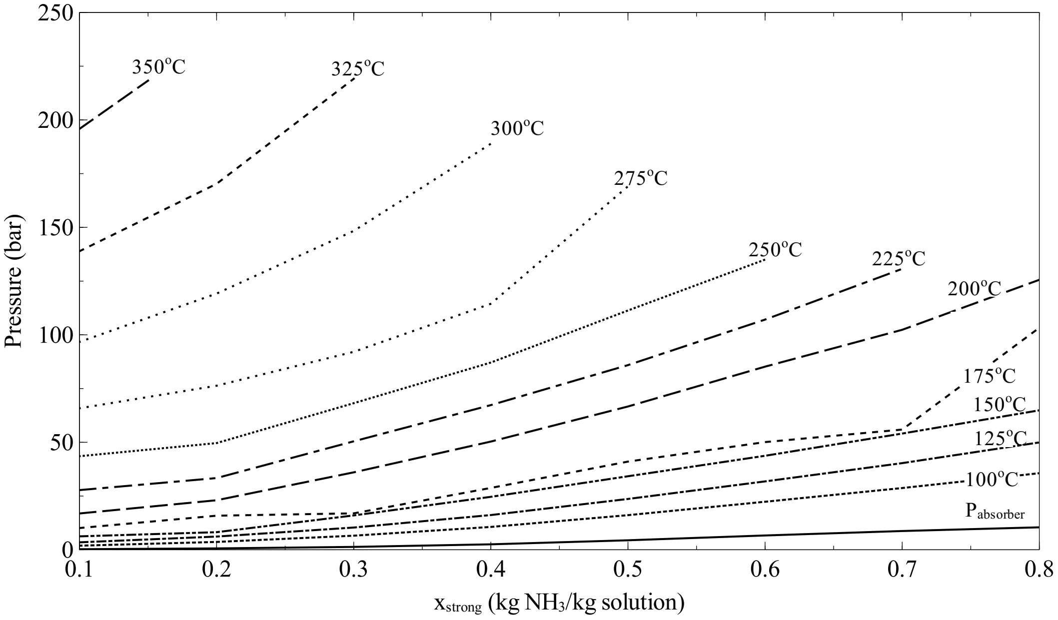

Figure 3.32 Boiler pressure values at boiler temperatures of 100-300 °C

المنارة للاستشارات
www.manaraa.com

Table 3.5 The number of stages used for multi-stage turbine case

	x (kg NH_3/kg solution)							
T (°C)	0.1	0.2	0.3	0.4	0.5	0.6	0.7	0.8
100	1	1	1	1	1	1	1	1
125	1	1	1	1	1	1	1	1
150	2	1	1	1	1	1	1	1
175	2	2	1	1	1	1	1	1
200	2	2	2	2	1	1	1	1
225	2	2	2	2	2	2	2	
250	2	2	2	2	2	2		
275	2	2	2	2	3			
300	3	3	3	3				
325	3	3	3					
350	3							

°C and strong solution concentration of 0.1 kg NH_3/kg solution, the work output increases significantly for the two stage case compared to single stage case.

Effective first law efficiency comparison of the Goswami cycle with multiple and single turbine stages at the boiler temperatures of 100-350 °C is shown in Figures 3.33-3.34. The maximum effective first law efficiency is between 18-31% for the heat source temperature of 250 °C and 350 °C. If the concentration value of 0.1 is chosen, the maximum effective first law efficiency values are in 23-31% range. It is also seen in the Fig. 3.33 that single and double stage results are similar for heat source temperatures up to 150 °C. However, the effective first law efficiency values for multiple stage case is significantly higher than the single stage case for heat source temperature above 150 °C, as shown in Fig. 3.34. Regarding the sensitivity of the effective first law efficiency with ammonia concentration, the results showed no significant changes with the strong solution concentration.

The effective first law efficiency increases when the heat source temperature increases until the boiler temperature of 300 °C. The number of stages required at low concentration

المنارة للاستشارات
www.manaraa.com

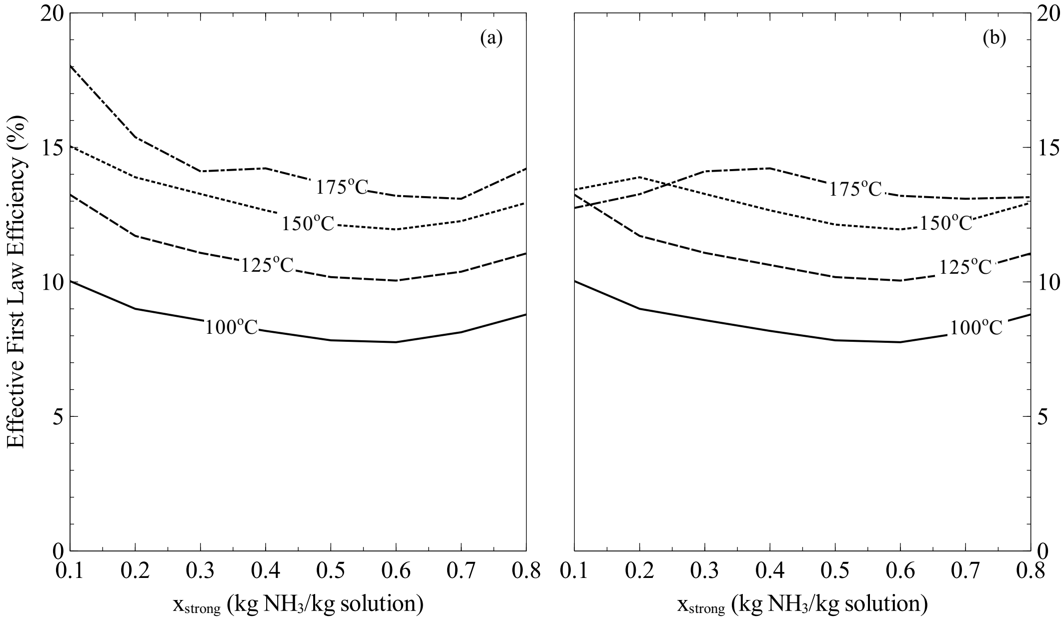

Figure 3.33 Effective first law efficiency comparison of the Goswami Cycle at boiler temperatures of 100-175 °C. a) Multiple Turbine Stages and b) Single Stage Turbine

is increased to 3 for the boiler temperature of 300 °C; however, the pressure ratio at the last stage is at least 6 times lower than the ratio of 275 °C boiler temperature. As an example, for the boiler temperature of 300 °C and strong solution concentration of 0.1, the temperature and pressure of the vapor after the second stage are 94.3 °C and 0.894 bar, and the system low pressure is 0.25 bar. As the fluid pressure is approximately 3.6 times higher than the system low pressure, it could be still utilized to produce work by the third turbine stage. The heat source temperature is assumed to be constant for the boiler and reheaters. Therefore, the exhaust vapor is reheated and expanded to the system low pressure. The temperature of the vapor after the last turbine is 174.9 °C, which is high compared to the previous stage exhaust temperature. If only two stages are used in this case, the effective first law efficiency would be 23.82%, which is lower than the three turbine

المنارة للاستشارات
www.manaraa.com

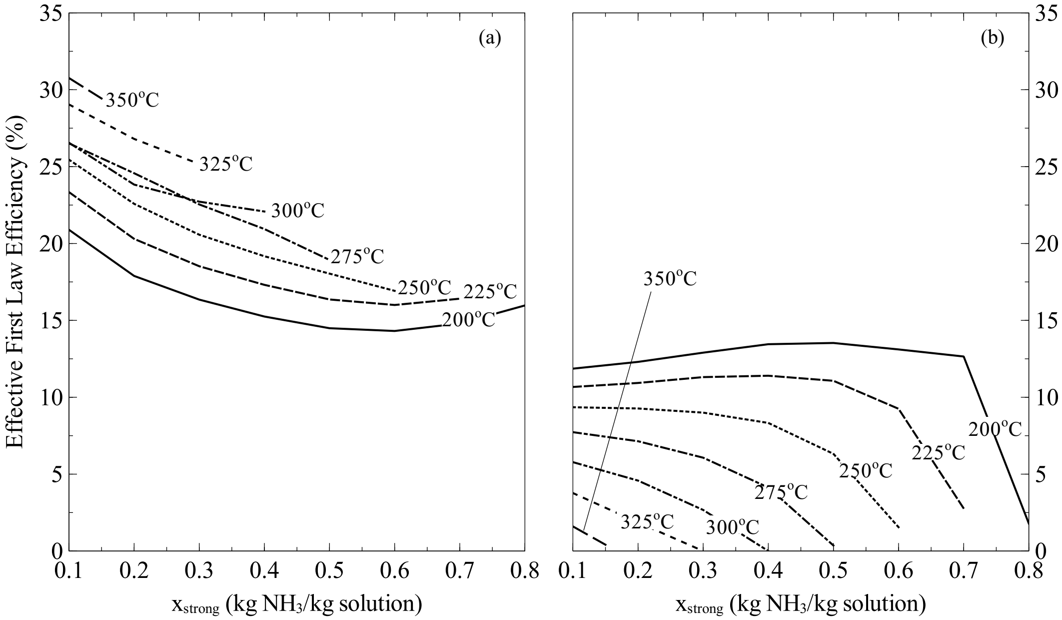

Figure 3.34 Effective first law efficiency comparison of the Goswami Cycle at boiler temperatures of 200-300 °C. a) Multiple Turbine Stages and b) Single Stage Turbine

stage efficiency value of 26.55%. This shows that the cycle efficiency improves with the third stage, however the third stage heat input is not utilized efficiently as the vapor exhaust is still at high temperature, which is 174.9 °C. This analysis will be expanded further by the exergy analysis in this chapter to find alternative ways to utilize the last stage waste heat.

Effective exergy efficiency comparison of the Goswami cycle with multiple and single turbine stages for boiler temperatures of 100-350 °C are shown in Figures 3.35-3.36. The effective exergy efficiency values are between 40-62% and 45-68% for 100-175 °C and 200-350 °C, respectively. As shown in Fig. 3.36, the effective exergy efficiency values for 300 °C were lower than for 250 and 275 °C, the reason is discussed above. The single and multi-stage expansion difference for the exergy efficiency is seen clearly in the Fig. 3.36,

المنارة للاستشارات
www.manaraa.com

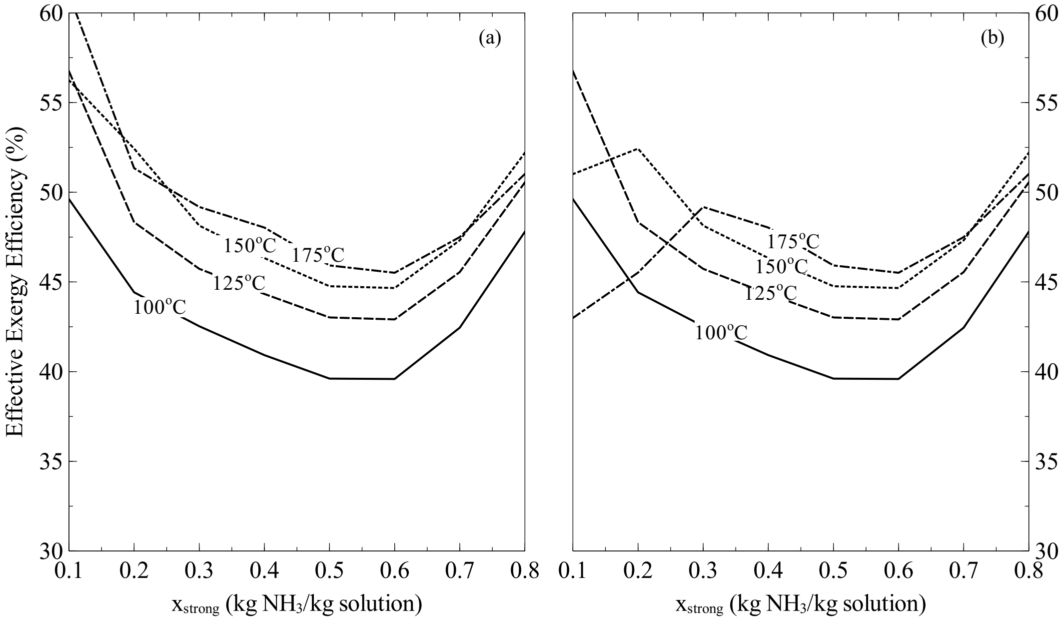

Figure 3.35 Effective exergy efficiency comparison of the Goswami Cycle at boiler temperatures of 100-175 °C. a) Multiple Turbine Stages and b) Single Stage Turbine

the exergy efficiency decreases with increasing heat source temperature for the single stage case.

It is seen from Fig. 3.36 that the boiler temperatures of 250-275 °C cases have higher exergy efficiency values than 300 °C. As it is stated above, the cycle requires 3 turbine stages for 300 °C; however, the last stage pressure is not high enough to utilize the reheater effectively. To quantify this statement, exergy analysis is conducted. Unlike energy, exergy is not conserved (except for ideal processes); rather it is destroyed due to irreversibilities in any real process. Exergy analysis is conducted to calculate the destruction of exergy, which is wasted potential for the production of work [30, 107]. Hasan and Goswami [97] performed the exergy analysis of the combined power/cooling cycle for heat source temperatures of 47-187 °C, so the same methodology was used here. If the ambient temperature

المنارة للاستشارات
www.manaraa.com

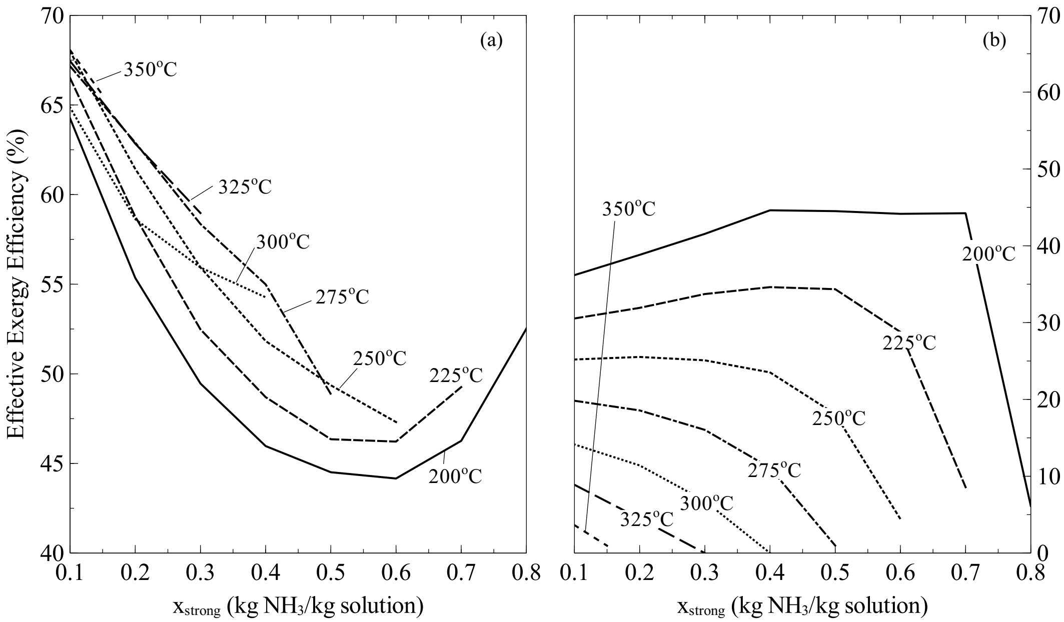

Figure 3.36 Effective exergy efficiency comparison of the Goswami Cycle at boiler temperatures of 200-300 °C. a) Multiple Turbine Stages and b) Single Stage Turbine

T_o is taken as the reference temperature, then exergy per unit mass of a stream, ε, is given as,

$$\varepsilon = (h - h_o) - T_o(s - s_o) \tag{3.4}$$

For a mixture, the exergy is given in terms of exergy of pure components evaluated at component partial pressure and mixture temperature. Szargut [108] suggested that for a binary mixture, exergy could be given in terms of enthalpy, entropy, and composition of mixture as follows,

$$\varepsilon = (h - T_o s) - \alpha + \beta x \tag{3.5}$$

where x is the mass fraction of one component in the mixture, and α and β are constants whose values are set arbitrarily such that exergy in the cycle is always positive. It can be

المنارة للاستشارات
www.manaraa.com

shown using material and exergy balances that in calculating the exergy destruction in the cycle for any control volume, the constants α and β vanish and, therefore, have no effect on the value of exergy destruction in the cycle. In this study, α is set as 50, β is set as 250, the reference state is calculated by using ambient temperature, T_o , 25 °C, and the strong solution concentration.

Exergy destruction X is calculated by rearranging the exergy balance equation for a control volume at steady state in the following form [30, 107],

$$X = \sum m_i \varepsilon_i - \sum m_e \varepsilon_e - W_{cv} + \sum \left(1 - \frac{T_o}{T}\right) Q \tag{3.6}$$

where W_{cv} is the work of control volume, m is the mass flow rate, X is exergy destruction within the control volume, Q is the heat transfer with the surroundings or other fluids, and subscripts i and e are used for inlet and exit, respectively. Average temperature is used whenever temperature is not constant. The exergy destruction of each component for the cycle (shown in Fig. 3.2) is as follows:

The exergy destruction in the pump, recovery heat exchanger, boiler heat exchanger, and separator and rectifier are given in Eqs. 3.7-3.10.

$$X_{pump} = m_1 \varepsilon_1 - m_2 \varepsilon_2 + W_{pump} \tag{3.7}$$

$$X_{recovery\,heat\,exchanger} = m_2 \varepsilon_2 + m_9 \varepsilon_9 - m_3 \varepsilon_3 - m_{10} \varepsilon_{10} \tag{3.8}$$

$$X_{boiler\,heat\,exchanger} = m_3 \varepsilon_3 + m_{hs,in} \varepsilon_{hs,in} - m_4 \varepsilon_4 - m_{hs,out} \varepsilon_{hs,out} \tag{3.9}$$

المنارة للاستشارات
www.manaraa.com

$$X_{separator+rectifier} = m_4\varepsilon_4 + m_{cf,in}\varepsilon_{cf,in} - m_9\varepsilon_9 - m_5\varepsilon_5 - m_{cf,out}\varepsilon_{cf,out} \tag{3.10}$$

where the subscripts cf refers to the cold fluid used for the rectification cooling needs. The exergy destruction in the superheater heat exchanger, turbine, and refrigeration heat exchanger are given Eqs. 3.11-3.13.

$$X_{superheater} = m_5\varepsilon_5 + m_{hs,in}\varepsilon_{hs,in} - m_6\varepsilon_6 - m_{hs,out}\varepsilon_{hs,out} \tag{3.11}$$

$$X_{turbine} = m_6\varepsilon_6 - m_7\varepsilon_7 - W_{turbine} \tag{3.12}$$

$$X_{refrigeration\,heat\,exchanger} = m_7\varepsilon_7 + m_{ref,in}\varepsilon_{cf,in} - m_8\varepsilon_8 - m_{ref,out}\varepsilon_{cf,out} \tag{3.13}$$

where the subscripts ref refers to the fluid that will be cooled by the turbine exhaust. The exergy destruction in the absorber and throttling valve are given Eqs. 3.14-3.15.

$$X_{absorber} = m_8\varepsilon_8 + m_{11}\varepsilon_{11} + m_{c,in}\varepsilon_{c,in} - m_1\varepsilon_1 - m_{c,out}\varepsilon_{c,out} \tag{3.14}$$

$$X_{throttling\,valve} = m_{10}\varepsilon_{10} - m_{11}\varepsilon_{11} \tag{3.15}$$

where the subscripts c refers to the condensing fluid which is used to regenerate the cycle working fluid. The heat losses from the heat exchangers and other components to the ambient are neglected. The sum of the each component exergy destruction will give the total exergy destruction in the cycle while in steady-state operation.

The exergy destruction in the cycle for different boiler temperature and basic solution concentration is shown in Fig. 3.37. As seen in the figure, the exergy destruction increases

المنارة للاستشارات
www.manaraa.com

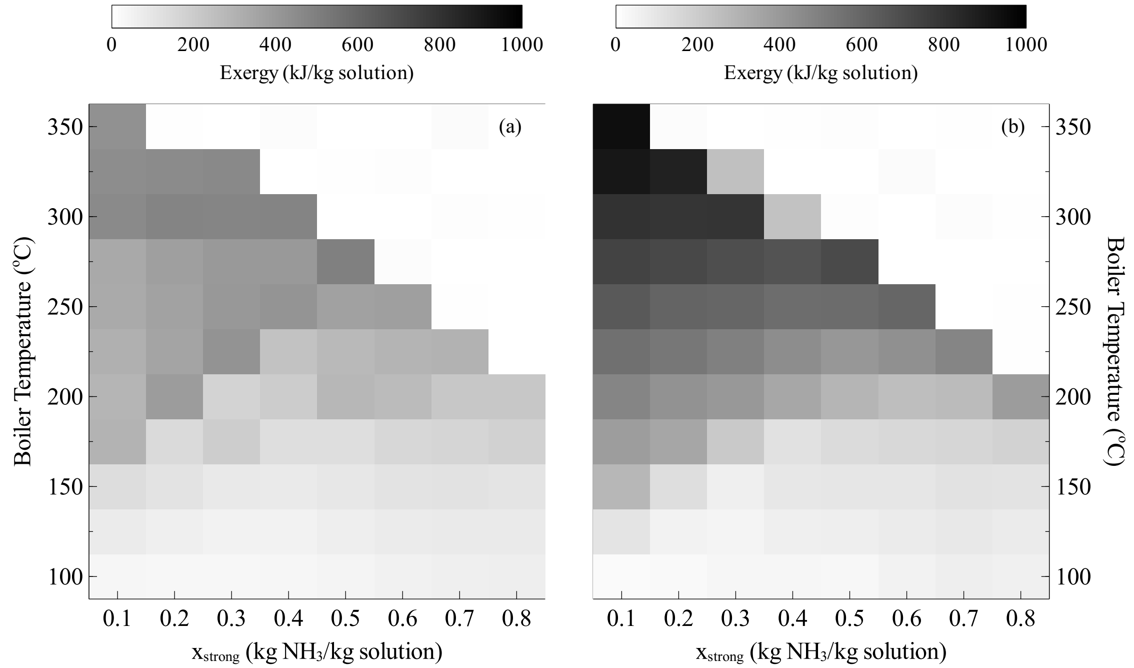

Figure 3.37 Exergy destruction values at boiler temperatures of 100-350 °C

with increasing boiler temperature. When the single and multi-turbine stage cases are compared, it is clear from the figure that cycles with the multi-stages have smaller exergy destruction above the boiler temperature of 175 °C. When the multi stage case is considered, it is seen from the Fig. 3.37(a) that the maximum destruction occurs at the boiler temperature of 300 °C. The sources of exergy destruction in the cycle for a strong solution of 0.1 kg NH_3/kg solution are tabulated in Table 3.6. The main sources of exergy destruction are heat exchangers, absorber, and turbine stages. For most of the cases, the dominant exergy destruction source is the absorber. The exergy destruction at the absorber peaks at the boiler temperature of 300 °C. As discussed before, the last stage turbine temperature is high compared to other cases, which increases the absorber cooling load as well.

المنارة للاستشارات
www.manaraa.com

Table 3.6 Exergy destruction in the cycle for various boiler temperatures and strong solution concentration of 0.1 kg NH_3/kg solution

T (°C)	Heat Ex.	Absorber	Turbine St.	Rest	Total
100	14.8 (48.8%)	10.0 (33.0%)	5.2 (17.0%)	0.4 (1.2%)	30.3
125	16.0 (18.1%)	52.5 (59.4%)	19.4 (22.0%)	0.4 (0.5%)	88.4
150	33.0 (26.4%)	65.7 (52.7%)	25.2 (20.2%)	0.9 (0.7%)	124.8
175	32.1 (10.9%)	191.5 (64.7%)	71.7 (24.2%)	0.6 (0.2%)	295.9
200	33.4 (11.1%)	185.2 (61.3%)	82.7 (27.4%)	0.9 (0.3%)	302.2
225	34.4 (11.2%)	179.5 (58.3%)	92.5 (30.0%)	1.6 (0.5%)	308.0
250	37.2 (11.8%)	174.0 (55.2%)	101.4 (32.2%)	2.5 (0.8%)	315.1
275	38.7 (11.4%)	170.3 (50.0%)	127.6 (37.5%)	3.8 (1.1%)	340.5
300	96.9 (21.2%)	237.6 (52.1%)	116.0 (25.4%)	5.7 (1.3%)	456.2
325	95.2 (21.2%)	203.2 (52.1%)	128.7 (25.4%)	8.4 (1.3%)	435.5
350	98.1 (22.7%)	186.1 (43.0%)	136.5 (31.5%)	12.3 (2.8%)	433.0

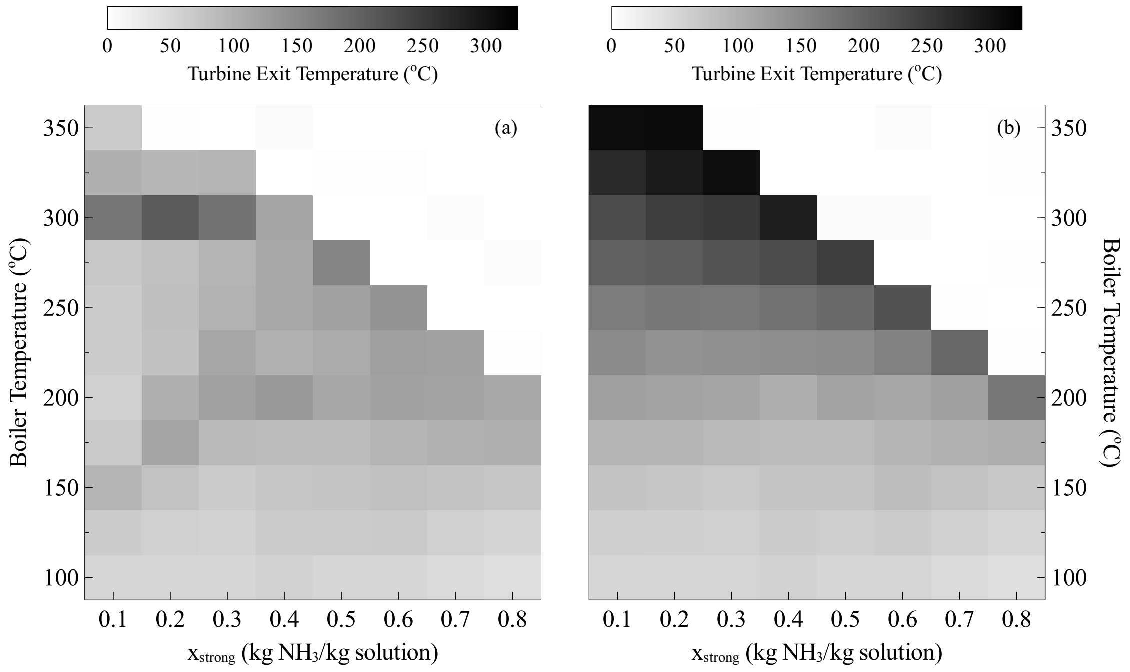

Figure 3.38 Turbine exit temperatures at boiler temperatures of 100-350 °C

The turbine exit temperatures of the cycle for all boiler temperatures and strong solution concentrations are shown in Fig. 3.38. For multi-turbine stage cases, the turbine exit temperature is at a maximum for the boiler temperature of 300 °C. The temperature of the vapor after the second turbine for the boiler temperature of 300 °C and strong solution

المنارة للاستشارات
www.manaraa.com

concentration of 0.1 to 0.4 kg NH_3/ kg solution are 94.3 °C, 107.9 °C, 136.8°C, and 206.6 °C, respectively. After reheating the vapor to 300 °C temperature, the vapor temperature after the last turbine are 174.9 °C, 203.4 °C, 177.85 °C, and 111.1 °C for the same boiler temperature and strong solution range. As discussed before, the effective exergy efficiency of 300 °C boiler case is lower than 275 °C. Therefore, it is obvious that reheating the vapor to 300 °C temperature does not work efficiently.

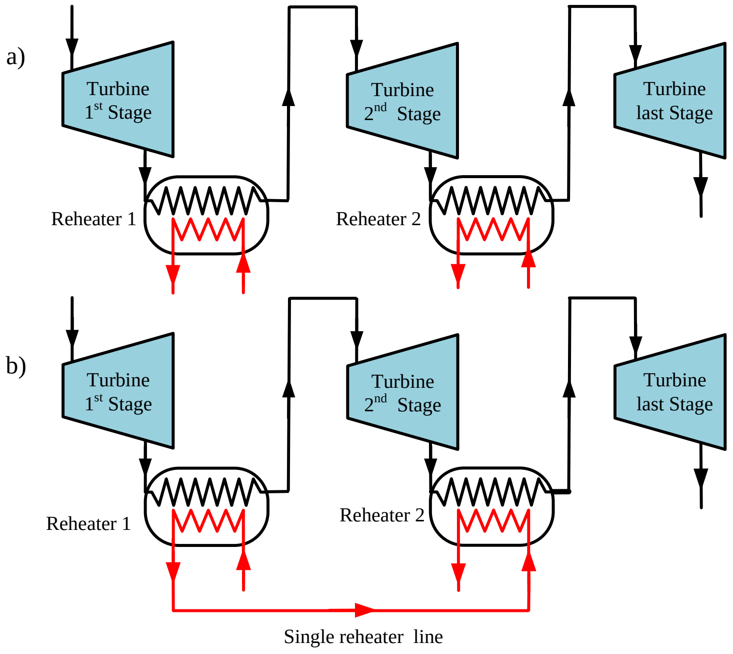

Figure 3.39 Partial superheating cases. a) Two hot water stream for reheating b) Single hot water stream for reheating

The partial superheating case was conducted to tackle this problem. The vapor is reheated to temperatures less than the boiler temperature and the efficiency values were recalculated. There might be a reheating temperature less than 300 °C where efficiency values are higher than the one at 300 °C. To give an example, the boiler temperature of 300 °C and strong solution of 0.1 kg NH_3/ kg solution is taken; the vapor temperature after the 2nd

المنارة للاستشارات
www.manaraa.com

Table 3.7 Effective first law and exergy efficiencies for partial superheating cases

	Reheating to 300 °C		PS D*		PS S**	
x_{strong}	$\eta_{I,eff}$	$\eta_{exergy,eff}$	$\eta_{I,eff}$	$\eta_{exergy,eff}$	$\eta_{I,eff}$	$\eta_{exergy,eff}$
0.1	26.55	64.86	27.48	66.52	27.47	67.03
0.2	23.83	58.63	25.26	60.99	25.33	62.25
0.3	22.72	55.93	23.41	58.09	23.71	59.00
0.4	22.08	54.27	22.08	54.38	21.98	54.51

*Partial Superheating, Double Reheater Stream
**Partial Superheating, Single Reheater Stream

turbine was 94.3 °C. The vapor is reheated from 95 °C to 300 °C and results were compared to find the maximum efficiency. This case is labeled as partial superheating with double reheater stream as two reheater water line at the same temperature were used. The second option can be using a single reheating stream instead of two for the 3 stage cases. As shown in Fig. 3.39(b), the reheating stream after the first reheater is directed to the second reheater. It should be kept in mind that, the temperature of the reheating hot water after the first reheater heat exchanger drops, so it is not possible to increase the vapor temperature to boiler temperature at the second reheater, the temperature is always less than the boiler temperature.

To compare the effect of partial superheating, the values at 300 °C are given in Table 3.7. The increase in efficiency terms are between 0.9% and 3.6%. It should be kept in mind that, the partial superheating case with single stream line can be applicable only to the 3 stage cases. The maximum effective first law and exergy efficiencies were updated with the partial superheating cases and given in Tables 3.8 and 3.9.

The partial superheating case studied previously to achieve a higher efficiency values at higher boiler temperatures. The reheating temperature was varied to find the best reheating

المنارة للاستشارات
www.manaraa.com

Table 3.8 The maximum effective first law efficiency values

	x (kg NH_3/kg solution)							
T (°C)	0.1	0.2	0.3	0.4	0.5	0.6	0.7	0.8
100	10.03	9.00	8.58	8.18	7.83	7.76	8.13	8.79
125	13.24	11.71	11.08	10.63	10.18	10.05	10.38	11.06
150	15.77*	13.89	13.27	12.66	12.13	11.95	12.29	12.94
175	18.50*	16.05*	14.11	14.22	13.61	13.20	13.09	14.21
200	21.00*	18.20*	16.85*	15.91*	14.49	14.31	14.91*	15.97
225	23.34	20.44*	18.58*	17.42*	16.39	16.00	16.41	
250	25.46*	22.58	20.57	19.17	18.04	16.92		
275	26.51	24.57	22.54	20.94	19.33**			
300	27.48*	25.33**	23.71**	22.08				
325	29.25*	26.80	25.17					
350	30.76							

*Partial Superheating, Double Reheater Stream
**Partial Superheating, Single Reheater Stream

temperature, which minimizes the exergy losses. If the reheating temperature was kept constant, the question arises whether the high temperature vapor can be used as waste heat to increase the overall cycle efficiencies. The high temperature vapor can be used as a heat source for a bottoming cycle or a heat recovery system. Therefore, in order to examine the possible use of the high temperature vapor, a combined cycle and a vapor heat recovery cases were conducted for the boiler temperature of 300 °C. Firstly, the combined cycle analysis is presented, it is followed by the vapor heat recovery case, and then the results will be presented.

The combined cycle has a top and bottom Goswami cycles. As shown in Fig. 3.40, the turbine exhaust of the top Goswami cycle can be utilized by heating the bottom Goswami cycles working fluid. The simulation of the combined cycle is a complex problem as the optimization of the bottom cycles is also required. The detailed description of the top cycle and the first bottoming cycle are shown in Fig. 3.41. The operating conditions of maximum

المنارة للاستشارات
www.manaraa.com

Table 3.9 The maximum effective exergy law efficiency values

	x (kg NH_3/kg solution)							
T (°C)	0.1	0.2	0.3	0.4	0.5	0.6	0.7	0.8
100	49.61	44.42	42.53	40.92	39.61	39.59	42.45	47.80
125	56.74	48.33	45.73	44.33	43.02	42.91	45.55	50.55
150	58.21*	54.43	48.14	46.33	44.76	44.66	47.32	52.20
175	61.48*	53.45*	49.18	48.03	45.92	45.51	47.50	51.02
200	64.58*	56.19*	51.26*	48.33*	44.51	44.16	47.33*	52.59*
225	66.57*	59.18*	53.24*	49.41*	46.88*	46.99*	49.30*	
250	67.98	61.50*	56.31*	52.51*	49.74*	47.32*		
275	67.17*	62.90	58.38*	54.99	50.85**			
300	67.03**	62.25**	59.00**	54.51**				
325	68.16**	63.33**	58.99**					
350	68.17**							

*Partial Superheating, Double Reheater Stream

**Partial Superheating, Single Reheater Stream

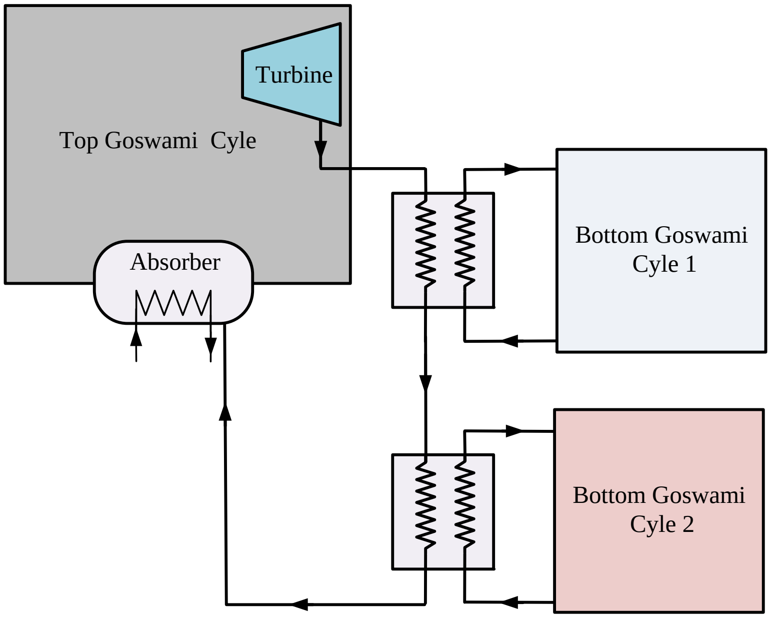

Figure 3.40 Schematic description of the combined cycle, top and bottom Goswami cycles

effective exergy efficiency are used to simulate the top cycle, therefore the mass flow rate and temperature of the vapor are known. The boiler temperature, system high pressure, and strong solution concentration of the bottom cycle will define the temperature of state

المنارة للاستشارات
www.manaraa.com

8’ as shown in Fig. 3.41, which enters the recovery heat exchanger. The temperature of state 8’ is independent of the strong solution mass flow rate. By performing recovery heat exchanger calculations, the temperature of state 3’ is determined. Then, the boiler heat exchanger calculations are performed and bottom cycle strong solution mass flow rate is found.

The entropy generation in a certain control volume cannot be lower than zero, based on the second law of thermodynamics, and this constraint is applied to all heat exchangers as well as boiler heat exchangers. In the previous analysis, the heat source mass flow rate of the top cycle is calculated based on the pinch point assumption, and then the entropy generation is calculated for the heat exchanger. If the entropy generation term is less than zero, which is an impossible process, the heat source mass flow rate is increased to satisfy the entropy generation constraint. In this case, the top cycle vapor mass flow rate is constant, therefore the bottom cycle mass flow rate is calculated based on the pinch point assumption, and then if the entropy generation term is negative, the pinch point value is increased until the entropy generation is higher than zero. Whenever the pinch point increases, the mass flow rate of the bottom cycle decreases, and the temperature of the top cycle vapor after the heat exchanger can be still high. For this reason, when the top cycle vapor is above 150 °C, two bottom cycles are required to cool down the high temperature vapor of the top cycle to lower than 100 °C.

In order to search the maximum work output from the bottoming cycle, the system high pressure is varied between the bubble and dew point pressures for the corresponding boiler

www.manaraa.com

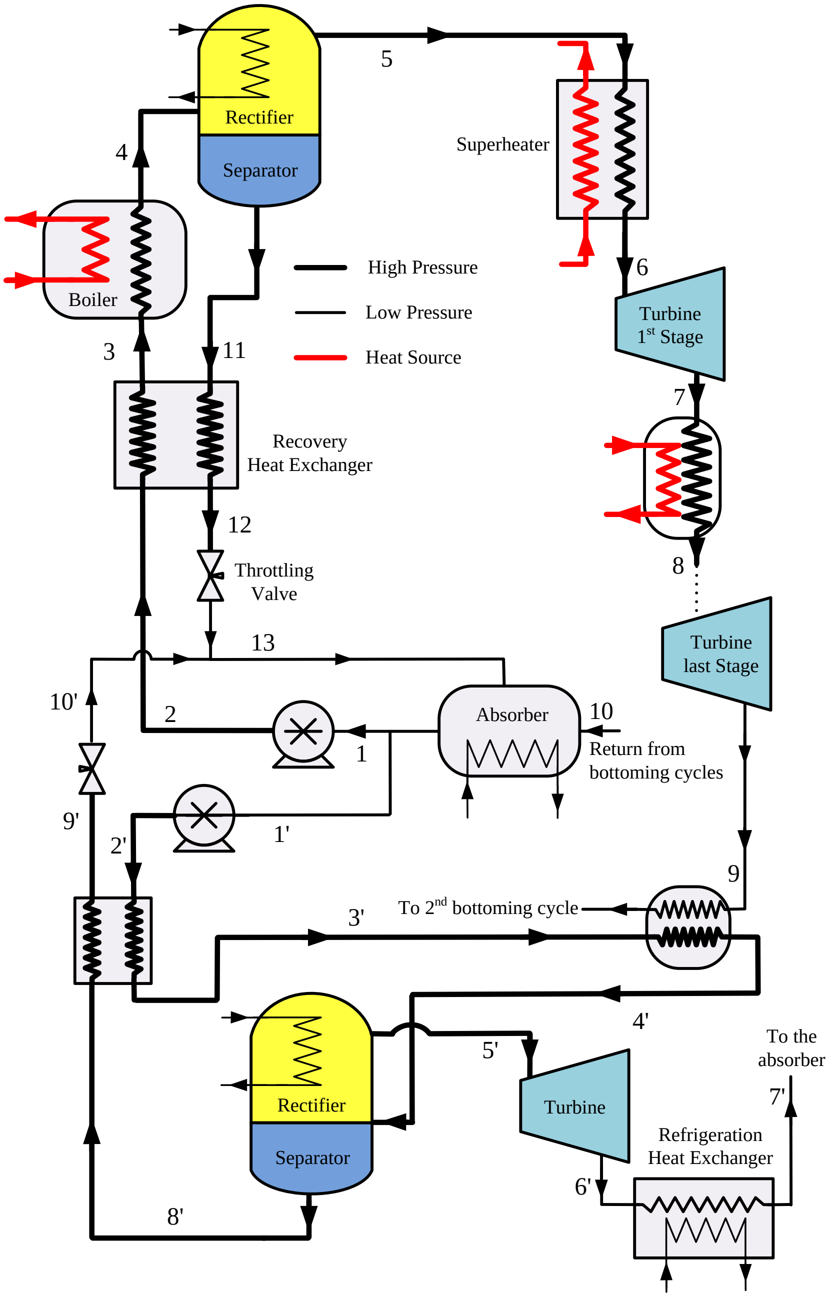

Figure 3.41 Detailed description of the combined cycle, top and the first bottoming Goswami cycles

temperature and strong solution concentration. The strong solution concentration is varied between 0.1 and 0.8 kg NH_3/kg solution for the bottom cycle simulations.

المنارة للاستشارات
www.manaraa.com

The vapor heat recovery system is shown in Fig. 3.42. The Goswami cycle system is simpler than the Kalina cycle distillation and condensation subsystems, it has two heat recovery heat exchanger, one separator and a pump as shown in Fig.3.42. The strong solution is reheated first by the liquid weak solution return from the separator. Then, it is reheated by the high temperature turbine exit vapor, and then it enters the boiler heat exchanger. As described above, entropy generation constraint is also implied to the vapor heat recovery exchanger.

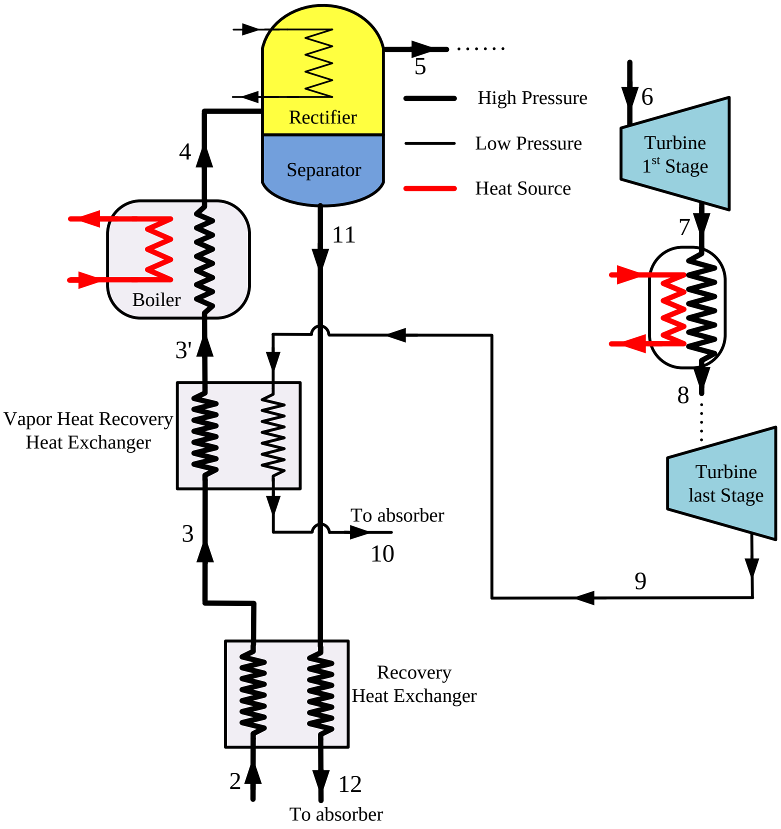

Figure 3.42 Schematic description of the vapor heat recovery system

The combined cycle and vapor heat recovery analysis are conducted for the top cycle boiler temperature of 300 °C. The efficiencies of the analysis are compared with the top

المنارة للاستشارات
www.manaraa.com

cycle alone for the boiler temperatures of 275 °C and 300 °C. The effective first law and exergy efficiencies are shown in Table 3.10. As it is seen in the table, when the two bottoming cycles are used for the top cycle boiler temperature of 300 °C, the effective first law efficiency increases approximately 1-3.5% compared to the stand alone top cycle. The effective exergy efficiency is also increased approximately 2.5-12.7%. In addition, it is shown in the Table 3.10 that the efficiency terms of 300 °C case are increased compared to the boiler temperature of 275 °C case by utilizing the turbine exhaust vapor. The vapor heat recovery system improves the efficiencies significantly for the concentration values of 0.1 and 0.2. Due to the entropy generation constraint, this system cannot be used for the strong solution concentration of 0.4. It is noteworthy that the use of bottoming cycles and vapor heat recovery system requires additional equipments, which will bring additional cost; however, the cost can be reduced if some components like absorber can be shared with cycles. If the same absorber is used for top and bottom cycles, the cost of the absorber per unit size can be reduced. The combined system can provide additional work, which would increase the overall capacity; on the other hand, the vapor heat recovery system can increase the cycle efficiencies significantly with an additional heat exchanger.

Dincer and Al-Muslim [109] conducted a thermodynamic analysis for the steam power plants with reheat. The temperature and pressure values were in the range between 400 and 590 °C, and 100 and 150 bar. The first law and exergy efficiencies for the corresponding boiler temperature range were approximately 38-43% and 53-58%. Kalina [34] investigated the Kalina cycle performance for a boiler temperature of 532 °C and found that the bottoming cycle produces 2.7 MW_e with a first law and exergy efficiencies of 32.9% and

المنارة للاستشارات
www.manaraa.com

Table 3.10 Effective first law and exergy efficiencies for vapor recovery and top and bottoming cycle cases

	$\eta_{I,eff}$				$\eta_{exergy,eff}$			
	T	T	T+B	VHR	T	T	T+B	VHR
x_{strong}	275 °C	300 °C	300 °C	300 °C	275 °C	300 °C	300 °C	300 °C
0.1	26.51	27.48*	28.49	30.84	67.17*	67.03	69.60	70.68
0.2	24.57	25.33**	27.14	28.90	62.90	62.25**	66.81	66.04
0.3	22.54	23.71**	26.58	25.93	58.38*	59.00**	65.85	60.23
0.4	20.94	22.08	27.35	22.08	54.99	54.51**	67.22	54.51

*Configuration: T= Topping cycle, T+B=Topping and Bottoming cycles, VHR=Vapor heat recovery

*Partial Superheating, Double Reheater Stream

**Partial Superheating, Single Reheater Stream

70.0%, respectively. Nag and Gupta [55] examined the exergy analysis of the Kalina cycle, they varied the temperature of ammonia-water mixture at the condenser, and they found that the cycle efficiency varies between 30-36% for a boiler temperature of 500 °C. The second law efficiency for the same operating conditions is in the range of 51-60%. In an another Kalina cycle study, Olsson et al. found the first law and exergy efficiencies as 23% and 69.7%, respectively for the turbine inlet pressure and temperatures of 110 bar and 494 °C.

As the efficiency results of the Goswami cycle are compared with the Kalina cycle, it is seen that the results are promising. The Goswami cycle can operate at an effective exergy efficiency of 60-68% with the boiler temperature range of 200-350 °C. The first law efficiency of 25-31% can be achievable with the boiler temperatures of 250-350 °C. In addition, this cycle can utilize low temperature sources such as 60-100 °C to produce work and cooling simultaneously.

المنارة للاستشارات
www.manaraa.com

Chapter 4

Experimental System

The experimental facility used in this research is a redesigned and improved version of the facility which was used for the first experiments on the combined power/cooling cycle at Solar Energy and Energy Conversion Laboratory, University of Florida, Gainsville, U.S. Tamm developed a boiling and absorption loop that demonstrates the vapor generation and absorption condensation processes, and theoretical model was compared with the experimental results [8]. As Tamm's setup simulated the turbine expansion with a throttling valve and a heat exchanger, Martin modified and expanded the experimental setup with a turbine and a rectifier column to demonstrate the sub-ambient turbine exhaust conditions [7]. After initial experiments, Martin replaced the separator tank with a smaller size one. In Martin's setup, the condensate line in the reflux cooler was connected into the absorber through the vapor line without measuring the flow rate of condensate in the rectifier column. This was affecting the calculations across the absorber, also rectifier column suffered from frequent flooding problems.

Following Martin's study, Goel increased the rectifier column from 2 inch diameter to 3 inch [9]. In addition, the separator vessel utilized in the setup was found to be quite large, the separator was replaced with another vessel of smaller size. Then, in order to decrease the size of the absorber, a new absorber with a micro channel falling film heat exchanger

المنارة للاستشارات
www.manaraa.com

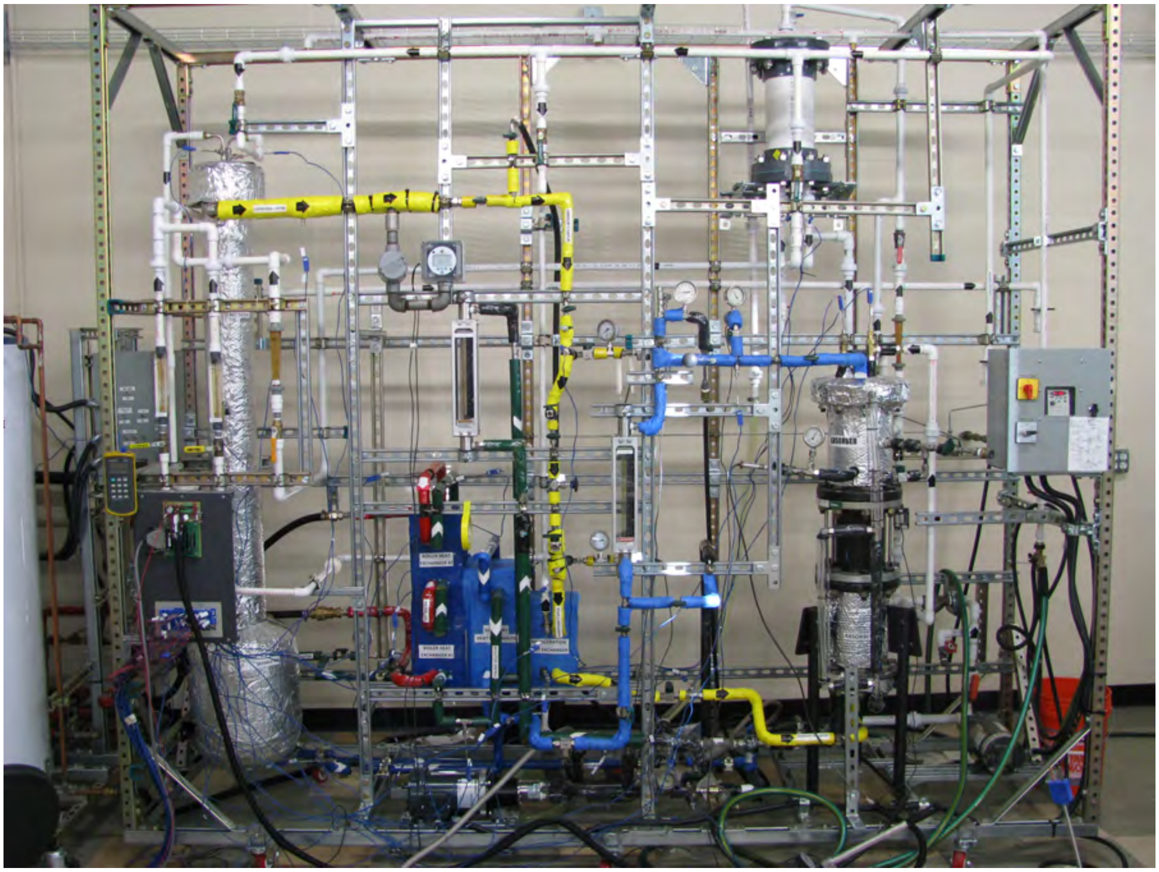

Figure 4.1 Photograph of the Goswami cycle experimental setup

was designed and manufactured. The design utilized the unused vertical spacing between the coolant tubes to form a falling film which increases the mass transfer area. The overall heat transfer coefficient value was found to increase by about 50% with the introduction of a screen mesh. This is attributable to the fact that the screen mesh enhances both mixing and wetting action in the liquid film.

After the last experiments performed by Goel [9], the setup was moved to University of South Florida, Tampa, U.S. The new setup was mounted on a strut channel frame as shown in Fig. 4.1. All of the components have been upgraded or replaced except the separator and the rectifier column. This chapter presents the details of components used in

المنارة للاستشارات
www.manaraa.com

the experimental setup, experimental procedures and the test conditions. The first section gives a detailed description of the components used in the experiments, which is followed by a section that gives the background of the expander types, and the scroll expander used for this study.

4.1 Setup Description

A schematic drawing of the current experimental system is shown in Fig. 4.2. The experimental setup was built in accordance with the conceptual design that was used for the theoretical simulations. The only difference was that an electrical heater was used instead of a superheater heat exchanger for practical purposes. The location and labels of the experimental system instruments are shown in Fig. 4.2, and the specifications of the instruments are given in Appendix C. Stainless steel tubing, fittings and valves were used to connect the components. After several tests of the system, piping path was modified several times to minimize the flow losses in the system. All the tubing and components were insulated, which reduced the heat transfer losses to the environment. A complete list of components is provided in Appendix C.

4.1.1 Absorber

The absorber vessel was a flanged container made from a 6 inch steel pipe. The absorber assembly is shown in Fig. 4.3. The high concentration ammonia vapor at low pressure flows upward though the absorber. The vapor gets absorbed by the weak solution which is uniformly distributed around the 1/8 inch diameter micro tubes. The vapor and weak solution flow in opposite directions and the strong solution forms by rejecting heat to the coolant fluid flowing inside the micro tubes.

www.manaraa.com

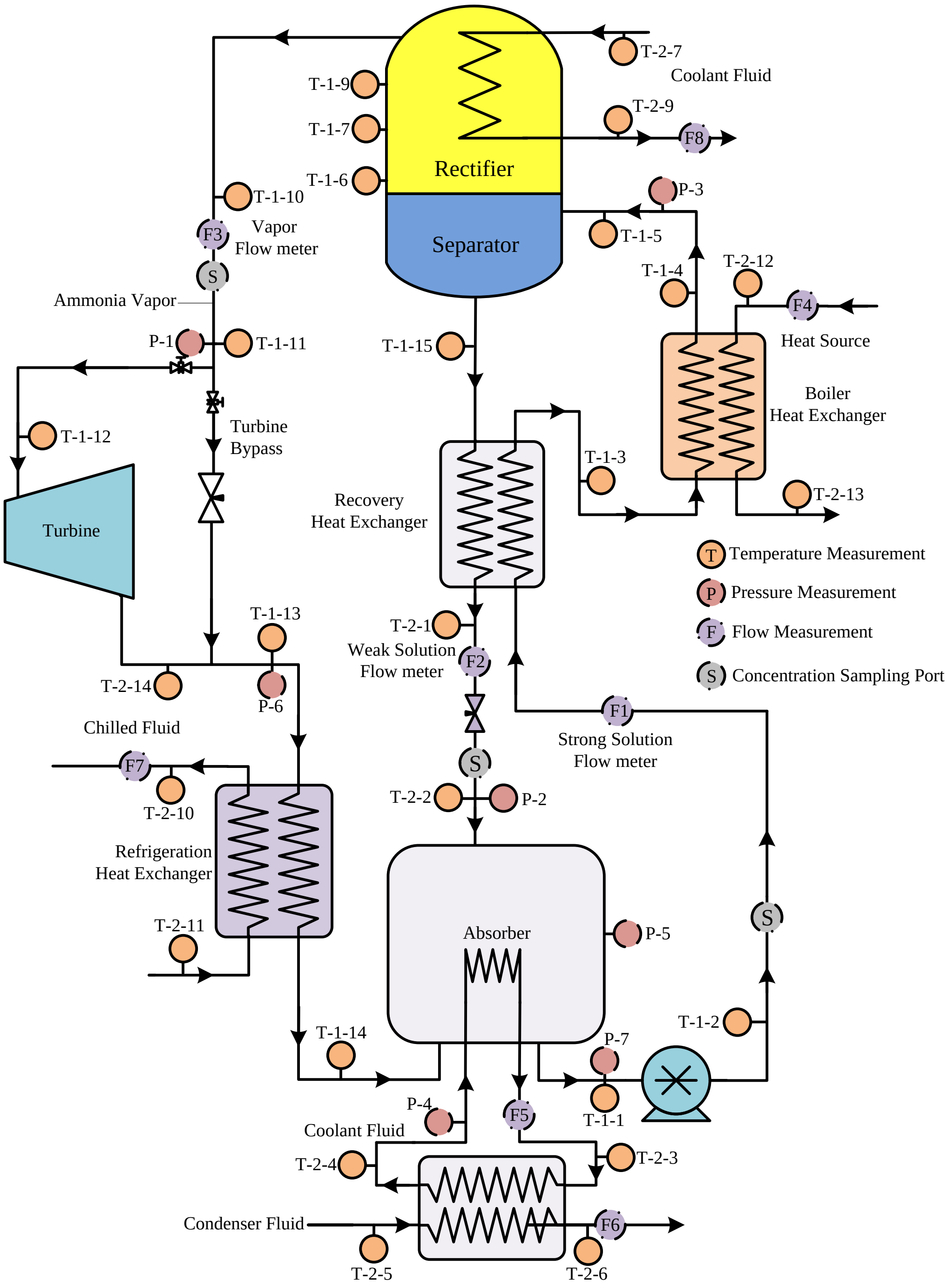

Figure 4.2 Schematic drawing of experimental system

Goel [9] fabricated the micro tube assembly in the laboratory by oxy-acetylene based nickel brazing. The unit that was fabricated used a total of 240 tubes. The tube assembly

المنارة للاستشارات
www.manaraa.com

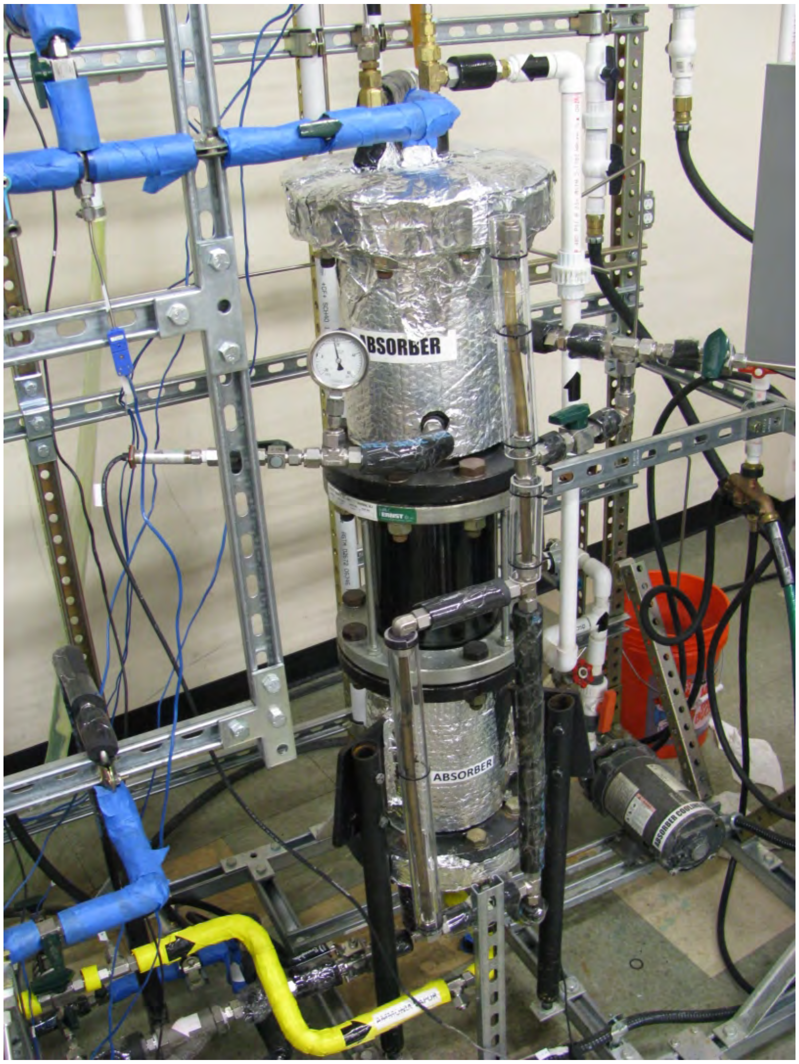

Figure 4.3 Photograph of the assembled absorber unit

consisted of 4 columns each having 60 horizontal tubes with their ends brazed to a stainless steel header of 1/2 inch outer diameter and 0.12 inch wall thickness. During the initial stages of experiments, leaking problems occurred with this unit. The reason is that nickel brazing requires special attention and needs a vacuum environment, however, Goel [9] did not weld the tubes in a vacuum space. The horizontal micro tubes connection at the header points became brittle due to improper nickel brazing, and vibrations in the setup caused

www.manaraa.com

failure at the connections which led to leaks. The ammonia entered the cooling water line and harmed the PVC lines. After several rounds of fixing, it was decided to design and manufacture a new unit. The designed new unit is shown in Figures 4.4 and 4.5.

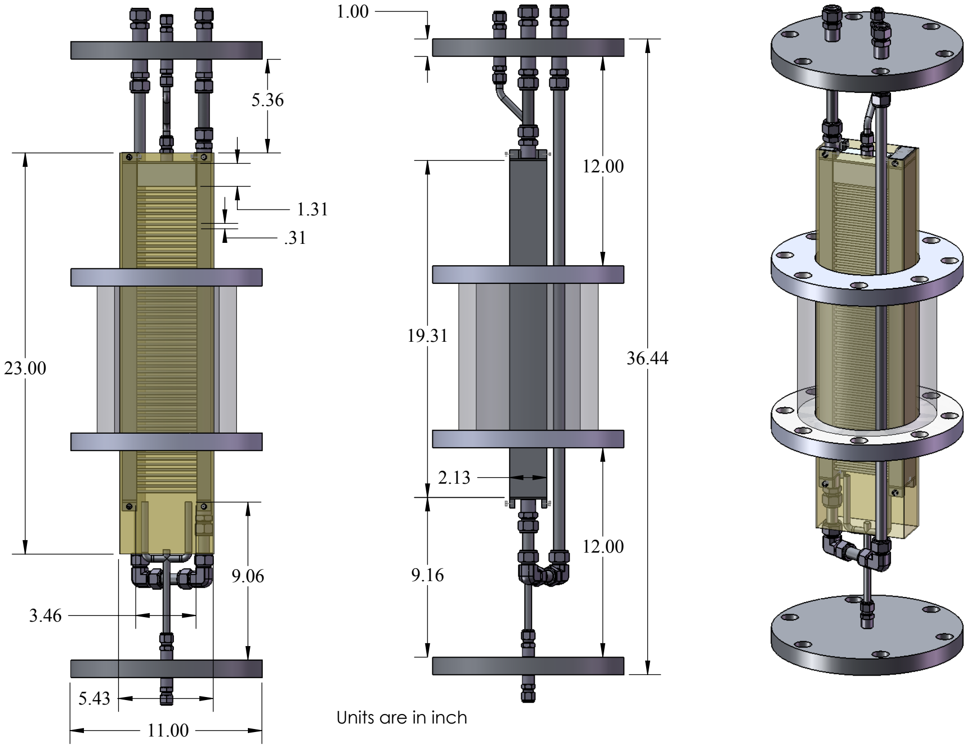

Figure 4.4 Front, right and and 3-D view of the designed micro channel heat exchanger

The new unit has four horizontal passes, each pass has 5 rows and the tubes are connected in a parallel-series arrangement with 14 tubes in parallel. A total of 280 tubes are used and the coolant tubes used in this experimental study are stainless steel tubing of 1/8 inch outer diameter and 0.016 inch wall thickness. The length of each horizontal tube is about 9.8 cm. The previous design total surface area was 0.24 m^2, but the new design sur-

www.manaraa.com

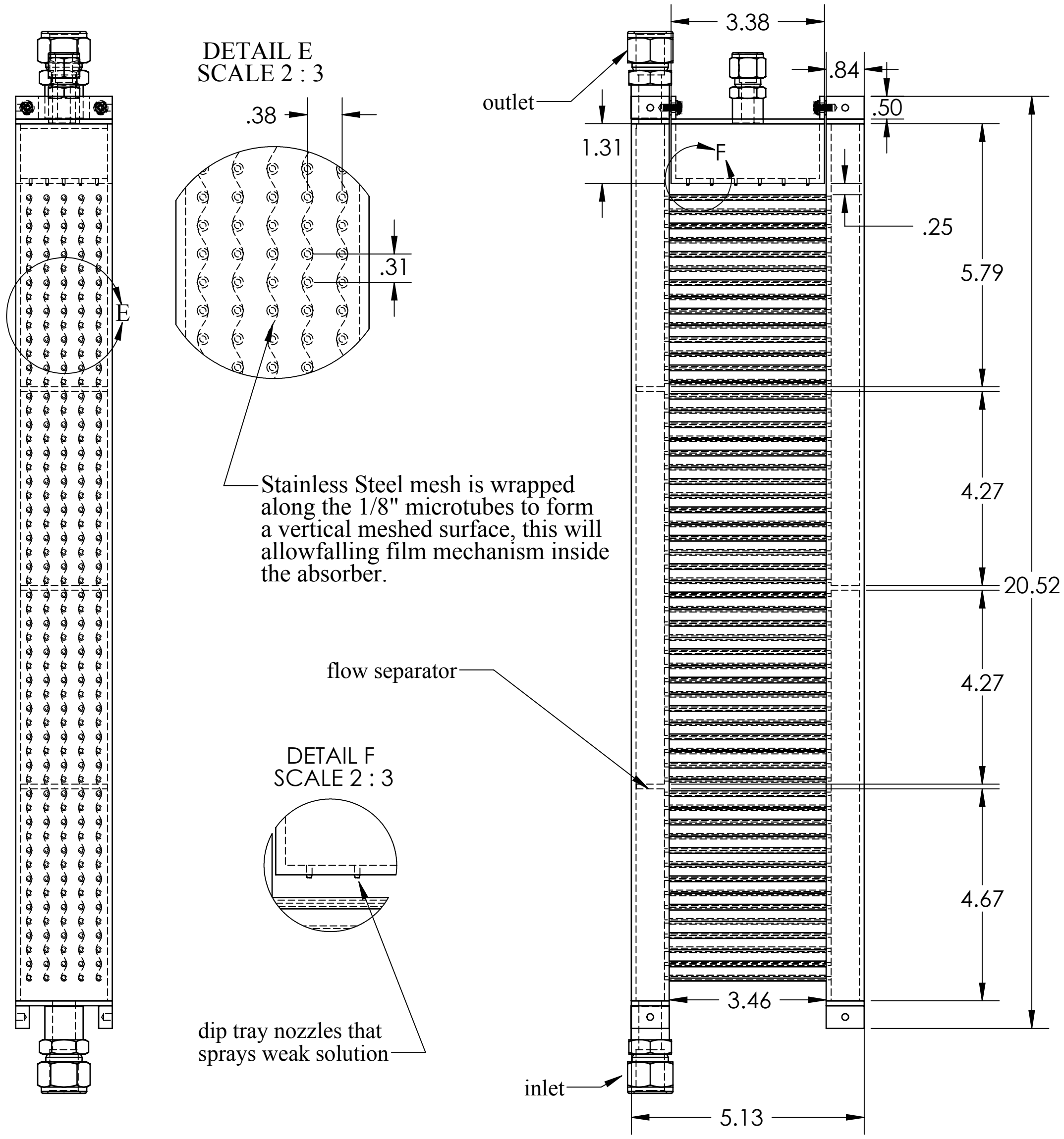

Figure 4.5 Side and front view of the designed micro channel heat exchanger with the dimensions

face area was increased to approximately 0.26 m^2. The manufactured new system is shown in Fig. 4.6.

www.manaraa.com

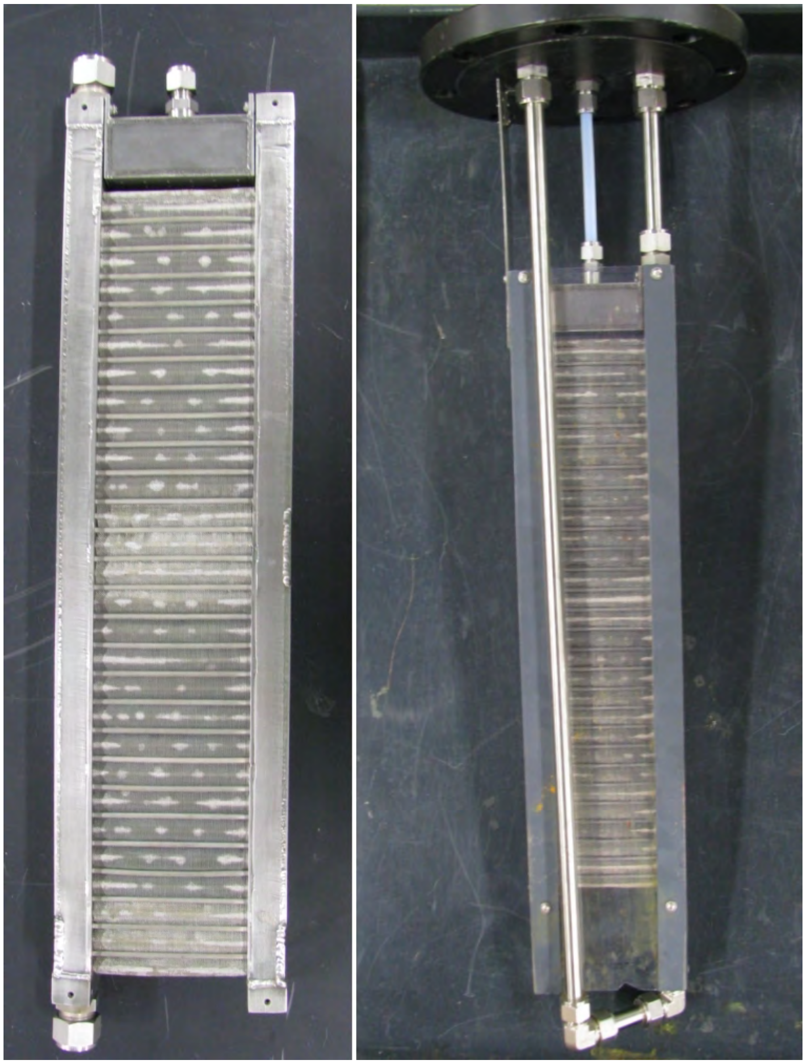

Figure 4.6 Manufactured micro channel heat exchanger (left), and connected to the top cap of the absorber (right)

4.1.2 Pump

Initial tests used an axial multi-stage booster type pump, however the viton type seal of the pump broke several times due to cavitation problems caused by pumping strong solution very near saturation. A magnetic coupled external gear pump provides leak free working conditions due to magnetic coupling of the motor and pump shafts. For this reason a positive displacement gear pump is used for the experiments and it is shown in Fig. 4.7.

المنارة للاستشارات
www.manaraa.com

A voltage/frequency adjusting AC drive is used to control the speed of the pump. This provides low speed start up conditions and the pump speed is increased afterwards. A strainer is at the pump inlet to prevent loose rust pieces from damaging the pump. To increase the suction head, the suction line is connected to the absorber with a 1 inch tubing. The piping connecting the outlet of the absorber to the inlet of the pump was also simplified by reducing the length and the number of bends.

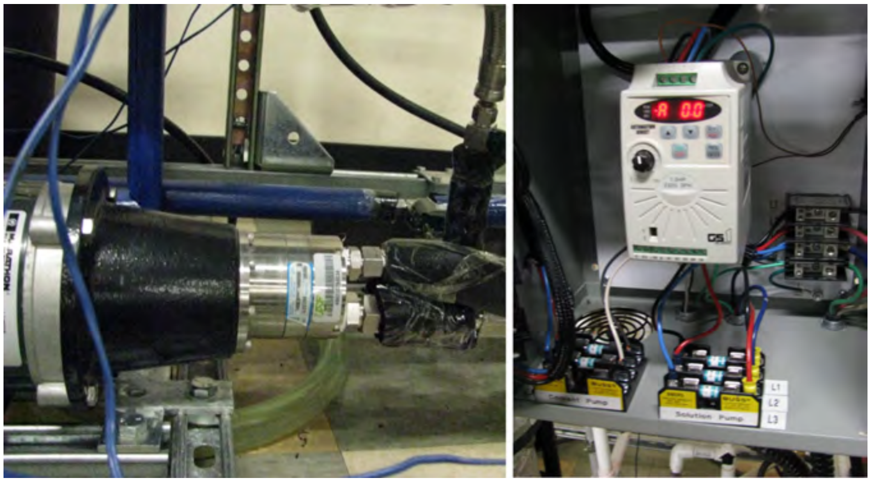

Figure 4.7 Photo of the strong solution pump (left), and the voltage/frequency adjusting AC drive (right)

4.1.3 Boiler, Recovery and Refrigeration Heat Exchangers

The strong solution leaves the pump, and it passes through a recovery heat exchanger where it recovers heat from the weak solution returning to the absorber. After exiting the recovery heat exchanger, the partially boiled mixture enters the boiling heat exchanger. The turbine exhaust is connected to the refrigeration heat exchanger. All the heat exchangers are nickel-brazed, stainless steel, vertically stacked plate type heat exchangers. All heat

www.manaraa.com

exchangers use counter-flow arrangement. The system heat exchangers are shown in Fig. 4.8.

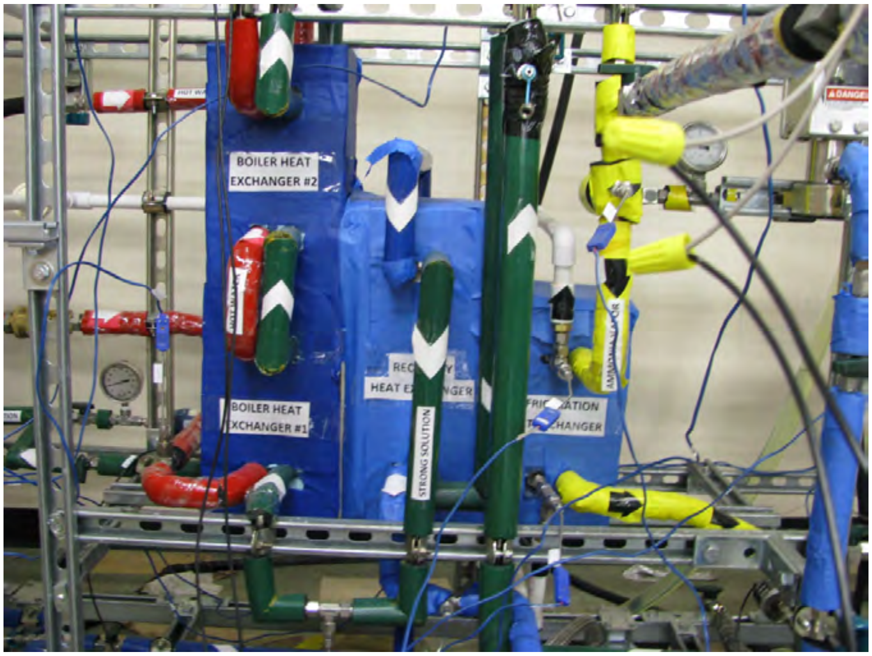

Figure 4.8 Photo of recovery, boiler and refrigeration heat exchangers

4.1.4 Rectifier

The liquid-vapor mixture leaving the boiler is directed to the separator vessel. The separator is an empty tank, it contains no baffles or special equipment. The schematic drawing and the photograph of the rectifier component is shown in Fig. 4.9. The rectification column is a 3 inch schedule 40 pipe of 6 ft length, which is filled with 1/2 inch ceramic Berl Saddle packings to a length of about 2 ft. The reflux cooler is installed in the remaining space of 4 ft in the rectification column. The vapor rises out of the top of the separator and it's concentration is increased by partial condensation of the vapor in the reflux cooler. Cooling for the rectifier is provided by the circulation of chilled water, and the same fluid is used to cool the absorber. The condensate returns back to the separator by gravity. The

للاستشارات المنارة
www.manaraa.com

weak liquid drains from the bottom of the separator and is pressure-driven through the recovery heat exchanger through a throttling valve into the absorber.

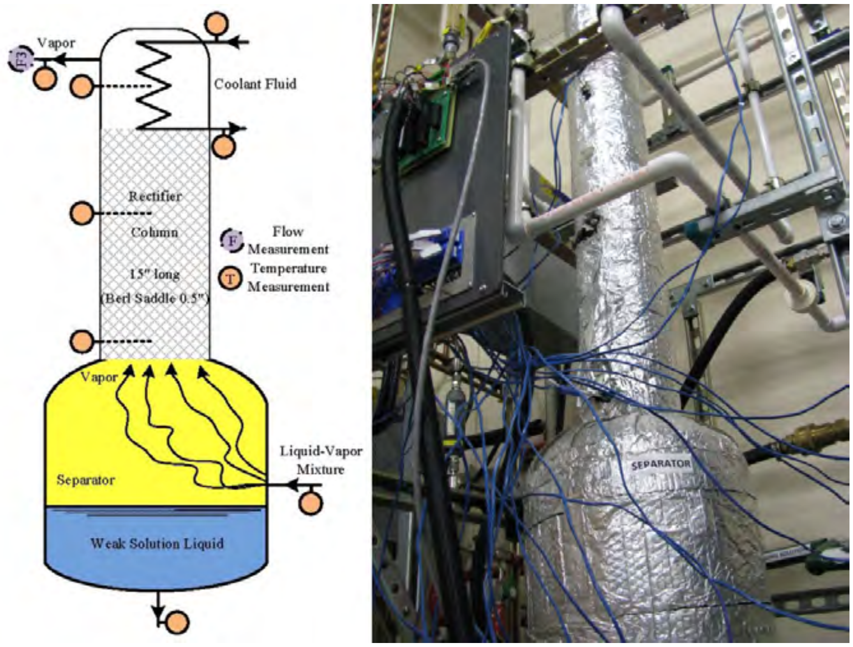

Figure 4.9 Schematic drawing (left) and photo (right) of the rectifier that is used in the experimental setup

4.1.5 Superheater

Superheating is accomplished by using a flexible electric heating tape. The tape is wrapped around tube that connects to the expander. The heat input to the tape is controlled by a variable voltage power controller. Depending on the inlet temperature, the superheating capacity of the tape varies between 1 °C to 8 °C. The superheater tape and the controller are shown in Fig. 4.10.

4.1.6 Hot Water Side

Hot water is used as the heat source for the experiment. It is heated in a storage electric water heater and four additional external heaters. Total heat input capacity of the boiler

المنارة للاستشارات
www.manaraa.com

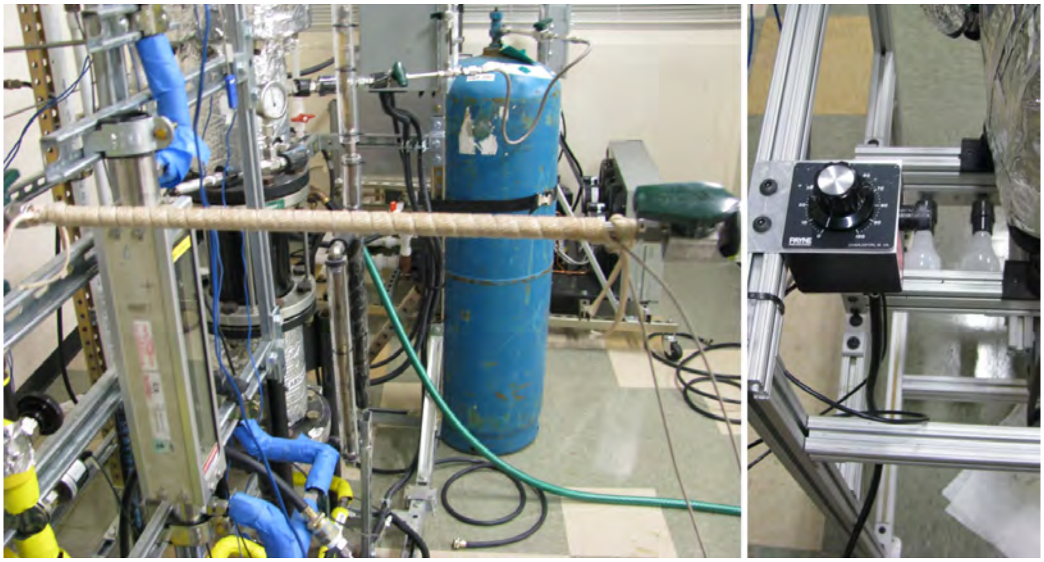

Figure 4.10 Photo of the superheater tape (left) and voltage controller (right)

system is 10.5 kW. A temperature/pressure safety valve at the top of the storage tank relieves the water at 100 °C. Therefore, the maximum temperature of the heat source was 99 °C during the experiments. The water heater is controlled by an adjustable thermostat. The capacity of the heater tank is 80 gallon. The flow rate from the heater system to the cycle is controlled by a valve and the maximum flow rate of 3 gpm can flow through the cycle. A photograph of the boiler system is shown in Fig. 4.11.

4.1.7 Coolant Side

The cooling water for the absorber and rectifier is chilled by a vapor-compression water chiller. The capacity of the tank is 60 gallon, and two radial pump are used when the chiller is operating. The first pump circulates the fluid between the storage tank and the vapor compression chiller heat exchanger. The maximum flow rate of chiller pump is approximately 5 gpm. The chiller has an internal, adjustable thermostat that controls the storage tank temperature. The capacity of the chiller is 2.5 tons at 35 °C ambient temper-

المنارة للاستشارات
www.manaraa.com

Figure 4.11 Photograph of the boiler system

ature, the minimum temperature that can be stored in the tank is 4-5 °C. A separate radial pump is used to circulate the fluid from the storage tank through the heat exchangers in the cycle. A schematic drawing and photograph of the rectifier component is shown in Fig. 4.12. Additional specifications of the chiller and boiler systems are given in Appendix C.

المنارة للاستشارات
www.manaraa.com

Figure 4.12 Photograph of the chiller used in the experiments

4.1.8 Data Collection

Most of the data is recorded with a computer-interfaced data collection system. All temperatures are measured with T-type thermocouples and pressures are detected with pressure transducers. Measurements are saved to a PC through appropriate interface cards and data acquisition software. Two instrument types are used for measuring flow rates: the vapor flow into the turbine is measured with a turbine-type flow meter that provides a signal whose frequency is proportional to flow rate, and the liquid flows of the strong and weak solutions, heat source fluid, and the coolant are measured with float-type rotameters and are recorded manually.

The liquid samples of the working fluid are sampled with a syringe and their concentration is determined with a gas chromatograph (GC). Syringe sampling ports were placed on the strong and weak solution sides. The previous experimental studies had concluded that

www.manaraa.com

measuring the vapor concentration using a GC was causing errors due to condensation of the vapor in the syringe [7–9]. Therefore, vapor concentrations are determined from property relations using the locally measured temperature and pressure, and assuming saturated vapor at the separator and rectifier exits. More details on the equipment used for data collection can be found in Appendix C. Uncertainities related to measurements are also given in details in the Appendix D.

4.1.9 Experimental Method

For each set of conditions to be tested, a standard test routine was established. The first step was to start the heat source and heat rejection sub-systems and to allow circulation in the sub-systems until temperatures were stabilized; then, circulation of the basic strong solution was started. The heat source flow rate was controlled to maintain the desired boiling temperature of the two phase mixture leaving the boiler. With basic solution flow established the weak solution flow from the separator to the absorber was controlled so as to maintain the desired level of solution in the absorber. The boiler pressure was controlled by the amount of vapor allowed to expand through the expander. If the vapor flow rate is increased the boiler pressure is decreased and vice versa. When the expander performance is tested, vapor flow can be varied only by the expander load. However, in order to be consistent with all the conditions tested, the same electrical load was used for all experiments, therefore for a given boiler temperature and strong solution concentration, the expander dictates the vapor flow rate which also controls the boiler pressure. As the solution in the absorber was heated by absorption condensation of vapor stream in the returning liquid, the absorber coolant flow was adjusted to maintain the desired absorber pool temperature.

www.manaraa.com

When the rectifier was active, vapor coolant flow was adjusted to maintain the desired rectifier exit temperature. The feedback and adjustments mentioned were performed manually. The warm-up period of the experiments was approximately 90 minutes, and the stability of the experiments was observed for an additional 30 minutes after reaching the steady-state condition. With the system operating at a specified set of conditions, data acquisition could begin. The data acquisition system recorded measurements at least five minutes, and the liquid solution samples were taken during this period. The experiment was repeated at least three times in order to ensure repeatability.

The mixture temperature exiting the boiling heat exchanger was controlled by the flow and temperature of the heat source fluid. A nominal exit temperature of 85° C was considered. The basic solution concentration was kept constant, approximately 0.40-0.42, as the previous experimental studies concluded that basic solution concentrations over 0.45 lead to larger discrepancy between the experimental and theoretical results [6, 8]. Also, whenever the basic solution is increased, the absorber pressure also needs to be increased in order to eliminate the vapor formation in the basic solution. The vapor was heated with an electrical resistance heating tape which was wrapped around the pipe. The electrical tape heating was controlled with a variable transformer. Given the arrangement only a small amount of superheating was possible, approximately 1-8 °C. The amount of rectification in the experimental setup was determined by the rectifier exit temperature. It should be mentioned that the rectifier coil pinch point limitation made it difficult to vary the rectifier exit temperature. So, the rectifier exit temperature was controlled by the inlet coolant temperature or the vapor inlet temperature.

المنارة للاستشارات

www.manaraa.com

4.2 Expander

Expanders convert mechanical energy from a fluid at high pressure to shaft work by expanding to a low pressure. Expanders are possibly the most crucial component in a power cycle as a small drop in it's efficiency substantially affects the economics. The heat input to the cycle must be increased in order to produce the same output work when turbine efficiency drops. The choice of the expander strongly depends on the operating conditions and on the size of the facility. Two main types of expanders can be distinguished as the dynamic (turbo) and displacement (volumetric) types.

Steam turbines are probably one of the most well established machines. Since early 1900s their capacities and sizes have been increasing. At present, 85% of the electricity generated in the U.S. is from steam turbines [29]. The working temperatures of steam turbines have increased from 400 °C to 600 °C, and pressures from 100 bar to 280 bar since 1930s. According to [29], specific cost for a turbine and a fossil-fuel plant can decrease by 30% and 15%, respectively, if the the system capacity is increased from 300 MW to 1200 MW. It is estimated that the capacity of the largest steam turbines will be around 1300-1500 MW in near future [29]. However, the interest in developing steam turbines of 100 kW to a MW has recently grown due to biomass, waste heat and combined system applications [110].

Inoue et al. [27] presented the results of the development of a simple and compact power generator driven by waste heat, assuming hot water at a temperature of 80 °C to 90 °C as the heat source. They did a feasibility study on the characteristics of a low temperature power cycle and selected Trifluoroethanol, R123 and F245fa as suitable for the cycle to optimize

www.manaraa.com

the cycle efficiency. A radial turbine was adopted as an expander and it was designed using an inverse design method, where the 3-D blade geometry for specified blade loading distribution was numerically obtained. Their experimental results showed that the electrical power output from their Rankine cycle was 13.5 kW, with a cycle efficiency of 7.0% at 77 °C evaporator temperature and 42 °C condenser temperature. The turbine efficiency was targeted at 80%, and their result showed that the efficiency was around 60-70% with a speed of 15000 rpm. Turbines are designed with a clearance between the blade tips and the volute to allow free rotation; however, leakage at the tips is the primary cause of irreversibility in the expansion process [110]. The amount that the blade tip clearances can be reduced is limited because of the centrifugal force applied on the blade and thermal expansion of the blade. Large scale turbines suffer significantly from radial blade deformation and are not suited for the reduction of blade tip clearances. On the other hand, when turbine size is decreased, blade tip clearances do not change significantly, and the tip clearance loss becomes significant as a percentage of the total loss of output.

Martin and Goswami [6, 7] used a radial turbine for the experiments to validate the sub-ambient turbine exhaust temperatures. The expander used in the experiments was a modified single-stage, partial admission turbine originally designed for use in an air-cycle cooling system. The potential of cooling output from the cycle was verified by the temperature difference between the absorber and expander exit. However, the minimum cooling temperatures obtained in the experiments were higher than expected, and they explained the reason as the poor performance of the expander. They discussed that the expander's isentropic efficiency was between 20% and 35%. The mechanical power generated by the

المنارة للاستشارات
www.manaraa.com

expander was not directly measured, also heat transfer across the expander was accounted for the low efficiency of the modified turbine. The turbine speed was approximately 20000-30000 rpm during the experiments.

Typical expander operating speeds range from 1000 to several thousands rpm. Centrifugal force applied on the blade is dependent on blade tip speed, and this is a function of the rotor rotational speed and the diameter. To investigate whether rotational turbines are applicable to low scale systems, a preliminary study is conducted and the results are shown at Table 4.1. Ammonia is used a working fluid, and the turbine inlet pressure and temperature are 6 bar and 80 °C, respectively and exit pressure is 3 bar. Two cases are investigated, in the first one turbine exit temperature is 40 °C, as the inlet and exit conditions are specified, the turbine efficiency can be calculated, which is approximately 75%. In the second case, the turbine exit temperature is 32 °C, and turbine efficiency is calculated approximately 91%.

The specific speed of a turbine is defined as,

$$N_s = \frac{\omega \sqrt{Q_2}}{(\Delta h_{ideal})^{3/4}} \tag{4.1}$$

where Q_2 is the volumetric flow rate through the turbine at rotor exit, ω (rad/s) turbine rotational speed, Δh_{ideal} (J/kg) ideal turbine work. The specific speed for a radial turbine is at optimum for a radial turbine at a value of 0.6 [110, 111]. The velocity ratio, U/C_o, where U is the rotor tip speed and C_o is the velocity based on the ideal enthalpy drop of turbine as $C_o = (\Delta h_{ideal})^{1/2}$, optimizes the turbine efficiency when it is equal to 0.7.

المنارة للاستشارات
www.manaraa.com

Table 4.1 Turbine parametric analysis for a given specific speed of 0.6

	Rotor (S: Speed, D:Diameter, MF: Mass flow)					
	Turbine Exit Temperature=40 °C			Turbine Exit Temperature=32 °C		
	Tip speed=197.8 m/s			Tip speed=219.3 m/s		
	Efficiency=~75%			Efficiency=~91%		
Power (kW)	S (rpmx10^3)	D (mm)	MF (g/s)	S (rpmx10^3)	D (mm)	MF (g/s)
1	345.3	10.9	12.5	453.4	9.2	10.2
5	154.4	24.5	62.6	202.9	20.6	50.9
10	109.2	34.6	125.3	143.5	29.2	101.9
25	69.1	54.7	313.2	90.7	46.2	254.7
100	34.5	109.4	1252.7	45.3	92.3	1018.7
500	15.4	244.6	6263.6	20.3	206.5	5093.6
1000	10.9	345.9	12527.2	14.4	292.0	10187.3

As it is seen in Table 4.1, when the output of the turbine is reduced from a MW scale to a kW scale, the turbine speed needs to be increased from 10 thousand rpm to 345 thousand rpm, which is significant. Two different turbine efficiencies are analyzed, when the efficiency goes up from 75% to 91%, the rotational speed needs to be increased approximately from 30% to 40%. It's clear from Table 4.1 that a rotary turbine design at a low power capacity is a challenging task. For ammonia, with high rotor tip speeds, the calculations resulted in high rotor speeds with small diameters, which will also cause impractically small inlet flow passages with enlarged rotor diameters for small scale systems. It is well known that designs for heavier organic fluids result in efficient geometries at small sizes, at reasonable shaft speeds and inlet flow areas even with small diameter rotors [112, 113].

Badr [114] stated that sealing is one of the important factors for the high speed turbines, and summarized the major problems of using expanders in Rankine engine of less than 50 kW output, as:

- Very low efficiencies

المنارة للاستشارات
www.manaraa.com

- High production costs, especially for multiple rotor expansion systems,
- The possibility of a high moisture content in the expanding vapor, which can result in rapid erosion of the turbine blades.

Efficiencies of turbines diminish when they operate at off-design conditions, i.e. rotational speeds other than the design-point speed, and on part loads. Also, excessive mechanical stresses and sealing problems may occur if a turbine is required to run at very high speeds. However, to maintain the rotational speed of a turbine at the design point, a complicated and expensive automatic speed control system is required. Mobarek et al. [115] suggested a specially-designed, 10 stage, radial outflow turbine for a solar Rankine cycle system providing power outputs in the range of 100 kW; their results showed an efficiency of 71% (at 8300 rpm and 100 kW output) and a rotor diameter of 0.52 m .

Comfort [116] developed and tested a two phase expander which uses a low quality steam-water mixture as the working fluid. The expander efficiency was 23% for a single-nozzle test, and for full admission performance, efficiency was measured between 38% to 41%. The inefficiencies in the turbine came from the droplets, therefore, reducing the droplet size is expected to increase the efficiency of the expander. Takeshita et al. [92] developed an ammonia-water mixture (AWM) turbine system to enhance the overall cycle efficiency of a “trianary turbine cycle system” which is composed of a gas turbine and a steam turbine and the AWM turbine system. The turbine type used for their experimental results is an axial impulse type Curtis turbine with 40% efficiency, inlet absolute pressure was 15 bar and the output capacity was 60 kW at 3000 rpm.

المنارة للاستشارات
www.manaraa.com

Positive displacement expanders are more suited for small scale systems when the tip losses are considered for rotating expanders [110, 111]. Positive-displacement machines such as reciprocating and rotary piston, rotary vane, and screw operate by expanding a fixed volume of fluid per oscillation. Balje [111] showed the performance characteristics of various expander types and it was shown that throughout the low specific-speed regime, positive-displacement expanders have greater efficiencies than single-stage turbines. Rotary positive-displacement expanders achieve about the same isentropic efficiencies as single-stage turbines at smaller specific diameters, and consequently allow rotor-tip speeds which are only one-quarter to one-third of the values required for single stage turbines. Besides, lower operational pressure ratios are needed for positive-displacement machines. However, reciprocating machines have some drawbacks;

- Torque pulsation is a common phenomenon due to the inherent discontinuity associated with the finite number of pistons or lobes and fixed displacement,
- Reliability is also an issue with positive-displacement machines because of a greater number of moving parts with the associated inherent balancing problems and in the case of pistons, a lubrication system to reduce leakage encountered in the gap between the moving seals and volute,
- Poor breathing characteristics due to the high fluid-friction losses across the valve systems,
- Lubrication difficulties, when operating with steam as the working medium
- High manufacturing costs.

المنارة للاستشارات
www.manaraa.com

As an example, Ibaraki et al. [117] applied to recover and reuse of waste heat from an automobile engine with a rotary piston type expander. They stated that the heat discarded from the engine accounts for at least 40% of the heat generated by the fuel. They selected a volumetric type expander with piston that can produce an output even from a small flow rate. The expander geometric expansion ratio and maximum speed were 14.7 and 3000 rpm, respectively. The calculated efficiency of the expander was 13% at it's peak value when the input heat rate was 23 kW. The theoretical efficiency calculated from the thermal properties of steam was approximately 25%. The problem encountered by Ibaraki et al. [117] was sealing; they mentioned the main losses of the expander were steam leakage because of sealing problem, friction losses of pistons (7 cylinder expander), and heat loss to the environment.

Rotary vane expanders possess high tolerances for a wide range of vapor qualities of the working fluid, also provide some additional advantages such as self-starting under load and smooth torque production. Badr et al. [118] measured the experimental performance of rotary vane expander using various organic fluids and steam as the working fluid, and found the isentropic efficiency of the expander to be in the range of 60% to 73% for the following operating condition ranges: rotational speed of 2000-2500 rpm, inlet pressure of 4-7 bar and inlet temperature of 102.2-131.5 °C, and working fluid as R-113. Some difficulties regarding the operation were noticed by Badr et al. [118], such as increased blade/stator friction caused consequent reduction of power output, and likelihood of mechanical failure of the blade.

www.manaraa.com

Another interesting device is the Wankel engine, which has been the subject of research and development for many years, primarily within the automotive industry. Wade et al. [119] tested a Wankel type expander where high pressure steam is used as the working fluid (27.6-65 bar, 231-410 °C). Their work suggested that the device reached mechanical efficiencies in the range 60 to 80%, though significant hydrodynamic losses were observed during the experiments. Badr et al. [114] indicated that Wankel engines encounters lubrication problems. Similar to the rotary vane expander, the major lubrication problem in a Wankel engine was associated with sealing.

Helical screw expanders have been widely used as the expansion devices in Rankine cycle plants, especially for solar-powered applications. Some research has been done on the performance of screw expanders; Merigoux and Pocard [120] worked on a screw expander with oil injection, which was the prime mover for a R-113 Rankine system in the 5-50 kW power range, with an isentropic efficiency of 70% when running at a speed of 4200 rpm. Lorenzo et al. [121] concluded that screw machines offered the advantages of simpler design and higher efficiencies in the 15-200 kW range while operating at 25% of the rotational speeds of turbines with the same power outputs. Steidel et al. [122] presented another screw type expander's performance which showed that for a rotor diameter of 0.13 m and a device length of 0.166 m, a maximum isentropic efficiency of approximately 40% was obtained at 9043 rpm, when employing steam of 32.4% quality as the working fluid at an inlet pressure of 7.8 bar and an operating pressure ratio of 7.1. In an another helical screw study [123], single-stage expansion of self-pumped geothermal fluids from reservoirs at 176 °C to 400 °C gave engine efficiencies in the range from 43.1% to 57.3%. In

المنارة للاستشارات
www.manaraa.com

this study, the rotor diameters ranged from 3.2 m to 12.7 m for a range of outputs of 5 MW to 40 MW. For a two stage expansion, with a 300 °C reservoir, the engine efficiency reached 62.3% and the diameter of the larger rotor was reduced by 21%. It was suggested that rotor diameters can be held to more reasonable sizes by using the expander in combination with a vapor turbine. In a different study [124], a 1 MW geothermal electric power plant that featured a helical screw expander was produced and then tested with a demonstrated average performance of approximately 45% expander efficiency over a wide range of test conditions in non condensing operation on two-phase geothermal fluids.

The rotational speeds of the screw expanders are higher than the recommended operational speeds of some of the driven equipment, so that reduction gear boxes and speed-control equipment might be required. Also, helical-screw expanders need a relatively high level of technology in their production. Lubrication of helical-screw machines is achieved principally by employing a working fluid/oil mixture as the lubricant between rotors, as well as the rotors and the casing. The lubrication problem in screw expanders is not as severe as in Wankel engines due to the relatively small, typically allowed running clearances (between the rotors and the casing) which do not lead to significant reductions in the machine efficiencies.

Tesla type [125] turbomachine has a rotor which is composed of flat parallel co-rotating disks spaced along a shaft instead. The working fluid flows between the disks, which results in momentum exchange between the fluid and the disks and hence shaft torque and power. While rotor efficiencies can be very high in this type of turbine, there are inherent losses in the fluid flows entering and exiting the rotor. As a turbine, the nozzles are necessarily

للاستشارات المنارة
www.manaraa.com

long and inefficient. Rice (1994) surveyed the literature for the Tesla turbine use with steam, gas and water, and it was stated that Tesla turbine efficiencies have been low and the machine sizes large per unit of power delivered. Rice (1994) concluded that Tesla type turbine probably cannot prove competitive in an application in which more conventional machines have adequate efficiency and performance. This type of turbomachinery can be applied to the conditions where shaft power is small, or the fluid is very viscous fluid or non-Newtonian. A study by Ke and Hashimoto [126] investigated the performance of Tesla turbine for cryogenic applications. Instead of using co-rotating disks, they used an expansion wheel which is a cylindiral shaft with shallow spiral grooves on its surface. They showed that adiabatic efficiencies of 41.5% can be reached at 20 K by the viscous expander with a 6.2 W of output power at 70,000 rpm, however experimental study is needed to verify the bearing stability.

4.2.1 Scroll Expander

Scroll compressors have been widely adopted by the HVAC industry because of the advantages they offer, including: simple design (i.e. fewer moving parts), low friction and low torque pulsations. High precision technologies are required to manufacture scrolls. For this reason, scroll devices emerged in the late 1980s with the development of computer guided manufacturing machines. Literature suggests the potential use of a scroll expanders modified from scroll compressors, as high efficiency expanders [10, 11].

A scroll device consists of two identical spiral elements assembled with a 180° phase difference as shown in Fig. 4.13. Two, spiral-shaped members fit together, forming crescent shaped gas pockets. During operation, one member remains stationary, while the

المنارة للاستشارات
www.manaraa.com

second orbits relative to the first. This configuration allows the moving scroll to rotate in an orbiting motion within the fixed scroll. The phase difference between the two scrolls is accomplished by using an anti-rotation device, such as an Oldham coupling. The expander inlet is at the center of the scrolls. The orbiting motion creates a series of gas pockets traveling between the two scrolls. On the inner portion of the scrolls, the pockets draw in the working fluid, from where the fluid progressively moves to the outer pockets of the scrolls. As the fluid moves through the increasingly larger outer pockets, the temperature and pressure decrease to the desired discharge pressure.

Another advantage of this device is that it does not require inlet or exhaust valves which reduces noise and improves the durability of the unit; furthermore the relative rolling motion of the contact points offers less resistance than sliding friction. Additionally, the rolling contacts provide a seal such that large volumes of oil used as a sealant are not required and leakage is reduced [127]. The scroll expander can start under any system load without any start components. Also current scroll devices have a compliant design which provides both axial and radial compliance between scroll members, and this increases the life of the scrolls. Axial compliance allows the scroll to remain in continuous contact in all normal operating conditions, ensuring minimal leakage without the use of tip seals. Radial compliance allows the scroll members to separate sideways so debris can pass through, substantially improving durability and reliability [127].

Quoilin et al. [113] carried an experimental study which tested the performance of a scroll expander. The working fluid was refrigerant R-123. The scroll expander was originally an oil free open-drive scroll compressor, adapted to operate in reverse. The

المنارة للاستشارات
www.manaraa.com

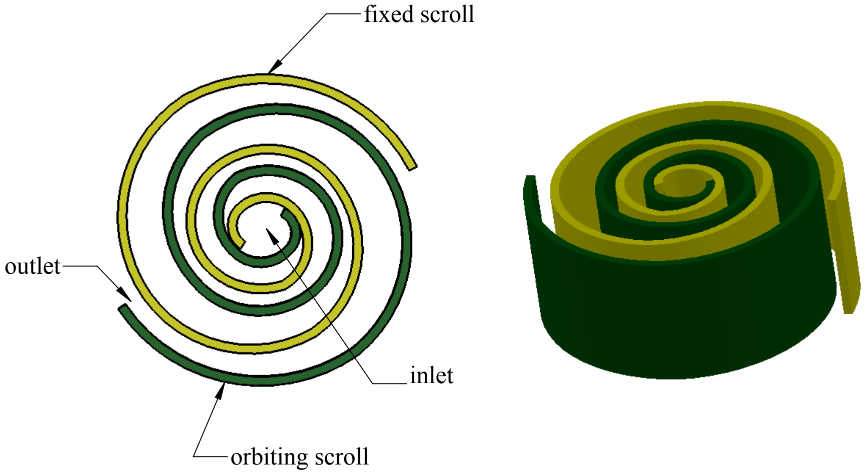

Figure 4.13 Scroll geometry and 3D views of scrolls

expander rotational speed was between 1771 rpm and 2660 rpm. An expander isentropic efficiencies of 42% to 68% were reached for the pressure ratios of 2.7-5.4.

It is a well-known fact that a reduction of the vehicle weight reduction and improvement of engine thermal efficiency are important for the improvement of vehicle fuel economy [128]. Oomori and Ogino [128] conducted research on the application of Rankine bottoming system to passenger cars, with an attempt to combine the evaporative engine cooling and Rankine bottoming system to simplify the overall waste heat recovery system. The expander used in their experiments was a scroll type expander with an inlet volume of 40 cc and an expansion ratio of 2. They varied the expander speed between 800 rpm and 2200 rpm, and the pressure ratio between 1.2 and 3.2. They found the maximum efficiency of the expander as 50%, operating speed at a speed of 1100-1500 rpm with the vapor inlet temperature of 70 °C to 100 °C. The efficiency of the expander began to drop as the rotational speed became lower than 1000 rpm, which was probably due to the deterioration

www.manaraa.com

of sealing performance between the rotor and the housing which resulted in leakage of the working fluid.

Ammonia offers particular challenges to the design or selection of any expander, such as corrosiveness. Ammonia is corrosive to copper and copper containing alloys present in the bearings and motor stators of hermetically sealed compressors. Additionally, ammonia is a small molecule (17 g/mole) and thus has relatively low density compared to hydrofluorocarbons used for refrigeration, such as, R134-A (102.0 g/mol), R245-FA (168.5 g/mole), R404-A (97.6 g/mole). Therefore, it is more prone to leak compared to hydrofluorocarbon based refrigerants.

The present experimental study was aimed to predict the scroll expander performance with ammonia vapor which is not available in the literature. Instead of using a custom scroll expander design, an off-the-shelf open drive unit used in the truck refrigeration units was bought and modified. Custom design and fabrication of scroll expander can be costly, however, its performance and feasibility in the combined power and cooling cycle will provide a basis for further research and design to improve the scroll expanders and other small scale power generation systems.

The scroll unit selected for the experimental study is shown in Fig. 4.14. The open drive unit is modified and the copper based materials used in the unit were replaced by ammonia compatible elements. A generator was coupled with the scroll expander in order to measure the power output directly from the experimental setup. The scroll shaft was connected to the generator by a pulley system and the electrical output of the generator was measured by voltage and current transducers. The loading of the system is done by electric

المنارة للاستشارات
www.manaraa.com

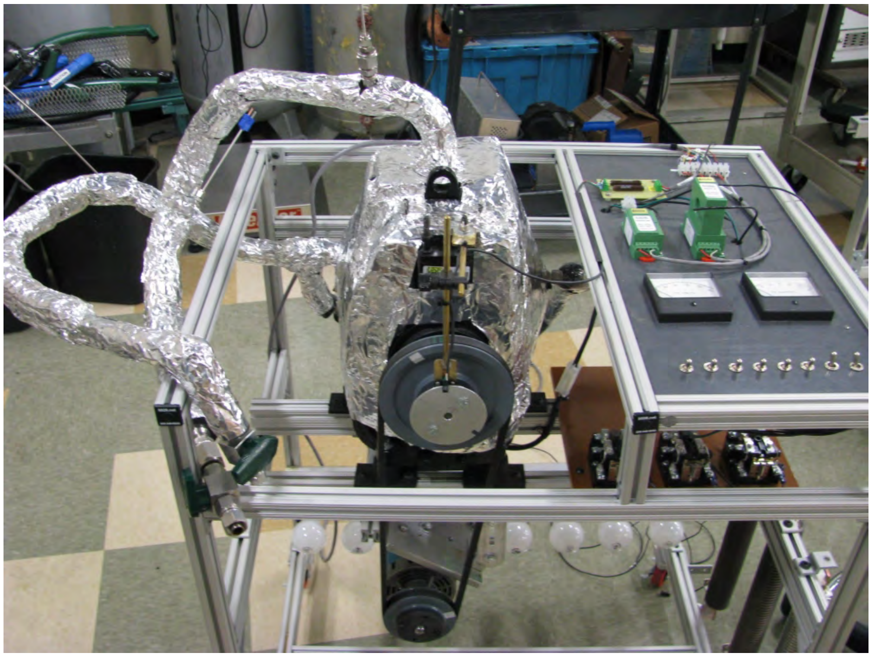

Figure 4.14 Modified scroll expander used for experimental testing

resistance light bulbs as shown in the bottom of the Fig. 4.14. One drawback of using a scroll device for an absorption based cycle is that oil can be carried to the absorber and mix with the strong solution ammonia-water mixture by the vapor flow. Scroll devices require oil to cool and seal between the orbiting and stationary scrolls as explained before. In order to maintain the oil lubrication, three devices are generally used: an oil separator, an oil level regulator, and oil reservoir. Other elements, such as oil strainers may be needed to complete the system. In a closed refrigeration system, oil is swept back to the compressor by the flow of refrigerant. The velocity in the evaporator tubes is usually sufficient to carry the oil back. However, when the scroll device is used as an expander for an absorption based system, without the oil separator and filters, some amount of oil is mixed with the working fluid.

المنارة للاستشارات
www.manaraa.com

Table 4.2 Scroll expander details

Volumetric ratio	4.20
Outlet volume (cm^3/rev)	98.16
Inlet volume (cm^3/rev)	23.37
Pulley diameter (cm)	15.11
Generator pulley diameter (cm)	10.03

The expander was connected to the inlet vapor tubing by using 3/8” O.D. stainless steel tubing, and the discharge port was 1/2” O.D. Due to the heat transfer losses at the flexible hoses which connect the scroll expander unit to the cycle, additional thermocouples were added at the inlet and exit tubing of the expander. Some details of the expander are given in Table 4.2. Additional details of the generator are given in Table C.5.

المنارة للاستشارات
www.manaraa.com

Chapter 5

Experimental Results

The experimental setup was designed to explore the operating issues with the power-cooling cycle and its components. Initial experiments were done by simulating the expansion process of the turbine by using a throttling valve and cooling the vapor after the valve. These initial experiments confirmed the operating trends of vapor production and concentration variation in the cycle. The experiments with the scroll expander were performed under three different conditions: the vapor exiting from the rectifier is saturated vapor (SV), superheated vapor (SHV), and rectified and superheated vapor (RSHV). These conditions will be explained in detail in the following subsections.

Martin's [7] experimental work showed the expected trend of an increase in vapor flow with temperature and concentration, which was also shown theoretically in Chapter 3. Therefore boiling temperature and ammonia concentration in the strong solution was not varied in this work; the ammonia concentration was kept in a range of 0.40-0.43. As most of the experimental components were upgraded or modified from the earlier setup, initial experiments were performed to test the vapor production and system stability. Therefore, experiments without the expander will be discussed first to show the system efficiency in vapor production. Then, experiments with the expander will be discussed in this chapter.

www.manaraa.com

Table 5.1 Averaged conditions for experiments without expander

Temperature	°C
Absorber	39.3±1.0
Separator inlet	88.9±1.0
Separator exit-weak solution	86.5±1.0
Rectifier exit-vapor	85.4±1.0
Pressure	bar
Absorber	2.87±0.02
Mass flow rate	g/s
Strong solution	22.04±3.85
Vapor	2.82±0.04
Ammonia concentration	kg NH_3/kg solution
Strong solution concentration	0.41±0.02

5.1 Experiments without the Expander

Initial experiments were performed to find out the stability conditions, including vapor production and ammonia concentration variation in the vapor and weak solution return line. Averaged conditions for the experiments are given in Table 5.1. The temperatures of the mixture entering the separator, weak solution leaving the separator, vapor exiting the rectifier and mixture in the absorber are plotted in Fig. 5.1 as a function of boiler pressure.

As it is shown in the figure, the absorber temperature is constant for different boiler temperature cases. Due to heat transfer losses, there is approximately 3 °C difference between the mixture leaving the boiler heat exchanger and vapor and weak solution mixture temperatures, as shown in detail in Fig. 5.2. Temparatures of the vapor leaving the rectifier column and the weak solution mixture are very close, which defines the boiler temperature to verify the experimental results. In the theoretical simulations, the temperature across the boiler and separator components were assumed as constant, heat transfer losses are neglected. In order to evaluate the experimental performance of the cycle, several data

www.manaraa.com

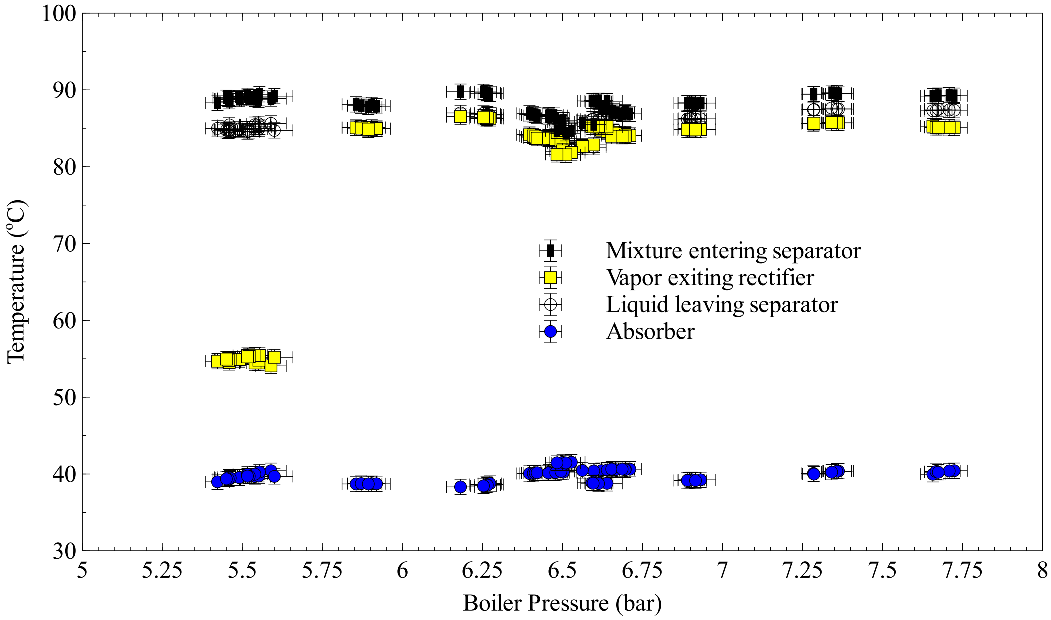

Figure 5.1 Temperature values showing the system stability during the experiments

from the experimental cycle were transferred to the simulation code. The weak solution temperature was assumed as the boiler temperature as uniform temperature conditions were assumed in the theoretical study.

5.1.1 Vapor Production with the Variation in Boiler Pressure

The boiling pressure was one of the most important parameter as it determines the vapor production for the boiler temperature and strong solution concentration in the separator. It was the first parameter that was considered as a system variable and its effect on the vapor production is shown in Fig. 5.3. As pressure decreases more vapor is formed as seen in Fig. 5.3. The value of the vapor mass flow fraction (the mass flow rate ratio of the vapor to the basic solution) error bars increases while the pressure decreases. At a lower boiler pressure, more vapor forms and the boiler heat input increases. For the cases

المنارة للاستشارات
www.manaraa.com

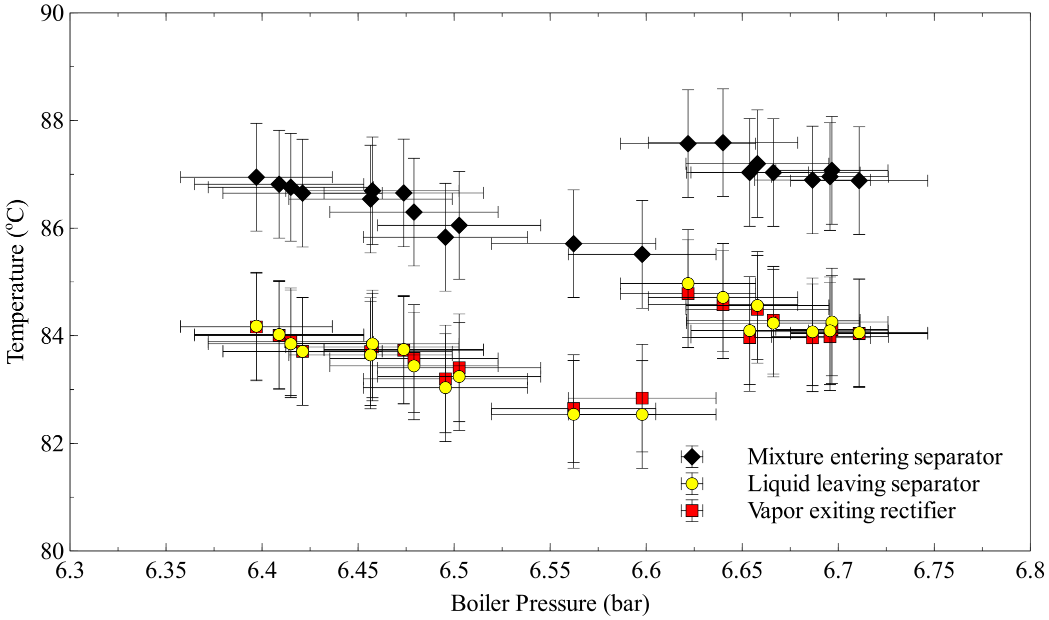

Figure 5.2 Temperature of various points in the cycle showing the system stability during the experiments

where heat input requirement was higher than the boiler heaters capacity, the flow rate of the strong solution was decreased instead of increasing the heat input to the cycle. This caused some instability and fluctuations in both vapor and liquid flow rates, and for this reason, the error bars related to the lower pressure vapor mass flow fraction are larger as compared to the high pressure cases. To obtain Fig. 5.3 throttling valve was used to adjust the vapor flow rate leaving the separator, when larger amounts of vapor was allowed to expand through the valve, the boiler pressure decreased. As it is seen from the figure, the discrepancy between the experimental results and the simulated results increases with the boiler pressure. The measured vapor flow rate is consistently lower than that expected from the equilibrium model indicating some inefficiencies in the vapor production process. After the vapor-liquid mixture enters the separator, the vapor is separated from the liquid

المنارة للاستشارات
www.manaraa.com

by gravity, however, even though the vessel was insulated, there are external losses, and the vapor condenses on the separator vessel wall. The value of the vapor mass flow fraction is reduced because of this additional condensation on the vessel wall.

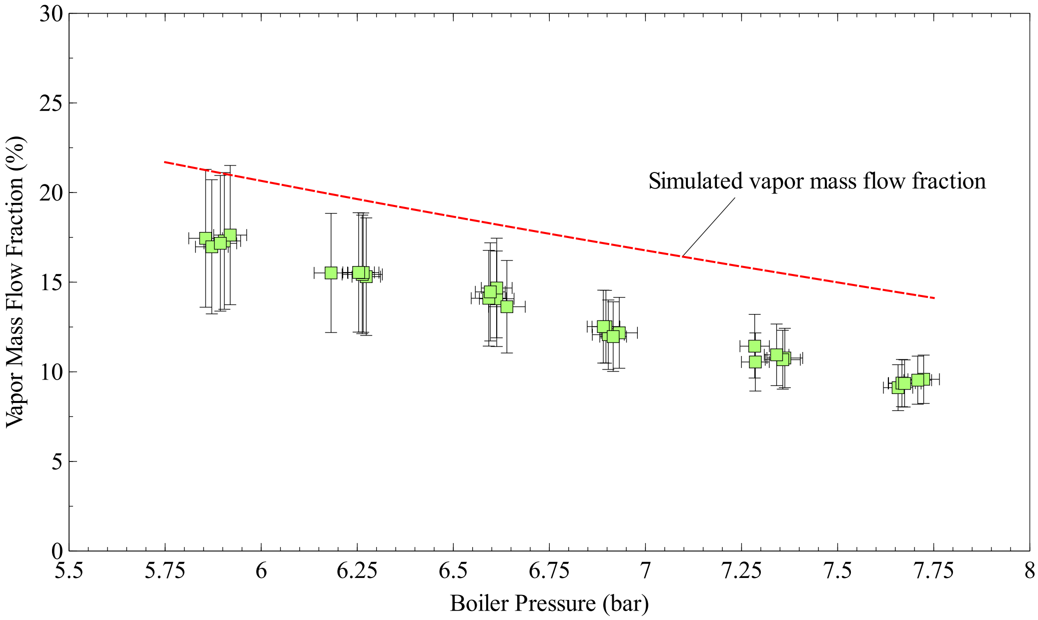

Figure 5.3 The effect of boiler pressure on experimental and simulation values of vapor mass fraction

5.1.2 Ammonia Concentrations with the Variation in Boiler Pressure

The concentrations of the strong solution, weak solution and vapor are shown in Fig. 5.4. As discussed in the previous chapter, the vapor concentration is not measured, it is assumed that the vapor leaving the rectifier is at saturated vapor condition, and the dew concentration value for the corresponding pressure and temperature is assumed for the vapor concentration. The vapor condensation on the separator vessel wall raises the vapor temperature and the ammonia mass fraction in the vapor region as discussed above, this raises the ammonia mass fraction in the weak solution as well. Water is more prone to

www.manaraa.com

condensation than ammonia, however the condensate liquid is still very high in ammonia concentration as shown in Fig. 5.4. The incomplete liquid and vapor separation contributes to the higher ammonia concentration in the vapor and weak solution than expected. As a result, it can be concluded that there is a some degree of inefficiency related to the vapor production, the vapor mass flow rate ratio and the concentration results shown in Figures 5.3 and 5.4, this causes lower vapor production rates, higher vapor and weak solution concentrations than expected. The discrepancy in the concentration values will be shown in the next section by a mass balance across the separator.

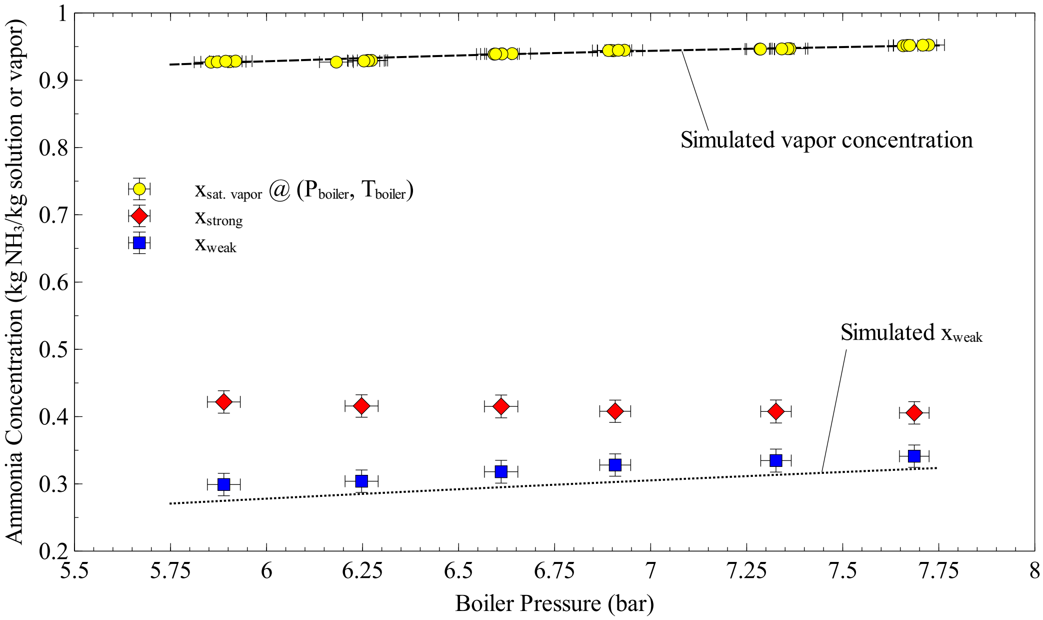

Figure 5.4 The effect of boiler pressure on experimental and simulation values of ammonia concentration

5.2 Experiments with the Expander

Experiments with the expander were performed for three different cases. Averaged conditions for the experiments are given in Table 5.2. The tubing that connects the rectifier

www.manaraa.com

and turbine inlet causes a temperature drop, even though the tubing was insulated. The first case, SV, examines the effect of this condition, both pressure and temperature drops through this tubing, so the turbine inlet condition is assumed as saturated vapor. In the second case, SHV, the vapor entering the turbine is heated until its temperature reaches the temperature at the rectifier exit, so the heat loss between the rectifier and the turbine connection tubing is compensated. Final case, RSHV, is similar to SHV except that the rectifier is in operation in this case. The rectified vapor is reheated before entering the turbine to make up for the heat loss in the piping between the rectifier and the turbine. The vapor production and concentration of the experiments are shown first for each case, and then the performance of the expander, work production and generator output will be shown lastly.

5.2.1 Vapor Mass Flow Fraction

Vapor mass fraction for the saturated (SV), superheated (SHV) and rectified and superheated (RSHV) cases are shown in Figures 5.5-5.7. As expected, there was a discrepancy between the simulated vapor mass fraction and the experimental values.

5.2.2 Ammonia Concentrations in the Liquid Solutions and Vapor

The concentration of strong solution, weak solution and vapor for the saturated (SV), superheated (SHV) and rectified and superheated (RSHV) cases are shown in Figures 5.8-5.10. Mass balance calculation across the separator was used to calculate the expected vapor concentrations. As discussed above, the assumption of saturated vapor condition to calculate the vapor concentration can be misleading when no rectifier is used. For the rectification case, the results agree as shown in Fig. 5.10. As shown in the figures, the error

www.manaraa.com

Table 5.2 Averaged conditions for the tests with the expander

	SV	SHV	RSHV
Temperature		°C	
Absorber	41.5±1.0	40.4±1.0	39.7±1.0
Separator inlet	84.7±1.0	86.8±1.0	89.0±1.0
Separator exit-weak sol.	82.1±1.0	83.9±1.0	84.9±1.0
Rectifier exit-vapor	81.8±1.0	83.9±1.0	55.0±1.0
Expander inlet	76.5±1.0	85.49±1.0	54.6±1.0
			58.4±1.0
			61.0±1.0
Expander exit	63.3±1.0	68.8±1.0	43.7±1.0
			44.6±1.0
			46.5±1.0
Pressure		bar	
Absorber	3.01±0.01	2.96±0.01	2.83±0.018
Expander inlet	6.03±0.02	6.13±0.02	5.11±0.02
Expander exit	3.85±0.01	3.97±0.01	3.35±0.01
Mass Flow Rate		g/s	
Strong solution	21.81±3.81	19.47±3.81	16.55±3.86
Vapor	3.21±0.04	3.24±0.04	2.58±0.04
Ammonia concentration		kg NH_3/kg solution	
Strong solution	0.43±0.02	0.43±0.02	0.40±0.02

bars related to x_{vapor} were very high compared to saturated vapor assumption value. This is due to the error related to the flow measurements of strong solution and weak solution. The uncertainty calculations are given in Appendix D.

5.2.3 Vapor Enthalpy

The vapor enthalpies for different concentration values are shown in Fig. 5.11, since the vapor concentration is very important to calculate the expander performance. The concentration calculation and the assumptions were discussed before, and it was shown that there was a significant discrepancy between the calculations based on saturated vapor assumption and mass balance.

www.manaraa.com

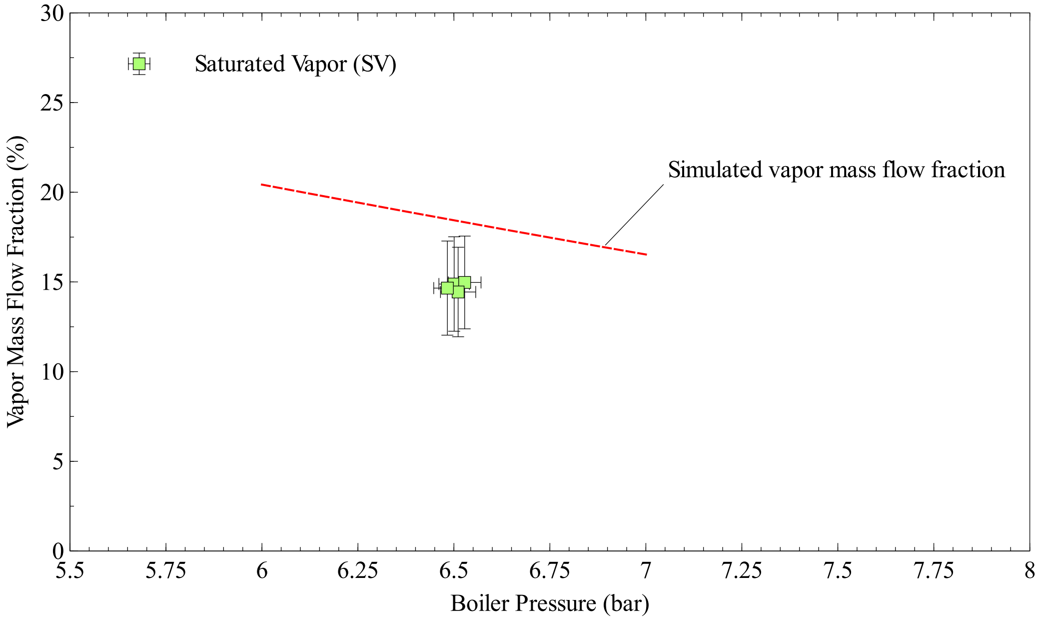

Figure 5.5 Measured and simulation values of vapor mass flow fraction for SV case

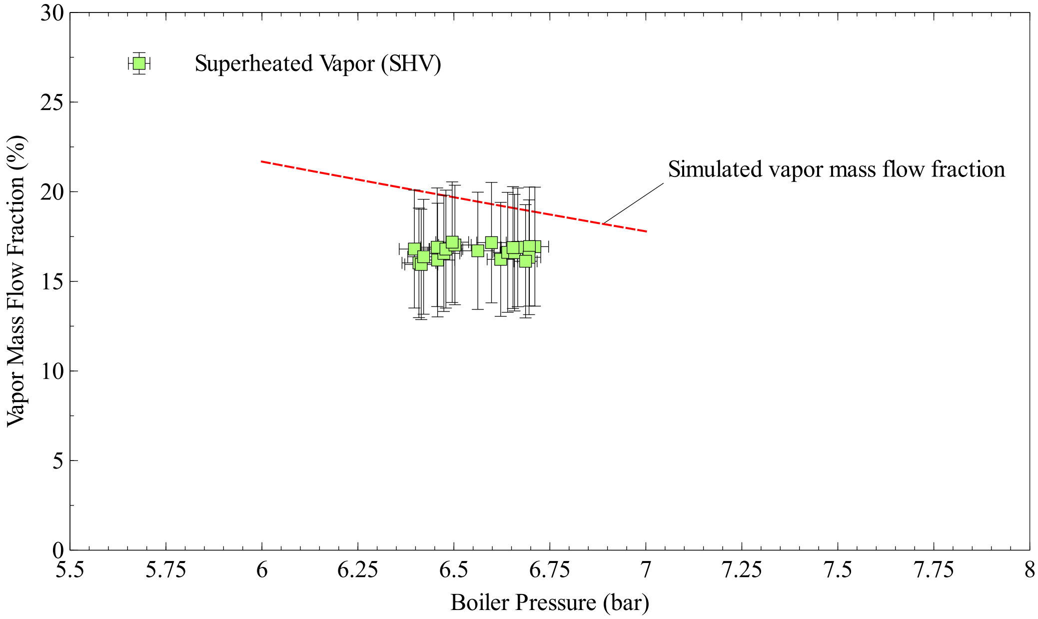

Figure 5.6 Measured and simulation values of vapor mass flow fraction for SHV case

www.manaraa.com

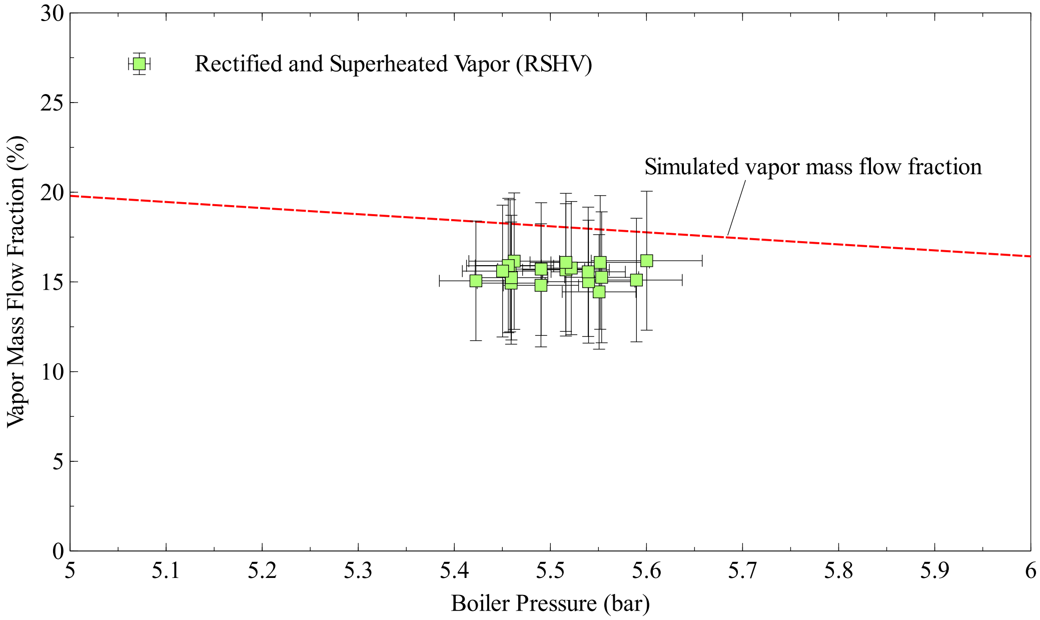

Figure 5.7 Measured and simulation values of vapor mass flow fraction for RSHV case

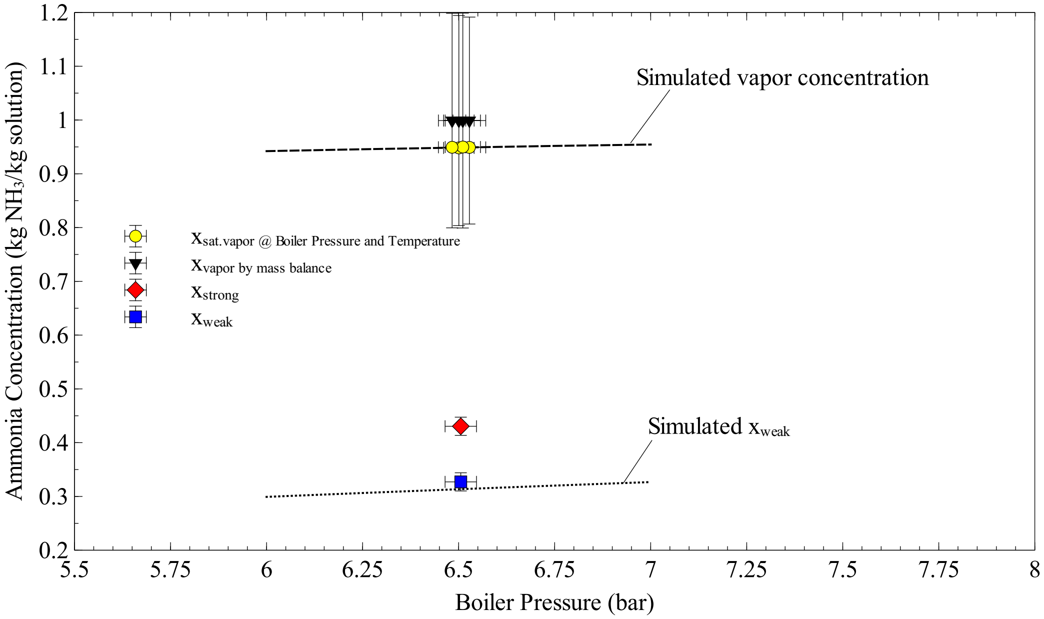

Figure 5.8 Measured and simulation values of ammonia concentration for SV case

المنارة للاستشارات
www.manaraa.com

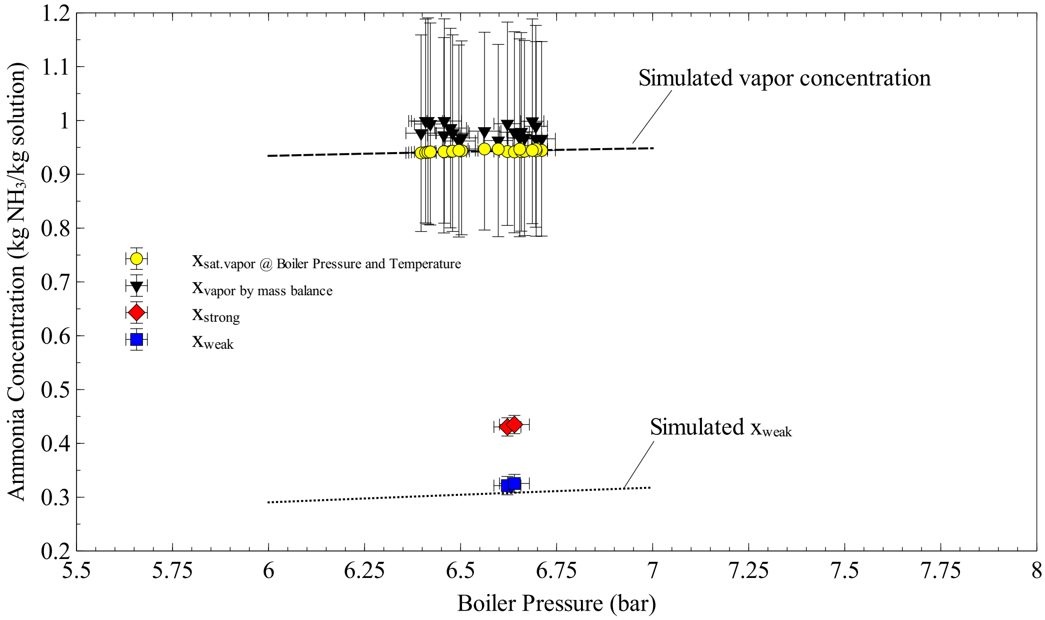

Figure 5.9 Measured and simulation values of ammonia concentration for SHV case

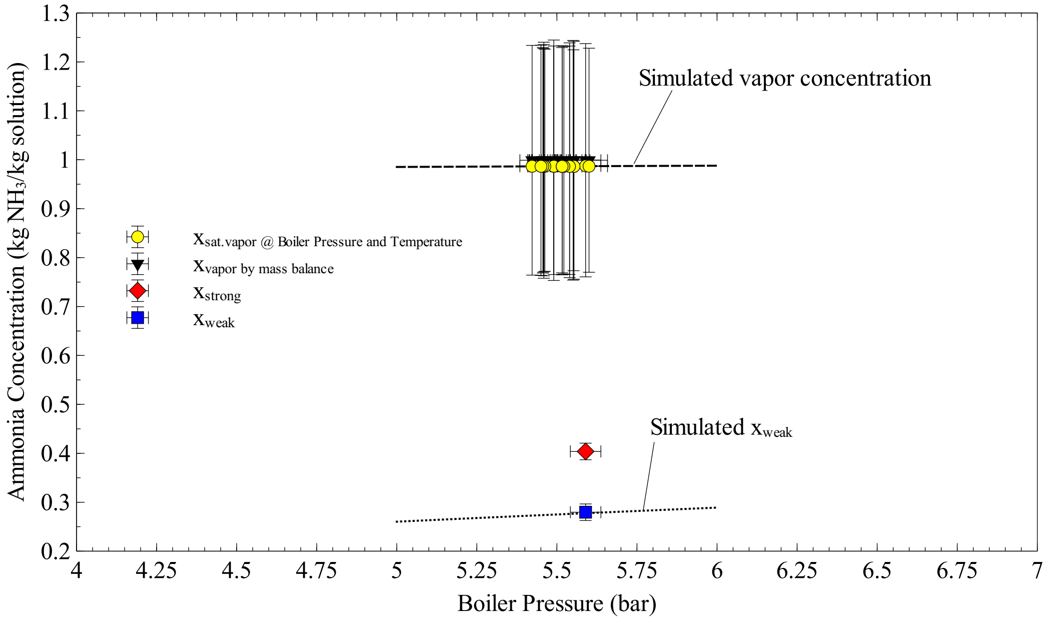

Figure 5.10 Measured and simulation values of ammonia concentration for RSHV case

www.manaraa.com

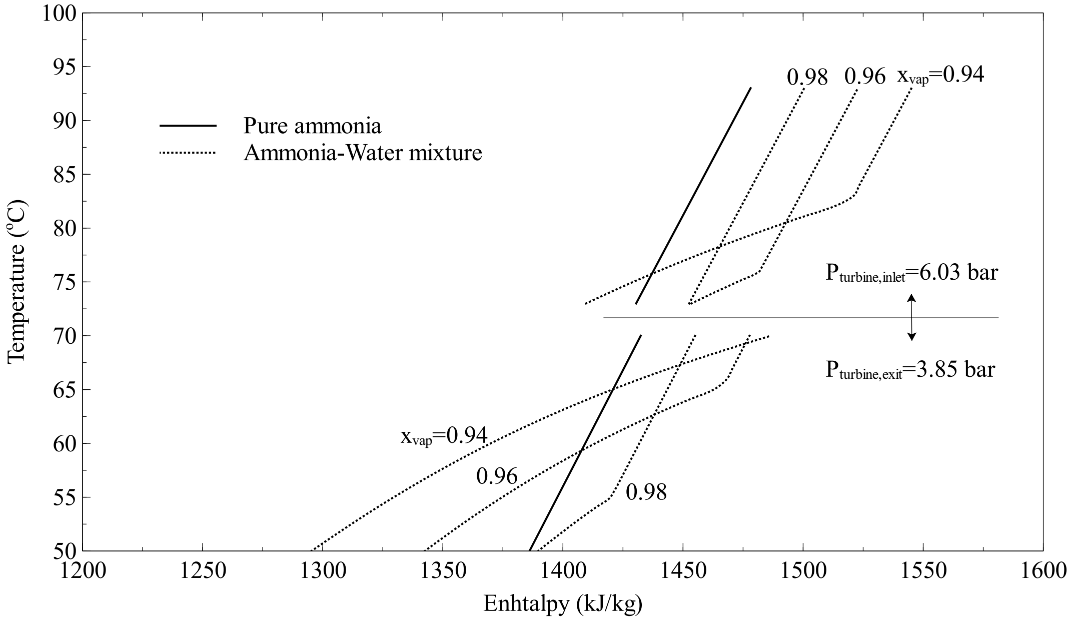

Figure 5.11 Enthalpy values for different vapor concentration

The vapor enthalpies calculated by the saturated vapor and mass balance assumptions for the saturated (SV), superheated (SHV) and rectified and superheated (RSHV) cases are shown in Figures 5.12-5.14.

As shown in Fig. 5.15, when the rectifier temperature is below 66 °C, the concentration value from the saturated vapor assumption is bound between 0.98 and 1.0. It was shown in Fig. 5.14 that the expander enthalpy drop is not affected significantly when the vapor concentration is above 0.98.

5.2.4 Expander Performance

Experimental measurements of the expander performance for all cases are shown in Fig. 5.16. As discussed above, the assumption of saturated vapor condition for the vapor concentration calculation leads to some difficulties for the thermodynamic performance

www.manaraa.com

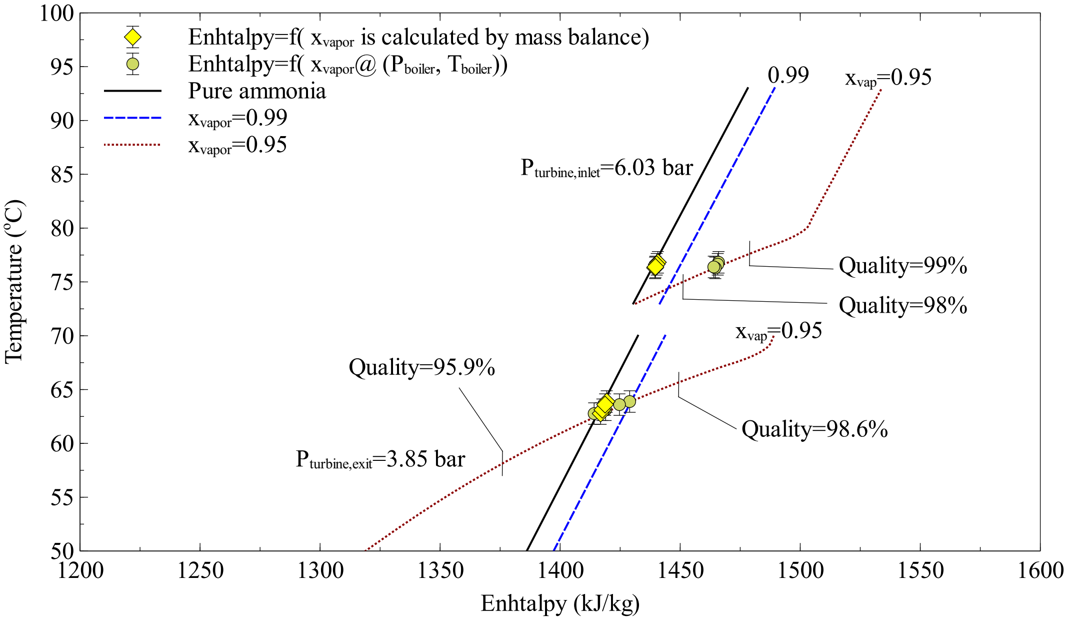

Figure 5.12 Effect of vapor concentration on enthalpy drop for SV case

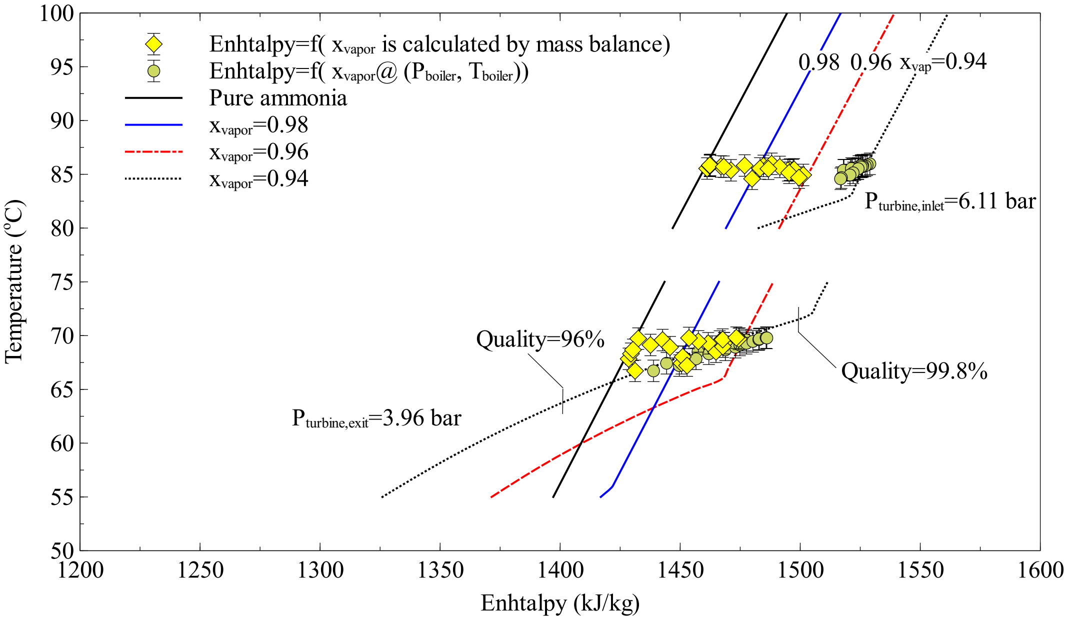

Figure 5.13 Effect of vapor concentration on enthalpy drop for SHV case

www.manaraa.com

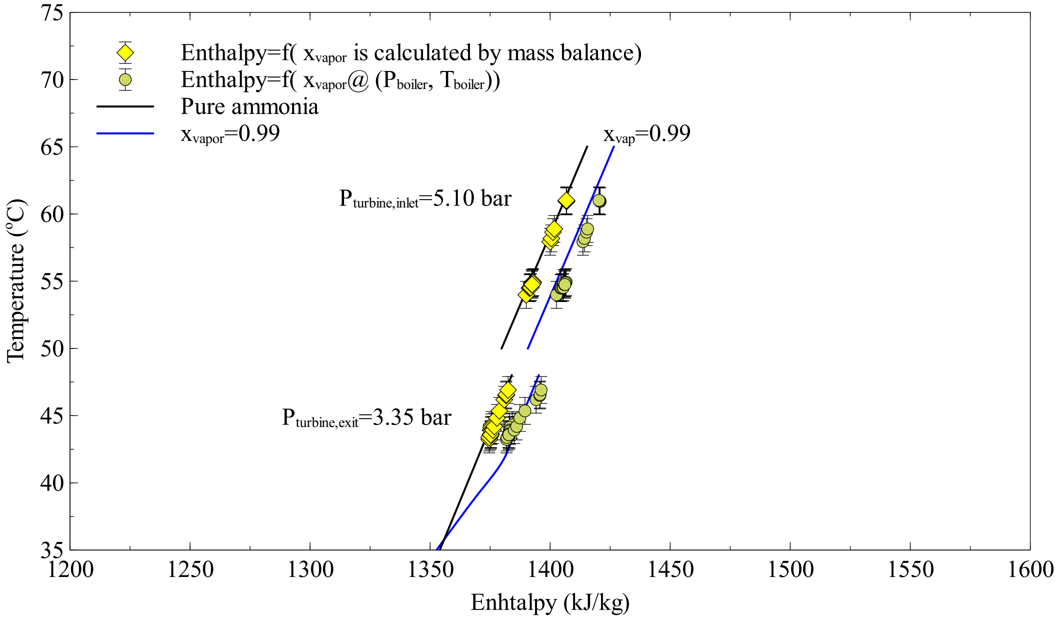

Figure 5.14 Effect of vapor concentration on enthalpy drop for RSHV case

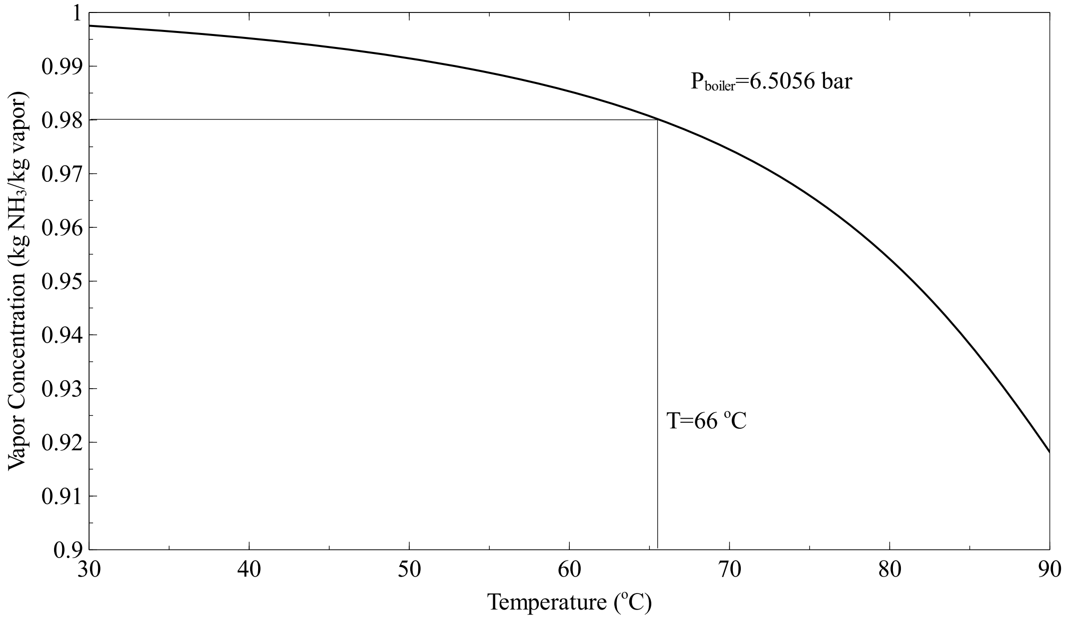

Figure 5.15 Measured effect of rectifier temperature variation on vapor quantity

www.manaraa.com

calculation of the expander. Specifically, the turbine efficiency values were higher than the theoretical limit of 100% for some of the saturated and superheated experiments. It was concluded that the efficiency calculations based on thermodynamic measurements seem to be very sensitive to the inlet conditions. Therefore, to calculate the concentration of vapor at the turbine inlet, mass balance calculations were used for the SV and SHV cases, and saturated vapor condition was assumed at the rectifier exit for the RHSV case. It is shown in Fig. 5.16 that the expander performance was between 40-50% for the SHV case, the expander operates poorly for the SV case. The rectification case also shows the effect of superheating on expander efficiency. As superheating was performed in three steps, the last two steps (3 °C and 6 °C of superheating) lies on the 40% expander efficiency line.

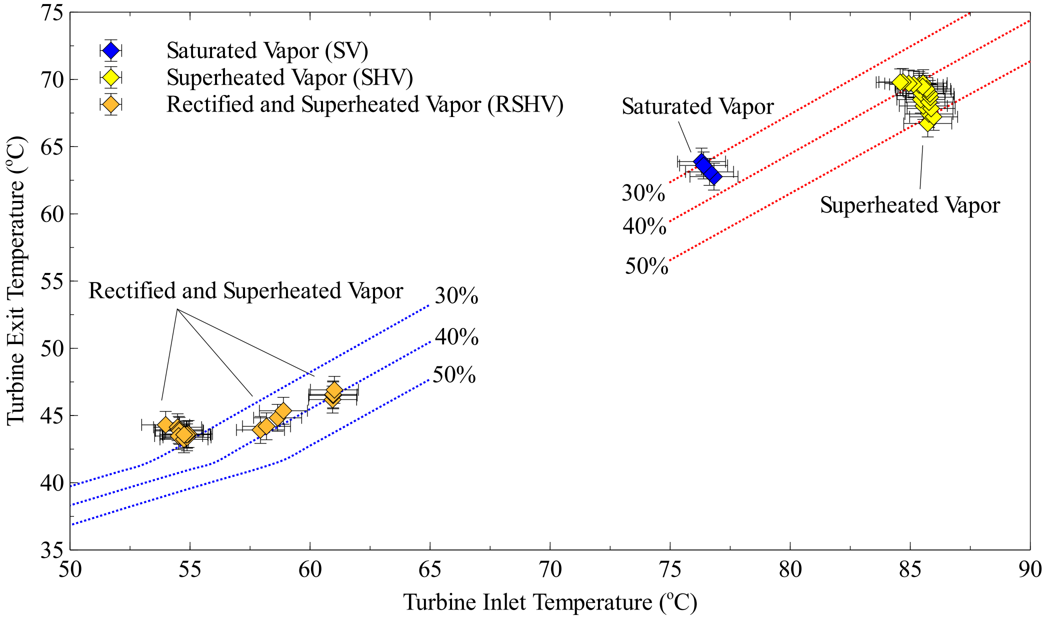

Figure 5.16 Experimental measurement of the expander performance for all cases

المنارة للاستشارات
www.manaraa.com

The conditions for all the experiments are averaged and the expander efficiency was extrapolated for low turbine inlet temperatures as shown in Fig. 5.17. It is clear from the figure that 30-35 °C turbine inlet conditions are required to reach sub-ambient temperatures. Another way to reach these temperatures is to lower the absorber pressure and temperature, which is also shown with the dashed lines in Fig. 5.17. It was mentioned that the rectifier coil pinch point limitation caused problems for varying the rectifier exit temperature. Therefore, in order to reach low rectifier exit temperatures, the cooling fluid temperature needs to be decreased from 20 °C or the vapor temperature entering the separator column should be decreased. The cooling fluid temperature decreased to 10 °C, and the absorber temperature to be around 25 °C, unfortunately the temperature of the cooling fluid increased during the experiment. The chiller cooling capacity was not enough and it should be increased in order to decrease the absorber temperature. Another option might be decreasing the flowrate of the working fluid; however, the system is more prone to become unstable. Expander rotational speed and calculated work output for all cases are also shown in Fig. 5.18.

5.2.5 Generator Performance

Calculated work output of the cycle and the generator measured output results for all the cases are shown in Fig. 5.19. As shown in the figure, the work output is always higher than the generator output. The discrepancy between the results is higher at the higher turbine inlet temperatures.

Generator rotational speed and output estimation for all cases are shown in Fig. 5.20. The generator output estimation was done with an AC motor and speed controller, the speed

المنارة للاستشارات

www.manaraa.com

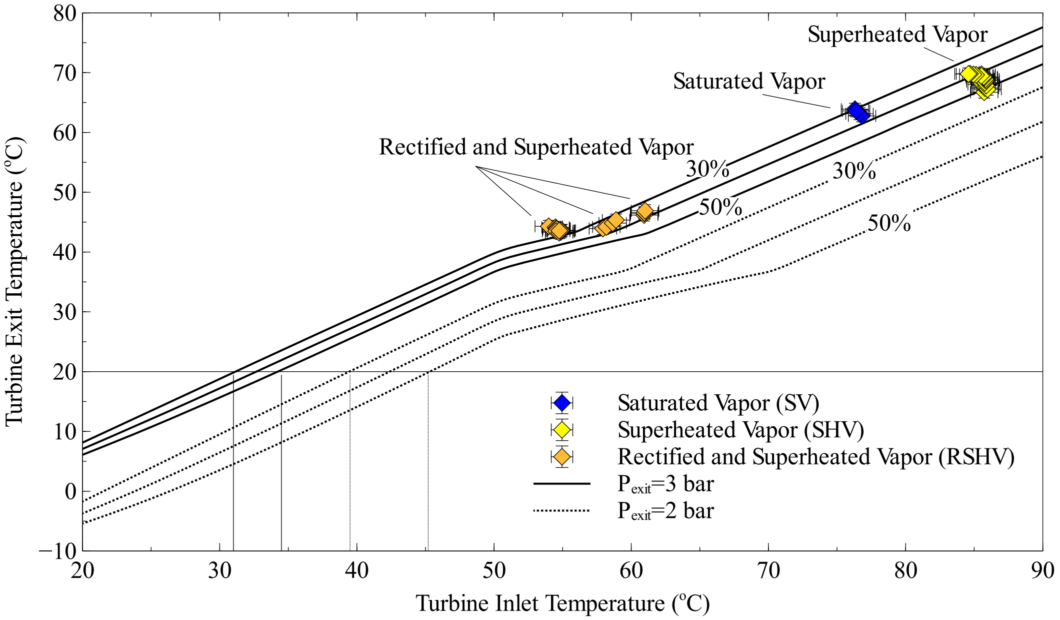

Figure 5.17 Expected performance of the expander for low expander temperature inlet

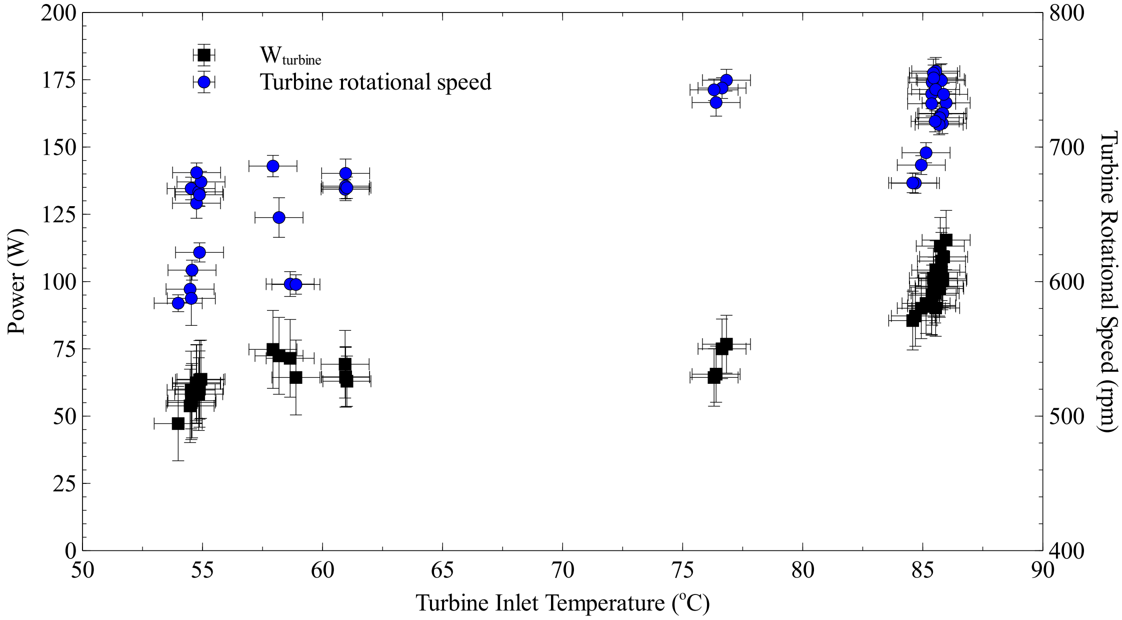

Figure 5.18 Expander rotational speed and calculated work output for all cases

المنارة للاستشارات
www.manaraa.com

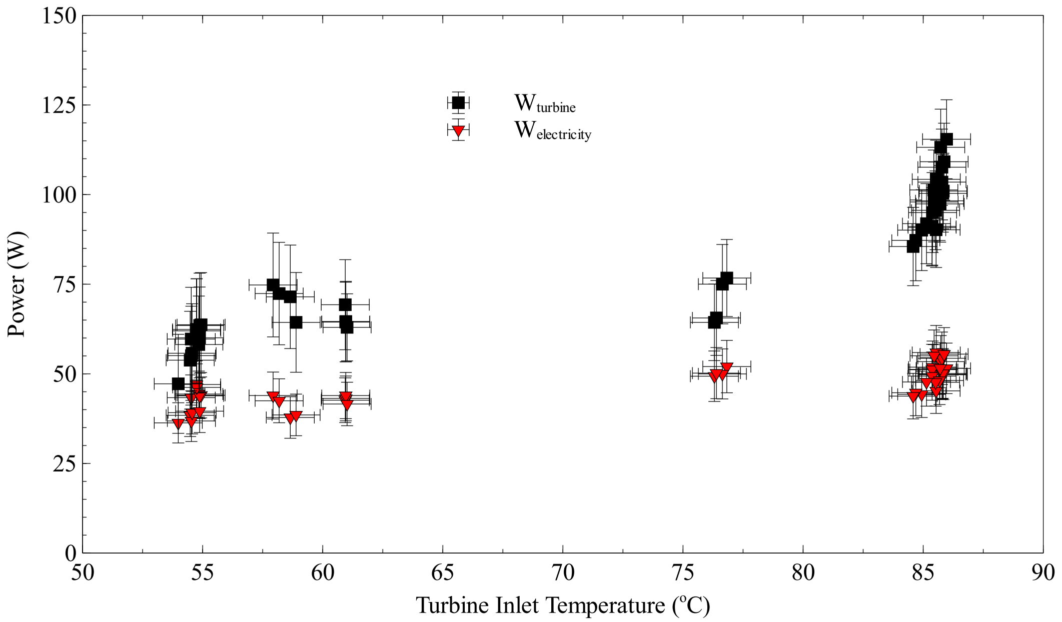

Figure 5.19 Expander calculated work output and generator output for all cases

of the generator was changed and expected speed range was covered. The generator and the AC motor was coupled with a pulley, and pulleys with different diameters were used to find out the generator output at different speeds. The generator characteristic is derived from these tests and shown in Fig. 5.20. The experimental results with the ammonia-water tests lie within the range of the performance estimation of the generator.

A demonstration of the important outputs of the Goswami cycle cycle has been provided. The experimental results of vapor production has been verified by the expected trends to some degree, due to heat transfer losses in the separator vessel. The scroll expander performance has been measured between 30-50%, the expander performs better when the vapor is superheated. The small scale of the experimental cycle affected the testing conditions and outputs, if the components capacities are increased and system is scaled

www.manaraa.com

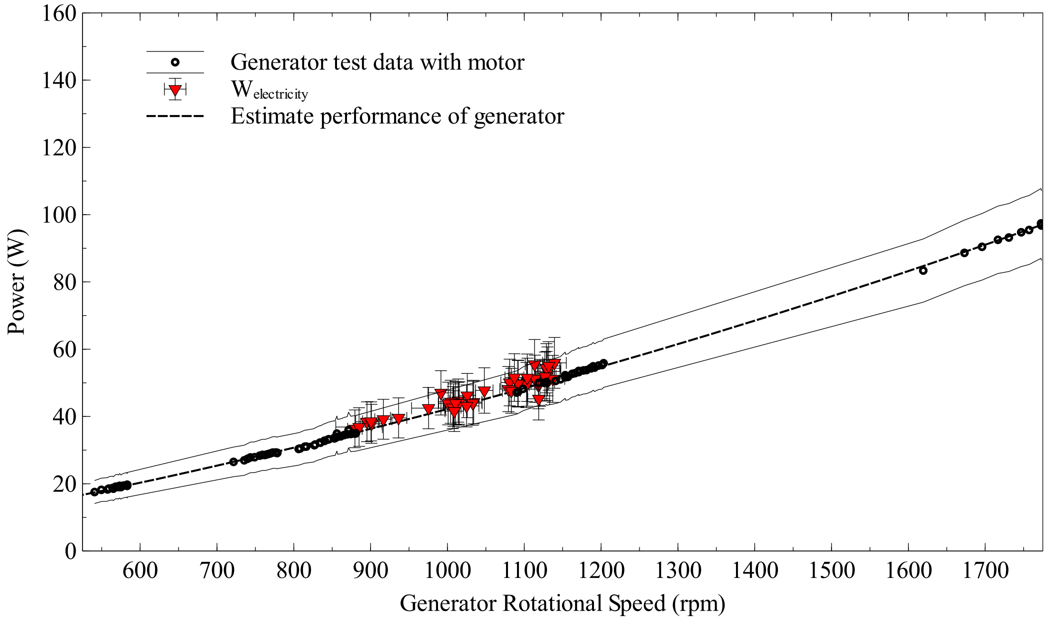

Figure 5.20 Generator rotational speed and output estimation for all cases

to higher outputs, the losses would be lower and the effect on the system would be smaller than what is observed by the current experimental setup.

www.manaraa.com

Chapter 6

Summary and Conclusions

The combined power/cooling cycle was studied theoretically and experimentally. A thermodynamic model was developed to conduct the performance analysis of the cycle. Using this model, the performance of the cycle was studied for a range of boiler pressures, ammonia concentrations, and isentropic turbine efficiencies, to find out the sensitivities of net work, amount of cooling and effective efficiencies. The thermodynamic analysis covered a broad range of boiler temperatures from 85 °C to 350 °C.

The combined cycle experimental setup was developed on a moveable strut-channel frame. A boiler and a condenser unit were also built to simulate the experiments in a laboratory environment. Based on the literature search, scroll type device was chosen as the expander. A scroll type device was modified to use it with high concentration ammonia. The experiments were accomplished to test the performance of the scroll expander at a boiler temperature of 85 °C.

6.1 Summary of Results

6.1.1 Theoretical Studies

The operating parameters that affect the cycle performance for low-grade heat sources were analyzed. It was shown that the cycle has maxima points for the efficiencies, work

المنارة للاستشارات
www.manaraa.com

and cooling outputs at a given boiler temperature. For the low temperature heat sources below 100 °C, the conclusions are as follows.

- The effect of rectification cooling source (external and internal) on the cycle output was investigated, and it was found that an internal rectification cooling source always produces higher efficiencies. However, no significant difference was observed between the external and internal cooling source for rectification at ammonia mass fractions higher than 0.35.
- The vapor concentration has a significant effect on the turbine exit temperature. The higher the vapor concentration at the turbine inlet, the lower the turbine exit temperature, which increases the cooling output from the cycle.
- The cooling output is always at a maximum when rectification is done and no superheater is used, therefore, installation of a rectifier column is necessary to maximize the refrigeration output. Irrespective of the turbine efficiency, higher rectification is required to produce higher cooling, which on the other hand reduces the work output and overall efficiency.
- Cooling output is limited at low pressures by higher turbine exhaust temperatures and bounded at higher pressures by the low production of vapor.
- When ammonia vapor is superheated after the rectification process, the cycle efficiencies increase but cooling output decreases. Superheating enhances the power output but the difference is not significant at high pressure ratios.

المنارة للاستشارات
www.manaraa.com

- If the cycle is used for maximum power, it is not necessary to use a rectifier or a superheater, which leads to a reduction in the initial costs.
- When ammonia mass fraction in the basic solution increases, ammonia vapor mass flow rate leaving the boiler increases. This leads to a higher net work output and cooling.

The theoretical study was extended to cover low to mid-grade heat sources, from 100 °C to 350 °C. It was shown that the cycle operates poorly above 150 °C when a single turbine stage is used. The turbine exit quality limits the exit temperature and pressure. In order to utilize the heat sources above 150 °C, multi turbine stages were used and compared with the single stage results. The results showed using multi stage turbines the Goswami cycle could operate at an effective exergy efficiency of 60% and higher for the boiler temperature range of 200-350 °C. The first law efficiency of 25-31% is possible with the boiler temperatures of 250-350 °C. The efficiency results of the Goswami cycle were compared with the other combined cycles found in the literature, it was seen that the Goswami cycle has better efficiencies.

- The work output of the Goswami cycle increases with the heat source temperature for the multi-stage expansion case, however it follows a reverse path for the single stage turbine for the heat source temperatures between 200-350 °C.
- The effect of using multi stage turbine is critical above the heat source temperatures of 175 °C.

المنارة للاستشارات
www.manaraa.com

- The maximum net work occurs at the lowest strong solution for the multi-stage expansion.
- The effective first law efficiency values for multiple stage case is significantly higher than the single stage case for heat source temperature above 150 °C.
- The first law efficiency of 25-31% is possible with the boiler temperatures of 250-350 °C. The cycle can operate at an effective exergy efficiency of 60-68% with the boiler temperature range of 200-350 °C.
- The exergy destruction increases with increasing boiler temperature. The main sources of exergy destruction are heat exchangers, absorber, and turbine stages. For most of the cases, the dominant exergy destruction source is the absorber/condenser.

6.1.2 Experimental Studies

An experimental study was conducted to verify the predicted trends and to test the performance of the scroll type expander. The experimental results of vapor production were verified by the expected trends to some degree, due to heat transfer losses in the separator vessel.

The measured vapor flow rate is lower than that expected from the theoretical model indicating some inefficiency in the vapor production process. After the vapor-liquid mixture enters the separator, the vapor is separated from the liquid by gravity, however, even though the vessel was insulated, there are external losses, and the vapor condenses on the separator vessel wall. The vapor mass flow fraction is reduced because of this additional condensation on the vessel wall. The vapor condensation on the separator vessel wall raises the

المنارة للاستشارات

www.manaraa.com

vapor temperature and the ammonia mass fraction in the vapor region as discussed above, this raises the ammonia mass fraction in the weak solution as well.

The scroll expander performance has been measured between 30-50%; the expander performs better when the vapor is superheated. The small scale of the experimental cycle affected the testing conditions and outputs. If the system size is increased, the losses would be lower, and the effect on the system would be smaller.

6.2 Future Work

The potential of the power and cooling cycle as an alternative to conventional fossil fuel technologies was acknowledged by the experimental work of this dissertation. However, further studies are necessary to realize this potential and to produce a complete demonstration of the proposed cycle.

More work is needed to better understand the performance of a power plant built on the combined power and cooling cycle. While some work is already in progress, some recommendations to extend the results of this work are presented below. The suggestions are listed and a discussion elaborating on some of these topics follows. The recommendations that should be considered for further research in this area are categorized in three sections; theoretical studies, experimental setup, scale of the cycle, and the economical aspect.

6.2.1 Theoretical Studies

All the theoretical work done so far on the cycle has been based on the basis of simulation models. The practical efficiency values of the components were assumed and simulations have been performed. This simulation approach is useful to find out the strengths and weaknesses of different cycle configurations. In the future, models that are more realistic

المنارة للاستشارات

www.manaraa.com

are necessary to determine the sizes of different equipment used in the simulations. This will also be useful for an economic analysis of the cycle.

Another realistic approach will be simulating the cycle with partial load conditions. Cycle performance, as a bottoming cycle, integrated with the topping cycle of a solar system or a gas turbine system should also be evaluated.

6.2.2 Current Experimental Setup

The integration of realistic heat and cooling sources with the prototype cycle is important to show the viability of the cycle with renewable sources. In a lab environment, the use of an electrical water heater is an easy solution for the simulation of the heat source. With an electrical controller, the heat source can be varied easily from 60 to 99 °C. In order to do the experiments under real heating systems, the heat source should be water heated by flat plate solar collectors. The chiller fluid system must also be more realistic; ambient air or ground water can be a good candidate for the cooling source of the absorber.

Other upgrades that should be considered for the current setup are as follows:

- The experiments were conducted at the boiler temperature of 85 °C; the heat source temperature for this boiler temperature was close to 97 °C. The experiments can be conducted at a higher heat source temperature, such as 120-130 °C. The heat source temperature can be increased with minor changes in the boiler heating system. The safety valve at the top of the hot water storage tank opens when the temperature of the water in the tank reaches to 100 °C. It can be replaced by a pressure safety valve and higher temperatures can be obtained.

المنارة للاستشارات
www.manaraa.com

- The strong solution flow rate was in the range of 0.4-0.8 gpm. In order to increase the vapor flow rate, the strong solution flow rate should also be increased. For this, additional electric heaters will be required. The current capacity of the hot water system is 10.5 kW. The hot water circulation pump also circulates the hot water at a maximum flowrate of 3 gpm. The hot water flowrate should be increased if the strong solution flowrate is increased for steady state experiment conditions. This would require a new pump.

- The chiller capacity is enough when the system works at the boiler and absorber temperatures of 85 °C and 35 °C. However, the experiments at the absorber temperature of 25 °C were not successful as the temperature of the chiller fluid steadily increased. The storage tank size for the chiller might be increased, so that the steady state operation at the absorber temperature of 25 °C can be extended.

- In a usual refrigeration system, 1-3% oil flows with the refrigerant, but it will return to the compressor with the pressure driven flow. In the current experimental system, the turbine exit is connected to the absorber, and the oil mixes with the ammonia-water mixture. Therefore, oil filter might be helpful at the exit of the scroll expander to minimize the oil amount that mixes with the ammonia-water mixture.

- As the current cycle was constructed with major modifications, there was not enough information on the vapor flow rate that the system could produce. The vapor production from the system was established by the experiments. The current scroll expander is oversized, as the rotational speed did not exceed 1000 rpm in the experiments.

المنارة للاستشارات
www.manaraa.com

Therefore, a smaller size new scroll device could perform better, with the known conditions such as temperature, pressure, and vapor flow rate, a better selection of the scroll device would give higher turbine efficiency.

- Power measurements were complicated as they are based on some assumptions. The vapor sample taken by a syringe was misleading the concentration value due to condensation of the vapor in the syringe. Therefore, vapor concentrations were determined from the property relations using the measured temperature and pressure at the separator and rectifier exits. As described in Chapter 5, the concentration value of the vapor is very crucial in the work output and expander efficiency calculations. Therefore, in the future studies, the GC can be moved close to the expander and a sample line can be developed between the turbine inlet and the GC, a small diameter stainless steel tube can be used for this purpose with a couple of valves.

6.2.3 Scale of the Future Demonstration Plant

The scale of the demonstration plant is very important. As discussed in chapter 4, the scale of the plant directly affects the selection of the expander, and costs of the plant. Clean Energy Research Center is planning to build a 50-75 kW solar thermal power plant at the University of South Florida campus. The parabolic troughs will be used to convert the sun energy to thermal heat and the expected heat source temperature will be around 200-250 °C. This could be a good opportunity to start the scaling of the cycle.

In the power industry, turbine efficiencies of 70% to 80% are achievable when the system size is at the scale of 100 kW. The size of 50 kW would require scaling up the

المنارة للاستشارات
www.manaraa.com

components of the system. The increase in the scaling of the cycle would also require an automation system. A study to develop a control scheme would be a vital step for the commercialization of the system.

6.2.4 Economical Aspect

The capital cost of energy per unit can be decreased by utilizing waste heat or low temperature. Industries such as steel manufacturing, textile, and cement consume high amount of energy, and their processes produce high temperature waste heat, which could be converted to power or cooling depending on their needs. In order to attract serious interest from these industries, an economic analysis should be performed. The economic costs would depend on the size of the unit and bulk manufacturing. Therefore, initial economical study can be started for a size of 500 kW to 1 MW; this would be the starting case for the commercialization of the cycle. This would give the viability of the proposed cycle in comparison with alternative energy conversion systems.

المنارة للاستشارات
www.manaraa.com

List of References

[1] International Energy Agency, 2010. World energy outlook. Tech. rep., OECD/IEA, Paris. Available at: http://www.worldenergyoutlook.org, last accessed June 1, 2011.

[2] U.S. Energy Information Administration, 2009. Annual energy outlook 2009 early release with projections to 2030. Tech. Rep. DOE/EIA-0383, U.S. Department of Energy, Washington, DC. Available at: http://www.eia.gov/oiaf/archive/aeo09/overview.html, last accessed June 1, 2011.

[3] U.S. Energy Information Administration, 2010. International energy outlook. Tech. Rep. DOE/EIA-0484, U.S. Department of Energy, Washington, DC. Available at: http://www.eia.gov/oiaf/ieo/index.html, last accessed June 1, 2011.

[4] Goswami, D. Y., 1995. "Solar thermal power: Status of technologies and opportunities for research". In Proc. of the 2nd ISHMT-ASME Heat and Mass Trans. Conf., Tata McGraw Hill, New Delhi, pp. 57–60.

[5] Goswami, D. Y., 1998. "Solar thermal power technology: Present status and ideas". *Energy Sources, 20*, pp. 137–145.

[6] Martin, C., and Goswami, D. Y., 2006. "Effectiveness of cooling production with a combined power and cooling thermodynamic cycle". *Applied Thermal Engineering, 26*(5-6), pp. 576–582.

[7] Martin, C., 2004. "Study of cooling production with a combined power and cooling thermodynamic cycle". PhD thesis, University of Florida.

[8] Tamm, G., 2003. "Experimental investigation of an ammonia-based combined power and cooling cycle". PhD thesis, University of Florida.

[9] Goel, N., 2005. "Theoretical and experimental analysis of absorption-condensation in a combined power and cooling cycle". PhD thesis, University of Florida.

المنارة للاستشارات
www.manaraa.com

[10] Yanagisawa, T., Shimizu, T., Fukuta, M., and Handa, T., 1988. “Study on fundamental performance of scroll expander”. *Transactions of the Japan Society of Mechanical Engineers, Series B, 54*(506), pp. 2798–2803.

[11] Kim, H., Ahn, J., Park, I., and Rha, P., 2007. “Scroll expander for power generation from a low-grade steam source”. *Proceedings of the Institution of Mechanical Engineers, Part A: Journal of Power and Energy, 221*(5), pp. 705–711.

[12] National Renewable Energy Laboratory, 2010. U.S. parabolic trough power plant data. Available at: http://www.nrel.gov/csp/troughnet/power_plant_data.html, last accessed June 1, 2011.

[13] Goswami, D. Y., Kreith, F., and Kreider, J. F., 2000. *Principles of solar engineering*. CRC.

[14] Goswami, D. Y., and Kreith, F., 2007. *Energy Conversion*. CRC.

[15] Huenges, E., 2008. *Renewable energy: sustainable energy concepts for the future*. Wiley-VCH, ch. Energy from the depths of the Earth, pp. 54–60.

[16] Sandia National Laboratories, 1999. Parabolic trough technology overview. Available at: http://www.energylan.sandia.gov/stdb.cfm, last accessed June 1, 2011.

[17] Wolff, G., 2010. Clean Power from Deserts. Available at: http://www.trec-uk.org.uk/resources/pictures/stills4.html, last accessed June 1, 2011.

[18] Franco, A., and Villani, M., 2009. “Optimal design of binary cycle power plants for water-dominated, medium-temperature geothermal fields”. *Geothermics, 38*(4), pp. 379–391.

[19] Demirkaya, G., Padilla, R. V., Goswami, D. Y., Stefanakos, E., and Rahman, M. M., 2011. “Analysis of a combined power and cooling cycle for low-grade heat sources”. *International Journal of Energy Research, 35: n/a. doi: 10.1002/er.1750.*

[20] Padilla, R. V., Demirkaya, G., Goswami, D. Y., Stefanakos, E., and Rahman, M. M., 2010. “Analysis of power and cooling cogeneration using ammonia-water mixture”. *Energy, 35*(12), pp. 4649 – 4657.

المنارة للاستشارات

www.manaraa.com

[21] Erkan, K., Holdmann, G., Benoit, W., and Blackwell, D., 2008. “Understanding the Chena hot springs, Alaska, geothermal system using temperature and pressure data from exploration boreholes”. *Geothermics, 37*(6), pp. 565–585.

[22] Kalina, A. I., and Leibowitz, H. M., 1989. “Application of the Kalina cycle technology to geothermal power generation”. *Geothermal Resources Council Transactions, 13*, pp. 605–611.

[23] Kose, R., 2007. “Geothermal energy potential for power generation in Turkey: A case study in Simav, Kutahya”. *Renewable and Sustainable Energy Reviews, 11*(3), pp. 497–511.

[24] J.W. Lund, T. B., 1999. Small geothermal power project examples. GHC Bulletin. Available at: http://geoheat.oit.edu/bulletin/bull20-2/art2.pdf, last accessed June 1, 2011.

[25] Somayaji, C., 2008. “First and second law analysis of Organic Rankine Cycle”. PhD thesis, Mississippi State University.

[26] Erickson, D., Anand, G., and Kyung, I., 2004. “Heat-activated dual-function absorption cycle”. *Transactions-American Society of Heating Refrigerating and Air Conditioning Engineers, 110*(1), pp. 515–524.

[27] Inoue, N., Kaneko, A., Watanabe, H., Uchimura, T., and Irie, K., 2007. “Development of electric power generation unit driven by waste heat: Study on working fluids and expansion turbines”. In Proceedings of ASME Turbo Expo 2007: Power for Land, Sea and Air; Montreal, Canada, pp. 927–938.

[28] Global Geothermal Ltd., 2011. Applications: Steel and other metal melting works, oil refineries, gas processing and gas turbines, cement and lime kilns, geothermal, ocean thermal, solar thermal. Available at: http://www.globalgeothermal.com/Applications.aspx, last accessed June 1, 2011.

[29] Leyzerovich, A., 1997. *Large power steam turbines: Design and operation*, Vol. 1. Pennwell Books.

[30] Cengel, Y. A., and Boles, M. A., 2002. *Thermodynamics: An engineering approach.* McGraw-Hill.

المنارة للاستشارات
www.manaraa.com

[31] Hedman, B. A., 2008. Waste energy recovery opportunities for interstate natural gas pipelines. White paper, Energy and Environmental Analysis, Inc. Available at: http://www.gulfcoastcleanenergy.org/Portals/24/Reports_studies/WHR Opportunities_ICF.pdf, last accessed June 1, 2011.

[32] Yamaguchi, H., Zhang, X., Fujima, K., Enomoto, M., and Sawada, N., 2006. “Solar energy powered Rankine cycle using supercritical CO2”. *Applied Thermal Engineering, 26*(17-18), pp. 2345–2354.

[33] Chen, H., Goswami, D., Rahman, M. M., and Stefanakos, E. K., 2011. “A supercritical Rankine cycle using zeotropic mixture working fluids for the conversion of low-grade heat into power”. *Energy, 36*(1), pp. 549–555.

[34] Kalina, A. I., 1984. “Combined cycle system with novel bottoming cycle”. *Journal of Eng. for Gas Turbines and Power, 106*, pp. 737–742.

[35] Ibrahim, O. M., and Klein, S. A., 1996. “Absorption power cycles”. *Energy, 21*, pp. 21–27.

[36] Ibrahim, O. M., and Klein, S. A., 1989. “Optimum power of Carnot and Lorentz cycles”. In Proceedings of Simulation of Thermal Energy Systems; San Francisco, CA, USA, pp. 91–96.

[37] Lee, W. Y., and Kim, S. S., 1992. “The maximum power from a finite reservoir for a Lorentz cycle”. *Energy, 17*, pp. 275–281.

[38] Maloney, J. D., and Robertson, R. C., 1953. Thermodynamic study of ammonia-water heat power cycles. Tech. Rep. CF-53-8-43, National Laboratory, Oak Ridge, TN.

[39] Kalina, A. I., and Leibowitz, H. M., 1989. “Off-design performance, equipment considerations, and material selection for a Kalina system 6 bottoming cycle”. In 3rd International Symposium on Turbomachinery, Combined-Cycle Technologies, and Cogeneration, Nice, France, pp. 347–355.

[40] Kalina, A. I., Leibowitz, H. M., Markus, D. W., and Pelletier, R. I., 1991. “Further technical aspects and economics of a utility-size Kalina bottoming cycle”. In International Gas Turbine and Aeroengine Congress and Exposition, Vol. 91-GT-365, pp. 1–8.

المنارة للاستشارات

www.manaraa.com

[41] Leibowitz, H. M., 1993. “Operating experiences with the 3 MW Kalina cycle demonstration plant”. In Proceedings of the 55th Annual Meeting of the American Power Conference, Vol. 55, Illinois Institute of Technology, pp. 173–178.

[42] Leibowitz, H. M., and Mirolli, M., 1997. “First Kalina combined-cycle plant tested successfully”. *Power Engineering, 101*(5), pp. 44–48.

[43] Leibowitz, H. M., and Micak, H. A., 1999. “Design of a 2 MW Kalina cycle binary module for installation in Husavik, Iceland”. *Global Geothermal Resources: Sustainable Energy for the Future*, pp. 75–80.

[44] Leibowitz, H. M., and Zervos, N., 1992. “Installation and early test results of a 3 MW Kalina cycle demonstration plant”. In Proceedings of the 27th Intersociety Energy Conversion Engineering Conference, Vol. 23, Society of Automotive Engineers, pp. 35–42.

[45] DiPippo, R., 2008. *Geothermal power plants: principles, applications, case studies and environmental impact*. Butterworth-Heinemann.

[46] Maack, R., and Valdimarsson, P., 2002. “Operating experience with Kalina power plants”. *VDI Berichte Series, 1703*, pp. 107–116.

[47] Mirolli, M., 2007. “Ammonia-water based thermal conversion technology: Applications in waste heat recovery for the cement industry”. In Proceedings of IEEE Cement Industry Technical Conference; Charleston, SC, USA, IEEE, pp. 234–241.

[48] Wang, J., Dai, Y., and Gao, L., 2009. “Exergy analyses and parametric optimizations for different cogeneration power plants in cement industry”. *Applied Energy, 86*(6), pp. 941–948.

[49] Wasabi Energy, 2011. Wasabi energy subsidiaries secure contract with FLSmidth to build 8,600 kW Kalina cycle power plant. Available at: http://www.wasabienergy.com/Downloads/News/FLS Contract Announcement - final 31 jan 11.pdf, last accessed June 1, 2011.

[50] Park, Y. M., and Sonntag, R. E., 1990. “A preliminary study of the Kalina power cycle in connection with a combined cycle system”. *International Journal of Energy Research, 14*(2), pp. 153–162.

المنارة للاستشارات

www.manaraa.com

[51] Olsson, E., Desideri, U., Stecco, S., and Svedberg, G., 1991. “An integrated gas turbine–kalina cycle for cogeneration”. In The 36th ASME International Gas Turbine and Aeroengine Congress and Exposition, Orlando, Florida, USA, June, Vol. 91-GT-202, pp. 1–6.

[52] Bisio, G., 1992. “Industrial waste heat recovery; the ideal thermodynamic cycle”. In Proceedings of the Florence World Energy Research Symposium, Firenze, Italy, June 7-12,1992, pp. 503–519.

[53] Olsson, E. K., Thorin, E. B., Dejfors, C. A. S., and Svedberg, G., 1994. “Kalina cycles for power generation from industrial waste heat”. In Proceedings of the Florence World Energy Research Symposium, Florence, Italy, Jul. 6-8, 1994.

[54] Bjorge, R., Boericke, R., O’Connor, M., and Smith, R. “Kalina combined cycle power plant design and performance characteristics”. In Power-Gen Europe, Vol. 97, pp. 219–234.

[55] Nag, P., and Gupta, A., 1998. “Exergy analysis of the Kalina cycle”. *Applied Thermal Engineering, 18*(6), pp. 427–439.

[56] Hettiarachchi, H., Golubovic, M., Worek, W., and Ikegami, Y., 2007. “The performance of the Kalina cycle system 11 (KCS-11) with low-temperature heat sources”. *Journal of Energy Resources Technology, 129*, pp. 243–247.

[57] Lolos, P., and Rogdakis, E., 2009. “A Kalina power cycle driven by renewable energy sources”. *Energy, 34*(4), pp. 457–464.

[58] Ogriseck, S., 2009. “Integration of Kalina cycle in a combined heat and power plant, a case study”. *Applied Thermal Engineering, 29*(14-15), pp. 2843–2848.

[59] Desideri, U., Olsson, E., Stecco, S., and Svedberg, G., 1991. “The ammonia-water mixture Rankine cycle: Considerations on its applicability as bottoming cycle”. In Proceedings of the 26th Intersociety Energy Conversion Engineering Conference; Boston, MA, USA, Vol. 2, pp. 449–454.

[60] Rogdakis, E., and Antonopoulos, K., 1991. “A high efficiency NH3/H2O absorption power cycle”. *Heat Recovery Systems and CHP, 11*(4), pp. 263–275.

المنارة للاستشارات

www.manaraa.com

[61] Philippe, R., Desilets, M., Galanis, N., Nesreddine, H., and Cayer, E., 2009. "Thermodynamic analysis of a power cycle using a low-temperature source and a binary NH3/H2O mixture as working fluid". *International Journal of Thermal Sciences*.

[62] Agnew, B., Talbi, M., and Mostafavi, M., 1999. "Combined power and cooling, an analysis of the combined Diesel-absorption cycle". *Applied Thermal Engineering, 19*(10), pp. 1097–1105.

[63] Talbi, M., and Agnew, B., 2002. "Energy recovery from diesel engine exhaust gases for performance enhancement and air conditioning". *Applied Thermal Engineering, 22*(6), pp. 693–702.

[64] Liu, Y. L., Wang, R. Z., and Xia, Z. Z., 2005. "Experimental study on a continuous adsorption water chiller with novel design". *International Journal of Refrigeration, 28*(2), pp. 218–230.

[65] Maidment, G. G., and Tozer, R. M., 2002. "Combined cooling heat and power in supermarkets". *Applied Thermal Engineering, 22*(6), pp. 653–665.

[66] Colonna, P., and Gabrielli, S., 2003. "Industrial trigeneration using ammonia-water absorption refrigeration systems (AAR)". *Applied Thermal Engineering, 23*(4), pp. 381–396.

[67] Alexis, G., 2007. "Performance parameters for the design of a combined refrigeration and electrical power cogeneration system". *International Journal of Refrigeration, 30*(6), pp. 1097–1103.

[68] Oliveira, A., Afonso, C., Matos, J., Riffat, S., Nguyen, M., and Doherty, P., 2002. "A combined heat and power system for buildings driven by solar energy and gas". *Applied Thermal Engineering, 22*(6), pp. 587–593.

[69] Nord, J. W., and andS. A. Sherif, W. E. L., 2001. "Analysis of heat-driven jet-pumped cooling system for space thermal management". *Journal of Propulsion and Power, 17*(3), pp. 566–570.

[70] Zheng, B., and Weng, Y., 2010. "A combined power and ejector refrigeration cycle for low temperature heat sources". *Solar Energy, 84*(5), pp. 784–791.

المنارة للاستشارات

www.manaraa.com

[71] Hasan, A. A., Goswami, D. Y., and Vijayaraghavan, S., 2002. “First and second law analysis of a new power and refrigeration thermodynamic cycle using a solar heat source”. *Solar Energy, 73*(5), pp. 385–393.

[72] Wang, J., Dai, Y., Gao, L., and Ma, S., 2009. “A new combined cooling, heating and power system driven by solar energy”. *Renewable Energy, 34*(12), pp. 2780–2788.

[73] Wang, J., Dai, Y., and Sun, Z., 2009. “A theoretical study on a novel combined power and ejector refrigeration cycle”. *International Journal of Refrigeration, 32*(6), pp. 1186–1194.

[74] Wang, J., Dai, Y., Zhang, T., and Ma, S., 2009. “Parametric analysis for a new combined power and ejector–absorption refrigeration cycle”. *Energy, 34*(10), pp. 1587–1593.

[75] Dai, Y., Wang, J., and Gao, L., 2009. “Exergy analysis, parametric analysis and optimization for a novel combined power and ejector refrigeration cycle”. *Applied Thermal Engineering, 29*(10), pp. 1983–1990.

[76] Wang, J., Dai, Y., and Gao, L., 2008. “Parametric analysis and optimization for a combined power and refrigeration cycle”. *Applied Energy, 85*(11), pp. 1071–1085.

[77] Zheng, D., Chen, B., Qi, Y., and Jin, H., 2006. “Thermodynamic analysis of a novel absorption power/cooling combined-cycle”. *Applied Energy, 83*(4), pp. 311–323.

[78] Liu, M., and Zhang, N., 2007. “Proposal and analysis of a novel ammonia-water cycle for power and refrigeration cogeneration”. *Energy, 32*(6), pp. 961–970.

[79] Zhang, N., and Lior, N., 2007. “Development of a novel combined absorption cycle for power generation and refrigeration”. *Journal of Energy Resources Technology, 129*, pp. 254–265.

[80] Zhang, N., and Lior, N., 2007. “Methodology for thermal design of novel combined refrigeration/power binary fluid systems”. *International Journal of Refrigeration, 30*(6), pp. 1072–1085.

[81] Zamfirescu, C., and Dincer, I., 2008. “Thermodynamic analysis of a novel ammonia–water trilateral Rankine cycle”. *Thermochimica Acta, 477*(1-2), pp. 7–15.

المنارة للاستشارات
www.manaraa.com

[82] Wagar, W. R., Zamfirescu, C., and Dincer, I., 2010. “Thermodynamic performance assessment of an ammonia-water Rankine cycle for power and heat production”. *Energy Conversion and Management, 51*(12), pp. 2501–2509.

[83] Badami, M., and Portoraro, A., 2009. “Performance analysis of an innovative small-scale trigeneration plant with liquid desiccant cooling system”. *Energy and Buildings, 41*(11), pp. 1195–1204.

[84] Zhai, H., Dai, Y. J., Wu, J. Y., and Wang, R. Z., 2009. “Energy and exergy analyses on a novel hybrid solar heating, cooling and power generation system for remote areas”. *Applied Energy, 86*(9), pp. 1395–1404.

[85] Aphornratana, S., and Sriveerakul, T., 2010. “Analysis of a combined Rankine-vapour-compression refrigeration cycle”. *Energy Conversion and Management, 51*(12), pp. 2557–2564.

[86] Takezawa, S., Wakahara, K., Araki, T., Onda, K., and Nagata, S., 2006. “Cycle analysis using exhaust heat of SOFC and turbine combined cycle by absorption chiller”. *IEEJ Transactions on Power and Energy, 126*, pp. 841–846.

[87] Al-Sulaiman, F. A., Dincer, I., and Hamdullahpur, F., 2010. “Exergy analysis of an integrated solid oxide fuel cell and organic Rankine cycle for cooling, heating and power production”. *Journal of Power Sources, 195*(8), pp. 2346–2354.

[88] Venegas, M., Izquierdo, M., De Vega, M., and Lecuona, A., 2002. “Thermodynamic study of multistage absorption cycles using low-temperature heat”. *International Journal of Energy Research, 26*(8), pp. 775–791.

[89] Suzuki, T., Noguchi, H., Amano, Y., Hashizume, T., Akiba, M., Tanzawa, Y., and Usui, A., 1999. “Effectiveness of an ammonia-water mixture turbine system to hot water heat source”. In Proceedings of Int. Joint Power Generation Conf. and Exhibition; Burlingame, CA, USA, Vol. 34.

[90] Amano, Y., Takeshita, K., Hashizuma, T., Akiba, M., Usui, A., and Tanzawa, Y., 2001. “Experimental results of an ammonia–water mixture turbine system”. In Proceedings of Int. Joint Power Generation Conf.; New Orleans, LA, USA, pp. 69–75.

[91] Amano, Y., Suzuki, T., Hashizume, T., Akaiba, M., Tanzawa, Y., and Usui, A., 2000. “A hybrid power generation and refrigeration cycle with ammonia–water mixture”. In Proceedings of Int. Joint Power Generation Conf., Miami, FL, USA, pp. 23–26.

المنارة للاستشارات
www.manaraa.com

[92] Takeshita, K., Amano, Y., Hashizume, T., Usui, A., and Tanzawa, Y., 2002. "Experimental results of an ammonia-water mixture turbine system (part 2: Effect of the ammonia mass fraction)". In Proceedings of International Power Generation Conference; Scottsdale, AZ, USA, ASME, pp. 959–964.

[93] Takeshita, K., Morimoto, K., Amano, Y., and Hashizume, T., 2004. "Experimental results of an ammonia-water mixture turbine system: Effectiveness with a low temperature heat source". In Proceedings of ASME Turbo Expo Power for Land, Sea and Air; Vienna, Austria, no. GT2004-53733, ASME, pp. 455–460.

[94] Takeshita, K., Amano, Y., and Hashizume, T., 2005. "Experimental study of advanced cogeneration system with ammonia–water mixture cycles at bottoming". *Energy, 30*(2-4), pp. 247–260.

[95] Wang, H., Peterson, R., Harada, K., Miller, E., Ingram-Goble, R., Fisher, L., Yih, J., and Ward, C., 2011. "Performance of a combined organic Rankine cycle and vapor compression cycle for heat activated cooling". *Energy, 36*(1), pp. 447–458.

[96] Xu, F., Goswami, D. Y., and Bhagwat, S. S., 2000. "A combined power/cooling cycle". *Energy, 25*(3), pp. 233–246.

[97] Hasan, A. A., and Goswami, D. Y., 2003. "Exergy analysis of a combined power and refrigeration thermodynamic cycle driven by a solar heat source". *Journal of Solar Energy Engineering, 125*, pp. 55– 60.

[98] Tamm, G., and Goswami, D. Y., 2003. "Novel combined power and cooling thermodynamic cycle for low temperature heat sources, part II: experimental investigation". *Journal of Solar Energy Engineering, 125*(2), pp. 223–229.

[99] Tamm, G., Goswami, D. Y., Lu, S., and Hasan, A. A., 2003. "Novel combined power and cooling thermodynamic cycle for low temperature heat sources, part I: theoretical investigation". *Journal of Solar Energy Engineering, 125*(2), pp. 218–222.

[100] Martin, C., and Goswami, D. Y., 2004. "Analysis of experimental power and cooling production in a combined power and cooling cycle". In Proceedings of the 17th Int. Conf. on Efficiency, Costs, Optimization, Simulation and Environmental Impact of Energy on Process Systems; Guanajuato City, Mexico, pp. 1235–1244.

[101] Vijayaraghavan, S., and Goswami, D. Y., 2003. "On evaluating efficiency of a combined power and cooling cycle". *Journal of Energy Resources Technology, 125*, pp. 221–227.

المنارة للاستشارات
www.manaraa.com

[102] Lu, S., and Goswami, D. Y., 2003. "Optimization of a novel combined power/refrigeration thermodynamic cycle". *Journal of Solar Energy Engineering, 125*(2), pp. 212–217.

[103] Goswami, D. Y., Tamm, G., and Vijayaraghavan, S., 2003. "A new combined power and cooling cycle for low temperature heat sources". In Proceedings of International Joint Power Generation Conference; Atlanta, GA, USA, ASME.

[104] Chemcad, 2008. *Version 6.1.2: Process Flow Sheet Simulator*. Chemstations Inc.: Houston, TX, USA.

[105] Herold, K. E., Radermacher, R., and Klein, S. A., 1996. *Absorption chillers and heat pumps*. CRC.

[106] Xu, F., and Goswami, D. Y., 1999. "Thermodynamic properties of ammonia- water mixtures for power-cycle applications". *Energy, 24*(6), pp. 525–36.

[107] Moran, M. J., Shapiro, H. N., Boettner, D. D., and Bailey, M., 2010. *Fundamentals of engineering thermodynamics*. John Wiley & Sons, Inc.

[108] Szargut, J., Morris, D. R., and Steward, F. R., 1988. *Energy analysis of thermal, chemical, and metallurgical processes*. Hemisphere Publishing.

[109] Dincer, I., and Al-Muslim, H., 2001. "Thermodynamic analysis of reheat cycle steam power plants". *International Journal of Energy Research, 25*(8), pp. 727–739.

[110] Logan, E., and Roy, R., 2003. *Handbook of turbomachinery*. CRC.

[111] Balje, O. E., and Japikse, D., 1981. *Turbomachines: Guide to Design Selection and Theory*. John Wiley & Sons, Inc.

[112] Wang, H., Peterson, R. B., and Herron, T., 2009. "Experimental performance of a compliant scroll expander for an organic Rankine cycle". *Proceedings of the Institution of Mechanical Engineers, Part A: Journal of Power and Energy, 223*(7), pp. 863–872.

[113] Quoilin, S., Lemort, V., and Lebrun, J., 2010. "Experimental study and modeling of an organic rankine cycle using scroll expander". *Applied Energy, 87*(4), pp. 1260–1268.

[114] Badr, O., Naik, S., and O'Callaghan, P. W., 1991. "Expansion machine for a low power-output steam Rankine-cycle engine". *Applied Energy, 39*, pp. 93–116.

المنارة للاستشارات
www.manaraa.com

[115] Mobarak, A., Rafat, N., and Saad, M., 1978. "Turbine selection for a small-capacity, solar-powered generator". In Proceedings of the International Symposium-Workshop; Cairo, Egypt, Vol. 3, pp. 1351–1367.

[116] Comfort III, W. J., 1977. Design and evaluation of a two-phase turbine for low quality steam–water mixtures. Tech. rep., California Univ., Livermore (USA). Lawrence Livermore Lab.

[117] Ibaraki, S., Endo, T., Kojima, Y., Takahashi, K., Baba, T., and Kawajiri, S., 2007. "Study of efficient on-board waste heat recovery system using Rankine cycle". *Review of Automotive Engineering, 28*, pp. 307–313.

[118] Badr, O., Probert, S. D., and O'Callaghan, P. W., 1986. "Optimal design and operating conditions for a multi-vane expander". *Applied Energy, 24*, pp. 1–27.

[119] Wade, J., Brown, G., Silvestri, G., and Tompkins, R., 1983. "Re 1-11 rotary expander engine testing and analysis". In Proceedings of the Intersociety Energy Conversion Engineering Conference; Orlando, FL, USA, Vol. 2, Naval Underwater Systems Center, pp. 636–641.

[120] Merigoux, J. M., and Pocard, P., 1978. "Solar power units with screw expanders". In Proceedings of the International Symposium-Workshop, Cairo, Egypt., Vol. 3, Pergamon Press, Inc., pp. 1293–1317.

[121] Lorenz, J., Fuestel, J., and Kraft, M., 1978. "New developments for future solar-power plants". In Proceedings of the International Symposium-Workshop, Cairo, Egypt, Vol. 3, Pergamon Press, Inc., pp. 1318–1328.

[122] Steidel, R. F., Pankow, D., and Berger, R. E., 1981. "Performance characteristics of the Lysholm engine as tested for geothermal applications". In Proceedings of the Intersociety Energy Conversion Engineering Conference, Vol. 2, ASME, pp. 1334–1340.

[123] House, P., 1976. Helical-rotor expander applications for geothermal energy conversion. Tech. rep., California Univ., Livermore (USA). Lawrence Livermore Lab.

[124] McKay, R., 1982. Helical Screw Expander Evaluation Project. Tech. rep., National Aeronautics and Space Administration, Pasadena, CA, USA; Jet Propulsion Lab., Pasadena, CA, USA.

المنارة للاستشارات
www.manaraa.com

[125] Rice, W., 1994. “Tesla turbomachinery”. In *Handbook of Turbomachinery*, E. Logan, ed. Marcel Dekker, New York, ch. 4, pp. 57–71.

[126] Ke, G., and Hashimoto, T., 1994. “Viscous expander”. *Cryogenics, 34*(1), pp. 9–18.

[127] Emerson Climate Technologies, 2011. Copeland Scroll Compressors. Available at: http://www.emersonclimate.com/en-US/products/compressors/scroll_compressors/Pages/scroll_compressors.aspx, last accessed June 1, 2011.

[128] Oomori, H., and Ogino, S., 1993. “Waste heat recovery of passanger car using a combination of Rankine bottoming cycle and evaporative engine cooling system”. In Proceedings of International Congress and Exposition; Detroit, MI, USA, SAE International, pp. 159–164.

[129] Ziegler, B., and Trepp, C., 1984. “Equation of state for ammonia-water mixtures”. *International Journal of Refrigeration, 7*(2), pp. 101–106.

[130] El-Sayed, Y., and Tribus, M., 1985. “Thermodynamic properties of water-ammonia mixtures theoretical implementation for use in power cycles analysis”. In Analysis of Energy Systems, Design and Operation; Miami Beach, FL, USA, ASME Special Publication AES 1, American Society of Mechanical Engineers, pp. 89–95.

[131] Tillner-Roth, R., and Friend, D., 1998. “A helmholtz free energy formulation of the thermodynamic properties of the mixture {Water+ Ammonia}”. *Journal of Physical and Chemical Reference Data, 27*, pp. 63–96.

[132] McLinden, M. O., Klein, S. A., and Lemmon, E. W., 2006. NIST Reference Fluid Thermodynamic and Transport Properties REFPROP V7. 0.

[133] Fischer, K., and Gmehling, J., 1995. “Further development, status and results of the PSRK method for the prediction of vapor-liquid equilibria and gas solubilities”. *Fluid Phase Equilibria, 112*(1), pp. 1–22.

[134] Abovsky, V., and Watanasiri, S., 1998. “Mixing rules for Van der Waals-type equations of state based on activity-coefficient models”. *International Journal of Thermophysics, 19*(5), pp. 1429–1445.

للاستشارات المنارة

www.manaraa.com

Appendices

www.manaraa.com

Appendix A: Thermodynamic Properties of Ammonia-Water Mixture

For the evaluation of the working fluid properties the method described by Xu and Goswami [106] is employed. The Gibbs free energy method is used to determine mixture properties while empirical equations for bubble and dew point temperatures are used to determine phase equilibrium. Good agreement between this method and experimental data have been shown [106].

A.1 Pure Component Properties

Beginning with the components needed to determine mixture properties, the Gibbs free energy for a pure component is given as Equation A.1.

$$G = h_0 - Ts_0 + \int_{T_0}^{T} c_p dT + \int_{P_0}^{P} v dP - T \int_{T_0}^{T} \frac{c_p}{T} dT \tag{A.1}$$

where the subscript 0 indicates reference state properties. The empirical relations used by Ziegler and Trepp [129] for constant pressure specific heat and specific volume are used here, Eqs. A.2-A.3 are for liquid phase relations, and Eqs. A.4-A.5 are for gas phase relations.

$$v^l = A_1 + A_2 P + A_3 T + A_4 T^2 \tag{A.2}$$

$$c_p^l = B_1 + B_2 T + B_3 T^2 \tag{A.3}$$

$$v^g = \frac{RT}{P} + C_1 + \frac{C_2}{T^3} + \frac{C_3}{T^{11}} + \frac{C_4 P^2}{T^{11}} \tag{A.4}$$

$$c_p^g = D_1 + D_2 T + D_3 T^2 \tag{A.5}$$

www.manaraa.com

Substitution and integration of Equations A.2 and A.3 into Equation A.1 results in the following expression for the reduced liquid phase Gibbs free energy.

$$\begin{aligned} G_r^l &= h_{r,0}^l + T_r s_{r,0}^l + B_1(T_r - T_{r,0}) + \left(\frac{B_2}{2}\right)(T_r^2 - T_{r,0}^2) + \left(\frac{B_3}{3}\right)(T_r^3 - T_{r,0}^3) \\ &\quad - B_1 T_r ln\left(\frac{T_r}{T_{r,0}}\right) - B_2 T_r (T_r - T_{r,0}) - \left(\frac{B_3 T_r}{2}\right)(T_r^2 - T_{r,0}^2) \\ &\quad + \left(A_1 + A_3 T + A_4 T^2\right)(P_r - P_{r,0}) + \left(\frac{A_2}{2}\right)(P_r^2 - P_{r,0}^2) \end{aligned} \tag{A.6}$$

Similarly, substitution and integration of Equations A.4 and A.5 into Equation A.1 results in the following expression for the reduced gas phase Gibbs free energy. Table A.1 presents the coefficient values for Equations A.6 and A.7. The reduced properties are defined in Equations A.8 through A.13. The associated reference values are presented in Table A.2.

$$\begin{aligned} G_r^g &= h_{r,0}^g - T_r s_{r,0}^g + D_1(T_r - T_{r,0}) + \left(\frac{D_2}{2}\right)(T_r^2 - T_{r,0}^2) + \left(\frac{D_3}{3}\right)(T_r^3 - T_{r,0}^3) \\ &\quad - D_1 T_r ln\left(\frac{T_r}{T_{r,0}}\right) - D_2 T_r (T_r - T_{r,0}) - \left(\frac{D_3}{2}\right)(T_r^2 - T_{r,0}^2) \\ &\quad + T_r ln\left(\frac{P_r}{P_{r,0}}\right) + C_1(P_r - P_{r,0}) + C_2\left(\frac{P_r}{T_r^3} - \frac{4P_{r,0}}{T_{r,0}^3} + \frac{3P_{r,0}T_r}{T_{r,0}^4}\right) \\ &\quad + C_3\left(\frac{P_r}{T_r^{11}} - \frac{12P_{r,0}}{T_{r,0}^{11}} + \frac{11P_{r,0}T_r}{T_{r,0}^{12}}\right) + \left(\frac{C_4}{3}\right)\left(\frac{P_r^3}{T_r^{11}} - \frac{12P_{r,0}^3}{T_{r,0}^{11}} + \frac{11P_{r,0}^3 T_r}{T_{r,0}^{12}}\right) \end{aligned} \tag{A.7}$$

$$T_r = \frac{T}{T_B} \tag{A.8}$$

$$P_r = \frac{P}{P_B} \tag{A.9}$$

المنارة للاستشارات

www.manaraa.com

$$G_r = \frac{G}{RT_B} \tag{A.10}$$

$$h_r = \frac{h}{RT_B} \tag{A.11}$$

$$s_r = \frac{s}{R} \tag{A.12}$$

$$v_r = \frac{vP_B}{RT_B} \tag{A.13}$$

Table A.1 Coefficients for the Gibbs energy relation

Coefficient	Ammonia	Water
A_1	0.03971423	0.02748796
A_2	-1.790557E-05	-1.016665E-05
A_3	-0.01308905	-0.004452025
A_4	0.003752836	0.000838925
B_1	16.34519	12.14557
B_2	-6.508119	-1.898065
B_3	1.448937	0.2911966
C_1	-0.01049377	0.02136131
C_2	-8.288224	-31.69291
C_3	-664.7257	-46346.11
C_4	-3045.352	0.0
D_1	3.673647	4.01917
D_2	0.09989629	-0.0517555
D_3	0.03617622	0.01951939
$h^l_{r,0}$	4.878573	21.821141
$h^g_{r,0}$	26.468873	60.965058
$s^l_{r,0}$	1.644773	5.733498
$s^g_{r,0}$	8.339026	13.45343
$T_{r,0}$	3.2252	5.0705
$P_{r,0}$	2.000	3.000

المنارة للاستشارات

www.manaraa.com

Table A.2 Reference values for reduced property computation

T_B	100 K
P_B	10 bar
R	8.314 kJ/(kmol K)

For a pure component, the molar specific properties of enthalpy, entropy, and volume are related to the reduced Gibbs free energy through Equations A.14 through A.16.

$$h_r = -RT_BT_r^2\left[\frac{\partial}{\partial T_r}\left(\frac{G_r}{T_r}\right)\right]_{P_r} \tag{A.14}$$

$$s_r = -R\left[\frac{\partial G_r}{\partial T_r}\right]_{P_r} \tag{A.15}$$

$$v_r = \frac{RT_B}{P_B}\left[\frac{\partial G_r}{\partial P_r}\right]_{T_r} \tag{A.16}$$

A.2 Liquid Mixture Properties

The Gibbs excess energy function for liquid mixtures allows for deviation from ideal solution behavior. The relation used here is the same one used by Zeigler and Trepp [129] and is given in Equation A.17. The parameter x in Equation A.17 is the ammonia mole fraction of the ammonia-water mixture. The coefficients are defined in Equations A.18 through A.20. In turn, the coefficients used in Equations A.18 through A.20 are those proposed by Ibrahim and Klein [129] and are given in Table A.3. The excess enthalpy, entropy and volume for liquid mixtures is presented in Equations A.21 through A.23.

$$G_r^E = \left[F_1 + F_2(2x-1) + F_3(2x-1)^2\right](1-x) \tag{A.17}$$

www.manaraa.com

Table A.3 Coefficients for the Gibbs excess energy relation

E_1	-41.733398	E_9	0.387983
E_2	0.02414	E_{10}	0.004772
E_3	6.702285	E_{11}	-4.648107
E_4	-0.011475	E_{12}	0.836376
E_5	63.608967	E_{13}	-3.553627
E_6	-62.490768	E_{14}	0.000904
E_7	1.761064	E_{15}	24.361723
E_8	0.008626	E_{16}	-20.736547

$$F_1 = E_1 + E_2 P_r + (E_3 + E_4 P_r) T_r + \frac{E_5}{T_r} + \frac{E_6}{T_r^2} \tag{A.18}$$

$$F_2 = E_7 + E_8 P_r + (E_9 + E_{10} P_r) T_r + \frac{E_{11}}{T_r} + \frac{E_{12}}{T_r^2} \tag{A.19}$$

$$F_3 = E_{13} + E_{14} P_r + \frac{E_{15}}{T_r} + \frac{E_{16}}{T_r^2} \tag{A.20}$$

$$h^E = -R T_B T_r^2 \left[\frac{\partial}{\partial T_r} \left(\frac{G_r^E}{T_r} \right) \right]_{P_r, x} \tag{A.21}$$

$$s^E = -R \left[\frac{\partial G_r^E}{\partial T_r} \right]_{P_r, x} \tag{A.22}$$

$$v^E = \frac{R T_B}{P_B} \left[\frac{\partial G_r^E}{\partial P_r} \right]_{T_r, x} \tag{A.23}$$

Finally, the liquid mixture properties can be computed with Equations A.24 through A.27.

$$h_m^l = x h_a^l + (1 - x) h_w^l + h^E \tag{A.24}$$

$$s_m^l = x s_a^l + (1 - x) s_w^l + s^E + s^{mix} \tag{A.25}$$

المنارة للاستشارات

www.manaraa.com

$$s^{mix} = -R\left[xln(x) + (1-x)ln(1-x)\right] \tag{A.26}$$

$$v_m^l = xv_a^l + (1-x)v_w^l + v^E \tag{A.27}$$

where the subscripts m, a, and w, indicate mixture, ammonia, and water properties respectively.

A.3 Vapor Mixture Properties

Vapor mixtures of ammonia and water are treated as ideal solutions. The following formulations are used to compute the mixture thermodynamic properties.

$$h_m^g = xh_a^g + (1-x)h_w^g \tag{A.28}$$

$$s_m^g = xs_a^g + (1-x)s_w^g + s^{mix} \tag{A.29}$$

$$v_m^g = xv_a^g + (1-x)v_w^g \tag{A.30}$$

A.4 Equilibrium Conditions

To determine the phase equilibrium of ammonia-water mixtures, the bubble and dew point temperatures are computed from the explicit relationships of reference [130]. The relations themselves and associated definitions are presented as Equations A.31 through A.34. Note that in Equations A.31 through A.34 the temperatures are in °F and pressures have units of psia. The coefficient values are presented in Tables A.4-A.6.

المنارة للاستشارات
www.manaraa.com

$$T_{bubble} = T_C - \sum_{i=1}^{7}\left(C_i + \sum_{j=1}^{10} C_{ij}x^j\right)\left(ln\left(\frac{P_c}{P}\right)\right)^i \tag{A.31}$$

$$T_{dew} = T_C - \sum_{i=1}^{6}\left(a_i + \sum_{j=1}^{4} A_{ij}\left(ln\left(1.0001 - x\right)\right)^j\right)\left(ln\left(\frac{P_c}{P}\right)\right)^i \tag{A.32}$$

$$T_C = T_{critical,water} - \sum_{i=1}^{4} a_{critical,i}x^i \tag{A.33}$$

$$P_C = P_{critical,water}exp\left(\sum_{i=1}^{8} b_{critical,i}x^i\right) \tag{A.34}$$

Table A.4 Coefficient values for the determination of mixture bubble and dew point temperatures ($a_{critical,i}$, a_i, $b_{critical,i}$ and C_i)

$a_{critical,i}$	a_i	$b_{critical,i}$	C_i
205.88890000	153.17055346	0.36810552	153.63452146
280.93055600	-11.77056875	-3.66795489	-13.03055439
-317.01388890	-1.78126356	46.60004708	-1.14845283
263.19444400	0.64738546	-262.92106200	0.55035809
	-0.07199508	732.99536936	-0.07534501
	0.00285424	-1076.06134890	0.00481117
		797.94807805	-0.00012043
		-235.90390422	

A.5 Comparison of Thermodynamic Property Calculation Methods

Xu and Goswami [106] model was compared with theoretical model based on Helmholtz free energy formulation [131] which is used in the National Institute of Standards and Technology (NIST) Reference Fluid Thermodynamic and Transport Properties Database (REFPROP) [132]. Figures A.1-A.3 show the comparison of the models for the saturation pressures, enthalpy and entropy of the saturated liquid and vapor of ammonia–water

www.manaraa.com

Appendix A: (Continued)

Table A.5 Coefficient values for the determination of mixture bubble and dew point temperatures (C_{ij})

C_{ij}			
-462.46032137	-9668295.89504000	-3583589.86875000	4807.07241098
23739.99863090	5922081.87086000	12243265.38150000	13565.10033090
-194504.35292000	-1432405.52125000	-22307970.01560000	-466407.78083200
639383.52886700	421.44312221	22896656.84990000	2827083.44764000
-523748.05763600	-14560.35492500	-12483324.80910000	-8469715.15799000
-2328271.47551000	53051.44956330	2813311.71633000	14459588.89620000
7562418.53499000	382763.79358200	-248.78380417	-14281087.53310000
7596403.59678000	2132412.46959000	-3064.82070658	-54497.09733360
-1684002.64482000	-3699199.65914000	71.79547521	3.97454954
126.96558073	3688365.22546000	51780.66665900	-77.02684647
-2090.45270574	-1975122.39296000	-209714.89985600	541.19105807
1993.17101166	440201.44606800	405011.98535500	-1696.60270972
100706.51039600	-33.53434462	-428310.46156600	1713.45942707
-687388.80861200	601.87858669	238153.69832600	4019.01019872
-14844.79280040	113.76206455		
19481.00945510	-258.75049692		
-12107.07945010	311.00258522		
2966.92804386	-123.91799345		
-0.17080617	-123.48062749		
3.48182859	154.37504211		
-27.79575877	-48.50838287		

Table A.6 Coefficient values for the determination of mixture bubble and dew point temperatures (A_{ij})

A_{ij}			
194.79391346	-4.78866919	-0.90857588	-0.01916646
74.23612419	-0.22541673	-0.35675269	-0.00170143
9.84103820	13.01754474	0.02380673	0.00195442
0.43684385	6.15865641	0.00495594	0.00280533
-74.35082834	0.78974034	-0.00071864	0.00138994
-33.29418798	0.03215108	-0.02510264	0.00011642

www.manaraa.com

mixtures. The maximum relative difference for the saturated liquid pressure, enthalpy and entropy is less than 3.5%. The maximum relative difference of saturation pressure, enthalpy and entropy for the saturated vapor are 9.8%, 0.3% and 1.0%, respectively.

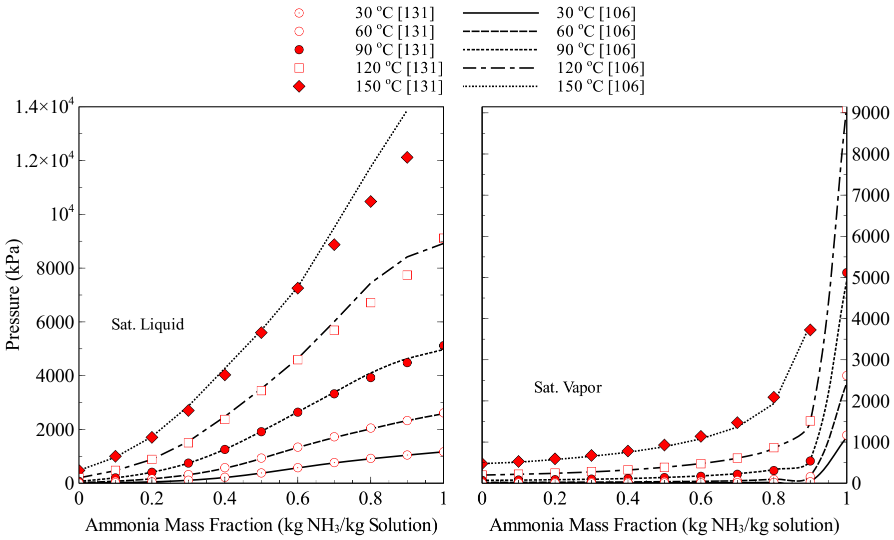

Figure A.1 Comparison of ammonia water mixture saturation pressures by Xu and Goswami [106] and Tillner-Roth and Friend [131]

Earlier studies of this work was accomplished by using Chemcad [104]. The Predictive Soave-Redlich-Kwong (PSRK) equation of state and Latent-heat H model were used in the software to obtain the thermodynamic properties and phase equilibrium of the ammonia-water mixture. The equation of state PSRK combines the Universal Quasi Chemical Functional Group Activity Coefficients (UNIFAC) model with the Soave-Redlich-Kwong (SRK) equation of state. Previous studies have shown that the PSRK is in good agreement with the experimental phase equilibrium of ammonia-water mixtures [133, 134]. The PSRK and Latent-heat H model were also compared with theoretical model based on Helmholtz free energy formulation [131]. Figures A.4-A.6 show the comparison of the PSRK and

للاستشارات المنارة
www.manaraa.com

Appendix A: (Continued)

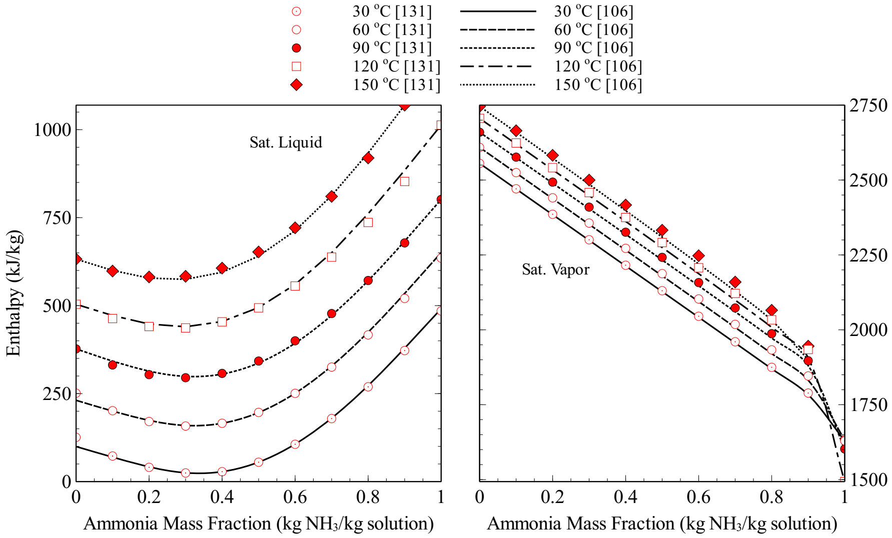

Figure A.2 Comparison of ammonia water mixture saturated liquid and vapor enthalpy by Xu and Goswami [106] and Tillner-Roth and Friend [131]

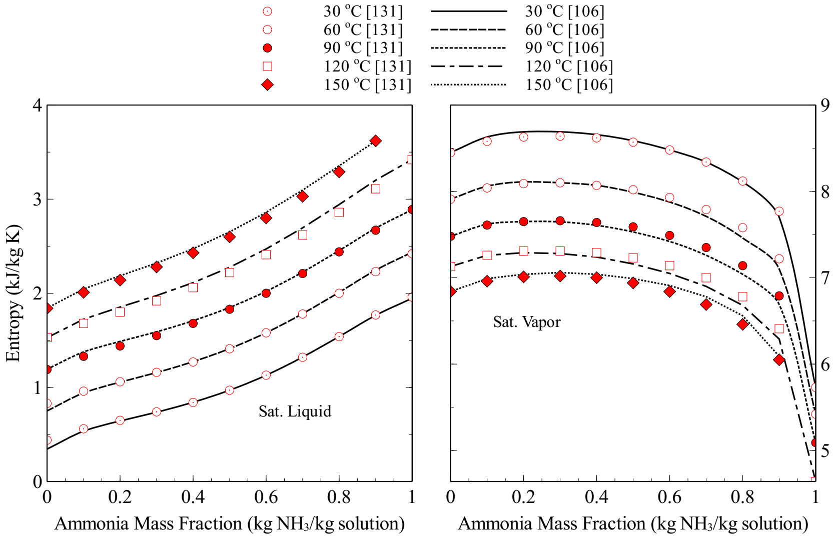

Figure A.3 Comparison of ammonia water mixture saturated liquid and vapor entropy by Xu and Goswami [106] and Tillner-Roth and Friend [131]

Latent-heat H models with Helmholtz free energy [131] models for the saturation pressures, enthalpy and entropy of the saturated liquid and vapor of ammonia–water mixtures. The average relative difference of saturation pressure, enthalpy and entropy values between

www.manaraa.com

the PSRK and Latent-heat H model and the two data sets for saturated liquid are 7.0%, 8.0% and 8.1%, respectively. The average relative difference for the saturated vapor is less than 3.2%.

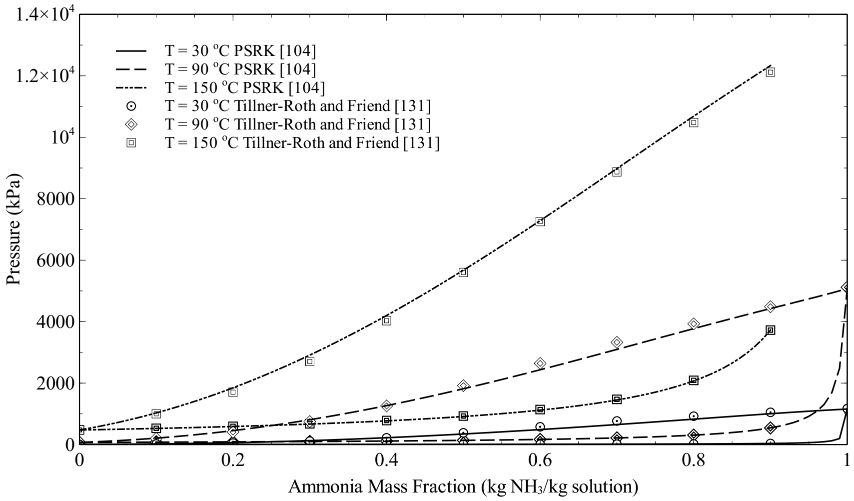

Figure A.4 Comparison of ammonia water mixture saturation pressures by PSRK [104] and Tillner-Roth and Friend [131]

www.manaraa.com

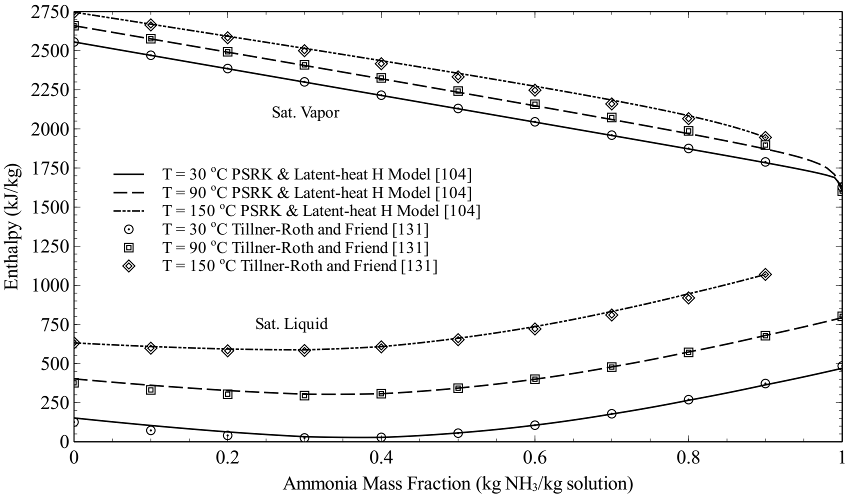

Figure A.5 Comparison of ammonia water mixture saturated liquid and vapor enthalpy by PSRK & Latent-heat H [104] and Tillner-Roth and Friend [131]

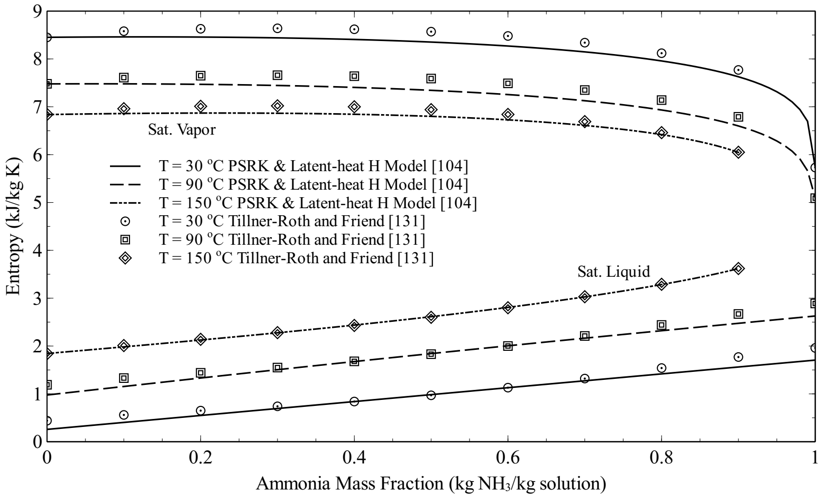

Figure A.6 Comparison of ammonia water mixture saturated liquid and vapor entropy by PSRK & Latent-heat H [104] and Tillner-Roth and Friend [131]

www.manaraa.com

Appendix B: Thermodynamic Model

The thermodynamic model used to generate the simulated results of this work is described here. The thermodynamic model is based on the cycle configuration shown in Fig. B.1. For a binary mixture, two intensive properties and the concentration of the mixture are sufficient to establish all the other properties. Some combinations include pressure, temperature and concentration (P,T,x); pressure, specific enthalpy and concentration (P,h,x); or pressure, specific entropy and concentration (P,s,x).

Formulation begins in the absorber where two inputs are given, the absorber exit temperature $(T_1 = T_{absorber})$ and basic solution concentration (x_1). Assuming the basic solution is at or very near saturation, property data is used to determine the system low pressure.

$$P_1 = P_{absorber} = P_{sat,liquid}(T_1, x_1) \tag{B.1}$$

Boiler pressure $(P_2 = P_{boiler})$ is another input; an energy balance across the pump yields Eq. B.2,

$$h_2 = \frac{(h_{2s} - h_1)}{\eta_{pump}} + h_1 \tag{B.2}$$

where h_{2s} is the enthalpy calculated at $(P_2, s_2 = s_1, x_2 = x_1)$, and η_{pump} is the pump efficiency. State 2 can be determined using property data at (P_2, h_2, x_2). Pump work is given in Eq. B.3.

$$\dot{W}_{pump} = \dot{m}_1 \times (h_2 - h_1) \tag{B.3}$$

The saturated liquid-vapor mixture enters the separator after the boiler heat exchanger, and the vapor and liquid components are separated by gravity at the separator. In order to calculate states 5 and 9, three hypothetical states are used; state "5^{pr}" is the vapor leav-

www.manaraa.com

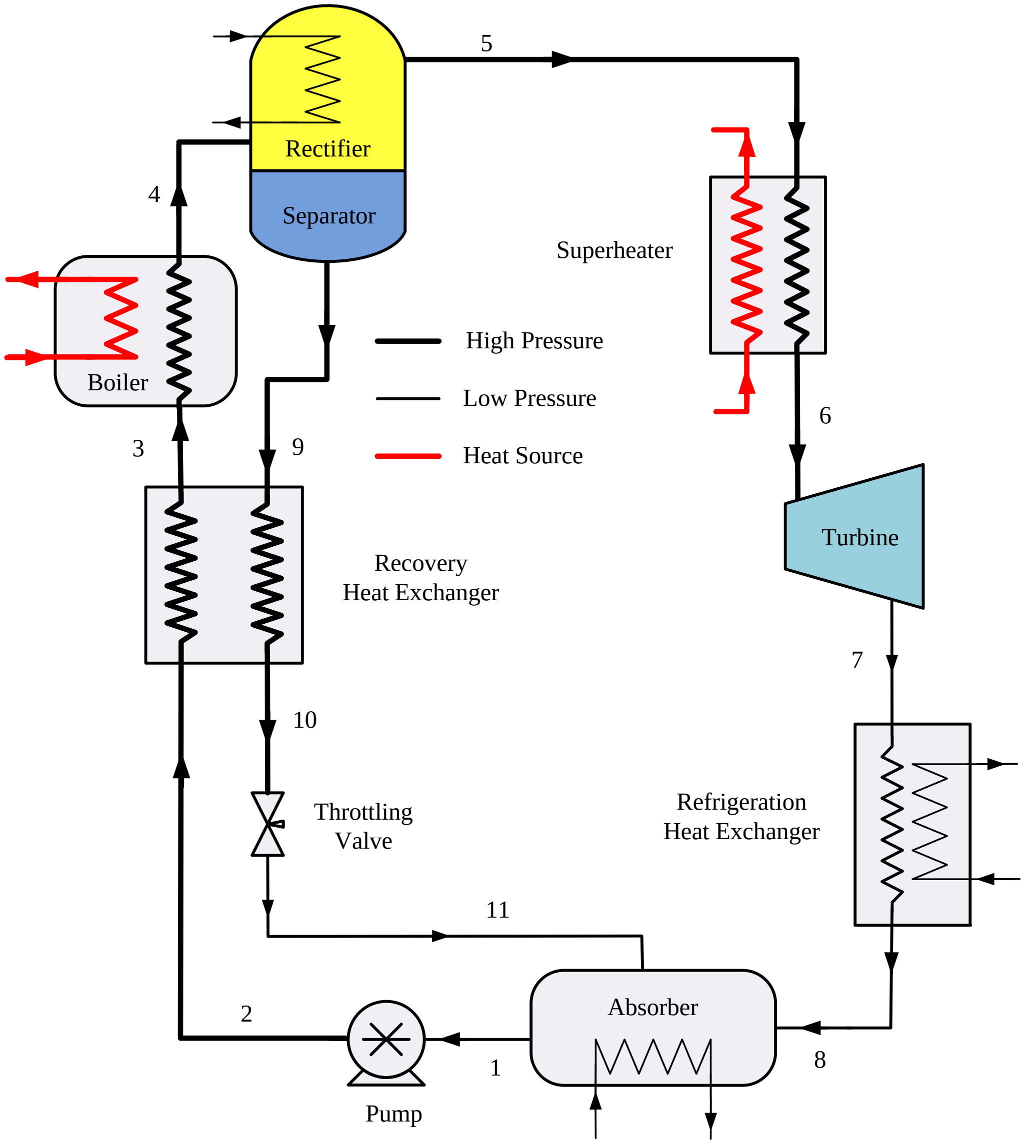

Figure B.1 Schematic description of the Goswami cycle used for thermodynamic formulations

ing the separator, state “9^{pr}” is the liquid separated from the vapor at the separator, state “*condensed*” is the liquid condensate formed at the rectifier. The ammonia concentrations of state 5 and hypothetical states are given in Eqs. B.4-B.7.

www.manaraa.com

$$x_5 = x_{dew}(P_5, T_5) \tag{B.4}$$

$$x_{condensed} = x_{bubble}(P_5, T_5) \tag{B.5}$$

$$x_{5^{pr}} = x_{dew}(P_4, T_4) \tag{B.6}$$

$$x_{9^{pr}} = x_{bubble}(P_4, T_4) \tag{B.7}$$

Furthermore, mass flow rates of the state 5 and hypothetical states are given in Eqs. B.8-B.9, which are found by the mass balance equations at the separator and rectifier.

$$\frac{\dot{m}_{5^{pr}}}{\dot{m}_4} = 1 - \frac{\dot{m}_{9^{pr}}}{\dot{m}_4} = \frac{x_4 - x_{9^{pr}}}{x_{5^{pr}} - x_{9^{pr}}} \tag{B.8}$$

$$\frac{\dot{m}_5}{\dot{m}_{5^{pr}}} = 1 - \frac{\dot{m}_{condensed}}{\dot{m}_{5^{pr}}} = \frac{x_{5^{pr}} - x_{condensed}}{x_5 - x_{condensed}} \tag{B.9}$$

There is now enough information to specify the weak solution (state 9); it is determined from the junction (states 9^{pr} and *condensed*) mass and energy balances. The mass flow rate, enthalpy and concentration of the state 9 are given in Eqs. B.10-B.12,

$$\dot{m}_9 = \dot{m}_{9^{pr}} + \dot{m}_{condensed} \tag{B.10}$$

$$h_9 = \frac{h_{9^{pr}}\dot{m}_{9^{pr}} + h_{condensed}\dot{m}_{condensed}}{\dot{m}_9} \tag{B.11}$$

$$x_9 = \frac{x_{9^{pr}}\dot{m}_{9^{pr}} + x_{condensed}\dot{m}_{condensed}}{\dot{m}_9} \tag{B.12}$$

المنارة للاستشارات
www.manaraa.com

Temperature and other properties of state 9 can be determined using property data at (P_9, h_9, x_9). For the recovery heat exchanger exit conditions, an effectiveness value is assumed, and based on the maximum heat transfer that can occur, the exit states can be determined. Assuming counter-flow operation, the limiting exit conditions are either that T_3 is raised to T_9 or T_{10} is cooled to T_2 so the maximum heat exchange is the minimum of Eq. B.13.

$$\dot{Q}_{max,recovery} = min\,of\,\dot{m}_3(h_{3,max} - h_2)\,or\,\dot{m}_9(h_9 - h_{10,min}) \tag{B.13}$$

where $h_{3,max}$ and $h_{10,min}$ are calculated at the temperatures of T_9 and T_2, respectively. Subsequently, the recovery unit exit states are determined by Eqs. B.14 and B.15.

$$h_3 = \frac{\dot{Q}_{max,recovery} \times \varepsilon}{\dot{m}_3} + h_2 \tag{B.14}$$

$$h_{10} = h_9 - \frac{\dot{Q}_{max,recovery} \times \varepsilon}{\dot{m}_9} \tag{B.15}$$

The weak solution throttle is assumed to be isenthalpic, Eq. B.16.

$$h_{11} = h_{10} \tag{B.16}$$

The boiler heat transfer and rectifier cooling load can be determined by the energy balance across the components, and given in Eqs. B.17-B.18.

المنارة للاستشارات
www.manaraa.com

$$\dot{Q}_{boiler} = \dot{m}_4(h_4 - h_3) \tag{B.17}$$

$$\dot{Q}_{rectifier} = \dot{m}_5 h_5 + \dot{m}_9 h_9 - \dot{m}_4 h_4 \tag{B.18}$$

The vapor entering the superheater is assumed to be saturated, state 5. As with the rectifier operation, the superheater operation is determined by specifying the exit temperature. Since pressure and concentration are also known, the other thermodynamic properties can be determined. This brings computation to the inlet of the expander. An isentropic expander efficiency is assumed and the exit conditions are found by the Eq. B.19.

$$h_7 = h_6 - \eta_{turbine}(h_6 - h_{7s}) \tag{B.19}$$

Turbine work output and the net work are calculated as given in Eqs. B.20-B.21,

$$\dot{W}_{turbine} = \dot{m}_5 \times (h_6 - h_7) \tag{B.20}$$

$$\dot{W}_{net} = \dot{W}_{turbine} - \dot{W}_{pump} \tag{B.21}$$

Having determined the expander exit enthalpy, there is sufficient information to determine its exhaust temperature at ($P_{absorber}$,x_{vapor},h_7). Based on this exhaust temperature, the cooling heat exchanger may not be active if the temperature is not below the limit specified for cooling production. For the analysis of cooling production, this threshold temperature was 15 °C. If T_7 is higher than this, then the cooling heat exchanger has no effect. If the

المنارة للاستشارات

www.manaraa.com

exhaust temperature is below the threshold, vapor is heated to the threshold temperature. The cooling output from the cycle is calculated as given in Eq. B.22.

$$\dot{Q}_{cooling} = \dot{m}_{vapor}\left(h_7 - h_8\right) \tag{B.22}$$

Finally, all of the conditions needed to compute the heat rejected in the absorber are know. From an energy balance of the absorber the rejected heat can be determined from Equation B.23. This concludes the calculations needed to solve for the conditions in this configuration of the power-cooling cycle.

$$\dot{Q}_{absorber} = \dot{m}_{11}h_{11} + \dot{m}_8 h_8 - \dot{m}_1 h_1 \tag{B.23}$$

المنارة للاستشارات
www.manaraa.com

Appendix C: Experimental Details

The experimental procedures have been described in Chapter 4, this section provides the details needed to operate ancillary equipment. This appendix provides the instrumentation details of the experimental setup. The basic operational principle of each instrument is followed by its specification, calibration technique, and measurement uncertainty.

C.1 Data Acquisition System

All of the data, aside from the manually recorded measurements, was collected with a DaqBook 200 acquisition system. For hardware information refer to the equipment list later in this Appendix, and for hardware configuration please refer to the operating manual for the DaqBook system. The acquisition software used is called DaqView. In this software each transducer is assigned a channel which can have its own calibration factors, i.e. for a linear fit, a slope and intercept. The factors used for this purpose were obtained by calibrating the transducers. As for data collection, a sampling rate of 25 scans per second for one second was used. The data was converted from binary-coded to ASCII format and saved as a text file.

C.2 Gas Chromatograph (GC)

Gas Chromatography is an analytical technique used to qualitatively and quantitatively identify the volatile substances in a mixture. It works on the principle that selective adsorption/desorption rate of volatile compounds over an adsorbent separates the volatile mixture into its individual constituents. The major components of a gas chromatograph include a carrier gas, an oven, a separation column and a detector. A carrier gas which is usually an inert gas, such as helium, argon or nitrogen, is used to move the sample through the separa-

www.manaraa.com

Figure C.1 Photograph of the gas chromatograph device used to calculate ammonia concentration

column at different time. The sample thus separates into individual constituents, and the components are separately analyzed by the detector.

The selection of detectors depends on the type of substance to be analyzed. The wide range of detectors include the flame ionization detector (FID), thermal conductivity detector (TCD), electron capture detector (ECD), photoionization detector (PID), flame photometric detector (FPD) and thermionic detector. The signal generated by the detector is later processed and plotted with respect to time. The components then appear as peaks on a time dependent chart. The retention time identifies the constituent, whereas, the area under the peak represents its concentration in the sample. The concentration of the ammonia-water binary solution was measured by a Gas Chromatograph having thermal conductivity detector (TCD). Samples of the binary mixture were collected in a syringe through septum ports

www.manaraa.com

installed in the experimental setup. The syringe was pre-cooled before analyzing a liquid mixture to prevent the boiling of the liquid sample in the syringe.

C.2.1 Gas Chromatograph Calibration

For the ammonia and water mixture, the ratio of the area under the ammonia peak to the total area under all of the peaks is given in Eq. 1 as a percentage.

$$\%A_{NH_3} = 100\frac{A_{NH_3}}{A_{NH_3} + A_{H_2O}} \tag{C.1}$$

The area of each component is proportional to the mass fraction of that species in the sample, according to Eqs. 2 and 3, and scales with the sample size, a. The constants on the right hand side of the equations, A, can be found for a unit sample size of pure water and pure ammonia.

$$\%A_{NH_3} = A_{NH_3}\,|_{x=1}\, x \tag{C.2}$$

$$\%A_{H_2O} = A_{H_2O}\,|_{x=0}\,(1-x) \tag{C.3}$$

Using the above equations as calibration curves is inconvenient, requiring exact measurement of every sample size and two calibration points to determine the constants. Eq. 1 can be written by combining it with Eqs. 2 and 3, and a general calibration curve as Eq. 5 can be obtained,

المنارة للاستشارات

www.manaraa.com

$$\%A_{NH_3} = 100\frac{cx}{(c-1)x+1} \tag{C.4}$$

$$C = \frac{A_{NH_3}\,|_{x=1}}{A_{H_2O}\,|_{x=0}} = \left(\frac{1-x_c}{x_c}\right)\left(\frac{\%A_{NH_3}\,|_{x=x_c}}{100-\%A_{NH_3}\,|_{x=x_c}}\right) \tag{C.5}$$

The obvious advantage of having an area percentage in the calibration curve rather than the area itself is to take sample size out of the correlation provided the sample size is within limits of the column and TCD performance. With the calibration constant found from Eq. 5, the ammonia mass fraction of any sample can be determined from the NH3 area percentage given by the GC analysis according to Eq. 4. The constant, C, is evaluated at a single calibration point, using a known sample of mass fraction xc. A standard ammonia-water liquid mixture at 29.95% of ammonia mass fraction is used for determining the calibration constant. A total of 15 measurements were made for the standard sample, and the average value of C was 0.9794.

C.2.2 GC Procedures

The startup and settings for the GC are as follows.

1. Verify that the HaysepT column for ammonia-water separation is installed.
2. The helium carrier gas supply tank is opened. The regulator valve leading to the GC is also opened. The regulator should be adjusted to approximately 60 psig. Gas flow past the thermal conductivity detector (TCD) can be verified by immersing the exhaust tube from the TCD oven, which is located inside the main oven, into a small vial of water and observing bubbles leaving the tube.

www.manaraa.com

3. Power is turned on to the data acquisition PC and the PC-GC interface. With the computer on, the GC software “PeakSimple” is started and the appropriate control file is loaded, “ThermodynamicCycle.con”. Set initial zero values for Channel 1 and Channel 2 from the event section. The temperature ramp file is included in the control file.

4. The GC itself can now be turned on and the settings verified. The on-board flow regulator should be set at 200 corresponding to 6.4 mL/min. The TCD attenuator switch should be set to 1. Using the GC’s digital readout the following temperatures and pressures should be verified.

5. Carrier 1 pressure should be 50 psig.

6. Head pressure 1 should be approximately 3.3-3.7 psig, pressures significantly different from this may require replacement of the injection septum.

7. Oven temperature set point of 80° C.

8. TCD set point of 95° C.

9. The filter bake switch on the GC is switched on.

10. The TCD current switch is switched to the high setting. The GC needs about one to two hours to warm up, such that the TCD output stabilizes. Samples typically cleared the detector in less than 25-30 minutes with these conditions, so this was chosen as the length of the data acquisition cycle. Shutdown of the GC is the reverse of startup.

www.manaraa.com

C.2.3 Syringe Sampling Techniques

The GC can determine ammonia mass fractions of both liquid and vapor samples that are inserted into its injection port via syringe. The liquid sample is vaporized while it passes through the packed column, such that the sample is a vapor as it reaches the TCD for analysis. Because the liquid sample specific volume is much smaller than that for a vapor sample, the liquid sample size is correspondingly smaller. Experimentally it has been determined that a liquid sample size of about 2.5-5 μL is sufficient to detect peaks. If the sample size is much larger, the ammonia and water peaks may not separate out well.

The temperature of the syringe is important for two reasons. A false sample may be drawn if the needle tip is above the bubble point in liquid sampling. This unwanted phase change at the needle tip will influence the composition of the sample being drawn. Secondly, it is desirable to avoid a liquid-vapor mixture in the sample, as during insertion not all of the liquid or vapor will be inserted. Since the liquid and vapor will not contain the same ammonia mass fraction, the sample that is inserted may not correctly reflect the sample that was drawn. For liquid samples, the syringe should thus be cooled prior to use to ensure the sample remains cooled below the bubble point during drawing. Note under normal operation, both liquid sampling ports in the system are at sub-cooled fluid regions. The syringe should be pumped a few times during drawing, to replace any dead volume and water that was used for cleaning it with the desired sample. Take care not to allow the system pressure to force the plunger out of the syringe, or the system will leak through the syringe. The syringe is then locked, removed from the sampling port, and transported

المنارة للاستشارات
www.manaraa.com

to the GC. After complete insertion into the GC, the syringe is unlocked and the contents injected quickly. The syringe is removed and cleaned with tap water to prevent corrosion, then cooled for the next use.

C.3 Equipment Specification

This section details the measurement equipment and generator used for this work. For details regarding the physical makeup of the rest of the experimental setup, which is not covered in detail here, the reader is referred to the description given in Chapter 5. The measurement devices are shown in Fig. C.2. The following table lists the specification of various measurement instruments as provided by the manufacturer. The pertinent descriptive information about the measurement equipment used is detailed in Table C.2.

This section also provides details of the calibration scheme used in the current experimental work. An instrument is usually not individually calibrated by the manufacture, rather a sample size of instruments are tested to obtain a generalized calibration curve. The variation among the sample size is overlapped by having a larger uncertainty band to

Table C.1 Gas chromatograph equipment list

Device	Manufacturer	Specifications
Gas Chromatograph	SRI	Model 8610
Ammonium Hydroxide	Fisher Scientific	29.95% assay
GC Column	HayeSep	S.S. HayeSep T packed column 3’ x 1/8”, 8600-PKTA
Liquid Sampling Needle	Hamilton	Hamilton # 80728 (22s/2”/2)L
Liquid Syringe	Hamilton	50 µL; removable needle type
Sampling Port	Flow Design	
Thermal Conductivity Detector	SRI	4 gold filaments; 8690-0007T

www.manaraa.com

Appendix C: (Continued)

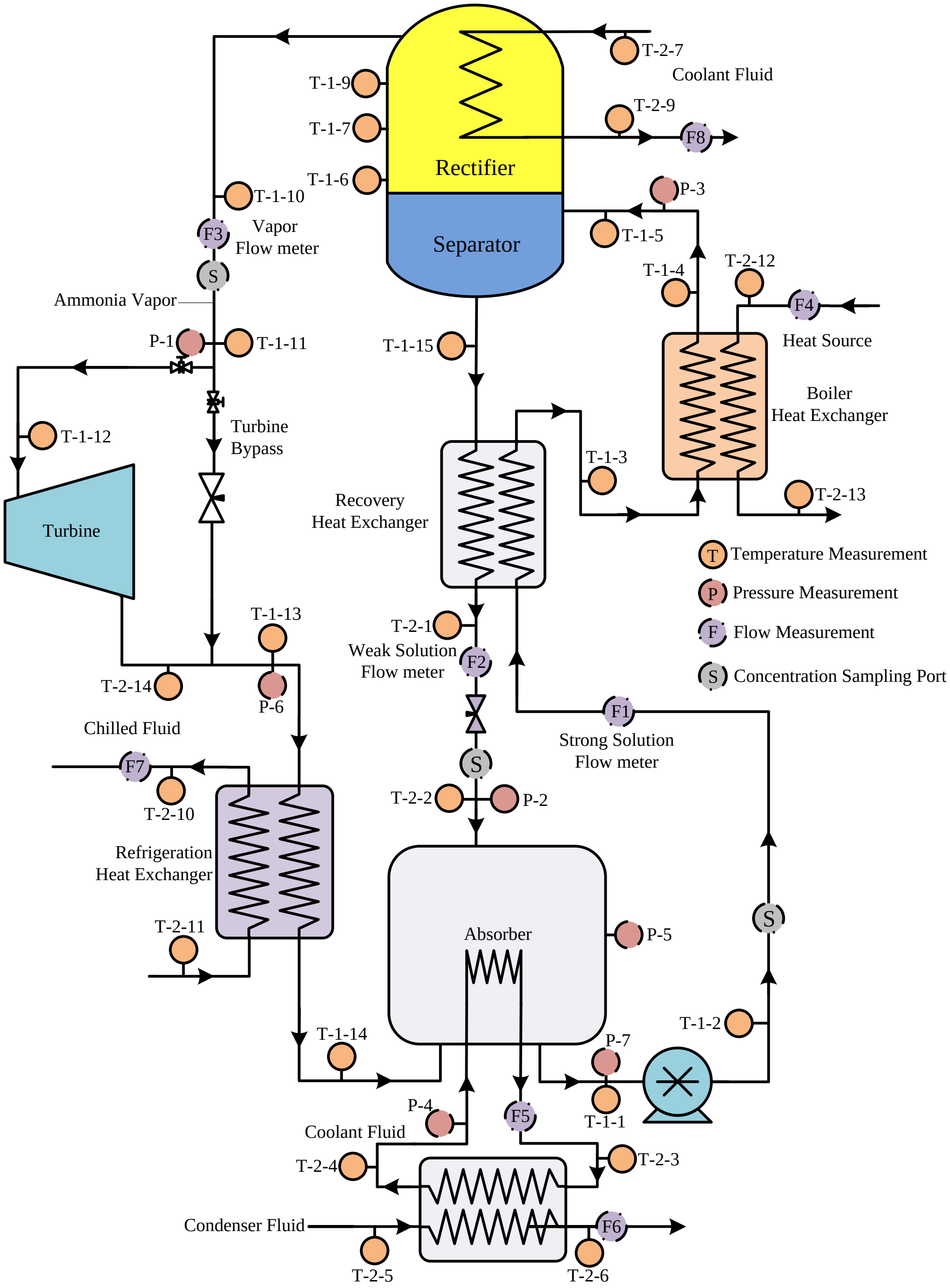

Figure C.2 Schematic description of the experimental Goswami cycle

المنارة للاستشارات
www.manaraa.com

Table C.2 Detailed descriptions of the instrumentation and measurement equipment used for this work, major equipment

Device	Manuf.	Model	Specifications
Data Acq. PC Interface	IoTech	DaqBook 200	16-bit analog to digital converter; 100 kHz sampling rate
Data Acq. Software	IoTech	Daq View	Version 3.14
Current/Voltage Meas. Card	IoTech	DBK 15	16 channels; measures 4 – 20 mA as well as voltage up to ±30 V
Thermocouple Meas. Card	IoTech	DBK 82	14 channels; accuracy ±0.5 °C
Thermocouple	Omega	TMQSS	T-type; accuracy ±1°C

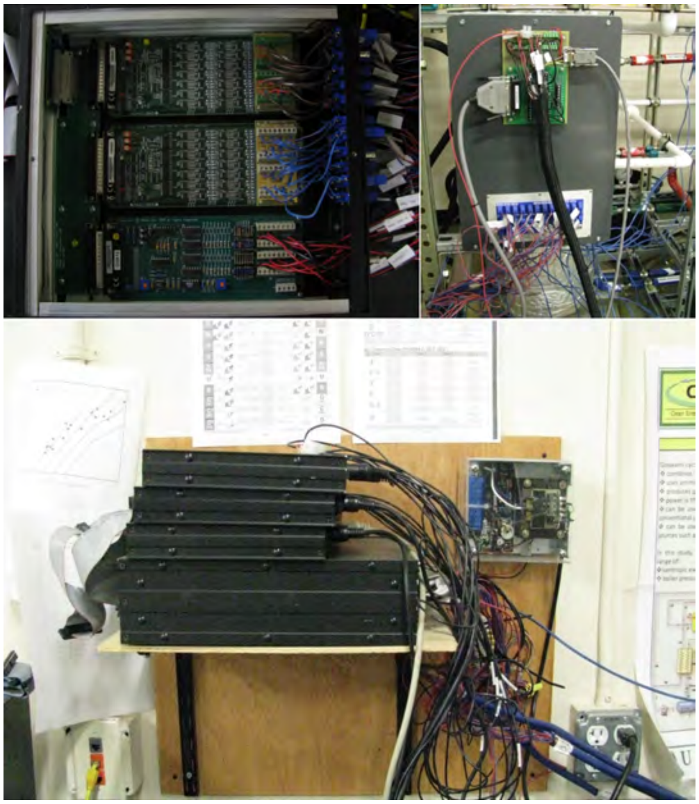

Figure C.3 Photograph of the data acquisition cards and cable connectors

eliminate the tedious and expensive calibration of individual instruments. Measurement inaccuracies are further increased by the introduction of external factors, such as instal-

www.manaraa.com

Table C.3 Detailed descriptions of the instrumentation and measurement equipment used for this work, pressure transducers

Pressure Transducers	Manufacturer	Part Number/Model	Specifications
Absorber	Cole Parmer	Model 68070-02	Range 0 – 50 psig; output 4 – 20 mA; input 24 VDC; accuracy ±0.13% full scale
Absorber Exit, 2	Cole Parmer	Model 68073-04	Range -14.7 – 60 psig; output 4 – 20 mA; input 24 VDC; accuracy ±0.13% full scale
Vapor Throttle Exit, 3	Cole Parmer	Model 68073-04	Range -14.7 – 60 psig; output 4 – 20 mA; input 24 VDC; accuracy ±0.4% full scale
Absorber Vapor Inlet, 4	Cole Parmer	Model 07356-13	Cole Parmer (800) 323-4340
Absorber Weak Inlet, 5	Cole Parmer	Model 68073-06	Range -14.7 – 100 psig; output 4 – 20 mA; input 24 VDC; accuracy ±0.13% full scale
Separator Entrance, 6	Setra	Model 256	Range 0 – 250 psig; output 4 – 20 mA; input 24 VDC; accuracy ±0.13% full scale
Turbine Inlet, 7	Setra	Model 256	Davis Inotek Instruments (800) 368-2516
Turbine Exhaust, 8	Cole Parmer	Model A-68073-04	Cole Parmer (800) 323-4340
Absorber coolant	Cole Parmer	68071-58	Range 0 – 10 psid; output 4 – 20 mA; input 24 VDC ; accuracy ±0.25% full scale

lation, noise and environmental effects. Thus, the individual calibration of instruments is desired to ensure and improve the accuracy of a measurement. An effort was made to test the instruments for the validity of their measurement accuracy, and incorporate a correction factor to further improve their precision. Though most of the instruments are calibrated in the laboratory, the error of instruments as reported by the manufacturer is still used for the

www.manaraa.com

Figure C.4 Photograph of a pressure transducer

experimental analysis. Numerous unaccountable errors like installation, noise and environmental effects make it infeasible to predict the actual error of the device after calibration. The purpose of calibration was to improve the precision of instruments, and to ascertain that the error is within the uncertainty bands as mentioned by the manufacturer.

Rotameter is the most common type of flow meter consisting of a uniformly tapered flow passage and a float. It is installed vertically along the length of the tapered tube with larger diameter end at the top. The fluid enters the tapered flow path from the bottom end, and it causes a resultant pressure differential across the float. The imbalance in vertical

www.manaraa.com

Figure C.5 Photograph of the voltage and current transducers

forces across the float causes it to rise in the tapered flow passage. The flow passage being tapered, the rise of the float increases the flow area and thus reduces the differential pressure. The float rises until a balance between the forces of gravity, buoyancy and upward differential pressure is achieved. The stable position of the float is indicative of the flow rate. The range of a rotameter for a given process fluid can be changed by changing the float density. Thus, they provide an economical, reliable and simple solution to a wide range of flow measuring requirements.

المنارة للاستشارات
www.manaraa.com

Table C.4 Detailed descriptions of the instrumentation and measurement equipment used for this work, flow meters

Flow meters	Manufacturer	Part Number/Model	Specifications
Vapor	Hoffer Flow Controls, Inc	Model HO3/4X3/4	Turbine flow meter; range 1.25 – 25 m3/hr; accuracy ±1% of reading
Basic Solution	Brooks Instrument	Model 1110	Variable area flow meter; range 0.11 – 1.11 gpm; accuracy ±1% full scale; calibrated at 0.833 sg and 1.08 cP
Weak Solution	Brooks	Model 1110	Variable area flow meter; range 0.08 – 0.84 gpm; accuracy ±1% full scale; calibrated at 0.88 sg and 1.08 cP
Absorber coolant	Model A1	Great Plains Industries, Inc.	Paddlewheel flow meter; range 0.3 – 3 gpm; accuracy ±1% full scale

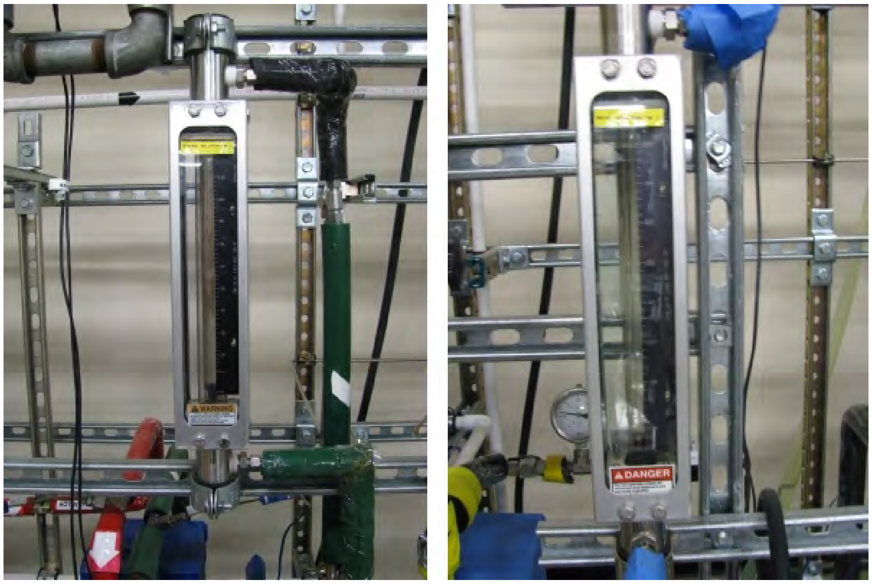

Figure C.6 Photograph of the strong and weak solution flow meters

www.manaraa.com

The weak and strong solution flow rates are measured with variable area flow meters. The material of the float in both rotameters is SS 316 (density 8016 kg/m3). The weak and strong solution flow meters were calibrated for fluids having specific gravity of 0.88 and 0.833, respectively. Thus, a correction factor is required to account for the difference in densities of actual and calibration fluids. The relation between the actual and measured volumetric flow rates is given by,

Figure C.7 Photograph of the vapor flow meter

$$\dot{V}_{actual} = \dot{V}_{measured} \left[\frac{\rho_{cal} \left(\rho_{float} - \rho_{actual} \right)}{\rho_{actual} \left(\rho_{float} - \rho_{cal} \right)} \right]^{1/2} \tag{C.6}$$

Turbine flow meter consists of a rotor having an axis of rotation perpendicular to the flow stream. The multi-bladed rotor is suspended in the flow path. The fluid flow causes the spinning of rotor, and its rotational speed is proportional to the flow rate. The rotational

www.manaraa.com

speed of rotor is measured by mechanical, optical or electrical sensors. Vapor flow rate in the current experimental study is measured with the help of a turbine flow meter. The rotational speed of the rotor is sensed by a magnetic pickup coil. The signal is processed by the turbine transmitter (Model HIT-2A, Hoffer Flow Controls, Inc.), and its output is a 4-20 mA linearized signal proportional to the volumetric flow rate. The flow meter was calibrated for ammonia gas by the manufacturer, and the reported uncertainty is ±1% of the reading. The knowledge of temperature, pressure and concentration of the vapor phase then yields the mass flow rate from volumetric flow rate.

The specifications of the generator are given in Table C.5. This generator was designed for wind turbine applications.

Table C.5 Generator specifications

Generator	Manufacturer: Shin FU Corporation Volts: 130 Amps: 10 HP: 2.5 RPM: 4500 Rotation CCW Duty: Continuous. Listing : SP99001687

The detailed description of the heating and chiller systems are given in Chapter 4. The schematic drawing of these systems are given in Figures C.9-C.8.

المنارة للاستشارات

www.manaraa.com

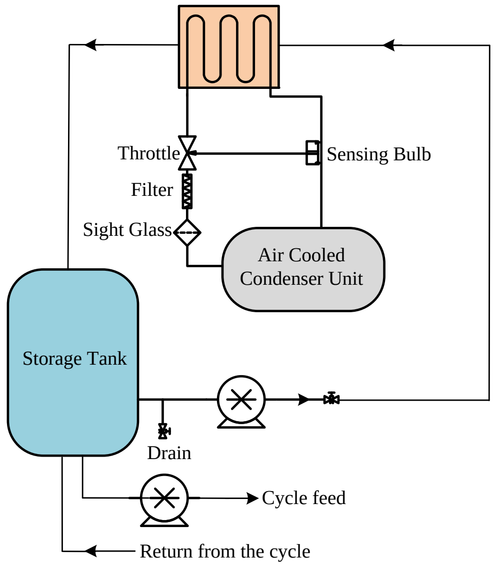

Figure C.8 Schematic drawing of the chiller system

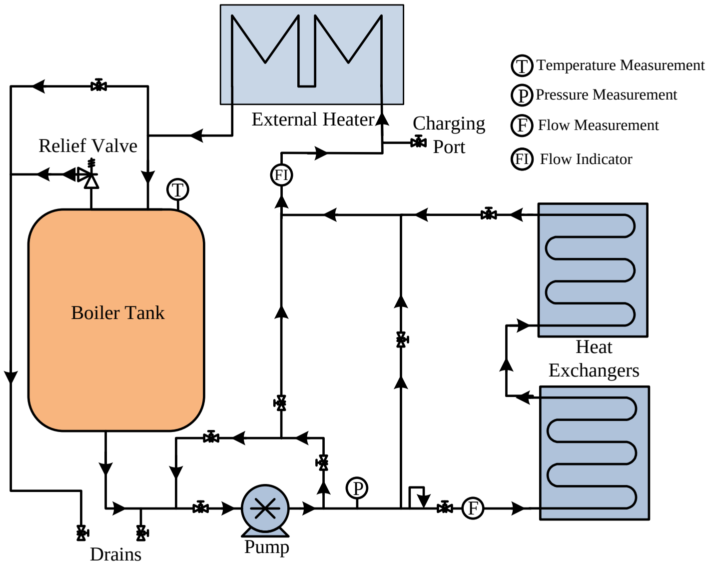

Figure C.9 Schematic drawing of the heat source system

المنارة للاستشارات
www.manaraa.com

Appendix D: Uncertainty Analysis

This Appendix provides the details of the uncertainty analysis used for the experimental study. The uncertainty analysis of the direct measurements are given first, and then the uncertainty of the derived measurements are presented later.

D.1 Uncertainty of Direct Measurements

The basic quantities, which define the state of a fluid are temperature, pressure, concentration and volumetric flow rate. These basic properties are much easier to measure, and are directly determined with the help of instruments. Other properties like work output, mass flow rate and turbine efficiency are theoretically related to the basic properties. Thus, uncertainties of these derived properties are also directly dependent on uncertainties of instruments used to measure basic properties. The root-sum-square method was used to combine the uncertainties of systematic and random errors. $\sigma_{systematic}$, is the fixed or constant component of the total error. The accuracy of the measurement device determines this systematic measurement uncertainty. σ_{random}, the random component of the total error is called the repeatability or precision error. The random error is calculated within the 90% confidence interval and given in Eq. D.1.

$$\sigma_{random} = \frac{\sigma_{measurements} \times 1.64485363}{\sqrt{N}} \tag{D.1}$$

The combined standard uncertainty U_C is given as,

$$U_c = \sqrt{\sigma_{systematic}^2 + \sigma_{random}^2} \tag{D.2}$$

www.manaraa.com

D.2 Uncertainty of Derived Measurements

To determine the accumulated error in derived measurements, those quantities that are functions of two or more primary measurements, the square root of the sum of the squares of the individual contributing errors is used. Consider a generalized derived measurement R as a function of several primary measurements r_i which is shown in Eq. D.3. The overall uncertainty of the derived measurement δ_R is dependent on the uncertainties of primary measurements and their individual sensitivity over the derived measurement, it is expressed in Eq. D.4.

$$R = f(r_1, r_2, \ldots, r_n) \tag{D.3}$$

$$\delta_R^2 = \left(\frac{\partial R}{\partial r_1}\right)^2 \delta_{r_1}^2 + \left(\frac{\partial R}{\partial r_2}\right)^2 \delta_{r_2}^2 + \ldots + \left(\frac{\partial R}{\partial r_n}\right)^2 \delta_{r_n}^2 \tag{D.4}$$

where $\delta_{r_1}, \ldots, \delta_{r_n}$ are uncertainties of the direct measurements. Many of the derived quantities depend on the fundamental measurements used with thermodynamic property data of ammonia-water. Since these relationships cannot be directly differentiated as indicated in the above equation, a finite difference numerical scheme is used to approximate them. The formulation for the central-difference approximation, neglecting higher order terms, is used, and shown in Eq. D.5.

$$\frac{\partial R}{\partial r_n} = \frac{f(r_1, r_2, \ldots, (r_n + dr_n)) - f(r_1, r_2, \ldots, (r_n - dr_n))}{2dr_n} \tag{D.5}$$

www.manaraa.com

The following paragraphs describe the derived measurements used in this work. The state numbers which will be given in the equations are shown in Fig. B.1. The measurement of the vapor composition by GC was unsuitable with the current configuration of sampling through a syringe. The vapor phase being at saturation state, it was decided to estimate its concentration by the application of vapor-liquid equilibrium correlations on the measured temperature and pressure of vapor stream. Thus, the uncertainty in determining the vapor concentration is directly related to the uncertainty of temperature and pressure measurements. The uncertainty of vapor concentrations are given in Eqs. D.6-D.8.

$$x_{vapor} = f(T,P) \tag{D.6}$$

$$x_{vapor} = f(T_5,P_5) \tag{D.7}$$

$$\delta^2_{x_{vapor}} = \left(\frac{\partial x_{vapor}}{\partial T_5}\right)^2 \delta^2_{T_5} + \left(\frac{\partial x_{vapor}}{\partial P_5}\right)^2 \delta^2_{P_5} \tag{D.8}$$

As mentioned in the Chapter 5, vapor concentration for the SV and SHV cases are initially calculated by the Eq. D.8. Later, the vapor concentration is also calculated by mass balance equations at the separator as discussed in the Chapter 5. Mass balance equations at the separator are given in Eqs. D.9-D.10, by using these equations we can find the vapor concentration, given in Eq. D.11. The uncertainty of vapor concentration based on the mass balance equations ($\delta_{\tilde{x}_{vapor}}$) are given in Eq. D.13. However, the work output and turbine efficiency uncertainties of the SV and SHV cases are calculated as the same as RHSV case; the uncertainty of work output and turbine efficieny are assumed as a function of vapor

المنارة للاستشارات
www.manaraa.com

mass flow rate, temperature and pressure, they are independent of the vapor concentration ($\tilde{x}_{vapor}$), which will be shown later in this appendix.

$$\dot{m}_{strong} = \dot{m}_{vapor} + \dot{m}_{weak} \tag{D.9}$$

$$\dot{m}_{strong}x_{strong} = \dot{m}_{vapor}\tilde{x}_{vapor} + \dot{m}_{weak}x_{weak} \tag{D.10}$$

$$\tilde{x}_{vapor} = x_{weak} + \frac{\dot{m}_{strong}}{\dot{m}_{vapor}}(x_{strong} - x_{weak}) \tag{D.11}$$

$$\tilde{x}_{vapor} = f(\dot{m}_{strong}, \dot{m}_{vapor}, x_{strong}, x_{weak}) \tag{D.12}$$

$$\begin{aligned}\delta^2_{\tilde{x}_{vapor}} \quad = \quad & \left(\frac{x_{strong} - x_{weak}}{\dot{m}_{vapor}}\right)^2 \delta^2_{\dot{m}_{strong}} + \left(\left(-\frac{\dot{m}_{strong}}{\dot{m}^2_{vapor}}\right)(x_{strong} - x_{weak})\right)^2 \delta^2_{\dot{m}_{vapor}} \\ & + \left(\frac{\dot{m}_{strong}}{\dot{m}_{vapor}}\right)^2 \delta^2_{x_{strong}} + \left(1 + \left(-\frac{\dot{m}_{strong}}{\dot{m}_{vapor}}\right)^2\right) \delta^2_{x_{weak}}\end{aligned} \tag{D.13}$$

The variable flow meters and the turbine flow meter utilized in the current experimental investigation measures volumetric flow rate. The weak and strong solution flow rates are measured through a variable flow meter, whereas the vapor flow rate is determined by a turbine flow meter. These measurements are converted into the mass flow rate with the multiplication of density, are given in Eq. D.14.

$$\dot{m}_{L,V} = \rho\dot{V} \tag{D.14}$$

Thermodynamic properties are used to compute the density of liquid and vapor phases at the given temperature, pressure and concentration. It should be noted that the concentration of vapor phase is determined from the temperature and pressure measurements, Eqs.

www.manaraa.com

D.15-D.17. Thus, the uncertainty in determining the mass flow rate is directly related to the uncertainty in volumetric flow, temperature, pressure and concentration measurements. The mass flow rate uncertainties are given in Eqs. D.18-D.20.

$$\dot{m}_{L,strong} = \rho(T,P,x)\dot{V} = f(T_2,P_2,x_{strong},\dot{V}_{strong}) \tag{D.15}$$

$$\dot{m}_{L,weak} = \rho(T,P,x)\dot{V} = f(T_{10},P_{10},x_{weak},\dot{V}_{weak}) \tag{D.16}$$

$$\dot{m}_{vapor} = \rho(T,P)\dot{V} = f(T_5,P_5,\dot{V}_{vapor}) \tag{D.17}$$

$$\begin{aligned}\delta^2_{\dot{m}_{L,strong}} &= \left(\dot{V}_{strong}\frac{\partial\rho}{\partial T_2}\right)^2 \delta^2_{T_2} + \left(\dot{V}_{strong}\frac{\partial\rho}{\partial P_2}\right)^2 \delta^2_{P_2} \\ &\quad + \left(\dot{V}_{strong}\frac{\partial\rho}{\partial x_{strong}}\right)^2 \delta^2_{x_{strong}} + (\rho)^2\,\delta^2_{\dot{V}_{strong}}\end{aligned} \tag{D.18}$$

$$\begin{aligned}\delta^2_{\dot{m}_{L,weak}} &= \left(\dot{V}_{weak}\frac{\partial\rho}{\partial T_{10}}\right)^2 \delta^2_{T_{10}} + \left(\dot{V}_{weak}\frac{\partial\rho}{\partial P_{10}}\right)^2 \delta^2_{P_{10}} \\ &\quad + \left(\dot{V}_{weak}\frac{\partial\rho}{\partial x_{weak}}\right)^2 \delta^2_{x_{weak}} + (\rho)^2\,\delta^2_{\dot{V}_{weak}}\end{aligned} \tag{D.19}$$

$$\delta^2_{\dot{m}_{vapor}} = \left(\dot{V}_{vapor}\frac{\partial\rho}{\partial T_5}\right)^2 \delta^2_{T_5} + \left(\dot{V}_{vapor}\frac{\partial\rho}{\partial P_5}\right)^2 \delta^2_{P_5} + (\rho)^2\,\delta^2_{\dot{V}_{vapor}} \tag{D.20}$$

For expander operation in the power-cooling setup, work output per unit time, power (P) was estimated from the thermodynamic states at turbine inlet and exhaust. The uncertainty of the power measurements are given in Eqs. D.21-D.25.

$$P = \dot{m}_{vapor}\left(h_{inlet} - h_{exit}\right) \tag{D.21}$$

المنارة للاستشارات

www.manaraa.com

$$P = \dot{m}_{vapor}\left(h_{inlet}(T,P) - h_{exit}(T,P)\right) \tag{D.22}$$

$$P = \dot{m}_{vapor}\left(h_6(T_6,P_6) - h_7(T_7,P_7)\right) \tag{D.23}$$

$$P = f\left(\dot{m}_{vapor}, T_6, P_6, T_7, P_7\right) \tag{D.24}$$

$$\begin{aligned} \delta_P^2 \;=\;& (h_6 - h_7)^2 \delta_{\dot{m}_{vapor}}^2 + \left(\dot{m}_{vapor}\frac{\partial h_6}{\partial T_6}\right)^2 \delta_{T_6}^2 + \left(\dot{m}_{vapor}\frac{\partial h_6}{\partial P_6}\right)^2 \delta_{P_6}^2 \\ & \left(-\dot{m}_{vapor}\frac{\partial h_7}{\partial T_7}\right)^2 \delta_{T_7}^2 + \left(-\dot{m}_{vapor}\frac{\partial h_7}{\partial P_7}\right)^2 \delta_{P_7}^2 \end{aligned} \tag{D.25}$$

Ideal computed power based on measured conditions are given in Eqs. D.26-D.30.

$$P_{ideal} = \dot{m}_{vapor}\left(h_{inlet} - h_{exit,(s_{inlet}=s_{exit})}\right) \tag{D.26}$$

$$P_{ideal} = \dot{m}_{vapor}\left(h_{inlet}(T,P) - h_{exit,(s_{inlet}=s_{exit})}(T,P)\right) \tag{D.27}$$

$$P_{ideal} = \dot{m}_{vapor}\left(h_6(T_6,P_6) - h_{7s}(T_6,P_6,P_7)\right) \tag{D.28}$$

$$P_{ideal} = f\left(\dot{m}_{vapor}, T_6, P_6, P_7\right) \tag{D.29}$$

$$\begin{aligned} \delta_{P_{ideal}}^2 \;=\;& (h_6 - h_{7s})^2 \delta_{\dot{m}_{vapor}}^2 + \left(\dot{m}_{vapor}\frac{\partial(h_6 - h_{7s})}{\partial T_6}\right)^2 \delta_{T_6}^2 \\ & + \left(\dot{m}_{vapor}\frac{\partial(h_6 - h_{7s})}{\partial P_6}\right)^2 \delta_{P_6}^2 + \left(-\dot{m}_{vapor}\frac{\partial h_{7s}}{\partial P_7}\right)^2 \delta_{P_7}^2 \end{aligned} \tag{D.30}$$

Based on the just-described, derived measurement, the expander efficiency is determined from two power output measurements are given in Eqs. D.31-D.34.

www.manaraa.com

$$\eta_{turbine} = \frac{P}{P_{ideal}} \tag{D.31}$$

$$\eta_{turbine} = f(P, P_{ideal}) \tag{D.32}$$

$$\delta^2_{\eta_{turbine}} = \left\{ \left(\frac{\partial\left(\frac{P}{P_{ideal}}\right)}{\partial P} \right)^2 \delta^2_P + \left(\frac{\partial\left(\frac{P}{P_{ideal}}\right)}{\partial P_{ideal}} \right)^2 \delta^2_{P_{ideal}} \right\} \tag{D.33}$$

$$\delta^2_{\eta_{turbine}} = \left\{ \left(\frac{1}{P_{ideal}} \right)^2 \delta^2_P + \left(-\frac{P}{P^2_{ideal}} \right)^2 \delta^2_{P_{ideal}} \right\} \tag{D.34}$$

Generator power output measurement is calculated by the multiplication of voltage and current measurement, and it is given in Eq. D.35. The uncertainty of the generator power measurements are given in Eqs. D.36-D.38.

$$P_e = V \times I \tag{D.35}$$

$$P_e = f(V, I) \tag{D.36}$$

$$\delta^2_{P_e} = \left(\frac{\partial P_e}{\partial V} \right)^2 \delta^2_V + \left(\frac{\partial P_e}{\partial I} \right)^2 \delta^2_I \tag{D.37}$$

$$\delta^2_{P_e} = (I)^2 \delta^2_V + (V)^2 \delta^2_I \tag{D.38}$$

المنارة للاستشارات

www.manaraa.com

About the Author

A Turkish citizen, Gökmen Demirkaya was born in Adana in 1977. He earned a BSc. degree in mechanical engineering from the Middle East Technical University (METU) in 2000. Upon graduation, he started to work on computational solutions of 3-D radiative heat transfer problems under the guidance of Dr. Faruk Arınç, and received his Master of Science in 2003. During his first two year at the graduate school, he also worked as an installation engineer at Aymet Singapore Land A.S. Later, he started to work as a research assistant at the International Centre for Heat and Mass Transfer before he moved to U.S. for pursuing a PhD. degree. He began doctoral studies at the University of South Florida under the guidance of Dr. Yogi Goswami. His doctoral research focused on experimental and theoretical modeling of power and cooling generation utilizing low temperature sources. During his graduate studies, Gökmen worked as a research assistant at the Clean Energy Research Center (CERC) and also assisted for graduate and undergraduate courses. In July 2008, Gökmen married Burcu Özgör. After graduation, he will pursue an industrial career in Turkey.

المنارة للاستشارات
www.manaraa.com